

DOMAIN-INTEGRAL METHODS FOR COMPUTATION OF
FRACTURE-MECHANICS PARAMETERS IN THREE-DIMENSIONAL
FUNCTIONALLY-GRADED SOLIDS

BY

MATTHEW C. WALTERS

B.S., Brigham Young University, 1997
M.S., University of Illinois at Urbana-Champaign, 2002

DISSERTATION

Submitted in partial fulfillment of the requirements
for the degree of Doctor of Philosophy in Civil and Environmental Engineering
in the Graduate College of the
University of Illinois at Urbana-Champaign, 2005

Urbana, Illinois

UMI Number: 3182412

INFORMATION TO USERS

The quality of this reproduction is dependent upon the quality of the copy submitted. Broken or indistinct print, colored or poor quality illustrations and photographs, print bleed-through, substandard margins, and improper alignment can adversely affect reproduction.

In the unlikely event that the author did not send a complete manuscript and there are missing pages, these will be noted. Also, if unauthorized copyright material had to be removed, a note will indicate the deletion.

UMI[®]

UMI Microform 3182412

Copyright 2005 by ProQuest Information and Learning Company.

All rights reserved. This microform edition is protected against unauthorized copying under Title 17, United States Code.

ProQuest Information and Learning Company
300 North Zeeb Road
P.O. Box 1346
Ann Arbor, MI 48106-1346

© 2005 by Matthew C. Walters. All rights reserved.

CERTIFICATE OF COMMITTEE APPROVAL

*University of Illinois at Urbana-Champaign
Graduate College*

April 13, 2005

We hereby recommend that the thesis by:

MATTHEW C. WALTERS


Entitled:


**DOMAIN-INTEGRAL METHODS FOR COMPUTATION OF
FRACTURE-MECHANICS PARAMETERS IN THREE-DIMENSIONAL
FUNCTIONALLY-GRADED SOLIDS**

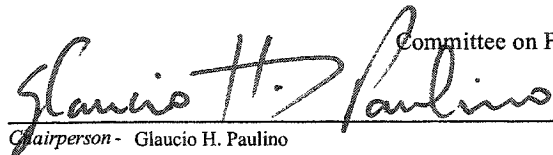
Be accepted in partial fulfillment of the requirements for the degree of:

Doctor of Philosophy

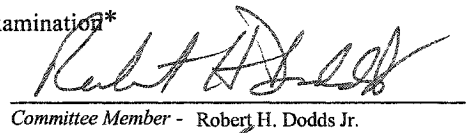
Signatures:

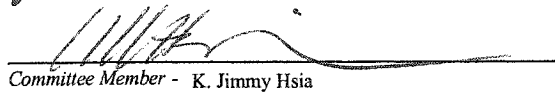

Director of Research - Glaucio H. Paulino


Head of Department - Robert H. Dodds Jr.


Chairperson - Glaucio H. Paulino

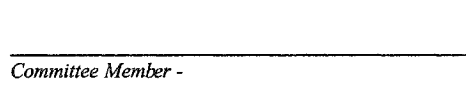
Committee on Final Examination*


Committee Member - Robert H. Dodds Jr.


Committee Member - K. Jimmy Hsia


Committee Member - John Lambros


Committee Member - C. Armando Duarte


Committee Member -

* Required for doctoral degree but not for master's degree

Abstract

Domain-Integral Methods for Computation of Fracture-Mechanics Parameters in Three-Dimensional Functionally-Graded Solids

A natural or engineered multiphase composite with macro-scale spatial variation of material properties may be referred to as a functionally graded material, or FGM. FGMs can enhance structural performance by optimizing stiffness, improving heat, corrosion or impact resistance, or by reducing susceptibility to fracture. One promising application of FGMs is to thermal barrier coatings, in which a ceramic coating with high heat and corrosion resistance transitions smoothly to a tough metallic substrate. The absence of a discrete interface between the two materials reduces the occurrence of delamination and spallation caused by growth of interface and surface cracks. Fracture remains an important failure mechanism in FGMs, however, and the ability to predict critical flaw sizes is necessary for the engineering application of these materials.

This presentation describes the development of numerical methods used to compute fracture parameters necessary for the evaluation of flaws in elastic continua. The current investigation employs post-processing techniques in a finite-element framework to compute the J -integral, mixed-mode stress intensity factors and non-singular T -stresses along generally-curved, planar cracks in three-dimensional FGM structures. Domain and interaction integrals developed to compute these fracture parameters have proved to be robust and accurate because they employ field quantities remote from the crack. The recent emergence of promising engineering applications of FGMs motivates the extension of these numerical methods to this new class of material.

This work first develops and applies a domain integral method to compute J -integral and stress intensity factor values along crack fronts in FGM configurations under mode-I thermo-mechanical loading. The proposed domain integral formulation accommodates both linear-elastic and deformation-plastic behavior in FGMs. Next discussed is the extension of interaction-integral procedures to compute mixed-mode stress intensity factors and T -stresses along planar, curved cracks in FGMs. The investigation addresses effects upon interaction integral procedures imposed by crack-front curvature, applied crack-face tractions and material nonhomogeneity. An additional consideration for T -stress evaluation includes the influence of mode mixity.

To my family.

Acknowledgements

The author is very grateful to those whose support and direction have assisted in the completion of this work. Thanks must first go to Professor Glaucio H. Paulino, who allowed me to join his group several years ago, and has been a continuous source of encouragement and direction ever since. Many thanks also to Professor Robert H. Dodds Jr., whose friendly guidance was always greatly appreciated. His approach to teaching, writing and research will remain with me as a standard.

I also gratefully acknowledge the financial support of NASA, through the Graduate Student Researchers Program under the direction of Tina L. Panontin at Ames Research Center. This support allowed me to undertake this study, and the experience of working at Ames during the summers of 2001 and 2002 was very pleasant and rewarding. Aloha, Danny Joe.

My class and office mates have become good friends, and have filled an important role in my graduate-school experience. Alok Sutradhar, Zhengyu Zhang, Faraz Hussain, Seong-Hyeok Song, Burak Ozturk, Masha Romadina, Jeong-Ho Kim, Dong Zhaoxu and Mariana Silva are names that evoke enough memories to fill a book.

Sincere thanks are due to my parents, whose constant support has made life for my family much more pleasant. They have consistently shared encouragement rather than criticism during this long academic sojourn. In part, the goal of a Ph.D. has been pursued as a tribute to them.

To my wonderful children: I can now begin to fulfill many promises that have awaited the completion of this study—freedom from this compuerta no. 12. Unfortunately, this work can never repay my prolonged absence from home; Our lost time together has been a painful sacrifice. And to my wife I owe the most, for her longsuffering without complaint, her patience, sound advice and encouragement, her hard work in the home, and her gift to me of our beautiful children. I thank a generous Father in Heaven for such a companion.

Table of Contents

List of Figures:	x
List of Tables:	xix
Chapter 1: Introduction	1
1.1 Overview	1
1.2 Some Useful Fracture-Mechanics Parameters	2
1.3 Research Objectives	8
Chapter 2: Computation of J for Cracks Under Mode-I Thermomechanical Loading	10
2.1 Introduction	10
2.2 Finite element analysis including graded material properties	11
2.2.1 Performance of graded 3-D elements	12
2.3 The domain integral for cracks in FGMs	16
2.3.1 The 3-D domain integral	16
2.3.2 Derivative of strain energy density: $W_{,1}$	21
2.3.3 Assessment of alternative forms of $(W_{,1})_{explicit}$	21
2.3.4 A general expression for $(W_{,1})_{explicit}$	22
2.4 Numerical computations	23
2.5 Numerical implementation in WARP3D	24
2.6 Verification of the general J -formulation for 2-D configurations	24
2.7 Computation of mode-I K_I -values for surface cracks	29
2.7.1 Crack geometries, material variations and loadings	29
2.7.2 Conversion of J to K	31
2.7.3 Stress intensity factors at the intersection of the crack front with the free surface	32
2.7.4 Mesh refinement	33
2.7.4.1 Effects of mesh refinement on K_I -values for FGM specimens	34
2.7.4.2 Verification of K_I -values for homogeneous specimens ..	35
2.7.4.3 Verification of K_I -values for FGM specimens	36
2.7.5 Effect of material gradient terms on J -values	39
2.8 Stress intensity factors for surface cracks in FGM plates	46
2.8.1 Tension loading	46
2.8.2 Bending loading	54
2.8.3 Thermal loading	59
2.9 Summary and Conclusions	61
Chapter 3: Interaction-Integral Procedures for Curved Cracks With Surface Tractions	63
3.1 Introduction	63
3.2 A domain integral for 3-D cracks with surface tractions	65
3.3 An interaction integral procedure for curved 3-D cracks with surface tractions	66

3.3.1	<i>Auxiliary fields</i>	66
3.3.2	<i>Interaction-integral formulation</i>	67
3.3.3	<i>Extraction of stress intensity factors</i>	70
3.4	Numerical procedures	71
3.4.1	<i>Numerical evaluation of volume and surface integrals</i>	71
3.4.2	<i>Computation of r and θ for auxiliary fields</i>	72
3.4.3	<i>Numerical evaluation of the crack-face-traction integral</i>	73
3.5	3-D analyses of plane-strain and plane-stress configurations	75
3.6	Curved cracks modeled with piecewise-linear fronts	77
3.6.1	<i>Penny-shaped crack in an infinite solid under mixed-mode loading</i>	79
3.6.2	<i>An infinite solid with a flat elliptical crack under tension</i>	84
3.6.3	<i>An infinite solid with a flat elliptical crack under shear</i>	88
3.7	Analysis of cracks modeled with curved elements along front	88
3.7.1	<i>An infinite solid with a flat penny-shaped crack under tension</i>	88
3.7.2	<i>An infinite solid with a flat penny-shaped crack under torsion</i>	93
3.8	Summary and conclusions	94
Chapter 4:	Computation of Mixed-Mode Stress Intensity Factors	97
4.1	Introduction	97
4.2	A domain integral for 3-D cracks in FGMs	98
4.3	An interaction integral for 3-D cracks in FGMs	101
4.3.1	<i>A domain integral for two superimposed equilibrium states</i>	101
4.3.2	<i>The interaction integral</i>	102
4.3.3	<i>Auxiliary fields</i>	103
4.3.4	<i>Constant constitutive tensor interaction-integral formulation</i>	104
4.3.5	<i>Non-equilibrium interaction-integral formulation</i>	104
4.3.6	<i>Incompatibility interaction-integral formulation</i>	106
4.3.7	<i>Influence of crack-front curvature on the interaction integral</i>	107
4.3.8	<i>An interaction integral for curved 3-D cracks in FGMs</i>	108
4.3.9	<i>Extraction of stress intensity factors</i>	108
4.3.10	<i>Behavior of volume and area integrals</i>	109
4.4	Numerical aspects	110
4.4.1	<i>Numerical evaluation of volume and surface integrals</i>	111
4.4.2	<i>Computation of material-property derivatives</i>	111
4.4.3	<i>Computation of r and θ for auxiliary fields</i>	112
4.5	Numerical examples	113
4.5.1	<i>Boundary-layer model (homogeneous material)</i>	113
4.5.2	<i>3-D analyses simulating plane-stress and plane-strain conditions</i>	113
4.5.3	<i>Analysis of planar, curved 3-D cracks in FGMs</i>	118
4.5.4	<i>Mode-I and mode-II loading of a penny-shaped crack in a graded interfacial layer</i>	119
4.5.5	<i>Contribution of crack-face-traction integral to mixed-mode stress intensity factors</i>	124

4.5.6	<i>Mode-III loading of a penny-shaped crack in a graded interfacial layer</i>	125
4.5.7	<i>Mode-I loading of a semi-elliptical surface crack in an FGM plate</i>	128
4.5.8	<i>Mixed-mode loading of a semi-elliptical surface crack in an FGM plate</i>	131
4.6	Discussion and conclusions	132
Chapter 5:	Computation of T-Stresses for Mixed-Mode Loading	137
5.1	Introduction	137
5.2	Interaction-integral formulation	138
5.2.1	<i>An interaction integral for FGMs including surface tractions</i>	138
5.3	Computation of T -stresses using interaction integrals	141
5.3.1	<i>Auxiliary fields for computation of $T_{11}(s)$</i>	141
5.3.2	<i>Extraction of $T_{11}(s)$ from interaction integral for in-plane loading</i>	142
5.3.3	<i>Computation of $T_{11}(s)$ along 3-D cracks under mode-I loading</i>	145
5.3.4	<i>Computation of $T_{11}(s)$ for 3-D cracks under mixed-mode loading</i>	146
5.3.5	<i>Computation of $T_{13}(s)$ for cracks under anti-plane shear</i>	147
5.4	Numerical aspects	148
5.4.1	<i>Numerical evaluation of the interaction integral</i>	148
5.4.2	<i>Computation of strain tangent to crack front, $\epsilon_{33}(s)$</i>	148
5.4.3	<i>Computation of stress intensity factors</i>	150
5.5	Numerical simulations of thin specimens	150
5.5.1	<i>Modified boundary-layer model</i>	150
5.5.2	<i>FGM plate with inclined center crack</i>	154
5.6	Numerical simulations of 3-D specimens	158
5.6.1	<i>Penny-shaped crack in an infinite body under uniform remote tension</i>	158
5.6.2	<i>Penny-shaped crack in an infinite body under mixed-mode loading induced by point forces</i>	161
5.6.3	<i>Penny-shaped crack in an infinite body under bending</i>	163
5.6.4	<i>Mode-I loading of a semi-elliptical surface crack in a graded plate</i>	166
5.6.5	<i>Mixed-mode loading of a semi-elliptical surface crack in an FGM plate</i>	169
5.7	Discussion and conclusions	170
Chapter 6:	Summary and Conclusions	174
6.1	Some comments on crack analysis techniques	175
6.2	Limitations of crack analysis with traditional finite elements	177
6.3	Future directions	178
Appendix A:	Asymptotic Crack-Tip Fields	180
Appendix B:	Exact Integration of Crack-Face-Traction Integral	181
Appendix C:	Computation of r and θ for Elements With Straight Edges	184
Appendix D:	Stress Intensity Factor Solutions	186
D.1	Circular crack in an infinite body loaded by point forces	186

D.2 Elliptical crack in an infinite body under shear	186
Appendix E: Constitutive Relations for FGM Interaction-Integral Terms .	188
E.1 Constitutive and compliance tensors	188
E.2 Derivatives of constitutive- and compliance-tensor components	189
References	191
Author's Biography	207

List of Figures

Figure 2.1	(a) Schematic of a semi-infinite strip of width W , with material properties graded exponentially in the x -direction. Poisson's ratio, ν , is constant, and E_i , α_i , and k_i , $i = 1, 2$, are the Young's modulus, coefficient of thermal expansion, and coefficient of heat conduction at $x = 0$ and $x = W$, respectively. The two load cases are: (1) an imposed, uniform axial stress, and (2) an imposed temperature field, with $T(x = 0) = T_1 = 0.05T_0$ and $T(x = W) = T_2 = 0.5T_0$. (b) $40 \times 10 \times 1$ -element mesh of the uncracked strip ($a = 0$) consisting of 20-noded brick elements. (c) Mesh for the cracked strip: $a/W = 0.4$ (d) Crack-front elements with quarter-point midside nodes and collapsed faces. Dimension R_D provides a measure of domain size, and L_e indicates the size of crack-front elements.	13
Figure 2.2	(a) Analytical and finite-element solutions for $\alpha_{yy}(x)$ in an uncracked semi-infinite strip (shown in Fig. 2.1) under axial tension loading, steady-state thermal loading, and combined (thermal plus tension) loading, with $E_2/E_1 = 10$, $\alpha_2/\alpha_1 = 2$, $k_2/k_1 = 10$, $T(x = 0) = T_1 = 0.05T_0$ and $T(x = W) = T_2 = 0.5T_0$. (b) Deformed shape of the graded finite-element strip under tension loading, (c) thermal loading, and (d) combined loading.	15
Figure 2.3	Schematic of $\Gamma(s)$ in Eq. (9). The domain for the analogous 2-D integral is the area A , bounded by the contour $C = C_1 + C^+ - \Gamma(s) + C^-$.	17
Figure 2.4	(after Shih et al. [192]) Virtual crack advance in the local X_1 - X_3 plane at crack-front location s . Crack advance occurs in the X_1 -direction, and is defined as $\delta l(s) = \Delta \alpha l_k(s) \nu_k(s)$.	18
Figure 2.5	Surface and volume domains used to calculate $J(s)$ at crack-front location $s = b$ extend from point a to point c , a length equal to L_C . Surfaces S_t and S_1 (cylindrical surfaces), S_2 and S_3 (flat lateral surfaces), and S^+ , and S^- (top and bottom crack-face surfaces) comprise surface S and enclose volume V of the domain integral. For general loading conditions, S_t must shrink to the crack tip, i.e. $r \rightarrow 0^+$. Vector m is the outward normal to S_t , S_1 , S^+ , and S^- .	19
Figure 2.6	The arbitrary function q_k is interpreted as a virtual crack-front displacement, and varies from unity on surface S_t at location $s = b$, to zero on surfaces S_1 , S_2 and S_3 (see Fig. 2.5).	20
Figure 2.7	(a) Normalized components of Eq. (36) for tension loading of SE(T) specimen in Fig. 2.1(c) for $a/W = 0.4$ and $E_2/E_1 = 10$. (b) Mesh used for thermally-loaded SE(T) specimen: $a/W = 0.5$. (c) Normalized components of Eq. (36) for uniform thermal loading for $T_1 = T_2 = 0.05T_0$, $E_2/E_1 = 5$, and $\alpha_2/\alpha_1 = 2$ ($\sigma_0 = E_1\alpha_1T_0/(1-\nu)$). (d) Scaled view of data in (c).	27

Figure 2.8	(a) Surface-crack specimen showing axial, bending and thermal loads. The hatched area illustrates the potential region for the “boundary layer” (see Section 2.7.3). Symmetry permits analysis using one quarter of the model. (b) Cross-section of plate showing unidirectional material variation from cracked face to uncracked face. Bending stress is calculated from total moment M as $\sigma_b = 3M/bt^2$.	30
Figure 2.9	Plan view of the crack plane shown in Fig. 2.8(a). (a) Measurement in radians of parametric angle, ϕ , for $a/c > 1.0$. (b) Parametric angle, ϕ , for $a/c \leq 1.0$, and intersection angle, ψ , describing the angle between the crack front and free surface. For all models in this study, $\psi = 90^\circ$.	31
Figure 2.10	Crack-front mesh with 7 rings of elements in the radial direction, and 10 elements along the θ -direction. The ratio of L_e to plate thickness t , $L_e/t = 7.66 \times 10^{-4}$, describes the level of mesh refinement. R_D provides a measure of domain size.	35
Figure 2.11	Comparison of normalized stress intensity factors, K_{In} , obtained using Eqs. (36) and (46) for 3-ring and 10-ring crack-front mesh refinements where $a/c = 2$ and $a/t = 0.8$.	36
Figure 2.12	Typical discretization along front for surface-crack configurations.	37
Figure 2.13	Normalized K_I -values, K_{In} , for surface-cracked plates with homogeneous material having $a/c = 1, 2$, and $a/t = 0.2, 0.8$. Comparison of values generated using Eq. (36) with those of (a) Raju and Newman [175] and (b) Newman and Raju [150].	38
Figure 2.14	(a) Comparison of normalized K_I -values from the J -integral, Eq. (36) and DCT, Eq. (46), for tension and bending with $E_2/E_1 = 5$, $a/t = 0.2, 0.5, 0.8$, and $a/c = 1/3$, (b) $a/c = 1$, (c) $a/c = 2$, and (d) thermal loading with $T_1/T_2 = 20$, $a/t = 0.2$ and $a/c = 1/3, 1, 2$ (Material properties correspond to those for a zirconia/Rene-41 FGM: see Table 2.4).	42
Figure 2.15	(a) Comparison of normalized K_I -values from J , Eq. (36) and DCT, Eq. (46), for tension and bending with $E_2/E_1 = 0.2$, $a/t = 0.2, 0.5, 0.8$, and $a/c = 1/3$, (b) $a/c = 1$, and (c) $a/c = 2$.	43
Figure 2.16	Normalized J -values at three crack-front locations computed using Eq. (36) with and without the second integral. (a) Tension loading for $E_2/E_1 = 5$. (b) Tension loading for $E_2/E_1 = 0.2$. (c) Bending load, for $E_2/E_1 = 5$. (d) Thermal loading ($\sigma_0 = E_1\alpha_1 T_0/(1-\nu)$) for $T_1/T_2 = 10$ (see Fig. 2.8). Table 2.4 lists material properties.	44

Figure 2.17 (a) Crack geometry, material variation and loading where $a/t=0.2$, and $a/c=1/3$, and individual terms of \bar{J} , normalized by $J(s)$. (b) Normalized terms of \bar{J} for specimen under tension loading where $E_2/E_1=5$; (c) bending load where $E_2/E_1=5$; and (d) thermal loading where $T_1/T_2=20$, $E_2/E_1=1.45$, and $\alpha_2/\alpha_1=20$ (see Fig. 2.8).	45
Figure 2.18 (a) Normalized K_I -values along a crack front under remote tension loading for a crack with $a/c=1/3$ and $a/t=0.2$. (b) Normalized values of J along the crack front corresponding to the K_{In} -values in (a).	47
Figure 2.19 Normalized K_I -values along a crack front under remote tension loading for a crack with $a/c=1/3$ and (a) $a/t=0.5$, and (b) $a/t=0.8$.	48
Figure 2.20 (a) Normalized K_I -values along a crack front loaded in remote tension, with $a/c=1$, $E_2/E_1=0.2, 5$ and 1 , and $a/t=0.2$, (b) $a/t=0.5$, and (c) $a/t=0.8$.	51
Figure 2.21 (a) Normalized K_I -values along a crack front loaded in remote tension, with $a/c=2$, $E_2/E_1=0.2, 5$ and 1 , and $a/t=0.2$, (b) $a/t=0.5$, and (c) $a/t=0.8$.	52
Figure 2.22 Comparison of trends in J , K_{In} and E along a crack front under tensile loading for the geometry $a/c=2$ and $a/t=0.8$, in material where (a) $E_2/E_1=0.2$ and (b) $E_2/E_1=1$. In FGMs, the location, ϕ , of maximum J along the curved crack front does not necessarily correspond to the location of maximum K_{In} .	53
Figure 2.23 (a) Normalized K_I -values along a crack front loaded in remote bending, with $a/c=1/3$, $E_2/E_1=0.2, 5$ and 1 , and $a/t=0.2$, (b) $a/t=0.5$, and (c) $a/t=0.8$.	56
Figure 2.24 (a) Normalized K_I -values along a crack front loaded in remote bending, with $a/c=1$, $E_2/E_1=0.2, 5$ and 1 , and $a/t=0.2$, (b) $a/t=0.5$, and (c) $a/t=0.8$.	57
Figure 2.25 (a) Normalized K_I -values along a crack front under remote bending, with $a/c=2$, $E_2/E_1=0.2, 5$ and 1 , and $a/t=0.2$, (b) $a/t=0.5$, and (c) $a/t=0.8$.	58
Figure 2.26 Normalized K_I -values for a specimen under thermal loading with $a/t=0.2$, $T_1/T_2=5, 10$ and 20 , and (a) $a/c=1/3$, (b) $a/c=1$, and (c) $a/c=2$. Material properties are listed in Table 2.4.	60

Figure 3.1	(a) Computation of r and θ values to determine auxiliary fields at integration point P for interaction integral evaluation at crack-front location s . In meshes with straight element edges, distance r spans point P and the element edge between nodes A and B , and angle PDC defines θ . Point C is the projection of P onto the X_1 - X_3 plane. (b) Quadrants I-IV in the plane PDC for computation of θ .	72
Figure 3.2	(a) Quarter section of a circular cylindrical mesh with an embedded penny-shaped crack used for some examples in Section 3.7. (b) View of crack front discretized by elements with straight edges, showing difference between crack front defined by the mesh and by an analytical expression.	74
Figure 3.3	(a) Schematic of a SE(T) specimen with crack-face tractions. (b) Symmetric mesh representing the cracked strip where $\alpha/W=0.4$. (c) Detail of mesh in crack-front region showing 10 semi-circular rings and 10 sectors of elements. (d) Elements incident on the crack front each have one collapsed face. Here, L_e describes the size of elements incident on the crack front, and R_D indicates domain size.	76
Figure 3.4	Convergence of standard Gauss quadrature for evaluation of the crack-face traction integral, Eq. (68), for the element incident on the crack front in the SE(T) model.	77
Figure 3.5	(a) Normalized terms of the interaction-integral vs. normalized domain size for the SE(T) specimen loaded by crack-face tractions. (b) Normalized stress intensity factors vs. domain size for the SE(T) specimen obtained using standard and modified quadrature for the surface integral, theoretical results and ABAQUS 6.4-3 [1].	78
Figure 3.6	(after Kassir and Sih [103]) A penny-shaped crack in an infinite homogeneous solid loaded by point forces P and R acting at point $x=0, y=0, z=b$, and directed parallel to the x and z axes, respectively. For the ABAQUS [1] benchmark model, $P=R=400.0E+6$, and $b=0.33$.	79
Figure 3.7	(a) Section view of cylindrical mesh representing an infinite body with an embedded penny-shaped crack (from ABAQUS 6.3 benchmark library [1]). Dimension ratios are $H/a=D/a=80$. (b) View of mesh discretization in crack-front region. Seven cylindrical domains with 24 sectors surround the crack front. For domain 1, $L_e/a=R_D/a=0.00129$. For domain 5, $R_D/a=0.04$.	81
Figure 3.8	(a) Normalized stress intensity factor values along the front of a penny-shaped crack under mixed-mode loading due to point forces P and R . (b) Normalized values of energy release rate determined from the J -integral, interaction-integral values and analytical solutions.	82

Figure 3.9	(a) One eighth of the mesh defined to model a planar, elliptical crack in an infinite solid. Loading includes crack-face pressure and crack-face shear. The full mesh includes 26,504 8-noded brick elements. (b) View of mesh in crack-front region, where 7 rings divided into 20 sectors surround the crack front. Ratios $L/c = 10$, and $a/c = 0.4$.	85
Figure 3.10	Description of parametric angle ϕ , on an elliptical crack front where $a/c \leq 1.0$. Angle ω describes the direction of crack-face shear loading, represented by T .	86
Figure 3.11	(a) Comparison of numerical and analytical mode-I stress intensity factors along a flat elliptical crack loaded by crack-surface pressure in an infinite solid. (b) Comparison of J -integral values with energy release-rate values computed from interaction integral.	87
Figure 3.12	Normalized analytical and numerical stress intensity factor values along the front of a flat elliptical carrying crack-face shear in an infinite solid. Crack-face shear induces loading in modes II and III for (a) shear parallel to the major axis ($\omega = 0$); (b) shear parallel to the minor axis ($\omega = 90$).	89
Figure 3.13	(a) Section view of cylindrical mesh representing an infinite body with a penny-shaped crack. 16,480 20-noded hexagonal elements comprise the mesh. Dimensions are $H/a = D/a = 80$. (b) View of mesh in crack-front region.	90
Figure 4.1	Surfaces enclosing volume domain for computation of $\bar{I}(s)$ at location $s=b$ along a curved crack front. For functionally-graded material, S_t must shrink to the crack front, i.e. $r \rightarrow 0^+$.	100
Figure 4.2	Computation of r and θ for an integration point in a domain of four straight-edged elements. $\bar{I}(s)$ values lead to stress intensity factors at crack-front location s .	112
Figure 4.3	Boundary-layer model used to verify correct calculation of stress intensity factors in a cracked homogeneous solid under plane (modes I-II, plane-stress, plane-strain) and anti-plane (mode-III) deformations. Dimension $t/R = 0.018$. Mesh has 11,054 nodes and 1548 20-noded hexagonal elements arranged in 36 circumferential sectors and 43 rings in the radial direction. 36 collapsed elements with quarter-point nodes surround the crack front.	114
Figure 4.4	(a) Mesh for fixed-grip displacement of a specimen with a crack inclined at 36° (see Table 4.1). Distance between crack fronts $s = 2a$. (b) 20 collapsed crack-front elements of size $L_e/a = 0.0177$ surround each crack front. Ratio R_D/a describes domain size in this work.	115

Figure 4.5	Relative contribution of interaction-integral terms vs. increasing domain size for (a) K_I and (b) K_{II} for an inclined crack in an exponentially-graded M(T) specimen under plane-strain, fixed-grip loading.	117
Figure 4.6	(a) Mesh for infinite body with a penny-shaped crack on the boundary of a graded interfacial layer. (b) View of mesh in crack-front region showing schematic of material variation in interfacial layer for $h/a = 1.0$. Twenty-four sectors of elements of size $L_e/a = 0.00129$ surround the crack front.	120
Figure 4.7	Normalized values of K_I vs. domain size R_D/a , for a penny-shaped crack in an infinite solid under remote tension. The FGM case is for a graded layer illustrated in Figs. 4.6(a)-(b) where $h/a = 1$ and $E_3/E_1 = 1.65$.	122
Figure 4.8	Contributions to $\bar{I}(s)$ from components $\bar{I}_1-\bar{I}_4$ for a penny-shaped crack subjected to surface pressure in a graded interlayer ($h/a = 1$, $E_3/E_1 = 1.65$) for (a) K_I and (b) K_{II} computations.	123
Figure 4.9	Normalized values of K_{III} vs. domain size R_D/a , for a penny-shaped crack in an infinite solid under remote torsion. The FGM case is for a graded layer illustrated in Figs. 4.6(a)-(b) where $h/a = 1$ and $E_3/E_1 = 22$.	127
Figure 4.10	Contribution to $\bar{I}(s)$ from components $\bar{I}_1-\bar{I}_3$ for a penny-shaped crack in a graded interlayer in an infinite solid under torsion, where $h/a = 1$ and $E_3/E_1 = 22$.	127
Figure 4.11	(a) Infinite plate with semi-elliptical surface crack under remote tension. Stress intensity factors decrease to zero in shaded "boundary-layer" region. (b) Parametric angle ϕ indicates location along the crack front.	128
Figure 4.12	(a) Quarter-symmetric mesh of semi-elliptical surface crack in plate under remote tension. (b) Detail of discretization in crack-front region. (c) Normalized K_I -values along crack.	130
Figure 4.13	(a) Mesh of semi-elliptical crack, inclined at $\omega = 45^\circ$, in plate under remote tension. (b) Detail of discretization in crack-front region. (c) Normalized K-values vs. domain size for twenty domains at crack-front location $\phi = 85^\circ$.	132
Figure 4.14	Variation of K_{In} along front of surface crack inclined at 45° in FGM plate under tension.	133

Figure 4.15	Variation of K_{II_n} along front of surface crack inclined at 45° in FGM plate under tension.	133
Figure 4.16	Variation of K_{III_n} along front of surface crack inclined at 45° in FGM plate under tension.	134
Figure 4.17	Components of $\bar{I}(s)$ for K_I computations at $\phi = 85^\circ$ along semi-elliptical crack inclined at 45° in FGM plate under remote tension where $E_2/E_1 = 20$.	134
Figure 4.18	Components of $\bar{I}(s)$ for K_{II} computations at $\phi = 85^\circ$ along semi-elliptical crack inclined at 45° in FGM plate under remote tension where $E_2/E_1 = 20$.	135
Figure 4.19	Components of $\bar{I}(s)$ for K_{III} computations at $\phi = 85^\circ$ along semi-elliptical crack inclined at 45° in FGM plate under remote tension where $E_2/E_1 = 20$.	135
Figure 5.1	Domain of integration used to evaluate $\bar{I}(s)$ at crack-front location $s = b$. Surfaces S_t , S_1 , S_2 , S_3 , S^+ , and S^- enclose a simply-connected volume. Surface S_t shrinks to the crack front, i.e. $r \rightarrow 0^+$, and surfaces S^+ and S^- represent the top and bottom crack faces, respectively.	140
Figure 5.2	Line loads f_1 and f_3 normal and tangent to the crack front, and T -stresses on a differential element at $\theta = \pi$.	141
Figure 5.3	Configuration studied by Cho et al. [37]: semi-infinite crack loaded with crack-face tractions that go to zero at the crack tip.	144
Figure 5.4	Gauss quadrature in parent coordinates ξ , of the Jacobian J , yields the undeformed and deformed lengths of crack-front segment L_C . The ratio of the change in length to the undeformed length, $\Delta L_C/L_C$, provides an approximate value for strain ϵ_{33} tangent to the crack front at location s , i.e. $\epsilon_{33}(s)$.	149
Figure 5.5	(a) Modified boundary-layer model for verification of T -stress computations for homogeneous materials. Dimension $R/t = 10$. Mesh has 4102 nodes and 2000 8-noded hexagonal elements arranged in 50 circular rings divided into 40 sectors around the circumference. Dimension R_D describes domain size in this study. (b) Collapsed elements of size $L_e = 0.000434$ surround the crack front.	152
Figure 5.6	Boundary-layer model with displacements prescribed by Eq. (202) where $K_{III} = 1.0$ and $T_{13} = 0.0$: (a) side view, (b) top view, (c) left view, (d) right view. Modified boundary-layer model with displacements prescribed by Eq. (202) where $K_{III} = 0.0$ and $T_{13} = 1.0$: (e) side view, (f) top view, (g) left view, (h) right view.	153

Figure 5.7	Model for fixed-grip displacement (Δ) of an infinite FGM plate with a through-crack inclined 30° from horizontal. Distance between left and right crack fronts = $2a$. Dimensions $H = W = 20a$, and $t = 0.125a$. The mesh discretization consists of 2057 20-noded brick elements. Twenty collapsed elements of size $L_e/\alpha = 0.0177$ surround each crack front.	155
Figure 5.8	Relative contribution of interaction-integral terms for various domain sizes used to compute values of (a) K_I and (b) T_{11} for an inclined crack in an exponentially graded M(T) specimen under plane-stress, fixed-grip loading. Percentages indicate relative contributions of individual terms at $R_D/\alpha = 1.0$.	156
Figure 5.9	(a) Section view of cylindrical mesh approximating an infinite body with a penny-shaped crack (from ABAQUS [1] benchmark library). Dimension ratios $H/\alpha = D/\alpha = 80$. (b) View of mesh discretization in crack-front region. Seven cylindrical domains with 24 sectors surround the crack front. For domain 1, $L_e/\alpha = R_D/\alpha = 0.00129$. For domain 9, $R_D/\alpha = 0.66$.	159
Figure 5.10	Effect of mesh refinement and domain size on convergence of J , K_I and T_{11} values computed using the domain integral (J) and the interaction integral (K_I , T_{11}) for a penny-shaped crack in an infinite homogeneous solid under remote tension σ_0 . The finite-element mesh comprises either 8-noded or 20-noded hexagonal elements.	160
Figure 5.11	(after Kassir and Sih, [103]) A penny-shaped crack in an infinite homogeneous solid loaded by point forces P and R acting at point $x = 0, y = 0, z = b$, and directed parallel to the x and z axes, respectively. For the ABAQUS [1] benchmark model, $P = R = 400.0E+6$, and $b = 0.33$.	162
Figure 5.12	Effect of increasing domain size on convergence of T_{11} and T_{13} values at the randomly-selected location $\theta = 84^\circ$ for a penny-shaped crack in an infinite homogeneous solid loaded by point forces P and R . The finite-element mesh comprised 8-noded hexagonal elements.	163
Figure 5.13	(a) Normalized analytical stress intensity factor values along the front of a penny-shaped crack in an infinite solid loaded by point forces P and R . (b) Normalized T -stresses along the penny-shaped crack computed using the mesh of 8-noded brick elements obtained from the ABAQUS 6.4-3 benchmark library.	164
Figure 5.14	View of one eighth of mesh generated by FEACrack [73] for analysis of a penny-shaped crack in an infinite solid under bending.	165

Figure 5.15	Path independence of computed T_{11} values for penny-shaped crack in an infinite solid under bending. Plotted values were computed using 5 different domains at $\theta = 45^\circ$.	166
Figure 5.16	(a) Normalized stress intensity factor values along the front of a penny-shaped crack in an infinite solid under bending. (b) Normalized T_{11} values.	167
Figure 5.17	(a) Quarter-symmetric mesh of a semi-elliptical surface crack in a plate under remote tension. (b) Detail of mesh discretization in crack-front region. (c) Normalized T -stress T_{11} computed from \bar{I} with and without FGM terms, and from values of σ_{xx} (stress in local crack-front coordinates) on the crack surface, $\theta = \pi$, extrapolated to $r = 0$.	168
Figure 5.18	(a) Mesh of semi-elliptical crack, inclined at $\omega = 45^\circ$, in plate under remote tension. (b) Detail of discretization in crack-front region. (c) Normalized T_{11} -values along crack generated using interaction integral and local σ_{xx} stresses on crack faces.	170
Figure 5.19	Variation of T_{11n} values along inclined surface crack, computed with and without FGM terms.	171
Figure 5.20	Components of $\bar{I}(s)$ for T_{11} computations at $\phi = 85^\circ$ along a semi-elliptical surface crack under mode-I loading.	171
Figure 5.21	Components of $\bar{I}(s)$ for T_{11} computations at $\phi = 85^\circ$ along an inclined, semi-elliptical surface crack under mixed-mode loading.	172

List of Tables

Table 2.1	Normalized K_I -values for a plane-strain, semi-infinite strip under axial tension (see Fig. 2.1): $E_2/E_1 = 10$, $\nu = 0.3$, $a/W = 0.4$.	25
Table 2.2	Normalized K_I -values for a crack in a plane-strain, semi-infinite strip under thermal loads (see Figs. 2.1(a) and 2.7(b)): $\nu = 0.3$, $a/W = 0.5$.	28
Table 2.3	Specified surface-crack geometries, material properties, and temperature loads.	30
Table 2.4	Properties for thermal loading of surface-crack specimens (Erdogan and Wu, [60]).	31
Table 2.5	Normalized stress intensity factors, K_{In} , along the crack front for specimens loaded in tension.	50
Table 2.6	Normalized stress intensity factors, K_{In} , along the crack front for bending loads. Dashes replace negative stress intensity factors caused by interpenetration of crack faces.	55
Table 2.7	Normalized stress intensity factors, K_{In} , along the crack front for thermal loading. Table 2.4 lists material properties, and Fig. 2.8 shows a schematic of the temperature distribution. Dashes replace stress intensity factors in the boundary layer (see Section 2.7.3).	59
Table 3.1	Integration schemes used in this study to evaluate the crack-face-traction integral in Eq. (68).	75
Table 3.2	Error measures of normalized stress intensity factors and energy release rates (see Figs. 3.8(a)-(b)) with respect to analytical solutions.	83
Table 3.3	Normalized stress intensity factors for a penny-shaped crack in an infinite homogeneous solid under torsion and tension, illustrated in Figs. 3.2 and 3.13. Normalization follows $K_{In} = K_I/(\sigma_0\sqrt{\pi a})$ for tension, and $K_{IIIIn} = K_{III}/(\tau_0\sqrt{\pi a})$, where $\tau_0 = 2T\alpha/(\pi b^4)$.	93
Table 4.1	Normalized stress intensity factors for in-plane displacement loading of a plate with a through crack inclined at 36° (see Fig. 4.4).	118

Table 4.2	Normalized stress intensity factors for a penny-shaped crack at the edge of a graded interface between two semi-infinite solids under tension (see Fig. 4.6).	121
Table 4.3	Normalized stress intensity factors for a penny-shaped crack at the edge of a graded interface between two semi-infinite solids under torsion (see Fig. 4.6).	126
Table 5.1	Imposed and computed stress intensity factor and T -stress values for the crack front in a homogeneous, modified boundary-layer model (Fig. 5.5(a)).	154
Table 5.2	T -stress T_{11} at the left and right crack-fronts of a through crack inclined at 30° in an FGM plate under fixed-grip loading and assumed plane-stress conditions (see Fig. 4.4). Young's modulus varies as $E(x) = E_0 e^{\beta x}$, and Poisson's ratio is constant at $\nu = 0.3$. Normalization follows $T_{11n} = T_{11}/E_0 \epsilon_0$.	157
Table 5.3	T -stresses for the left and right fronts of an inclined crack in an FGM plate under remote tension loading (Fig. 4.4(a)). Normalization follows $T_n = T/\sigma_0$.	157
Table 5.4	Components of Eq. (195) for T_{11} , and of Eq. (186) for T_{33} , computed with the mesh of 8-noded brick elements shown in Fig. 3.7. Values demonstrate the contribution of tangential strain ϵ_{33} for a penny-shaped crack in an infinite solid under remote tension σ_0 .	161

Chapter 1

Introduction

1.1 Overview

A natural or engineered multiphase composite with macro-scale spatial variation of material properties may be referred to as a functionally graded material, or FGM. FGMs can enhance structural performance by optimizing stiffness, improving heat, corrosion or impact resistance, or by reducing susceptibility to fracture. One promising application of FGMs is to thermal barrier coatings, in which a ceramic coating with high heat and corrosion resistance transitions smoothly to a tough metallic substrate. The absence of a discrete interface between the two materials reduces the occurrence of delamination and spallation caused by growth of interface and surface cracks. Fracture remains an important failure mechanism in FGMs, however, and the ability to predict critical flaw sizes is necessary for the engineering application of these materials.

This work describes the development of numerical methods used to compute fracture parameters necessary for the evaluation of crack-like flaws in elastic continua. The current investigation employs post-processing techniques in a finite-element framework to compute the J -integral, mixed-mode stress intensity factors and non-singular T -stresses along generally-curved, planar cracks in three-dimensional (3-D) FGM configurations. Domain and interaction integrals developed over the past thirty years to compute these fracture parameters have proved to be robust and accurate because they employ field quantities remote from the crack. The recent emergence of promising engineering applications of FGMs motivates the extension of these numerical methods to this new class of material.

This work first develops and applies a domain integral method to compute J -integral and stress intensity factor values along crack fronts in FGM configurations under mode-I thermo-mechanical loading. The proposed domain integral formulation accommodates both linear-elastic and deformation-plastic behavior in FGMs. Next discussed is the extension of interaction-integral procedures to compute directly mixed-mode stress intensity factors and T -stresses along planar, curved cracks in FGMs under linear-elastic loading. The investigation addresses effects upon interaction integral procedures imposed by crack-front curvature, applied crack-face tractions and material non-homogeneity. Additional considerations for T -stress evaluation include the influence of mode mixity, crack-face tractions and computation of the anti-plane shear component of non-singular stress, T_{13} .

The present chapter provides a brief background for domain and interaction-integral methods by reviewing the relationship between the energy release rate G , mixed-mode stress intensity factors K_I , K_{II} and K_{III} , the J -integral, and T -stresses. Then follows a brief review of the development of domain-integral techniques, including those developed from the J -integral and interaction integrals, to compute these parameters. The term “domain integral” is used to describe an area or volume integral, as opposed to a line integral. The J -integral and interaction integrals studied in this work were originally developed in line-integral form. Extensions of these methods to 2-D areas, 3-D surfaces and 3-D volumes simplified the implementation of these integrals as post-processing steps to finite-element analyses.

1.2 Some Useful Fracture-Mechanics Parameters

Irwin [89] defined the energy release rate, G , as the decrease of potential energy, Π , in a cracked body caused by an increment of crack growth [6]:

$$G = - \frac{d\Pi}{dA}. \quad (1)$$

Here, dA denotes the new area of crack surface exposed by the increment of crack propagation. Theoretically, a crack propagates when G reaches a critical level, called the critical energy release rate, G_C , which is a material property. Actually, G_C depends upon the crack-growth-resistance curve, or R -curve, which may depend upon the configuration of the cracked body, the rate of applied loading, material temperature etc. [6]. A flat R -curve allows G_C to be defined uniquely, whereas a rising or falling R -curve requires special considerations to be made in estimating G_C . Energy release rates can be computed analytically for simple geometries and loading conditions, but numerical procedures such as the finite-element method enable the evaluation of G for complex bodies loaded arbitrarily, as will be discussed shortly.

Another important fracture parameter is the stress intensity factor, K , which describes the amplitude of stresses in cracked bodies some region near the tip of a crack in which material behavior is linear elastic. In the immediate vicinity of a crack exists a process zone, where new crack surfaces initially appear. In this region, voids grow and coalesce in ductile materials, crazing and crack bridging may occur in polymers and heterogeneous materials, and crack branching and micro-cracking often occur in brittle solids [6]. Analyses of the process zone typically require special treatment of discontinuities in which the material behavior deviates from that of a solid continuum. Beyond the process zone lies a region in which material behavior acts as a nonlinearly-deforming continuum, and beyond this area lies a region referred to as the zone of K -dominance, where material deformation is linear-elastic and throughout which the stress in-

tensity factor, K , defines the amplitude of stresses and displacements. The K -dominant zone must be fully contained within the cracked configuration, and must be small enough so that stresses are dominated by the crack-tip fields and not by remote loading or edge effects.

There are three orthogonal crack-opening displacement modes, including opening, sliding and anti-plane shear. When a K -dominant region exists, one stress intensity factor describes each opening mode, namely K_I , K_{II} and K_{III} , respectively. The stresses in the K -dominant zone are defined as [221]

$$\lim_{r \rightarrow 0} \begin{bmatrix} \sigma_{11}(r, \theta) & \sigma_{12}(r, \theta) & \sigma_{13}(r, \theta) \\ \sigma_{21}(r, \theta) & \sigma_{22}(r, \theta) & \sigma_{23}(r, \theta) \\ \sigma_{31}(r, \theta) & \sigma_{32}(r, \theta) & \sigma_{33}(r, \theta) \end{bmatrix} = \frac{K}{\sqrt{2\pi r}} \begin{bmatrix} f_{11}(\theta) & f_{12}(\theta) & f_{13}(\theta) \\ f_{21}(\theta) & f_{22}(\theta) & f_{23}(\theta) \\ f_{31}(\theta) & f_{32}(\theta) & f_{33}(\theta) \end{bmatrix} + \begin{bmatrix} T_{11} & 0 & T_{13} \\ 0 & 0 & 0 \\ T_{31} & 0 & T_{33} \end{bmatrix} + O(r^{1/2}) + O(r^{3/2}) + \dots, \quad (2)$$

where the stresses are a function of distance r from the crack tip and angle θ from the plane of the crack, and where the functions f_{ij} represent angular variations with respect to the crack plane. The matrix components in Eq. (2) are symmetric. Notice that this expression is in the form of a series, with the lowest order of r being $-1/2$. Williams [221] derived this stress variation, and proved that Eq. (2) is valid within the K -dominant region of any cracked body regardless of the configuration of the specimen or the type of loading. The inverse square-root singularity in r causes the first terms on the right-hand side of Eq. (2) to dominate the other terms in the vicinity of the crack. The constant ($O(r^0)$) T -stress terms, so called by Rice [182], act tangent to the crack plane, and play a significant role in elastic-plastic fracture mechanics as will be discussed later. The higher-order terms in r ($O(r^{1/2})$, $O(r^{3/2})$, $O(r^{5/2})$...) dominate the stresses far from the crack, and include the influence of remote loading or edge effects. The form of these terms may be obtained analytically, and the coefficients may be computed by fitting the expressions with data from experiments [221, 164].

Equation (2) illustrates why the stress intensity factor, K , rather than near-tip stresses, is useful as a fracture parameter. Cracks propagate when stresses cause the material in the process zone to separate. The process zone, however, is the most complicated region to analyze. If crack growth can somehow be linked with the stresses in the K -dominant region, then analyses involving linear-elastic conditions or small-scale yielding will be sufficient. In theory, however, stresses within the K -dominant region approach infinity near the crack tip, and it is unclear at what distance from the crack tip stresses correspond to crack growth. Fortunately, the stress intensity factor K , is constant throughout this region, being dependent only upon the loading, crack configu-

ration, and in some cases, the material properties, such as in an FGM. Therefore, for specimens in which a stress intensity factor can be computed, K defines the amplitude of crack-tip fields that are induced by a particular applied loading. If K can be determined for a laboratory specimen under a particular loading, the value of K when the crack begins to grow is called the critical stress intensity factor K_C , and is a material parameter referred to as the fracture toughness. If K is below K_C , then theoretically, the crack cannot grow, and K may be used to predict the onset of crack propagation. When a crack does propagate, a dynamic stress intensity factor K_D , defines the amplitude of the dynamic stresses within the K -dominant region that translates with the crack. The K_C value obtained from a laboratory specimen, because it is a material property, may be compared with K -values computed for cracks in configurations composed of the same material that have different geometries and different loads. Thus it becomes very useful to be able to determine stress intensity factors for arbitrary configurations under arbitrary loading conditions.

Irwin [90] established a relationship between the energy release rate, G , and the stress intensity factor, K . For mixed-mode loading, this relationship is [6]

$$G = \frac{K_I^2 + K_{II}^2}{E^*} + \frac{K_{III}^2}{2\mu}, \quad (3)$$

where $E^* = E$ for plane stress conditions, $E^* = E/(1 - \nu^2)$ for plane-strain conditions, and $\mu = 2E/(1 - \nu)$. Rice [182] proved that Eq. (3) is not influenced by the non-singular T -stresses shown in Eq. (2). Equation (3) therefore enables analytical or numerical solutions for G to lead to stress intensity factor solutions. Thus, through energy-based approaches (direct computation of G) and stress-based approaches (direct computation of stress intensity factors) analytical, semi-analytical, experimental and numerical techniques have been derived and developed to compute stress intensity factors in a wide variety of cracked bodies. Analytical solutions are typically available for relatively simple crack configurations or idealized geometries, such as flat circular, elliptical or rectangular cracks, e.g. [156]. The analytical solutions are extremely useful, however, because irregular cracks can often be analyzed by assuming an idealized shape and bounding parameters for the actual crack between solutions for an ideal crack. Analytical solutions also serve an important role by enabling verification of numerical methods used to estimate stress intensity factors. Once numerical methods have been established, they may be used to compute stress intensity factors along cracks in complex geometries under arbitrary loading. Experimental procedures provide the validation of analytical and numerical techniques, and drive the development of theoretical methods to account for observed phenomena. Due to the widespread problem of cracks in engineered structures, one of the primary focuses of fracture mechanics is to estimate stress

intensity factors and their relationship to the material fracture toughness and crack growth in order to evaluate structural reliability.

An important development in computational fracture mechanics came when Rice [181] introduced the J -integral, which may be written as

$$J = \lim_{\Gamma \rightarrow 0} \int_{\Gamma} (W\delta_{1i} - \sigma_{ij}u_{j,1})n_i dC, \quad (4)$$

where W is strain energy density, σ_{ij} denotes stress, u_j represents displacement, and $(\cdot)_{,1} = \partial(\cdot)/\partial X_1$, where X_i defines 2-D Cartesian coordinates. The curve Γ in the X_1 - X_2 plane extends from the bottom crack face to the top crack face of a planar crack, enclosing the crack tip. For homogeneous material under nonlinear-elastic, quasi-static, mechanical loading in the absence of body forces and crack-face tractions, the limit in Eq. (4) is not necessary, and J in this case is path independent. The J -integral in Eq. (4), is infrequently referred to as the Eshelby or Cherepanov integral, because it is the X_1 -component of the energy-momentum tensor developed by Eshelby [63, 64], and is analogous to an integral derived previously by Cherepanov [36]. Rice [181] proved that J is path-independent and equivalent to G . (Jin and Sun [100] discuss a commonly-employed, mathematically inconsistent approach to equate J and G , and then provide a mathematically rigorous derivation as an alternative to Rice's [181] method.) The J -integral, therefore, became a powerful tool to compute the energy release rate for a nonlinear-elastic solid, but also offered a new approach for computing stress intensity factors, through the relationship in Eq. (3). For computation of J , the contour of integration, Γ , may lie outside of the K -dominant region, which may make its evaluation simpler ([181]) and more accurate by avoiding the potentially inaccurate singular-field solutions in the vicinity of the crack.

It is straightforward to compute G for an arbitrary cracked configuration using two finite-element analyses. After computing the potential energy of the cracked solid, a second mesh of the cracked body can be generated with the only difference being that the crack is made slightly longer. The difference between the computed potential energy of the cracked bodies divided by the difference in crack surface area between the two meshes leads to G . This procedure is simple, but inconvenient, because it requires the generation of two finite-element meshes and the solution of two boundary-value problems. Alternatively, the J -integral can be computed along an arbitrary path of the cracked body, and requires only post-processing of numerical results. This procedure is simpler and more efficient than solving two boundary-value problems, but it applies only to 2-D structures. The 3-D analog of the J -integral [27] is a surface integral which can provide only a global measure of the energy release rate for a crack, not the local variation of stress intensity factors along the crack front.

The difficulties associated with both the computation of G and the evaluation of the J -integral for cracks in 3-D bodies motivated Parks [165, 166], and Hellen [82] to develop procedures, based on a finite-element framework, to compute G using the solution to a single boundary-value problem. Parks [165] takes the derivative of the finite-element stiffness matrix with respect to a change in crack length, and obtains an expression for G that requires minor post-processing computations involving only a ring of elements surrounding the crack front. This method and subsequent related procedures are commonly referred to as “virtual crack extension” techniques. He develops and employs the method for 2-D and 3-D cracks, and is able to compute the local stress intensity factor along a curved 3-D crack. For a specific 2-D case, he demonstrates that his method and the numerical evaluation of the J -integral yield identical values of G . He indicates that the new method is “an area-analogue of the J line integral [165].” The work by Parks [165] appears to be the first step in the evolution of domain-integral techniques, and he later extends the method to incorporate the effects of nonlinear material behavior [166]. The approach developed by Hellen [82] is very similar to that of Parks, and employs a finite-element framework.

DeLorenzi [46] used a continuum-mechanics approach to derive a 3-D volume integral for G that, for special cases, is equivalent to the J -integral evaluated on a 3-D surface. DeLorenzi and Shih demonstrate their technique in the investigation of side-grooved specimens under elastic-plastic loading [47]. The use of this virtual crack extension method to evaluate a 3-D volume integral equivalent to J and G , gradually developed during the next several years with Shih and fellow researchers [133, 147, 192, 140, 141]. The nomenclature “domain integral” refers to the use of area or volume integrals, rather than line or surface integrals, to compute J . These methods are powerful because of the domain independent character of computations, and because they employ system energy distributed throughout the body to compute G , rather than employing computed stresses and displacements at specific locations to correlate with stress intensity factors. With the establishment of domain integrals to compute the energy release rate and stress intensity factors, the procedures became widely used in finite element codes as post-processing routines [1, 51], and were developed for problems including thermal loads, plasticity and dynamic effects [192, 147]. From the above discussion, it is clear that researchers at Brown University, including Rice, Parks, Shih, Nakamura, Freund and Moran have played the leading role in extending the J -integral to the robust domain-integral widely used today.

The relationship expressed in Eq. (3) makes it apparent that a domain-integral technique that leads to a value of J (and thus G), is insufficient to decompose the independent contributions of the three stress intensity factors under mixed-mode loading. The domain integral is a powerful method to compute the local energy release rate along a 3-D crack front in a specimen under thermo-mechanical loading, and including the ef-

fects of body forces, crack-face tractions, plastic strains (nonlinear-elastic or deformation plastic material response) and inertia under single-mode loading. The importance of mixed-mode loading on phenomena such as crack branching encouraged researchers to devise methods to decompose the J -integral into orthogonal components that would enable computation of the three stress intensity factors [152, 151, 194, 86]. The decomposition of the J -integral into orthogonal components is a powerful technique to extract mixed-mode stress intensity factors, but another technique was under development concomitantly, and proves to be much simpler for computation of the mixed-mode stress intensity factors.

Stern et al. [203], Chen and Shield [34], and Yau et al. [226] introduce the theory and usage of “interaction integrals,” which are path-independent integrals obtained by superimposing two distinct equilibrium states. Stern et al. [203] derive their integral using Betti’s reciprocal work theorem, whereas Chen and Shield [34] (of the University of Illinois) employ the J -integral. Both approaches enable the direct computation of mixed-mode stress intensity factors. Yau et al. [226] employ the interaction integral based on the J -integral, to numerically integrate line forms of the interaction integral in 2-D bodies. Wang et al. [216] then extend the procedure to anisotropic solids. When the domain integral had finally been developed into its modern form (e.g. Shih et al. [192]), and others such as Nikishkov and Atluri [151] were able to decompose it into orthogonal components in order to extract mixed-mode stress intensity factors, other researchers, such as Nakamura and Parks [145, 143] (again, the link to Brown University), began to employ a domain-integral (volume) form of the interaction integral to accomplish the same task. The widespread use of domain-based interaction-integral procedures, ever since their appearance, indicates their preferability to decomposed forms of the J -integral to compute mixed-mode stress intensity factors. Abaqus [1], for example, includes domain-integral (J -integral) and interaction-integral capabilities, but has not incorporated decomposed J -integral techniques.

In 1985, Cardew et al. [29], and later Kfoury [105], employed a theorem attributed to Eshelby, to devise an interaction-integral procedure based on a J -type integral for the computation of T -stress T_{11} in 2-D cracked bodies. Sladek and Sladek [197] developed an interaction-integral method to compute T -stresses, that is based on Betti-Rayleigh reciprocal theorem, just as Stern et al. [203] had used the theorem to derive an interaction integral for stress intensity factors. Chen et al. [33] prove that the interaction integrals of Cardew et al. [29] and Sladek and Sladek [197] are equivalent. Nakamura and Parks [146] again extend the interaction-integral method to a domain integral form suitable for computing T_{11} along a curved, planar 3-D crack. For 2-D bodies, the out-of-plane T -stress T_{33} equals zero for plane stress conditions, and equals νT_{11} for plane strain conditions. Nakamura and Parks define T_{33} to also depend upon the strain tangent to the crack front, ϵ_{33} . The third constant T -stress component T_{13} occurs in conjunc-

tion with mode-III, anti-plane shear loading. Moon and Earmme [139] develop an interaction-integral procedure based on the J -integral to compute T_{13} in bi-materials. Kim et al. [107] further extend this interaction integral for anisotropic bimaterials. These works treat only the theoretical aspects of the anti-plane interaction integral and T_{13} computations. Although some works employ T_{13} for theoretical and analytical investigations, no works have investigated methods to compute T_{13} .

Much work has been performed to extend domain-integral and interaction-integral techniques for the analysis of cracks in 2-D FGMs. The current work is an investigation of domain integrals and interaction integrals for the computation of energy release rates, mixed-mode stress intensity factors, and T -stresses along planar, generally curved cracks in 3-D FGMs. The following section describes specific contributions of this work.

1.3 Research Objectives

This thesis explores the application of domain-integral techniques to cracks in 3-D FGM configurations. The procedures examined herein include J -integral methods for computation of the energy release rate, interaction (I) integrals for computation of stress intensity factors, and I -integrals for computation of T -stresses. Contributions of this study to each of these areas include the following:

- Development of a simplified domain integral to compute the J -integral in 3-D FGM configurations under thermo-mechanical loading. Justification for using numerically-computed derivatives of field quantities, rather than explicit expressions, to simplify implementation and encompass arbitrary material gradients and nonlinear-elastic behavior. Provides sets of stress intensity factors computed along semi-elliptical surface cracks of varying geometry.
- Investigation of interaction-integral procedures for curved, planar cracks in homogeneous materials under mechanical loading. Suggests distinct approaches for computation of special quantities, depending upon the type of mesh discretization used to define the crack. Examines the effect of crack-front curvature on accuracy of computed stress intensity factor values, and justifies the use of simplified procedures that omit terms to incorporate curvature effects. Develops a simple numerical integration scheme to improve the accuracy of computed stress intensity factors for cracks that carry surface tractions.
- Examines the accuracy of an interaction integral procedure to compute stress intensity factors along curved, planar cracks in 3-D specimens under

mechanical loading. Proposes treatment of plane-strain computations using 3-D models. Examines the accuracy of computations that omit terms which incorporate curvature effects.

- Examines the validity of an interaction integral for computation of T -stresses in 3-D solids under mixed-mode loading. Explores an interaction integral procedure for computing T -stresses along curved, planar cracks in 3-D FGM specimens under mixed-mode, remote mechanical loads. Demonstrates the accuracy of a simple procedure to compute tangential strain of crack-front segments.
- Implementation and verification of the above domain-integral procedures in a robust, public-domain finite-element code with user manual.

Chapters 2-5 of the present work address specifically the above developments, and each of these chapters is a self-contained, stand-alone study. Chapter 6 discusses the findings of the previous chapters, and discusses limitations and future directions of techniques employed herein. Several appendices include expressions employed in the work that are available in the literature, in addition to details of numerical procedures discussed in the body of text.

Chapter 2

Computation of J for Cracks Under Mode-I Thermomechanical Loading

2.1 Introduction

In structures composed of functionally graded materials (FGMs), the spatial variation of thermal and mechanical properties influences strongly the response to loading (see Miyamoto et al. [138] for a general discussion). The presence of a functionally-graded interface between two dissimilar materials, for example, can lead to a relaxation in stresses associated with discontinuities at bi-material interfaces [81, 127, 180, 155, 157]. Because fracture remains a key failure mode of FGMs, successful application of these materials depends upon an understanding of their fracture mechanics.

Eischen [59] and Jin and Noda [97] demonstrated the correspondence between near-tip fields in homogeneous and nonhomogeneous bodies, which permits the application of standard analysis techniques to cracks in FGMs. Delamination and cracking of FGMs at coating/substrate interfaces due to thermal loads are the focus of investigations by Lee and Erdogan [127], Bao and Cai [14], Lee and Erdogan [128], Quian et al. [173], and Gaudette et al. [73]. Takahashi et al. [209] and Fujimoto and Noda [70, 71] examine the influence of material gradation and thermal shock on crack propagation. Ravichandran [180], Jin and Batra [94], Cai and Bao [28], and Jin and Batra [95], discuss residual stresses, crack bridging, residual strength, fracture toughness and R -curve behavior. The edge crack in a graded semi-infinite strip under thermal and mechanical loads is a case studied by Erdogan and Wu [60], Erdogan and Wu [61], Gu and Asaro [76], Noda [154], and Noda and Jin [153].

Analytical and numerical studies of fracture in FGMs reported in the literature focus primarily on plane stress, plane strain and axisymmetric configurations [45, 59, 124, 44, 131, 189]. As understanding of the micromechanical behavior of crack growth in FGMs progresses, computational techniques enable the analysis of realistic configurations in three-dimensions for which analytical solutions do not exist. This work discusses a formulation of the J -integral (e.g. [181]) for three-dimensional (3-D) models of FGMs with numerical implementation using a domain integral approach. Applications focus on semi-elliptical surface cracks that have received much attention for homogeneous materials, and that represent a common failure mechanism in brittle materials and FGMs [13, 104, 209, 123].

Techniques to obtain stress intensity factors in components made of homogeneous and nonhomogeneous materials include the displacement correlation technique (DCT) ([191, 109]), the modified crack closure integral [187, 110], the interaction integral [226] and stress correlation [175]. For nonlinear behavior, the domain-integral technique [133] based on the J -integral [181] remains (strictly) valid for deformation plasticity and approximately valid for incremental plasticity. The current study considers only linear-elastic behavior.

The next section examines the finite element analysis of uncracked bodies with smoothly-graded material properties under thermomechanical loads, and verifies the numerical techniques by comparison with published analytical solutions. A general, and numerically convenient, formulation of the domain integral for nonhomogeneous materials and quasi-static thermomechanical loads is then developed, followed by a description of the numerical evaluation in a finite-element setting. The literature provides examples to verify this technique for two-dimensional (2-D) geometries, and the DCT verifies new stress intensity factors derived here using the J -integral approach for 3-D configurations. The study includes an initial parametric study and discussion of K_I -values calculated for a number of semi-elliptical, surface-crack geometries in functionally-graded plates under mode-I tension, bending and thermal loads. Some final remarks and observations conclude the study.

2.2 Finite element analysis including graded material properties

With the finite element method, material properties can vary between elements or between integration points. The term *homogeneous element* here describes an element with all integration points assigned a common property value; the term *graded element* here describes an element with integration points that may have different property values. Many researchers, including Williamson and Rabin [222], Lee and Erdogan [127], Anlas et al. [7], Li et al. [132], Santare and Lambros [188], Bruck and Gershon [26], and Kim and Paulino [111] apply homogeneous and graded elements to model uncracked FGMs. For a given level of mesh refinement, solutions generated with graded elements generally approximate the true solution more accurately than solutions generated using homogeneous elements [111]. In addition to the zero-energy modes and shear-locking mechanisms associated with homogeneous elements [24, 120, 41], property variation between integration points may introduce additional sources of poor element behavior. For example, with full (four-point) integration, spurious shear strains develop in a four-noded (bilinear) quadrilateral element under a pure tension loading which acts perpendicular to a gradation in elastic modulus. This study employs tri-quadratic (20-noded brick) elements with graded material properties and reduced ($2 \times 2 \times 2$) Gaussian integration—a combination shown here to yield good accuracy.

Within graded elements, the calculation of stiffness, stress and other quantities requires the value of properties at integration points. One technique to assign a spatially-varying property at integration points employs temperature-dependent material properties. For example, we may define Young's modulus, $E(\mathbf{x})$, $\mathbf{x} = (x_1, x_2, x_3)$, as a function of temperature, and then define temperature as a function of spatial position such that the expression $\partial E(\mathbf{x})/\partial T(\mathbf{x}) \times \partial T(\mathbf{x})/\partial x_i$ yields the desired value for $\partial E(\mathbf{x})/\partial x_i$. The assignment of a zero thermal expansion coefficient then eliminates unwanted thermal strains. Rousseau and Tippur [186] adopt this approach which is useful to verify other implementations including those described below. This method permits only one form of spatial variation, $\partial T(\mathbf{x})/\partial x_i$, and is not suitable for thermomechanical analyses where temperatures and material properties vary distinctly. The current study employs a more general procedure.

To support multiple material gradients and simultaneous thermal and mechanical loads, element-level routines can retrieve analyst-defined values of material properties at integration points or model nodes. An explicit function that defines the spatial material variation, [7], or a routine that calculates properties according to a micromechanical model [149] are two commonly-used methods to produce the required property values. With analyst-specified nodal values for the properties, interpolation using element shape functions determines property values at integration points. This method incorporates an additional approximation into the boundary-value problem by linking the accuracy of material properties computed at integration points, to the integration order employed within elements. This approach has been shown to provide good accuracy, however [132, 111], and the current study employs the nodal-values approach.

2.2.1 Performance of graded 3-D elements

This section examines the accuracy of finite-element procedures for the analysis of uncracked bodies with graded elastic moduli and graded coefficients of thermal expansion (CTE). Simple boundary-value problems for 2-D (plane-strain) graded solids that have analytical solutions available in the literature provide benchmarks to assess the performance of the finite element analyses. To simulate plane-strain conditions, the finite-element models described in this section have one layer of 20-noded bricks in the thickness direction, and have out-of-plane displacements constrained to zero. Erdogan and Wu [61] derive semi-analytical solutions for stresses in an uncracked, semi-infinite graded strip (Fig. 2.1) subjected to fixed-grip displacement, tension and bending loads. The strip has an exponential variation of Young's modulus in the form $E(x) = E_1 e^{\beta x}$. The constant of material nonhomogeneity, β , follows the relation

$$\beta = \frac{1}{W} \ln \left(\frac{E_2}{E_1} \right), \quad (1)$$

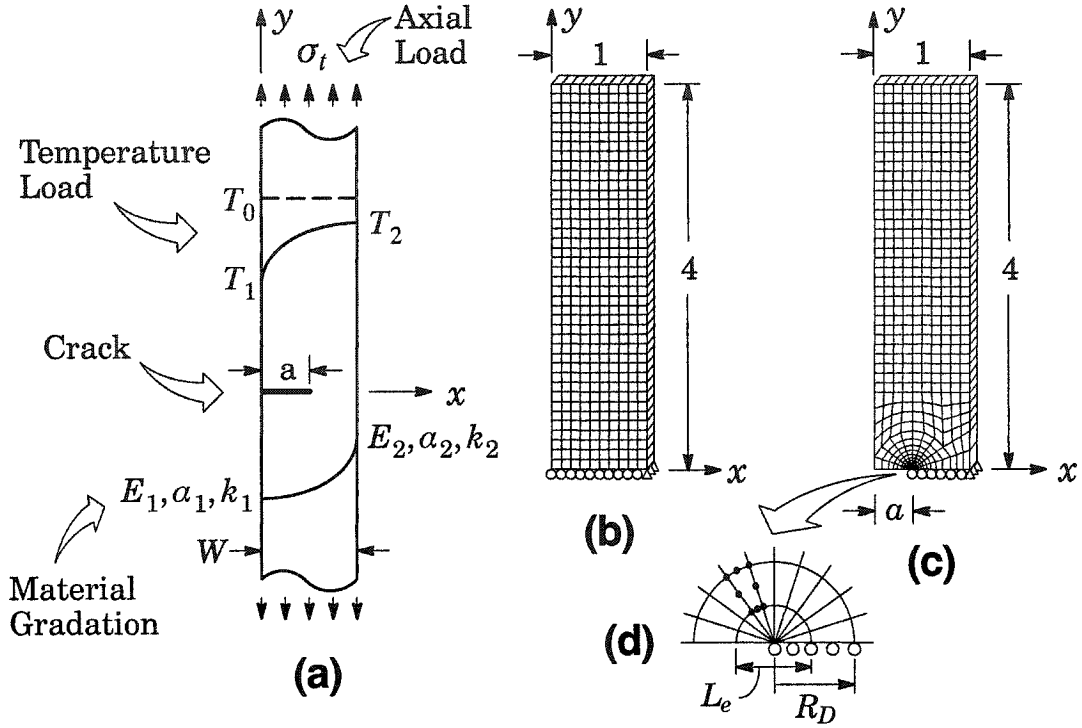


Fig. 2.1. (a) Schematic of a semi-infinite strip of width W , with material properties graded exponentially in the x -direction. Poisson's ratio, ν , is constant, and E_i , α_i , and k_i , $i = 1, 2$, are the Young's modulus, coefficient of thermal expansion, and coefficient of heat conduction at $x = 0$ and $x = W$, respectively. The two load cases are: (1) an imposed, uniform axial stress, and (2) an imposed temperature field, with $T(x = 0) = T_1 = 0.05T_0$ and $T(x = W) = T_2 = 0.5T_0$. (b) $40 \times 10 \times 1$ -element mesh of the uncracked strip ($a = 0$) consisting of 20-noded brick elements. (c) Mesh for the cracked strip: $a/W = 0.4$ (d) Crack-front elements with quarter-point midside nodes and collapsed faces. Dimension R_D provides a measure of domain size, and L_e indicates the size of crack-front elements.

where W denotes the specimen width and E_2/E_1 is the ratio of Young's modulus at $x = W$ and $x = 0$. Notice that $1/\beta$ represents the length scale of material nonhomogeneity. Poisson's ratio, ν , remains constant throughout the specimen. In the semi-infinite strip, the plane-strain stress σ_{yy} due to a remotely applied axial force, N , is [61]

$$\sigma_{yy}(x) = E_0 e^{\beta x} (Ax + B), \quad (2)$$

where values of A and B follow by enforcing the boundary conditions for axial force N and moment M :

$$\int_0^W \sigma_{yy}(x) dx = N \quad \text{and} \quad \int_0^W \sigma_{yy}(x) x dx = M = \frac{NW}{2}. \quad (3)$$

Figure 2.2(a) shows $\sigma_{yy}(x)$ on each $y = \text{constant}$ section of the strip given by Eq. (2). This curve corresponds to the ratio $E_2/E_1 = 10$, with normalization by the applied stress, σ_t .

The symbols indicate finite-element stresses at integration points along a constant y -value. They agree very well with the semi-analytical solution. Figure 2.2(b) shows the computed deformation of the finite-element model under tension loading.

Erdogan and Wu [60] also determine the stress distribution in a functionally-graded, semi-infinite strip subjected to thermal loading. They adopt an exponentially-varying Young's modulus and constant Poisson's ratio. For the thermal properties, they also adopt exponentially-varying coefficients of thermal expansion, $\alpha(x) = \alpha_1 e^{\omega x}$, and heat conduction, $k(x) = k_1 e^{\eta x}$, where α_1 and k_1 denote the values of the coefficients at $x=0$. Here, ω and η set the material nonhomogeneity according to

$$\omega = \frac{1}{W} \ln\left(\frac{\alpha_2}{\alpha_1}\right) \quad \text{and} \quad \eta = \frac{1}{W} \ln\left(\frac{k_2}{k_1}\right). \quad (4)$$

Accordingly, $1/\omega$ and $1/\eta$ represent the length scales of material nonhomogeneity associated with thermal expansion and conductivity, respectively. The temperature distribution follows by solution of the one-dimensional (1-D), steady-state diffusion equation with spatially-dependent conductivity, i.e.

$$\frac{\partial}{\partial x} \left(k(x) \frac{\partial T}{\partial x} \right) = 0, \quad (5)$$

which yields

$$T(x) = Ce^{-\eta x} + D, \quad (6)$$

where C and D denote constants of integration found by assigning values for k_2/k_1 , $T(x=0)$ and $T(x=W)$. With the known temperature distribution, Erdogan and Wu [60] show that the plane-strain stress $\sigma_{yy}(x)$ has the form

$$\sigma_{yy}(x) = \frac{E(x)}{(1-\nu^2)} \left[Ax + B - (1+\nu)\alpha(x)(T(x) - T_0) \right]. \quad (7)$$

Values for A and B follow upon application of the boundary conditions requiring, respectively, zero net axial force and zero net moment:

$$\int_0^W \sigma_{yy}(x) dx = 0 \quad \text{and} \quad \int_0^W \sigma_{yy}(x)x dx = 0. \quad (8)$$

Figure 2.2(a) shows the semi-analytical and finite-element stresses for this simple thermal loading in a model with the following material properties: $E_2/E_1 = 10$, $\alpha_2/\alpha_1 = 2$, $k_2/k_1 = 10$, $T(x=0) = T_1 = 0.05T_0$, and $T(x=W) = T_2 = 0.5T_0$ (see Fig. 2.1). The quantity $\sigma_0 = E_1\alpha_1 T_0/(1-\nu)$ defines the conventional normalizing stress for thermal loading in plane strain. Figure 2.2(c) shows the computed deformation of the finite-element model for the above boundary conditions and material properties.

The semi-analytical solution for the combined tension and thermal loadings superposes the normalized results from Eqs. (2) and (7). The corresponding finite element

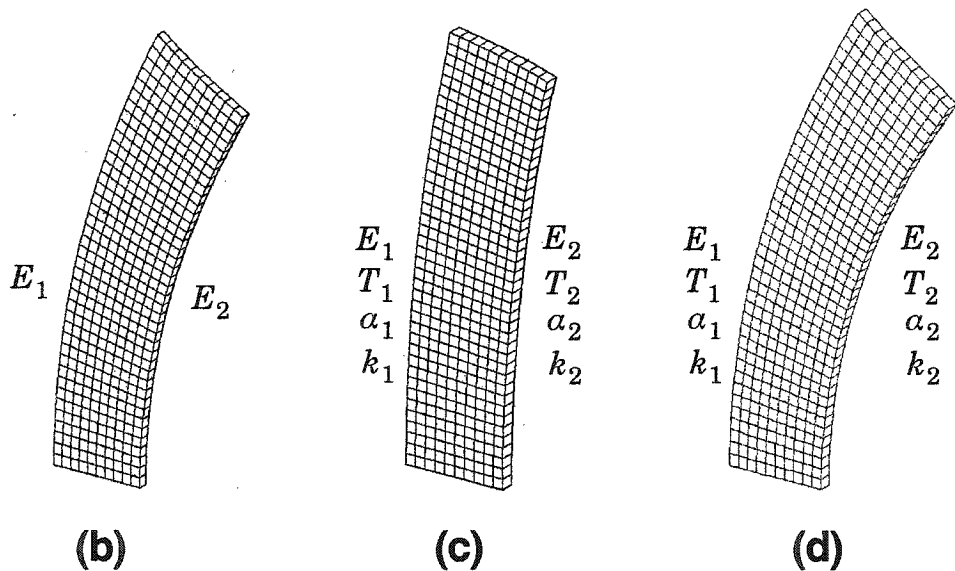
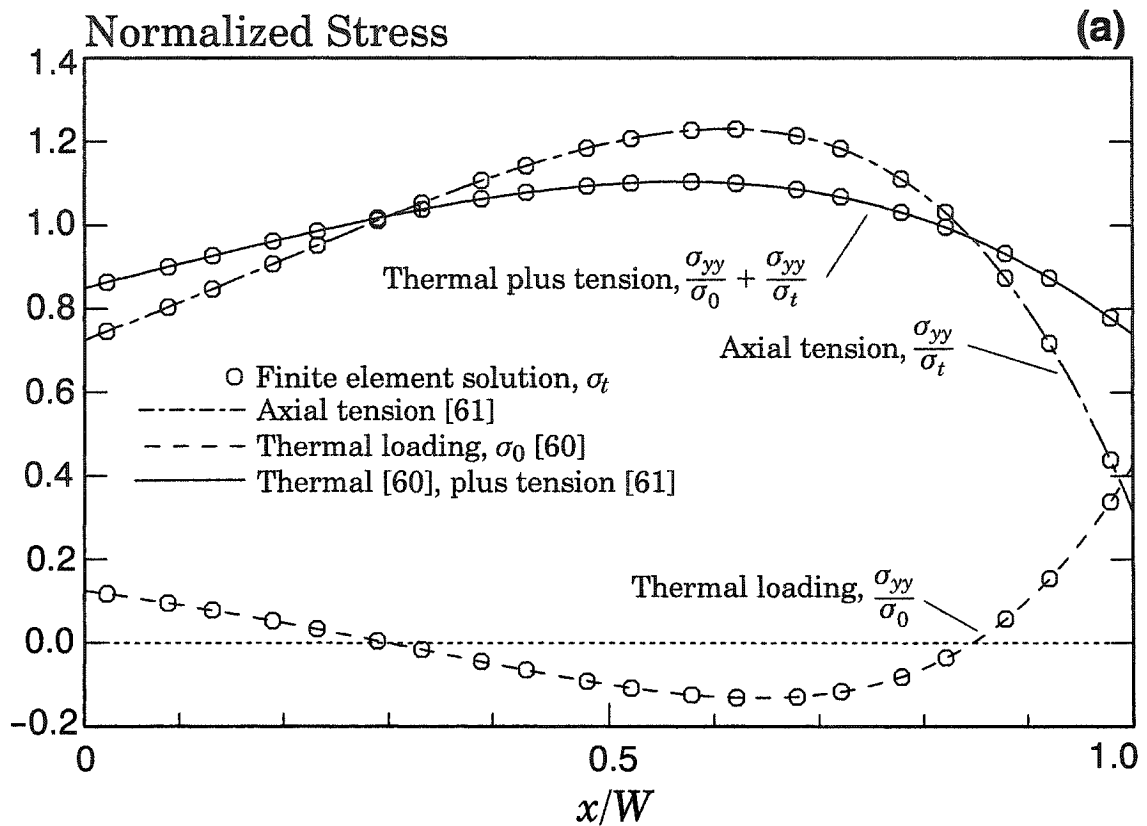


Fig. 2.2. (a) Analytical and finite-element solutions for $\sigma_{yy}(x)$ in an uncracked semi-infinite strip (shown in Fig. 2.1) under axial tension loading, steady-state thermal loading, and combined (thermal plus tension) loading, with $E_2/E_1 = 10$, $\alpha_2/\alpha_1 = 2$, $k_2/k_1 = 10$, $T(x=0) = T_1 = 0.05T_0$ and $T(x=W) = T_2 = 0.5T_0$. **(b)** Deformed shape of the graded finite-element strip under tension loading, **(c)** thermal loading, and **(d)** combined loading.

solution represents one analysis including combined thermal and tension loading (see Fig. 2(a)). Figure 2.2(d) shows the deformed shape of the finite-element model under the combined loading. This 2-D example provides a partial verification of the 3-D numerical procedures used in this study to model FGMs.

2.3 The domain integral for cracks in FGMs

Three-dimensional domain integral methods rely upon volume integrals to compute J -values pointwise along crack fronts. Early works on the domain integral method [133, 192, 140, 152, 151, 194] formulate the procedure for 2-D (area) and 3-D (volume) domains, and apply the technique to cracks in homogeneous solids under linear-elastic and elastic-plastic deformations arising from mechanical and thermal loads. Gu et al. [77], Chen et al. [35], and Kim and Paulino [109, 112] extend the domain-integral method to 2-D FGM specimens under isothermal, linear-elastic loading. The interaction-integral method, based upon the J -integral, is useful to obtain mixed-mode stress intensity factors in linear-elastic 3-D solids [145]. Dolbow and Gosz [53] apply the interaction integral method to FGM specimens under mechanical loading. These studies of simple 2-D models with through cracks in FGMs determine stress intensity factors that compare well with analytical values, but none of them investigate 3-D configurations. The following sections describe the formulation of the 3-D domain integral for FGMs.

2.3.1 The 3-D domain integral

The following derivation of the 3-D domain integral parallels Shih et al. [192] and Moran and Shih [140] for homogeneous materials. The pointwise energy release rate along a generally-curved, planar crack front in 3-D has the form

$$J(s) = \lim_{\Gamma \rightarrow 0} \int_{\Gamma} (W\delta_{1i} - \sigma_{ij}u_{j,1})n_i dC, \quad (9)$$

where W is strain energy density, σ_{ij} denotes stress, u_j represents displacement, and $(\cdot)_{,i} = \partial(\cdot)/\partial X_i$, where X_i refers to local coordinates defined at each point, s , along a crack front. Figure 2.3 illustrates the local coordinate system at location s , where X_2 is normal to the crack plane, X_3 defines the in-plane tangent to the crack, and X_1 defines the in-plane normal. The curve Γ encloses the crack front in the X_1 - X_2 plane. As written, Eq. (9) remains valid for nonlinear-elastic material behavior, and equals the standard J -integral [181] including effects of body forces, crack-face tractions, thermal strains and general material property gradation only when $r \rightarrow 0^+$.

In global coordinates, x_i , let $v_k(s)$ be defined as the unit normal to the crack front at position s , lying in the X_1 - X_3 plane. Equation (9) then represents the first component of the vector integral

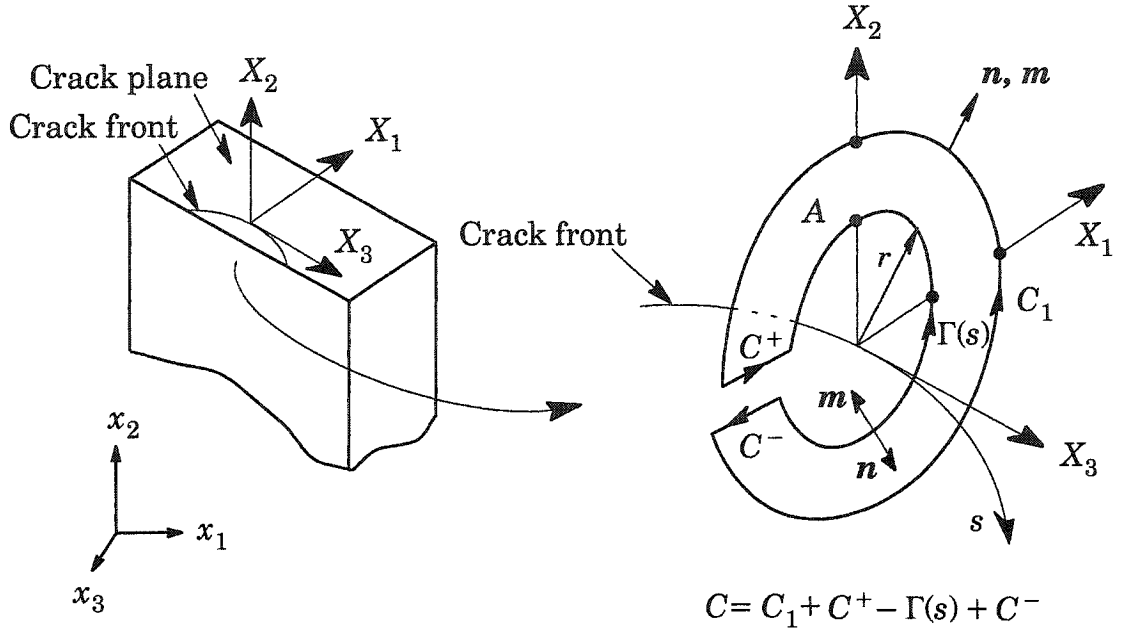


Fig. 2.3. Schematic of $\Gamma(s)$ in Eq. (9). The domain for the analogous 2-D integral is the area A , bounded by the contour $C = C_1 + C^+ - \Gamma(s) + C^-$.

$$J(s) = J_k(s)v_k(s) = \lim_{\Gamma \rightarrow 0} \int_{\Gamma} (\sigma_{ij}u_{j,k} - W\delta_{ik})m_i v_k dC, \quad (10)$$

where $m_i = -n_i$ on $\Gamma(s)$ as shown in Fig. 2.3. A virtual displacement applied to a segment of the crack front takes the form

$$\delta l(s) = \Delta a l_k(s) v_k(s), \quad (11)$$

as illustrated in Fig. 2.4. Here, Δa is the amplitude of the arbitrary displacement, l_k . A first-order approximation of the energy released due to the crack advance, $-\delta\pi$, is [184]

$$-\delta\pi = \int_{L_C} J(s)\delta l(s)ds, \quad (12)$$

where L_C refers to a finite segment of the crack front, as illustrated in Figs. 2.4 and 2.5. Equations (11) and (12) together give

$$-\delta\pi = \bar{J}\Delta a = \Delta a \int_{L_C} J(s)l_k(s)v_k(s)ds, \quad (13)$$

where \bar{J} represents the energy released when crack segment L_C advances by $\delta l(s)$. By combining Equations (10) and (13), one obtains

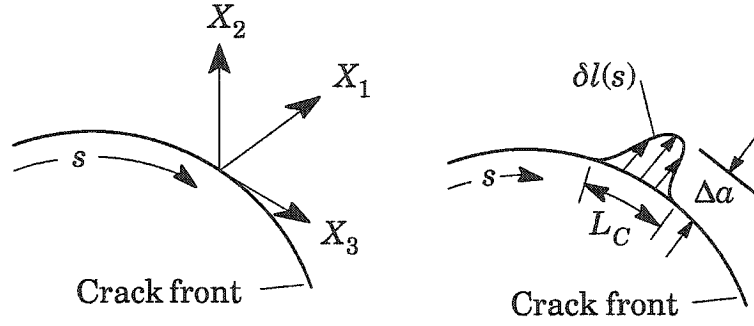


Fig. 2.4. (after Shih et al. [192]) Virtual crack advance in the local X_1 - X_3 plane at crack-front location s . Crack advance occurs in the X_1 -direction, and is defined as $\delta l(s) = \Delta a l_k(s) v_k(s)$.

$$\bar{J}\Delta a = \Delta a \int_{L_C} l_k(s) \left[\lim_{\Gamma \rightarrow 0} \int_{\Gamma} (\sigma_{ij} u_{j,k} - W \delta_{ik}) m_i dC \right] ds \quad (14)$$

$$= \Delta a \lim_{\Gamma \rightarrow 0} \int_{S_t} (\sigma_{ij} u_{j,k} - W \delta_{ik}) l_k m_i dS, \quad (15)$$

where S_t , shown in Fig. 2.5, is the surface created by “extruding” $\Gamma(s)$ in Fig. 2.3 over a distance L_C along the crack front. The radius of this surface shrinks to the crack front in the limiting process. The divergence of the integrand in Eq. (15) is zero for the same conditions that guarantee path independence of the 2-D J -integral, i.e. quasistatic, isothermal loading, elastic constitutive behavior, and no body forces or inertia. In the presence of general loading conditions, the integrand is not divergence free, and takes the form

$$(\sigma_{ij} u_{j,k} - W \delta_{ik})_{,i} = (\sigma_{ij,i} u_{j,k} + \sigma_{ij} u_{j,ki} - W_{,k}). \quad (16)$$

In this expression, the definition of strain energy density, W , includes the effects of thermal strains, nonlinear (elastic) deformation and material gradients, as discussed in a following section. The present goal is to obtain a volume integral equivalent to Eq. (15). To accomplish this, we multiply both sides of Eq. (16) by an arbitrary, sufficiently smooth vector field q_k , and integrate over any simply connected region V within the loaded body to obtain

$$\int_V (\sigma_{ij} u_{j,k} - W \delta_{ik})_{,i} q_k dV = \int_V (\sigma_{ij,i} u_{j,k} - W_{,k}) q_k dV, \quad (17)$$

where the present assumption of zero body forces and inertia causes $\sigma_{ij,i} u_{j,k}$ to vanish. An alternative expression for the left side of Eq. (17) is

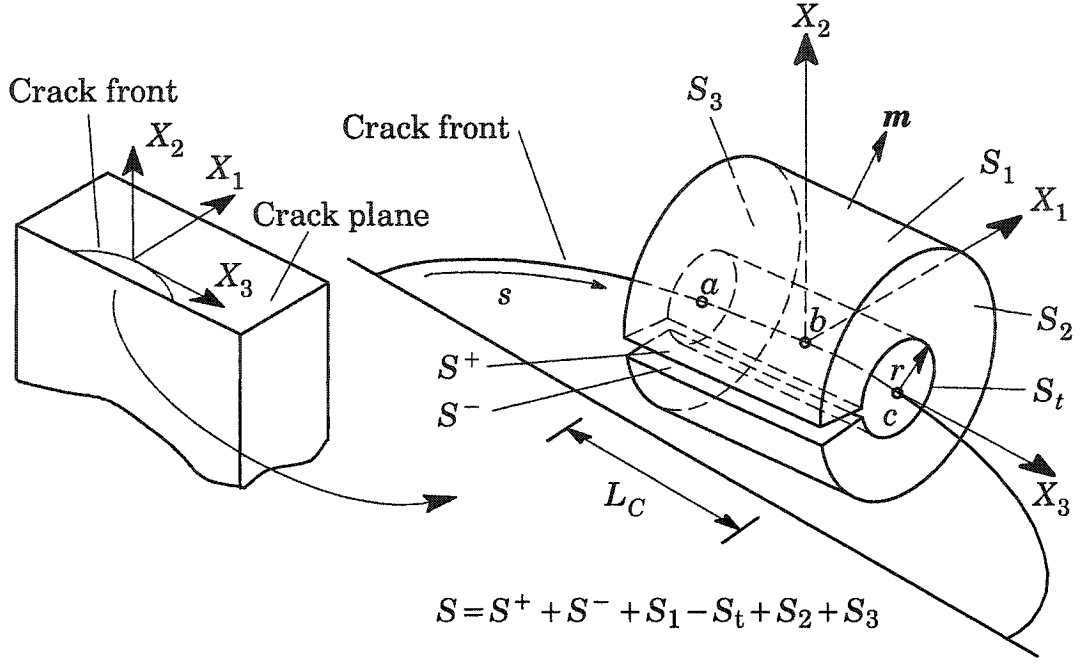


Fig. 2.5. Surface and volume domains used to calculate $J(s)$ at crack-front location $s = b$ extend from point a to point c , a length equal to L_C . Surfaces S_t and S_1 (cylindrical surfaces), S_2 and S_3 (flat lateral surfaces), and S^+ , and S^- (top and bottom crack-face surfaces) comprise surface S and enclose volume V of the domain integral. For general loading conditions, S_t must shrink to the crack tip, i.e. $r \rightarrow 0^+$. Vector m is the outward normal to S_t , S_1 , S^+ , and S^- .

$$\begin{aligned}
 & \int_V (\sigma_{ij} u_{j,k} - W \delta_{ki})_{,i} q_k dV \\
 &= \int_V [(\sigma_{ij} u_{j,k} - W \delta_{ki}) q_k]_{,i} dV - \int_V (\sigma_{ij} u_{j,k} - W \delta_{ki}) q_{k,i} dV. \quad (18)
 \end{aligned}$$

A surface integral results from applying the divergence theorem to the first integral on the right side of Eq. (18). An expression for this surface integral follows from Eqs. (17) and (18):

$$\begin{aligned}
 & \int_S (\sigma_{ij} u_{j,k} - W \delta_{ki}) q_k m_i dS \\
 &= \int_V (\sigma_{ij} u_{j,k} - W \delta_{ki}) q_{k,i} dV + \int_V (\sigma_{ij} u_{j,ki} - W_{,k}) q_k dV. \quad (19)
 \end{aligned}$$

Because surface S of the above surface integral encloses an arbitrary volume V , a suitable definition is $S = S^+ + S^- + S_1 - S_t + S_2 + S_3$ (see Fig. 2.5). The arbitrary function q_k varies smoothly within V as follows [192]:

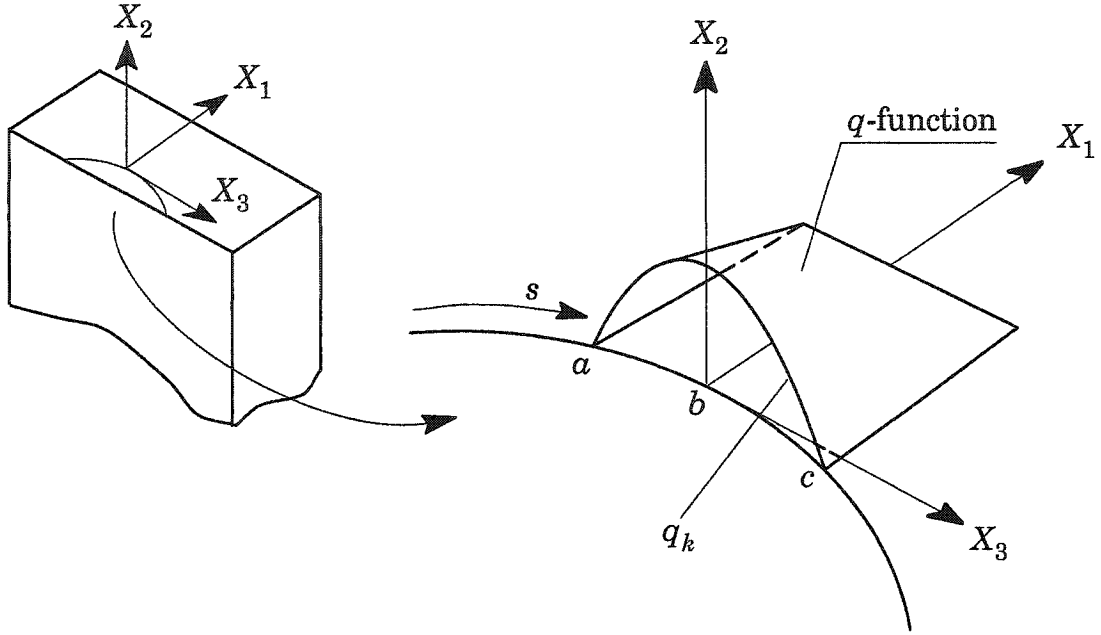


Fig. 2.6. The arbitrary function q_k is interpreted as a virtual crack-front displacement, and varies from unity on surface S_t at location $s = b$, to zero on surfaces S_1, S_2 and S_3 (see Fig. 2.5).

$$q_k = \begin{cases} l_k & \text{on } S_t \\ 0 & \text{on } S_1, S_2, S_3 \\ \text{arbitrary elsewhere} & \end{cases} \quad (20)$$

Figure 2.6 illustrates schematically a permissible definition of q_k . According to this definition of S and q_k , the right-hand side of Eq. (19) equals the integral in Eq. (15), and one may write

$$\bar{J} = \int_V (\sigma_{ij} u_{j,k} - W \delta_{ki}) q_{k,i} dV + \int_V (\sigma_{ij} u_{j,ki} - W_{,k}) q_k dV, \quad (21)$$

when body forces, inertia and crack-face tractions are absent. As mentioned previously, the second integrand in this expression vanishes for a homogeneous body under isothermal, quasi-static loading and elastic material behavior.

By assuming that the energy release rate varies little over the length, L_C , of the domain under consideration, $J(s)$ may be moved outside the integrand in Eq. (13). Equations (13) and (21) then combine to yield an expression for the pointwise value of $J(s)$:

$$J(s) = \frac{\bar{J}}{\int_{L_C} l_k(s) v_k(s) ds}. \quad (22)$$

The transformation of stresses and displacements to the crack-front coordinate system (X_i in Figs. 2.3-2.6) simplifies the form of Eq. (21). In this case, $v_k(s) = X_1(s)$, and

all subscripts “ k ” in Equations (21) and (22) become “1.” The discussion below adopts this approach to evaluate $J(s)$.

2.3.2 Derivative of strain energy density: $W_{,1}$

The strain energy density, W , can be defined as a function of the total strain ε_{ij}^t , temperature Θ , and spatial position $\mathbf{x} = (x_1, x_2, x_3)$:

$$W(\varepsilon_{ij}^t, \Theta, \mathbf{x}) = \int_0^{\varepsilon_{ij}^m} \sigma_{ij} d\varepsilon_{ij}^m, \quad (23)$$

where for uncoupled, quasi-static thermomechanical analysis, mechanical strains, ε_{ij}^m , equal total strains, ε_{ij}^t , minus thermal strains, ε_{ij}^{th} :

$$\varepsilon_{ij}^m = \varepsilon_{ij}^t - \varepsilon_{ij}^{th} = \varepsilon_{ij}^t - \alpha(\mathbf{x})\Theta(\mathbf{x})\delta_{ij}. \quad (24)$$

Here, $\alpha(\mathbf{x})$ is the pointwise-isotropic coefficient of thermal expansion, $\Theta(\mathbf{x})$ is the relative change in temperature, and δ_{ij} represents the Kronecker delta. The derivative of strain energy density, $W_{,1}$, needed to evaluate Eq. (21), becomes

$$W_{,1} = \frac{\partial W}{\partial \varepsilon_{ij}^m} \varepsilon_{ij,1}^m + (W_{,1})_{explicit}, \quad (25)$$

which, combined with Eq. (24), yields

$$W_{,1} = \sigma_{ij}(\varepsilon_{ij}^t - \varepsilon_{ij}^{th})_{,1} + (W_{,1})_{explicit} \quad (26)$$

$$= \sigma_{ij}(\varepsilon_{ij,1}^t - \alpha_{,1}(\mathbf{x})\Theta(\mathbf{x})\delta_{ij} - \alpha(\mathbf{x})\Theta_{,1}(\mathbf{x})\delta_{ij}) + (W_{,1})_{explicit}, \quad (27)$$

where $(W_{,1})_{explicit}$ denotes the derivative of strain energy density with respect to spatially-dependent parameters. Substitution of Eq. (27) into Eq. (21) causes $\sigma_{ij} u_{j,1i}$ to cancel with $\sigma_{ij} \varepsilon_{ij,1}^t$ and the result is

$$\begin{aligned} \bar{J} &= \int_V (\sigma_{ij} u_{j,1} - W \delta_{1i}) q_{1,i} dV \\ &+ \int_V \left[\sigma_{ij} (\alpha_{,1}(\mathbf{x})\Theta(\mathbf{x})\delta_{ij} + \alpha(\mathbf{x})\Theta_{,1}(\mathbf{x})\delta_{ij}) - (W_{,1})_{explicit} \right] q_1 dV. \end{aligned} \quad (28)$$

The second integral of (28) represents a *correction* term to account for the non-vanishing divergence of the J -integral in the presence of thermal strains and material property gradients. Terms related to thermal effects are easily calculated from known distributions of CTEs and temperature [192]. Typically for FGMs, $(W_{,1})_{explicit}$ derives from a specific definition of strain energy density [35, 109, 112]. A description of two forms for this term follows in the next section.

2.3.3 Assessment of alternative forms of $(W_{,1})_{explicit}$

For small displacement gradients in a nonhomogeneous, linear-elastic isotropic material, Eq. (23) becomes

$$W(\varepsilon_{ij}^t, \mathbf{x}, \Theta) = \int_0^{\varepsilon_{rs}^m} C_{ijkl}(\mathbf{x}) \varepsilon_{kl}^m d\varepsilon_{ij}^m, \quad (29)$$

where $C_{ijkl}(\mathbf{x})$ is the spatially-varying isotropic elastic constitutive tensor

$$C_{ijkl}(\mathbf{x}) = \lambda(\mathbf{x})\delta_{ij}\delta_{kl} + \mu(\mathbf{x})(\delta_{ik}\delta_{jl} + \delta_{il}\delta_{jk}), \quad (30)$$

in which δ_{ij} is the Kronecker delta, and the spatially-varying Lamé constants $\lambda(\mathbf{x})$ and $\mu(\mathbf{x})$ are

$$\lambda(\mathbf{x}) = \frac{E(\mathbf{x})\nu(\mathbf{x})}{(1+\nu(\mathbf{x}))(1-2\nu(\mathbf{x}))}, \quad \text{and} \quad \mu(\mathbf{x}) = \frac{E(\mathbf{x})}{2(1+\nu(\mathbf{x}))}. \quad (31)$$

$(W_{,1})_{\text{explicit}}$ is

$$(W_{,1})_{\text{explicit}} = \frac{\partial W}{\partial E(\mathbf{x})}E_{,1}(\mathbf{x}) + \frac{\partial W}{\partial \nu(\mathbf{x})}\nu_{,1}(\mathbf{x}). \quad (32)$$

For homogeneous materials governed by Eq. (29), $(W_{,1})_{\text{explicit}} = 0$, and under isothermal conditions, the second integral of Eq. (28) vanishes completely. In graded materials where $(W_{,1})_{\text{explicit}} \neq 0$, Eq. (29) leads to analytical expressions for $\partial W/\partial E(\mathbf{x})$ and $\partial W/\partial \nu(\mathbf{x})$. For material variations expressed by smooth analytical functions, e.g. $E(\mathbf{x}) = E_1 e^{\beta x_1}$, the evaluation of $E_{,1}(\mathbf{x})$ and $\nu_{,1}(\mathbf{x})$ becomes straightforward, e.g. $E_{,1}(\mathbf{x}) = \beta E(\mathbf{x})$.

Another example of nonzero $(W_{,1})_{\text{explicit}}$ arises when a function such as the Ramberg-Osgood equation describes the multi-axial nonlinear stress-strain relationship: $\varepsilon_{ij} = \varepsilon_m \delta_{ij} + \varepsilon_{ij}^e + 3/2 \times \omega(\mathbf{x})[\sigma_e/\sigma_0(\mathbf{x})]^{n(\mathbf{x})-1} \times S_{ij}/E(\mathbf{x})$, where ε_m is the mean strain, δ_{ij} the Kronecker delta, ε_{ij}^e the elastic deviator strain, σ_e the equivalent (Mises) stress, $\sigma_0(\mathbf{x})$ the yield stress, S_{ij} the deviator stress, $E(\mathbf{x})$ the Young's modulus, and $\omega(\mathbf{x})$ and $n(\mathbf{x})$ are the spatially-varying scalar parameters. In this case, one expression for strain energy density is

$$W(\varepsilon_{ij}^t, \mathbf{x}, \Theta) = \frac{1+\nu(\mathbf{x})}{3E(\mathbf{x})}\sigma_e^2 + \frac{3}{2} \frac{1-2\nu(\mathbf{x})}{E(\mathbf{x})}p^2 + \frac{\sigma_e^2 n(\mathbf{x}) \omega(\mathbf{x})}{n(\mathbf{x})+1 E(\mathbf{x})} \left(\frac{\sigma_e}{\sigma_0(\mathbf{x})} \right)^{n(\mathbf{x})-1}, \quad (33)$$

where p is the hydrostatic pressure, i.e. $p = -(\sigma_{xx} + \sigma_{yy} + \sigma_{zz})/3$. The explicit derivative $(W_{,1})_{\text{explicit}}$ now becomes difficult to evaluate, i.e.,

$$(W_{,1})_{\text{explicit}} = \frac{\partial W}{\partial E}E_{,1}(\mathbf{x}) + \frac{\partial W}{\partial \nu}\nu_{,1}(\mathbf{x}) + \frac{\partial W}{\partial \omega}\omega_{,1}(\mathbf{x}) + \frac{\partial W}{\partial n}n_{,1}(\mathbf{x}) + \frac{\partial W}{\partial \sigma_0}\sigma_{0,1}(\mathbf{x}). \quad (34)$$

These two examples illustrate that although Eq. (23) is quite general, the analytical form of $(W_{,1})_{\text{explicit}}$ is material-specific and likely becomes tedious to evaluate when the "1" direction changes continuously along a 3-D curved crack relative to the property gradient directions.

2.3.4 A general expression for $(W_{,1})_{\text{explicit}}$

Rearrangement of Eq. (27) provides an expression for $(W_{,1})_{\text{explicit}}$ that leads to more convenient numerical evaluation:

$$(W_{,1})_{explicit} = W_{,1} - \sigma_{ij}(\varepsilon_{ij,1}^t - \alpha_{,1}(\mathbf{x})\Theta(\mathbf{x})\delta_{ij} - \alpha(\mathbf{x})\Theta_{,1}(\mathbf{x})\delta_{ij}). \quad (35)$$

Substitution of this expression into Eq. (28) gives

$$\bar{J} = \int_V (\sigma_{ij} u_{j,1} - W\delta_{1i})q_{1,i} dV + \int_V (\sigma_{ij} \varepsilon_{ij,1}^t - W_{,1})q_1 dV, \quad (36)$$

which is equivalent to Eq. (21) since $\sigma_{ij} u_{j,1} = \sigma_{ij} \varepsilon_{ij,1}^t$. This expression yields $J(s)$ when combined with Eq. (22). This is an expected result because the terms in Eq. (35) are the same as those used to transform Eq. (21) into Eq. (28). Equation (36) now replaces Eq. (21) for numerical computation, and specifically accounts for the effects of material gradients and thermal strains. The appearance in Eq. (36) of $\sigma_{ij} \varepsilon_{ij,1}^t$ rather than $\sigma_{ij} u_{j,1}$ follows from the derivation rather than from a deliberate substitution. Both terms include second derivatives of displacement, and provide similar accuracy. Equation (36) is the three-dimensional equivalent of Eq. (6.7) in Moran and Shih [140], which defines J for an elastic-plastic material.

Equation (36) accounts for material gradients and thermal stresses, but omits other standard terms to account for body forces, inertia and crack-face tractions [6]. The use of Eq. (36) to calculate J remains valid for nonlinear elasticity (deformation plasticity), and leads to computational generality since all quantities are available from standard finite-element calculations except $W_{,1}$ and $\varepsilon_{ij,1}$. For analyses using flow-theory constitutive models with parameters that vary spatially, the proposed form of J does not retain strict validity—this is the same issue of computing the ordinary J for incremental-flow theory of plasticity *vs.* deformation plasticity. Another consideration regarding Eq. (36) is the replacement of analytically-defined derivatives in the second integrand of Eq. (28) by derivatives (including $\varepsilon_{ij,1}$) obtained via potentially less accurate, mesh-dependent interpolation schemes. For homogeneous materials, Eq. (28) yields greater accuracy than Eq. (36) because $(W_{,1})_{explicit}$ and $\alpha_{,1}$ vanish and the temperature derivative, $\Theta_{,1}$, is generally quite smooth. The remainder of this study examines the implementation, accuracy and application of Eq. (36) for graded materials under thermomechanical loading.

2.4 Numerical computations

Numerical evaluation of the integrals in Eq. (36) uses the same quadrature schemes employed for element stiffness computation. The discretized form of Eq. (36) is

$$\bar{J} = \sum_{elems} \sum_p \left\{ [(\sigma_{ij} u_{j,1} - W\delta_{1i})q_{1,i} + (\sigma_{ij} \varepsilon_{ij,1}^t - W_{,1})q_1] \det\left(\frac{\partial X_k}{\partial \eta_l}\right) \right\} w_p. \quad (37)$$

For the equivalent expression derived from Eq. (28), $[\cdot]$ in Eq. (37) is

$$\left[(\sigma_{ij} u_{j,1} - W \delta_{1i}) q_{1,i} + (\alpha_{,1}(\mathbf{x}) \Theta(\mathbf{x}) \delta_{ij} + \alpha(\mathbf{x}) \Theta_{,1}(\mathbf{x}) \delta_{ij} - (W_{,1})_{explicit}) q_1 \right]. \quad (38)$$

In both expressions, the outer sum includes all elements in the domain, and the inner sum ranges over each element integration point p with corresponding weight w_p . The determinant of the coordinate Jacobian, $\det(\cdot)$, relates local crack-front coordinates X_k to parent-element coordinates η_k . Computation of spatial derivatives for strain and strain energy density at integration points proceeds as follows:

- Use a standard procedure [41] to extrapolate strains and strain energy density from element integration points to element nodes.
- Average these extrapolated nodal values with contributions from adjoining elements.
- Calculate derivatives at integration points using isoparametric interpolation, i.e.

$$\frac{\partial(\varepsilon_{ij}^t)_p}{\partial x_1} = \sum_{I=1}^n \sum_{k=1}^3 \frac{\partial N_I}{\partial \eta_k} \frac{\partial \eta_k}{\partial x_1} (\varepsilon_{ij}^t)_I, \quad \text{and} \quad \frac{\partial W_p}{\partial x_1} = \sum_{I=1}^n \sum_{k=1}^3 \frac{\partial N_I}{\partial \eta_k} \frac{\partial \eta_k}{\partial x_1} W_I, \quad (39)$$

where $(\varepsilon_{ij}^t)_p$ and W_p denote integration point quantities, n is the number of element nodes, N_I is the element shape function corresponding to node I , η_k are parent coordinates, and $(\varepsilon_{ij}^t)_I$ and W_I are the nodal values of total strain and strain energy density.

The WARP3D fracture code used for this implementation is a free, open-source, general-purpose finite-element software developed at the University of Illinois at Urbana-Champaign [78]. J -integral results reported here employ Eqs. (37) and (39) with 20-noded isoparametric “brick” elements with reduced $(2 \times 2 \times 2)$ integration.

2.5 Numerical implementation in WARP3D

The code employed for this study is publicly available in the WARP3D finite-element software developed at the University of Illinois at Urbana-Champaign (see <http://cee-ux49.cee.uiuc.edu/cfm/warp3d.html>). This general-purpose software was created specifically for the analysis of 3-D cracked solids. WARP3D includes nonlinear and dynamic loading capabilities, finite-strain formulations, serial and parallel architectures, sparse solvers, multiple material-damage models, and crack-analysis capabilities that include the J and interaction integrals and cohesive-zone models (Gullerud et al. [78]). The software runs on UNIX and Windows platforms, and includes readable input files and convenient interface programs for MSC Patran.

2.6 Verification of the general J -formulation for 2-D configurations

Erdogan and Wu [61] describe analytical solutions for a crack located in a semi-infinite strip and subjected to tensile, fixed-grip and bending loads. Figure 2.1(c) shows the

cracked strip where $\alpha/W=0.4$, and a group of ten focused (collapsed) elements, shown in Fig. 2.1(d), surround the crack-front region. This mesh employs quarter-point elements, and coincident crack-front nodes share the same x -displacement, i.e. they have identical node numbers. The ratio of the length, L_e , of crack-front elements on the crack plane to the strip width, W , is $L_e/W=0.007$ (see Fig 2.1(d)). Thirteen semicircular domains produce J -values in a mesh consisting of 496 20-noded bricks and 3735 nodes. An exponential variation, $E(x) = E_1 e^{\beta x}$, describes the gradient of Young's modulus, where $E_2/E_1 = 10$, and β follows from Eq. (1). Poisson's ratio remains constant at $\nu = 0.3$, and constrained out-of-plane displacements enforce plane-strain conditions. Equation (36) leads to $J(s)$ for an imposed tensile stress σ_t . The conversion of J -values to K_I -values here follows the standard expression

$$K_I(s) = \left(J(s) E^*(s) \right)^{1/2}, \quad (40)$$

where $E^*(s) = E(s)/(1 - \nu^2)$ for plane-strain conditions, $E^*(s) = E(s)$ for plane-stress conditions, and $E(s)$ denotes the value of Young's modulus at crack-front location s . The use of $E(s)$ follows from the identical form of the asymptotic crack-front fields in homogeneous and functionally graded materials [59, 97]. For discussion, normalized K_I -values equal

$$K_{In} = \frac{K_I}{\sigma_t \sqrt{\pi a}}, \quad (41)$$

where σ_t is the applied tensile stress, and a is crack depth (see Fig. 2.1). Table 2.1 lists K_{In} -values for two different analyses and compares them with those of Erdogan and Wu [61]. The first analysis employs Eq. (36). To avoid the interpolations used to evaluate Eq. (36), the second analysis uses the analytical expression for $(W,1)_{explicit}$ given in Eq. (32), together with Eqs. (21) and (25). In all cases, an average of the J -values from domains three through thirteen is inserted into Eqs. (40) and (41) to define a single K_{In} -value shown in Table 2.1. Each domain consists of a semi-circular volume of elements surrounding the crack front.

Table 2.1. Normalized K_I -values for a plane-strain, semi-infinite strip under axial tension (see Fig. 2.1): $E_2/E_1 = 10$, $\nu = 0.3$, $\alpha/W = 0.4$.

Analysis	Method	K_{In}	% diff.
Reference	Erdogan and Wu (1997)	1.588	—
1 st	Eq. (36)	1.579	-0.57
2 nd	$(W,1)_{explicit}$ Eq. (32)	1.588	+0.00

The influence of the two integrals in Eq. (36) becomes apparent in Fig. 2.7(a), which compares the value of each integral *vs.* the radius, R_D , shown schematically in Fig.

2.1(d), of the specific computational domain. With increased domain size, the influence of the second integral increases steadily, and without this term, the J -integral becomes proportionately inaccurate.

Through a two-step perturbation procedure, Erdogan and Wu [60] obtain K_I -values for a semi-infinite, exponentially-graded, cracked strip subjected to thermal loading (see Fig. 2.1(a), and [223]). Equations (1) and (4) describe the exponential material variation specified for the strip. In the first step of the solution procedure, Erdogan and Wu determine the axial stress distribution, σ_{yy} , in an uncracked, thermally-loaded strip. This stress, shown as the lower curve in Fig. 2.2(a), represents a crack-closure stress, which, in the second step, produces crack-face tractions acting to drive crack opening in the cracked strip. Integral equations then yield stress intensity factors generated by these crack-face tractions. Values taken from the graphical results of Erdogan and Wu [60] enable comparisons with the present finite-element analyses.

In the finite-element analysis procedure used here, thermal loads act directly upon the cracked strip. The mesh used for this analysis, shown in Fig. 2.7(b), has a height-to-width ratio of four, a crack-length-to-width ratio, a/W , of 0.5, and constrained out-of-plane displacements to enforce plane-strain conditions. As in the previous example, a group of ten focused (collapsed) elements surround the crack-front region, the ratio of crack-front element length, L_e , to strip width, W , is 0.007, and all crack-front nodes have zero y -displacement. This mesh employs quarter-point elements, and coincident crack-front nodes share the same x -displacement, i.e. they have identical node numbers. The mesh consists of 508 20-noded brick elements and 3829 nodes. The following examples employ two material variations and two thermal loading conditions selected from Erdogan and Wu [60] which Table 2.2

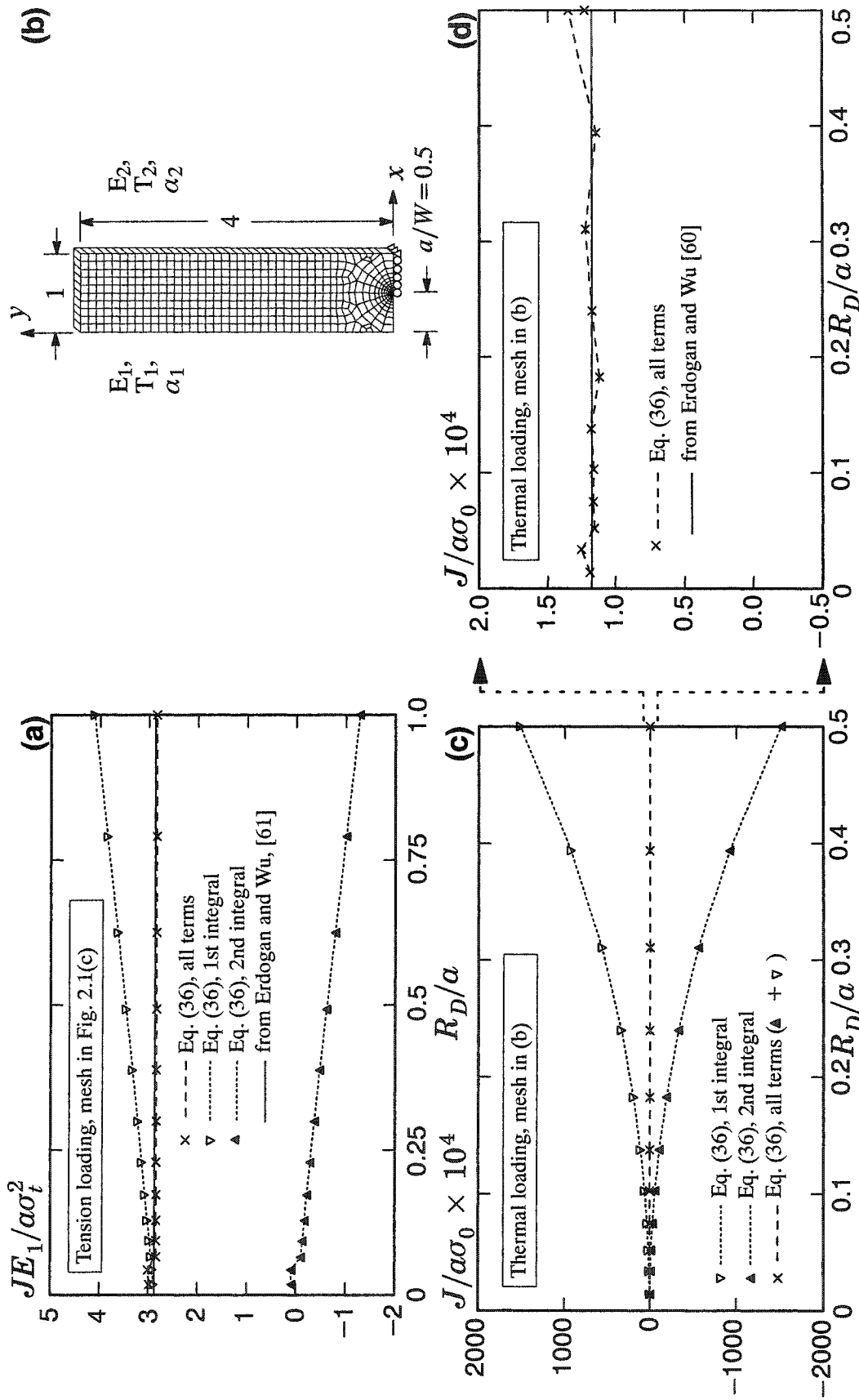


Fig. 2.7. (a) Normalized components of SE(T) for tension loading of SE(T) specimen in Fig. 2.1(c) for $a/W = 0.4$ and $E_2/E_1 = 10$. (b) Mesh used for thermally-loaded SE(T) specimen: $a/W = 0.5$. (c) Normalized components of Eq. (36) for uniform thermal loading for $T_1 = T_2 = 0.05T_0$, $E_2/E_1 = 5$, and $\alpha_2/\alpha_1 = 2$ ($\sigma_0 = E_1\alpha_1T_0/(1 - \nu)$). (d) Scaled view of data in (c).

describes. They include the application of two uniform temperature loads to an exponentially-graded strip where $E_2/E_1=5$, $a_2/a_1=2$, and $\nu=0.3$, and two exponentially-varying temperature loads to an exponentially-graded strip where $E_2/E_1=10$, $k_2/k_1=10$, $a_2/a_1=2$, and $\nu=0.3$. A common normalization for K_I -values obtained from thermal loading is

$$K_{In} = \frac{K_I}{E_1' \alpha_1 T_0 \sqrt{\pi a}}, \quad (42)$$

where a is crack depth, T_0 is initial temperature, and α_1 is the value of the CTE at the cracked surface. For plane-strain conditions, $E_1' = E_1/(1-\nu)$, and for plane stress conditions, $E_1' = E_1$, where E_1 is the value of Young's modulus at the cracked surface. Table 2.2 lists stress intensity factors obtained from each of the four cases and their deviation from the solution obtained from Erdogan and Wu [60]. In each of the four analyses, an average of the J -values from fourteen domains, inserted into Eqs. (40) and (42), leads to a single value of K_{In} .

Table 2.2. Normalized K_I -values for a crack in a plane-strain, semi-infinite strip under thermal loads (see Figs. 2.1(a) and 2.7(b)): $\nu=0.3$, $a/W=0.5$.

Material Variation	Thermal Load (see Fig. 2.1)	K_{In}		
		Erdogan & Wu (1996)	Eq. (36)	% diff.
$E_2/E_1=5$	$T_1=T_2=0.5T_0$	0.0125	0.0127	+1.6
$a_2/a_1=2$				
k_2/k_1 is arbitrary	$T_1=T_2=0.05T_0$	0.0245	0.0241	-1.6
$E_2/E_1=10$	$T_1=0.2T_0$	0.0335	0.0335	+0.0
	$T_2=0.5T_0$			
$a_2/a_1=2$				
$k_2/k_1=10$	$T_1=0.05T_0$	0.0410	0.0409	-0.2
	$T_2=0.5T_0$			

Figure 2.7(c) shows the contribution to J of both integrals in Eq. (36). Both integrals show strong path dependence with an increase in domain size to crack length ratio, R_D/a (see Fig. 2.1(d)). Because inhomogeneity in both elastic properties and thermal expansion coefficients contribute to J , the path dependence is more severe than for the mechanical loading studied above. Figure 2.7(d) shows values of Eq. (36) with an enhanced scale. The J -values for both mechanical and thermal loading show good domain independence.

2.7 Computation of mode-I K_I -values for surface cracks

Procedures for obtaining K_I -values for 3-D cracks include the line-spring method [183], the modified crack-closure integral (MCCI) [187, 177, 176, 148], the displacement correlation technique (DCT) [191], stress correlation [175], the domain integral technique [192], the interaction integral method [145], and the F -integral [62].

Raju and Newman [175] and Newman and Raju [150] apply the force method to surface cracks in homogeneous plates under tension and bending loads. Although more recent works report stress intensity factors for surface cracks [174, 12], the extensive solutions of Newman and Raju remain a frequently-cited benchmark. For homogeneous materials, the current study uses their results to verify mesh-refinement levels.

The methods listed above also apply to the analysis of FGMs [109]. The MCCI, DCT and stress correlation methods are particularly useful for linear-elastic analyses of FGMs because the presence of material gradients does not influence their formulation. Erdogan and Wu [61] suggest that the line-spring method, combined with their semi-analytical solutions for the graded 2-D strip discussed in Section 2.6, provides an approach for the calculation of stress intensity factors in FGMs with surface cracks. The current study employs the DCT to verify K_I -values obtained through Eq. (36).

2.7.1 Crack geometries, material variations and loadings

Figure 2.8(a) illustrates a plate with a semi-elliptical surface crack under tension, bending and thermal loads. Material properties vary only in the thickness (x) direction. The geometry, loading and material property variations lead to mode-I conditions on the crack plane. Symmetry permits modelling of only one quarter of the specimen. Variables of interest in this study include: crack depth, a ; crack half-length, c ; and plate thickness t . Dimensions h and b remain fixed at five times the larger of a and c such that the K_I -values approximate those in a semi-infinite plate. The current work includes analyses of plates for a range of practical crack geometries of $a/c = 1/3$, $a/c = 1$ and $a/c = 2$ and crack depths of $a/t = 0.2$, $a/t = 0.5$ and $a/t = 0.8$. A specimen cross-section, illustrated in Fig. 2.8(b), indicates through-thickness material variation, assigned to follow the form $E(x) = E_1 e^{\beta x}$, where $E_1 = E(x=0)$, $E_2 = E(x=t)$, with β given by Eq. (1) such that $E_2/E_1 = 0.2$, 1.0 and 5.0. Poisson's ratio remains constant at 0.25 in all cases. Figure 2.8(b) also illustrates the applied tensile stress, σ_t , and bending stress, σ_b , where $\sigma_b = 3M/bt^2$. Table 2.3 summarizes the surface-crack geometries, material properties, and temperature variations employed in this study.

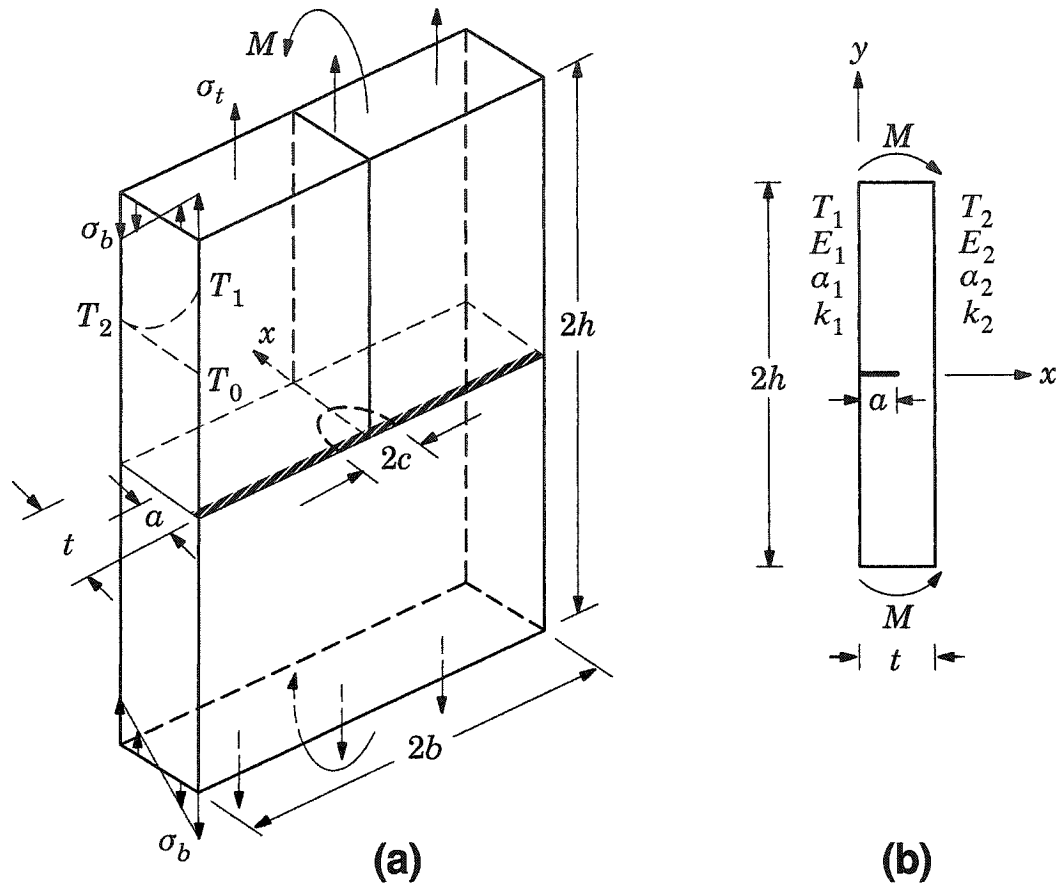


Fig. 2.8. (a) Surface-crack specimen showing axial, bending and thermal loads. The hatched area illustrates the potential region for the “boundary layer” (see Section 2.7.3). Symmetry permits analysis using one quarter of the model. (b) Cross-section of plate showing unidirectional material variation from cracked face to uncracked face. Bending stress is calculated from total moment M as $\sigma_b = 3M/bt^2$.

Table 2.3. Specified surface-crack geometries, material properties, and temperature loads.

Quantity	Specified Values
a/c	1/3, 1, 2
a/t	0.2, 0.5, 0.8
E_2/E_1	0.2, 1.0, 5.0
ν_2/ν_1	1.0
T_1/T_2	5, 10, 20

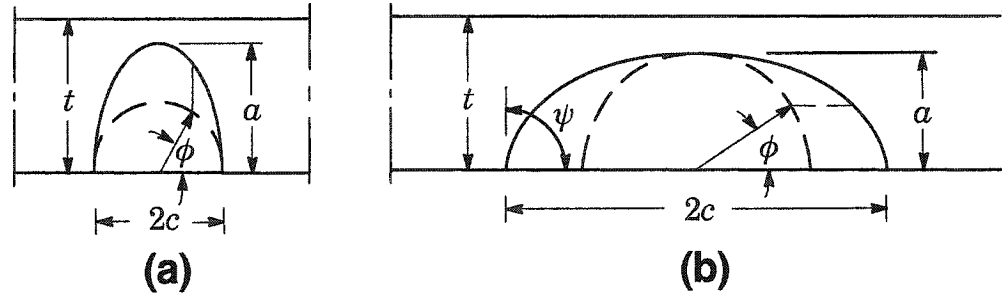


Fig. 2.9. Plan view of the crack plane shown in Fig. 2.8(a). **(a)** Measurement in radians of parametric angle, ϕ , for $a/c > 1.0$. **(b)** Parametric angle, ϕ , for $a/c \leq 1.0$, and intersection angle, ψ , describing the angle between the crack front and free surface. For all models in this study, $\psi = 90^\circ$.

Thermal loading conditions follow those used by Erdogan and Wu [60] who analyzed a zirconia/Rene-41 composite with the properties listed in Table 2.4. Young's modulus (E), CTE (α), and conductivity (k) vary exponentially according to $E(x) = E_1 e^{\beta x}$, $\alpha(x) = \alpha_1 e^{\omega x}$, and $k(x) = k_1 e^{\eta x}$, where $(\cdot)_1$ is the property value at $x = 0$. The coefficients of nonhomogeneity, β , ω and η have values given by Eqs. (1) and (4). These material properties are taken as temperature independent.

Table 2.4. Properties for thermal loading of surface-crack specimens (Erdogan and Wu, [60]).

Material	E (GPa)	ν	α (K^{-1})	k (Cal/mmSecK)
($x = 0$) Zirconia	151	0.33	1.0×10^{-5}	0.05
($x = t$) Rene-41	219.7	0.33	1.67×10^{-5}	0.61

Figure 2.8(a) shows the qualitative temperature distribution which follows solution of the 1-D diffusion equation described in Section 2.2. The selected range of boundary temperatures includes: $T_1 = 5T_2$, $T_1 = 10T_2$ and $T_1 = 20T_2$, where $T_1 = T(x = 0)$ and $T_2 = T(x = t) = T_0$. To illustrate the application of Eq. (36) to thermal loading, the present work includes analyses of plates with the three crack geometries listed in Table 2.3, each with a crack depth of $a/t = 0.2$.

2.7.2 Conversion of J to K

This paper reports values of the domain integral, Eq. (36), calculated at the corner nodes of all crack-front elements. Parametric angle, ϕ , measured in radians, describes the location of crack-front nodes on the crack front for possible ranges of the ratio a/c (see Fig. 2.9). At each crack-front location ϕ , Eq. (40) yields K_I -values from J and E_{front} , the value of Young's modulus at that location. For through-thickness material variation

and semi-elliptical cracks, E_{front} at ϕ equals $E(x)$ at distance $x = a \sin \phi$ from the cracked surface.

A general form for mode-I stress intensity factors for semi-elliptical surface cracks is

$$K_I = S \sqrt{\frac{\pi a}{Q}} F\left(\frac{a}{t}, \frac{a}{c}, \phi, \mathbf{P}\right), \quad (43)$$

where $S = \sigma_t$ for tension, and $S = \sigma_b$ for bending. For plane-strain thermal loading, $S = \alpha_1 E_1 T_0 / (1 - \nu)$, and for plane-stress, $S = \alpha_1 E_1 T_0$ [60]. Figure 2.1 defines α_1 , E_1 , and T_0 . The shape factor, Q , denotes the square of the complete elliptic integral of the second kind. \sqrt{Q} equals half the arc length of an ellipse divided by the length of the major axis (Merkle, 1973), a ratio commonly approximated by

$$Q = \begin{cases} 1 + 1.464 \left(\frac{a}{c}\right)^{1.65} & \text{for } a/c \leq 1 \\ 1 + 1.464 \left(\frac{c}{a}\right)^{1.65} & \text{for } a/c > 1. \end{cases} \quad (44)$$

Function F in Eq. (43) includes the effects of plate dimensions, crack geometry, location along the crack front and material property variation, represented by \mathbf{P} . A normalized stress intensity factor expressed by

$$K_{In} = \frac{K_I}{S \sqrt{\frac{\pi a}{Q}}} = F\left(\frac{a}{t}, \frac{a}{c}, \phi, \mathbf{P}\right), \quad (45)$$

represents a “shape factor” for the geometry, material and loading conditions under consideration.

2.7.3 Stress intensity factors at the intersection of the crack front with the free surface

Researchers employ analytical and numerical techniques to examine the change in the singular behavior at the intersection of a 3-D crack front with a traction-free surface [80, 20, 15, 171]. These studies demonstrate the existence of a “boundary layer” very near the free surface over which a generalized stress intensity factor may vary sharply. The change in singular behavior depends upon Poisson’s ratio and the angle of intersection between the crack front and the free surface, illustrated by ψ in Fig. 2.9(b). For FGMs, the length scale of material gradation (e.g. parameter $1/\beta$, where Eq. (1) defines β) should also affect the stress state and the size of the boundary layer. For a crack front that intersects the free surface at $\psi = 90^\circ$, when Poisson’s ratio is greater than zero, the stress singularity ($r^{-\lambda}$) in the boundary layer becomes weaker ($\lambda < 1/2$), and the mode-I stress intensity factor tends toward zero at the surface [171].

Raju and Newman [175] verify the decrease in stress intensity factors near the free surface through a detailed mesh-refinement study of a semi-circular surface crack.

More importantly, their study shows that the effects of the boundary layer are highly localized, and do not influence stress intensity factors on the interior of the specimen. Chuntu and Yingzhi [40], Li et al. [134], Rajaram et al. [174], Ayhan and Nied [12] and Frangi [69] also demonstrate the localized influence of the boundary layer on stress intensity factors through numerical analyses of straight cracks and semi-circular, quarter-circular and semi-elliptical surface cracks. Nakamura and Parks [144] estimate the region of influence of the corner singularity in semi-elliptical surface cracks as $\approx 0.03 \times a^2/c$, where a and c are the crack dimensions shown in Fig 2.8. Because a detailed study of the boundary-layer influence in FGMs is not the focus of this paper, the present work does not include sufficient mesh refinement in this region to determine adequately the layer's size, or to capture the true variation of stress intensity factors within the boundary layer. To acknowledge the effect of the weak corner singularity, however, for mechanical loading, the plane-stress conversion applies here to J -values calculated at the free surface, i.e. $\phi = 0$, and the plane-strain conversion applies here for $\phi > 0$. Although stress intensity factors near $\phi = 0$ should tend toward zero in order to conform with theory, the nonzero values reported here represent *average* stress intensity factors *near* the free surface [175]. For thermal loading, plane-stress K_{In} -values obtained using Eqs. (40) and (45), exceed plane-strain values by a factor of $[(1 - \nu)/(1 + \nu)]^{1/2}$. To avoid reporting an increase in K_{In} -values in the boundary layer, we simply omit stress intensity factors at $\phi = 0$ for thermal loading.

2.7.4 Mesh refinement

A mesh that is adequately refined for the correct solution of a boundary-value problem of a homogeneous body may require further refinement in order to capture the effects of material gradients. To confirm adequate refinement of meshes used in this study, values of K_{In} published in the literature and those obtained here using the DCT verify values of K_{In} obtained from Eq. (36) for both homogeneous and nonhomogeneous specimens.

For 2-D cracked configurations, Eischen [59] and Jin and Noda [97] prove that the near-tip displacement field for functionally graded materials has the same form as for homogeneous materials. Hartranft and Sih [79] show that the singularity along a 3-D crack front in homogeneous material (remote from boundaries) has the same form as the crack-tip singularity in a 2-D configuration. Based on these two results, the opening displacement of the crack face, normal to the crack plane, has the asymptotic form

$$u_2 = \frac{4K_I}{E^*(s)} \sqrt{\frac{r}{2\pi}}, \quad (46)$$

where u_2 denotes the displacement in the X_2 -direction of the coordinate system shown in Fig. 2.3, K_I is the mode-I stress intensity factor, and r is the distance behind and nor-

mal to the crack front. The use of $E^*(s)$ in Eq. (46) is justified by the equivalence of asymptotic crack-front fields in homogenous and functionally graded materials [59, 97].

The DCT utilizes the relationship between displacement and K_I expressed in Eq. (46) to estimate stress intensity factors based on u_2 nodal displacements behind the crack front. Here, element boundaries on the crack face define approximate normals to the crack front. Values of u_2 and r at several nodes along one boundary, when inserted into Eq. (46), permit the calculation of a K_I -value that corresponds to each node. A plot of these K_I -values vs. r yields an approximately linear relationship between K_I and r . The intersection of this line with $r = 0$ provides the estimated crack-front K_I -value for the DCT. Equation (45) describes the normalization of these values.

2.7.4.1 Effects of mesh refinement on K_I -values for FGM specimens

Stress intensity factor solutions from four different meshes of a plate with crack geometry $a/t = 0.8$ and $a/c = 2$, and an exponential material variation where $E_2/E_1 = 5$, provide insight into the effects of mesh refinement on the values of K_{In} . Ten 20-noded, quarter-point, hexagonal elements with collapsed faces immediately surround each crack front in the θ direction (see Fig. 2.10). In the radial direction, the four meshes have respectively 3, 5, 7, and 10 rings of elements surrounding the crack front, corresponding to the number of domains used to produce J -values. Sixteen elements lie along the crack front between $\phi = 0$ and $\phi = \pi/2$. Figure 2.10 shows a typical crack-front location in the local x_1 - x_2 coordinate system for the 7-ring mesh. Ratios of crack-front element length, L_e , to plate thickness, t , L_e/t , range from 1.47×10^{-2} for the 3-ring mesh, to 5.41×10^{-5} for the 10-ring mesh. The 3-ring mesh has 7632 elements and 34013 nodes, and the 10-ring mesh has 8752 elements and 39053 nodes. The number of nodes and elements in each model reflects the large plate dimensions h and b . Increased mesh refinement in the four models focuses primarily on the crack-front region. Figure 2.11 shows normalized K_I vs. location along the crack front for $0 < \phi < \pi/2$, and compares K_{In} obtained through Eqs. (36) and (46) for the 3-ring and 10-ring models. The meshes yield results which show little variation between refinement levels, and which show close agreement between the two methods, i.e. Eq. (36) and Eq. (46).

The reduced ($2 \times 2 \times 2$) integration triggers a small amount of hourglassing in crack-front elements for the 7-ring model, which becomes more pronounced in the 10-ring model. Hourglassing does not significantly affect K_I in the 7-ring model—the refinement level selected to discretize all subsequent models of surface-cracked plates. Figure 2.12 shows typical mesh refinement in the crack region for the three crack geometries analyzed in this study, i.e. $a/c = 1/3, 1$ and 2 . J -values obtained from all 7-ring meshes are an average of domains three through seven.

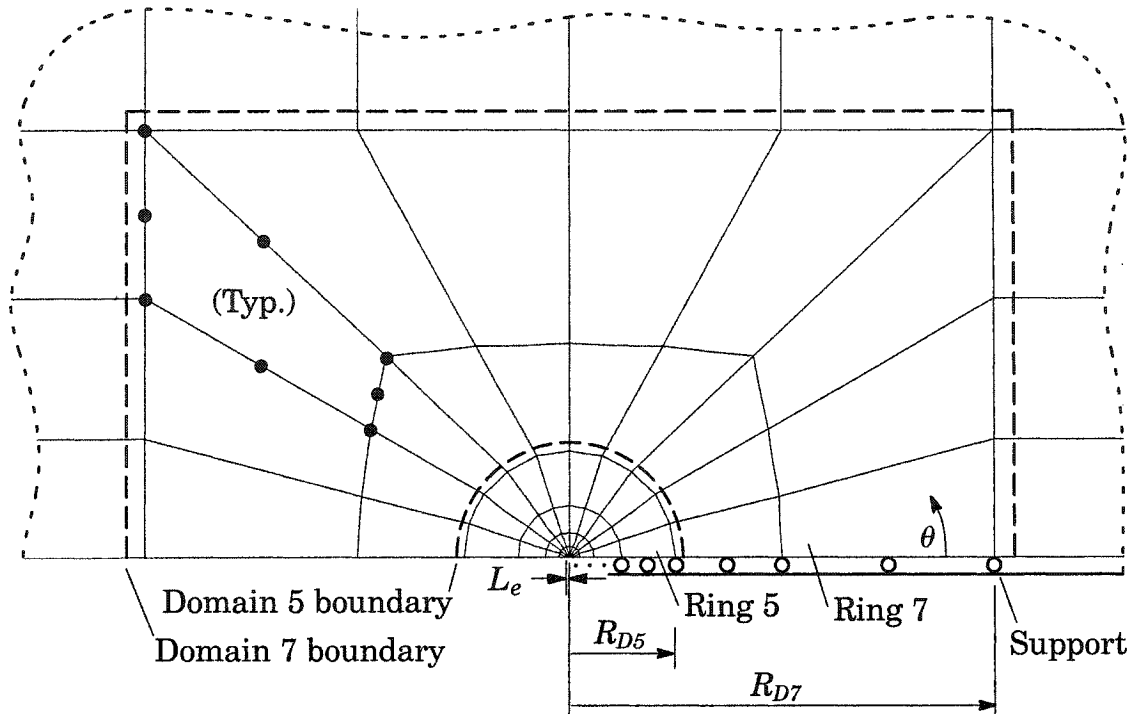


Fig. 2.10. Crack-front mesh with 7 rings of elements in the radial direction, and 10 elements along the θ -direction. The ratio of L_e to plate thickness t , $L_e/t = 7.66 \times 10^{-4}$, describes the level of mesh refinement. R_D provides a measure of domain size.

2.7.4.2 Verification of K_I -values for homogeneous specimens

A comparison of K_I -values obtained from Eq. (36) with those reported by Newman and Raju [150] verifies the present solution of the boundary-value problem for the homogeneous plate specimens. Figure 2.13(a) compares values of K_{In} derived from Eq. (36) with the Raju and Newman [175] solutions for tension loading of homogeneous material, crack geometries $a/c=1$ and 2, and crack depths $a/t=0.2$ and 0.8. Figure 2.13(b) compares K_{In} -values from Eq. (36) with Newman and Raju [150] solutions for the same models under bending. Bending loads cause portions of the crack face to close. Without contact surfaces, finite-element solutions for these cases permit spurious crack-face displacements (i.e. crack-face interpenetration) which cause some domains to produce negative J -values. Newman and Raju [150] list the negative values; here we report only positive values. Lee and Erdogan [128] and Anifantis [5] describe techniques to include crack-face contact in 2-D cases. Figure 2.13 shows agreement between K_{In} -values obtained from Eq. (36) for both tension and bending loads with the Newman and Raju solutions.

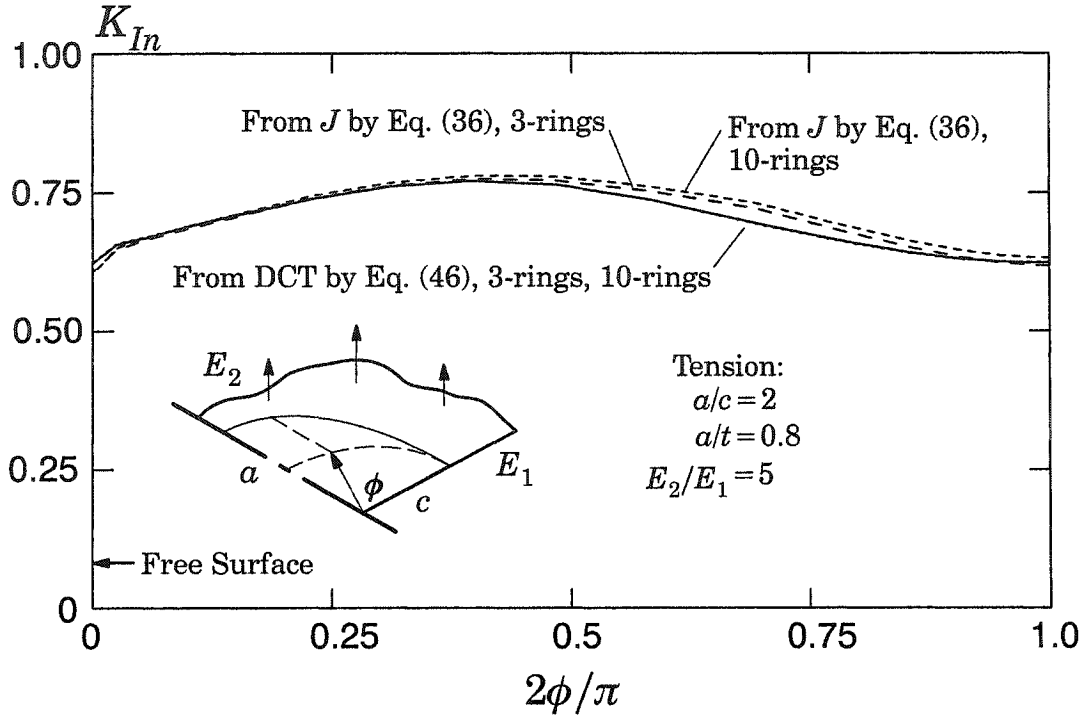


Fig. 2.11. Comparison of normalized stress intensity factors, K_{In} , obtained using Eqs. (36) and (46) for 3-ring and 10-ring crack-front mesh refinements where $a/c=2$ and $a/t=0.8$.

2.7.4.3 Verification of K_I -values for FGM specimens

For FGM cases, the good agreement between K_{In} -values obtained using Eq. (36) and those obtained using the DCT confirms that the adopted level of mesh refinement captures the effects of material property gradients. Previous applications of the DCT to 2-D models for FGMs include Li et al. [131], Marur and Tippur [135], Rousseau and Tippur [186] and Kim and Paulino [109]. For an exponential material variation with $E_2/E_1 = 5$, Figs. 2.14(a)-(c) compare tension and bending results for each crack geometry and crack depth. Figure 2.14(d) compares results for thermally-loaded plates with three crack geometries: $a/c = 1/3, 1$, and 2 , each with crack depth $a/t = 0.2$. The specified surface temperature ratio is $T_1/T_2 = 20$, with the through-thickness temperature distribution as described in Section 2.2 (and shown schematically in Fig. 2.8).

K_{In} -values for all loading cases show good agreement between the two methods (i.e. from J and the DCT), with the largest difference occurring along crack-front sections with high curvature. In Fig. 2.14(a), the largest difference for $a/c = 1/3$ is less than 7% of the smaller value. For $a/c = 2$, the maximum difference in Fig. 2.14(c) is less than 5% of the smaller value. Figures 2.15(a)-(c) compare K_{In} -values derived from Eq. (36) with K_{In} -values obtained via the DCT for all crack geometries and crack depths, for an exponential material variation with $E_2/E_1 = 0.2$. In this case, a maximum difference slightly

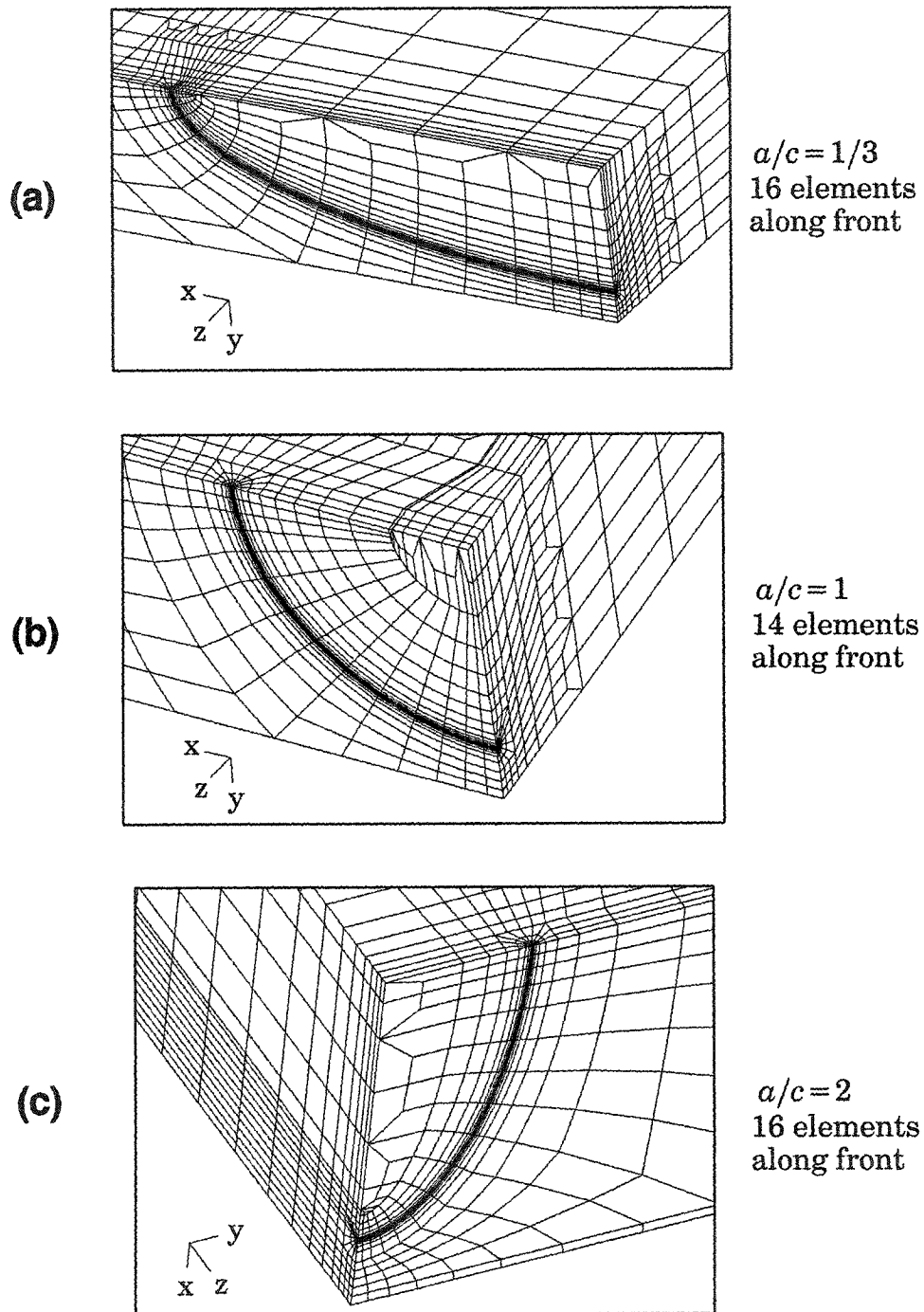


Fig. 2.12. Typical discretization along front for surface-crack configurations.

greater than 7% occurs under tension loading near $\phi = 0.25$ for $a/c = 1/3$ and $a/t = 0.8$ (see Fig. 2.15(a)).

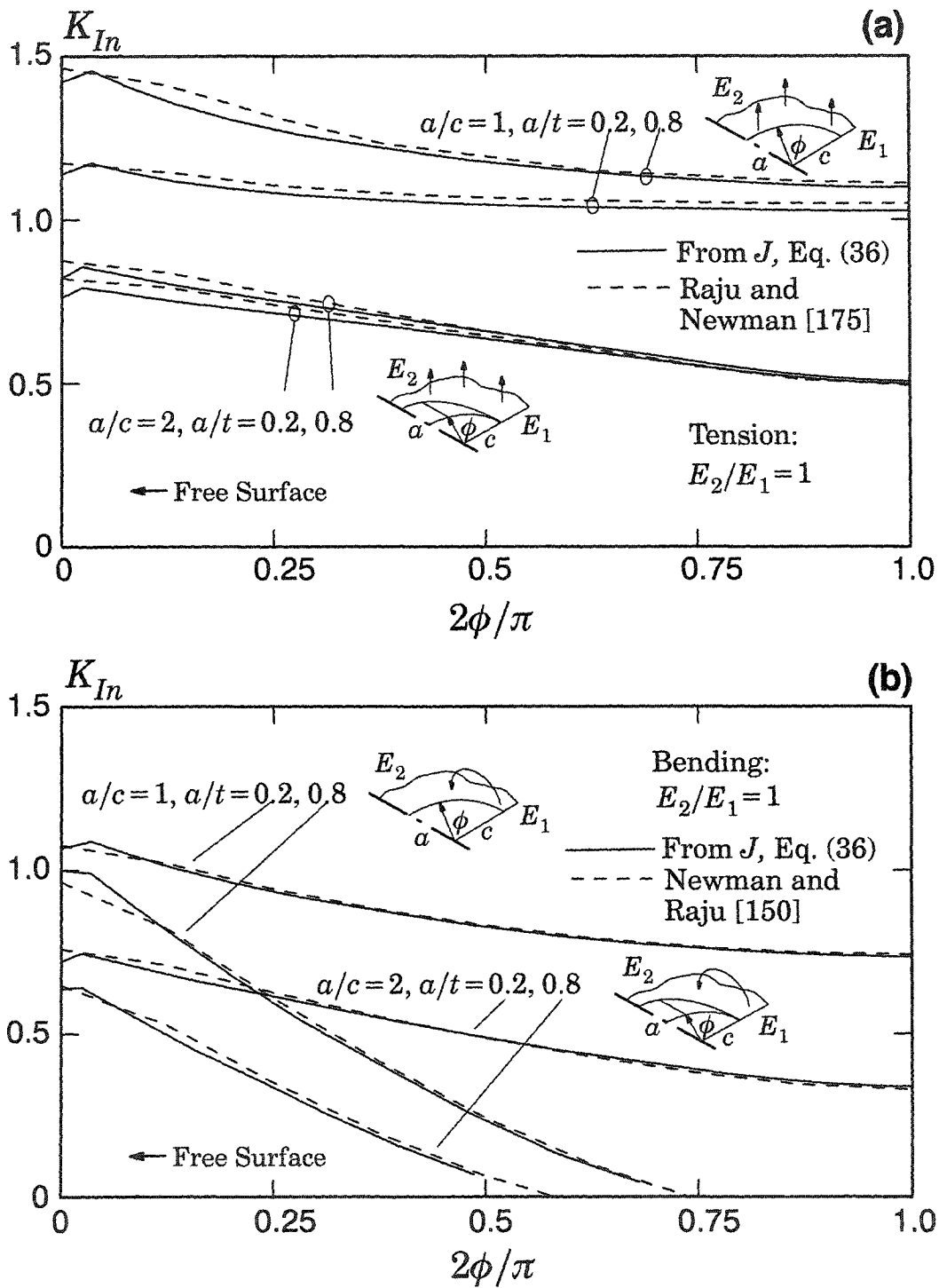


Fig. 2.13. Normalized K_I -values, K_{In} , for surface-cracked plates with homogeneous material having $a/c = 1, 2$, and $a/t = 0.2, 0.8$. Comparison of values generated using Eq. (36) with those of (a) Raju and Newman [175] and (b) Newman and Raju [150].

2.7.5 Effect of material gradient terms on J -values

Figures 2.16(a)-(d) show J -values, calculated with and without the second integral of Eq. (36), at three locations, ϕ , along the crack front for four different combinations of crack geometry and loading. Each curve in the figure has seven points that correspond to the seven domains used to calculate J -values. Here, R_D/a equals the radius of the domain, measured at $\phi = \pi/2$, divided by the crack depth, a . Figure 2.10 illustrates R_D , which is measured ahead of the crack front on the plane of symmetry. For the purpose of interpreting the results shown in these figures, Eq. (28) is more intuitive than its equivalent used for numerical implementation, Eq. (36). For tension and bending loads, the contribution of gradient terms at small ϕ is insignificant for all domains. This reflects the vanishing of $E_{,1}(\mathbf{x})$ as the crack-front normal X_1 , becomes orthogonal to the direction of material variation. Figures 2.16(a) and 2.16(c) show that for $E_2/E_1 = 5$, omission of gradient terms leads to increased J -values as the domain size increases. This increase arises from an increase in both $\partial W/\partial \mathbf{E}(\mathbf{x})$ and $E_{,1}(\mathbf{x})$ in the direction of the crack-front normal. For a softening material, i.e. $E_2/E_1 = 0.2$, J -values decrease as the domain size increases (see Fig. 2.16(b)). For the thermally-loaded specimens, the second integrand of Eq. (36) shows a much greater influence on J than in the tension and bending cases, as seen in Fig. 2.16(d). Referring to Eqs. (28) and (32), when $\phi = 0$, the gradient terms $E_{,1}(\mathbf{x})$, $\alpha_{,1}(\mathbf{x})$, and $\Theta_{,1}(\mathbf{x})$ all vanish. At other front locations, the gradient terms become significant as the domain size increases, reflecting the combined effects of thermal loading and material gradients on J .

For all loading cases, the relative contribution of the second integrand increases with domain size, and becomes necessary to maintain domain independence of the J -values. Because R_D/a ratios are small for the domains employed to generate the curves shown in Fig. 2.16, domain dependence of J -values is not as significant as that shown in Figs. 2.7(c) and (d) for an SE(T) specimen where R_D/a are larger. As domains decrease in size, the magnitude of the second integral of Eq. (36) becomes much smaller than the first (conventional) integral. This difference in relative magnitude is a function of the derivative $(q_{,1})$ in the first integral. Figure 2.6 shows that q decreases from unity at the crack front to zero at the outer boundary of the domain. As the domain shrinks in size, the distance from the crack front to the outer boundary of the domain also shrinks, and causes the derivative of q to become very large, thereby heavily weighting the first integral [77]. This trend in J with decreasing domain size agrees with observations made by Aoki et al. [9], Tohgo et al. [211] and Gu et al. [77] who suggest that very small, near-tip domains yield accurate values of J in an FGM without including gradient terms—at least for linear-elastic analyses. This eliminates one advantage of the J -integral, however, which is good accuracy when evaluated over large domains in a relatively coarse mesh. Path independence, which does not generally result without the use

of gradient terms, indicates an acceptable level of mesh refinement. The omission of gradient terms removes these two advantages of J -integral calculations.

It is also very useful to compare the contribution to J from individual terms in Eq. (36). Figures 2.17(b), 2.17(c), and 2.17(d) show the influence of Eqs. (47)-(50) for tension, bending and thermal loading conditions, respectively. Results plotted in these figures correspond to the seven domains evaluated at $\phi \approx 19^\circ$ on a crack where $a/c = 1/3$ and $a/t = 0.2$. Material variation for axial and bending loads is $E_2/E_1 = 5$, and for thermal loading is given in Table 2.4. Applied temperature for the thermal case is $T_1/T_2 = 20$. The plots show values of the following normalized, numerically evaluated integrals:

$$\frac{1}{J(s)} \int_V (\sigma_{ij} u_{j,1}) q_{1,i} dV, \quad (47)$$

$$\frac{1}{J(s)} \int_V (\sigma_{ij} \varepsilon_{ij}^t) q_1 dV, \quad (48)$$

$$\frac{1}{J(s)} \int_V -W q_{1,1} dV, \text{ and} \quad (49)$$

$$\frac{1}{J(s)} \int_V -W_{,1} q_1 dV, \quad (50)$$

where volume V includes all elements in the current domain. Also shown in the plots are the values obtained by combining Eq. (47) with Eq. (48) and Eq. (49) with Eq. (50). In Figs. 2.17(a) and 2.17(b), irregularity in the magnitude of Eq. (48) and Eq. (50) occurs in the first two domains. In Fig. 2.17(c), the irregularity extends through domain four. This lack of smoothness indicates that convergence has not been achieved in these domains. At each crack-front location of this crack geometry under the given loading conditions, cancellation between the integrands in Eq. (49) and Eq. (50) occurs after convergence has been reached. For the particular crack geometries and loading conditions under consideration, when J has converged, the stress work density terms described by Eq. (49) and Eq. (50) contribute negligibly to Eq. (36), and we may consider

$$\int_V (W q_1)_{,1} dV = 0 \quad (51)$$

for the numerical results presented in this chapter. Figures 2.17(b)-(d) indicate that with the numerical approach outlined in Section 2.4, the evaluation of Eq. (36) over small domains produces a more accurate value of J when strain energy density terms are omitted, and that a converged value of J may be recognized by a negligible contribution from the sum of strain energy density terms. Although this is true for the loading and material assumptions considered in this study, it is not argued here that the result

expressed by Eq. (51) is applicable to more general crack geometries and loading/material response conditions. Equation (51) may simply be an artefact of the symmetry of the selected q -function or of the strain-energy density.

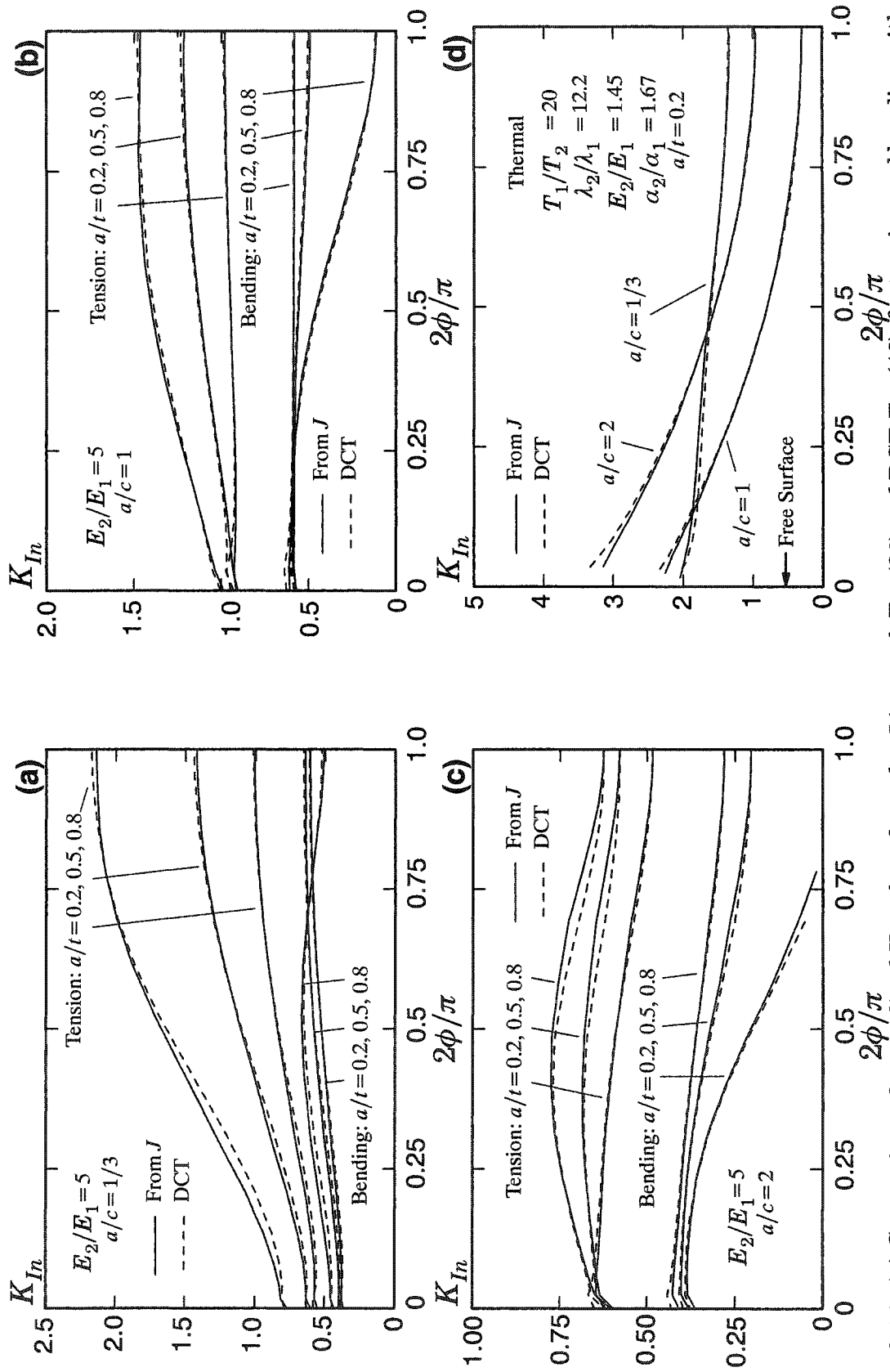


Fig. 2.14. (a) Comparison of normalized K_I values from the J -integral, Eq. (36) and DCT, Eq. (46), for tension and bending with $E_2/E_1=5$, $a/t=0.2, 0.5, 0.8$, and $a/c=1/3$, (b) $a/c=1$, (c) $a/c=2$, and (d) thermal loading with $T_1/T_2=20$, $a/t=0.2$ and

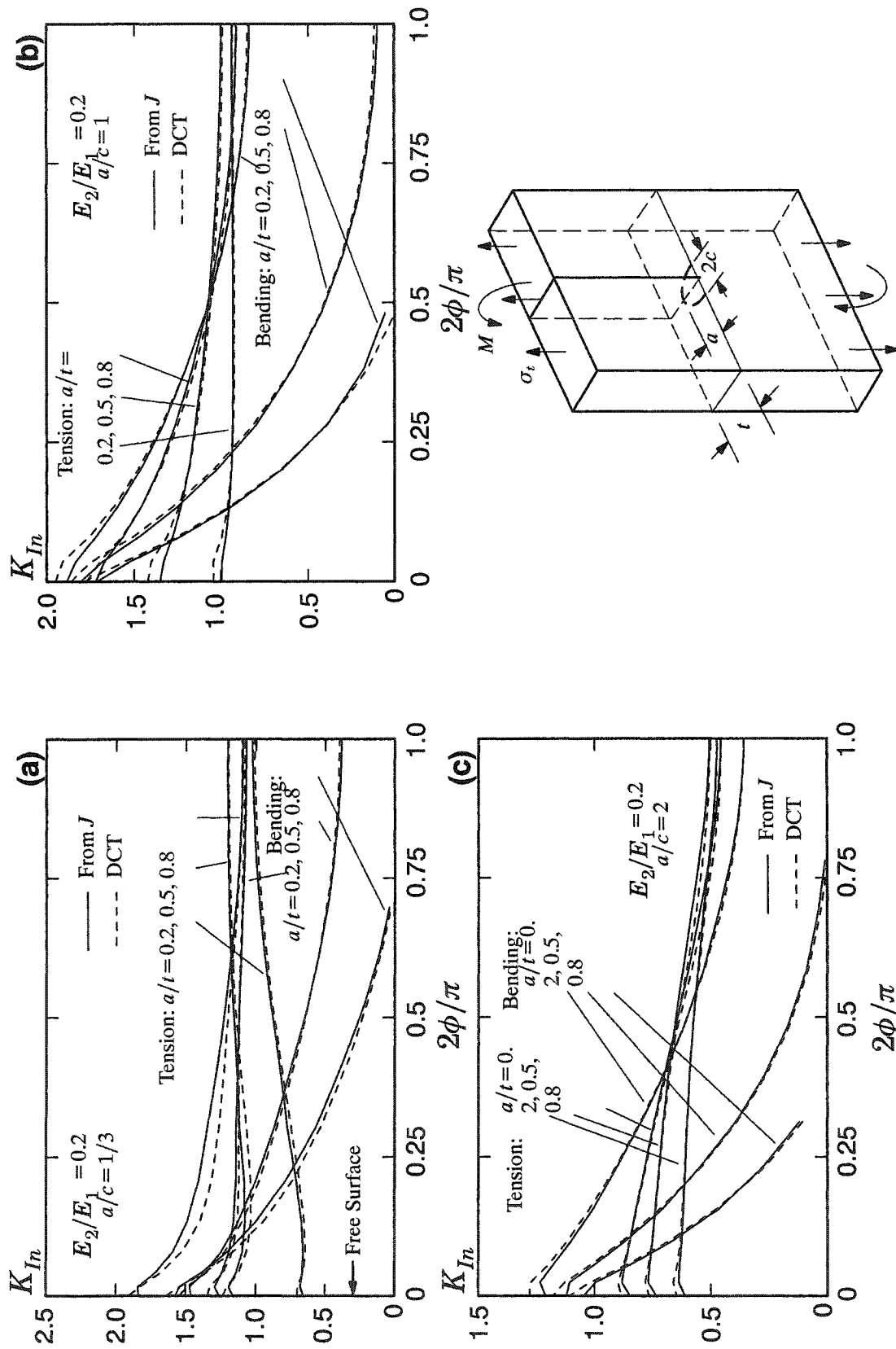


Fig. 2.15. (a) Comparison of normalized K_I values from J , Eq. (36) and DCT, Eq. (46), for tension and bending with $E_2/E_1 = 0.2$, $\alpha/c = 1/3$ and $a/t = 0.2, 0.5, 0.8$ and $\alpha/c = 1/3$. (b) $\alpha/c = 1$ and (c) $\alpha/c = 2$.

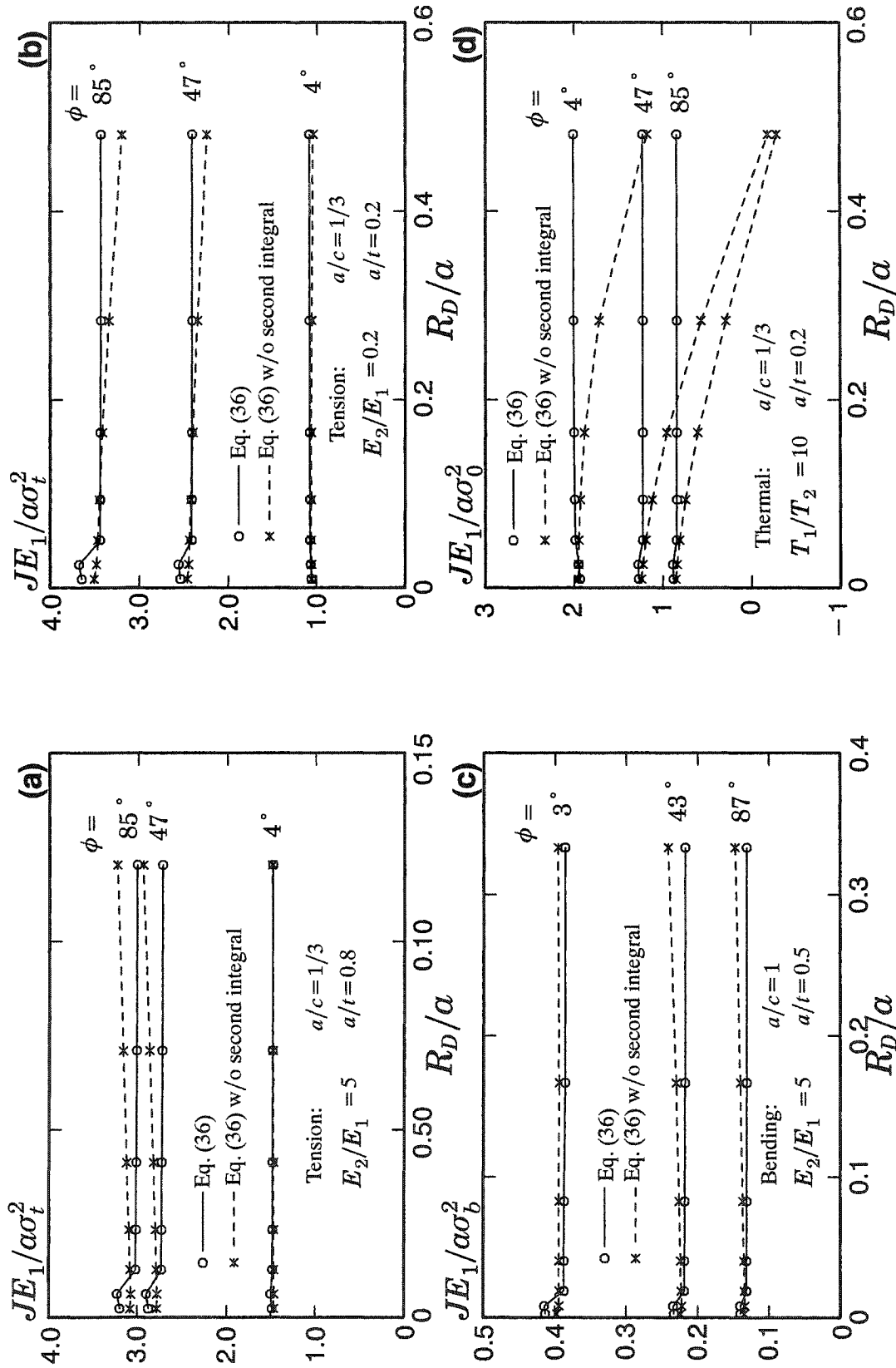


Fig. 2.16. Normalized J -values at three crack-front locations computed using Eq. (36) with and without the second integral. (a) Tension loading for $E_2/E_1 = 5$. (b) Tension loading for $E_2/E_1 = 0.2$. (c) Bending load, for $E_2/E_1 = 5$. (d) Thermal loading ($\sigma_0 = E_1 \alpha_1 T_0 / (1 - \nu)$) for $T_1/T_2 = 10$ (see Fig. 2.8). Table 2.4 lists material properties.

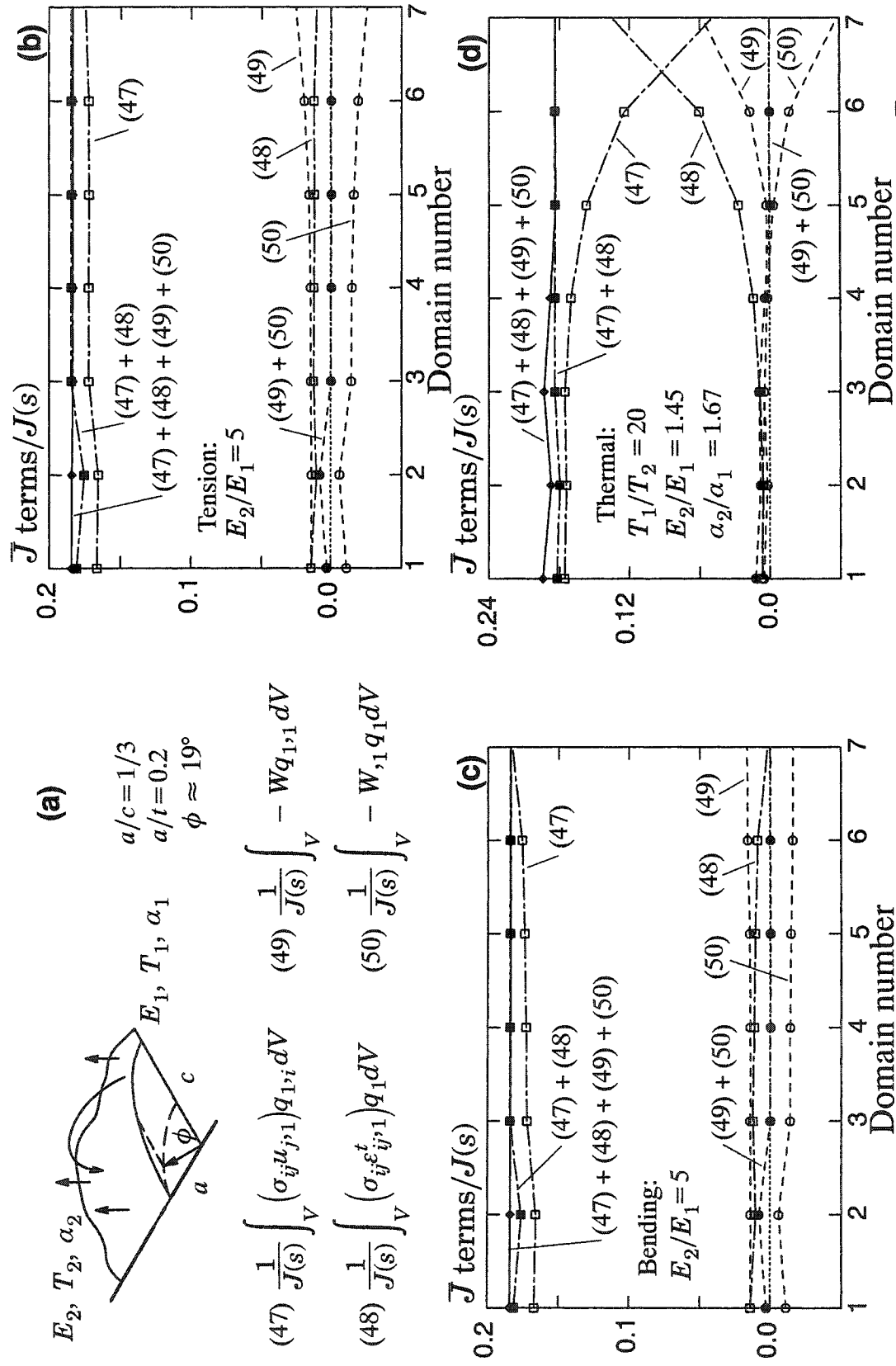


Fig. 2.17. (a) Crack geometry and loading where $a/t = 0.2$, and $a/c = 1/3$, and individual terms of \bar{J} , normalized by $J(s)$. (b) Normalized terms of \bar{J} for specimen under tension loading where $E_2/E_1 = 5$; (c) bending load where $E_2/E_1 = 5$; and (d) thermal loading where $T_1/T_2 = 20$, $E_2/E_1 = 1.45$, and $\alpha_2/\alpha_1 = 20$ (see Fig. 2.8).

2.8 Stress intensity factors for surface cracks in FGM plates

2.8.1 Tension loading

Figures 2.18-2.21 show K_{In} -values for a selected range of specimen and crack geometries, all loaded by remote tension. Because the plane-stress assumption applies to the J - K_{In} conversion at the free surface, and the plane-strain assumption applies at interior points [see Eq. (40) and Section 2.7.3], each of the curves exhibits a small kink between values of K_{In} at $\phi = 0$ and the first interior point. To simplify discussions here, the term “soft” applies to specimens with a material variation of $E_2/E_1 = 0.2$, and “stiff” applies to specimens with a variation of $E_2/E_1 = 5.0$.

Figure 2.18(a) shows that for $a/c = 1/3$ and $a/t = 0.2$, K_{In} -values at all points along the crack front are greater in the homogeneous material than in the soft material, and greater in the soft material than in the stiff material. To explain this perhaps unexpected result, Fig. 2.18(b) shows the corresponding energy release rates (J -values). The energy release rate along the deeper portion of the crack is higher in the soft material than in the homogeneous material, as expected. In this figure, the values of J for $E_2/E_1 = 5.0$ clearly show that as Young’s modulus increases along the crack front, the energy release rate decreases with respect to the homogeneous material. As the modulus decreases along the crack front, the energy release rate increases with respect to the homogeneous material, as demonstrated by the J -values for $E_2/E_1 = 0.2$. Because of the proximity of the J -curves for the soft and homogeneous materials, the values of $E(s)$ used to convert J into K_{In} drive the stress intensity factors of the soft material below the stress intensity factors of the homogeneous material.

For each ratio of a/c , an increase in crack depth in the soft material causes the magnitude of K_{In} near the cracked surface to increase relative to the value of K_{In} at the deepest point along the crack. For all ratios of a/c , an increase in crack depth in the stiff material causes the magnitude of K_{In} to increase overall, but causes K_{In} near the cracked surface to decrease relative to the value of K_{In} at the deepest point along the crack. In all materials, for a constant ratio of a/t , a decrease in a/c causes the value of K_{In} near the cracked surface to increase relative to the value of K_{In} at the deepest point in the crack.

In all geometries of nonhomogeneous material examined here, Young’s modulus, $E(s)$, varies along the curved crack front. Because $E(s)$ influences the conversion from J to K_I (see Eq. (40)), the crack-front location, ϕ , of maximum J does not necessarily correspond to the location of maximum K_I . The curves in Fig. 2.22(a) show trends in the variation of J , K_{In} and E along the front of a surface crack under remote tension loading with $a/c = 2$, $a/t = 0.8$ and $E_2/E_1 = 5$. Here $J_n(\phi) = J(\phi)E_1/(\sigma_i^2\pi a/Q)$ defines a normalized value of J along the crack front, and $E_n(\phi) = E(\phi)/E_1$ defines a normalized value of Young’s modulus. In this figure, the maximum J -value occurs near $2\phi/\pi \approx 0.5$, while

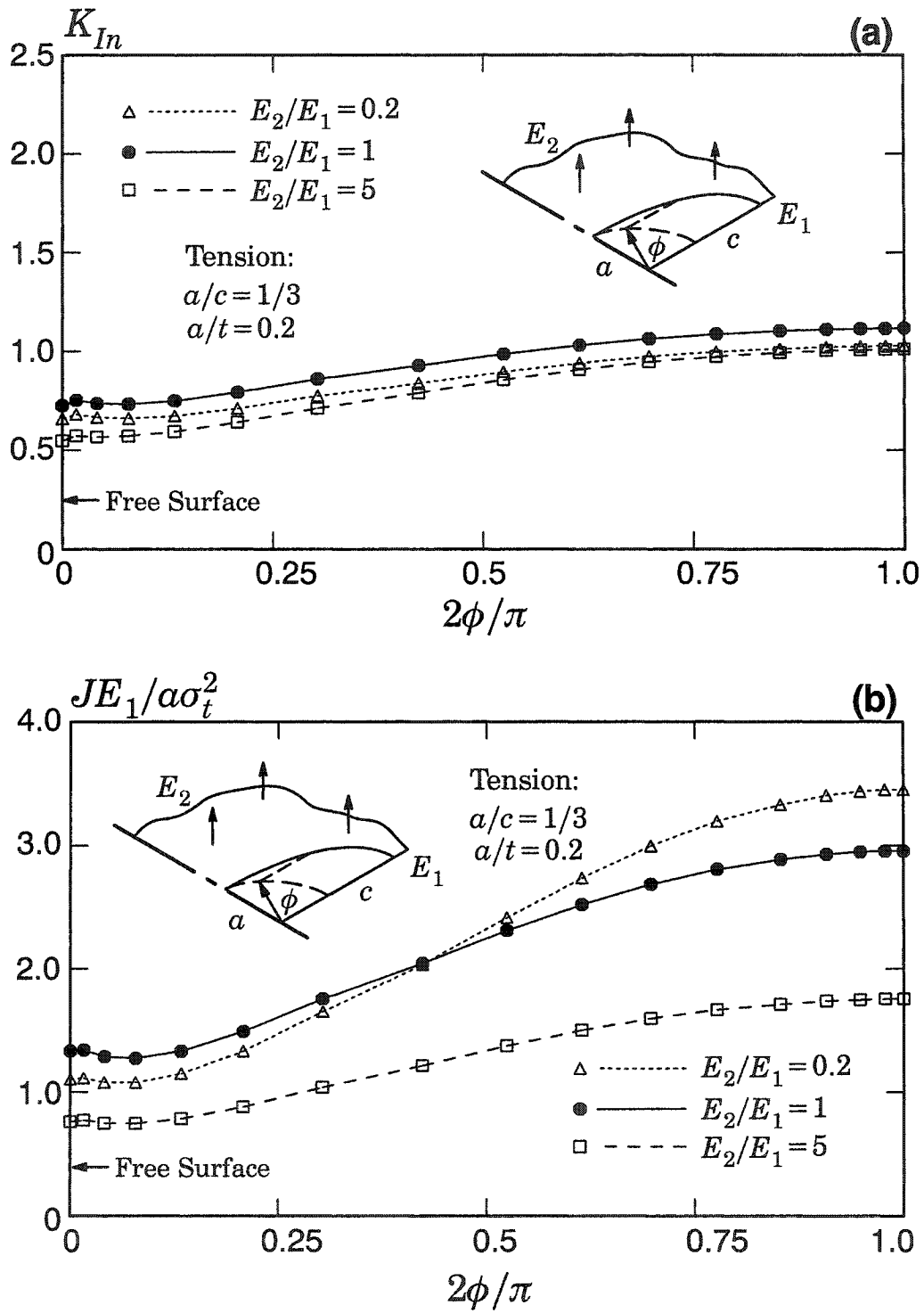


Fig. 2.18. (a) Normalized K_I -values along a crack front under remote tension loading for a crack with $a/c = 1/3$ and $a/t = 0.2$. (b) Normalized values of J along the crack front corresponding to the K_{In} -values in (a).

the maximum K_{In} occurs near the free surface. Figure 2.22(b) shows trends in J , K_{In}

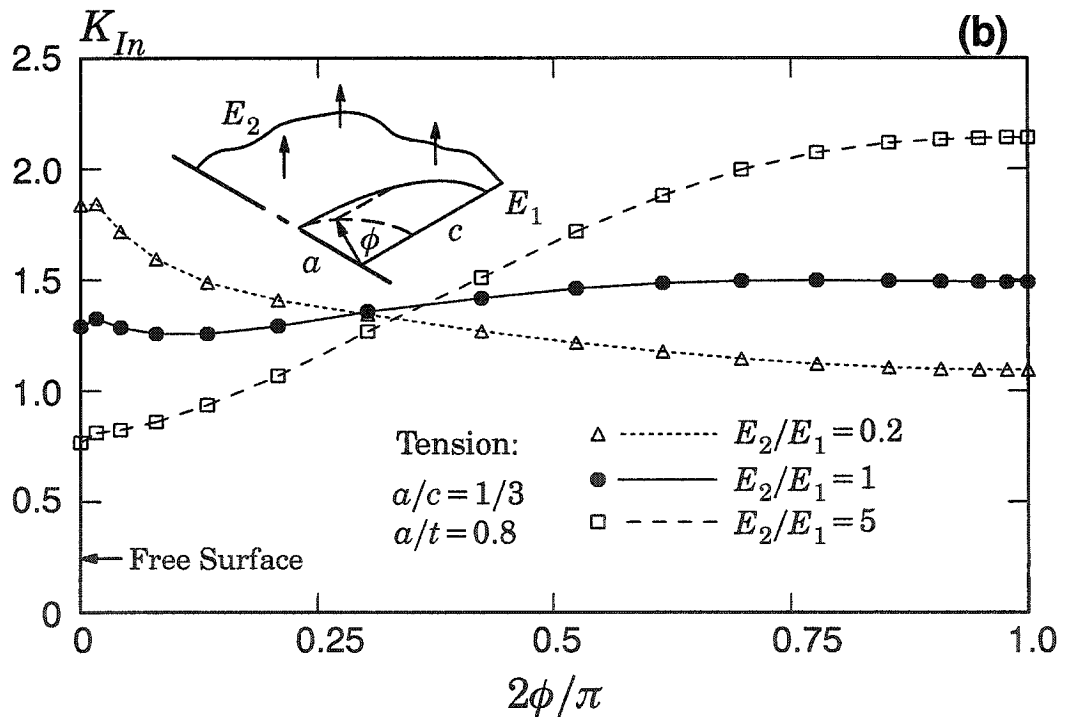
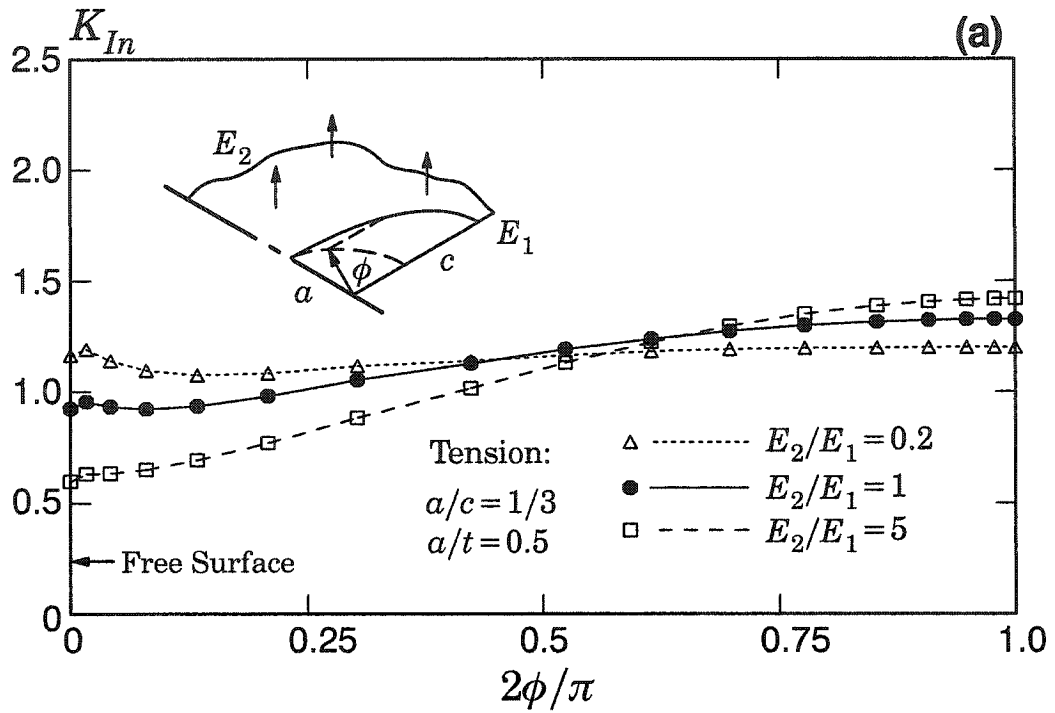


Fig. 2.19. Normalized K_I -values along a crack front under remote tension loading for a crack with $a/c = 1/3$ and (a) $a/t = 0.5$, and (b) $a/t = 0.8$.

and E for an identical crack in a homogeneous material. In this case, the crack-front locations of maximum/minimum J correspond to locations of maximum-minimum K_I .

To tabulate these normalized stress intensity factors, cubic-spline interpolation provides estimates of K_{In} at equally spaced (ϕ) crack-front locations in the range $0 \leq \phi \leq \pi/2$. Table 2.5 lists normalized K_I -values for the selected surface crack/material combinations under remote tension loading. Because the calculation of J occurs at a larger number of crack-front locations than the tabulated data reflects, the tables do not necessarily capture the exact maximum-minimum values of K_{In} . For example, Fig. 2.21(c) shows a maximum value of $K_{In} = 0.857$ at $\phi = 0.024$ for $E_2/E_1 = 1$, whereas Table 2.5 lists a maximum value of $K_{In} = 0.823$ at $\phi = 0.0$.

Table 2.5. Normalized stress intensity factors, K_{In} , along the crack front for specimens loaded in tension.

		Tension								
a/c	$2\phi/\pi$	$a/t=0.2$			$a/t=0.5$			$a/t=0.8$		
		E_2/E_1			E_2/E_1			E_2/E_1		
		0.2	1.0	5.0	0.2	1.0	5.0	0.2	1.0	5.0
1/3	0.000	0.660	0.725	0.548	1.164	0.925	0.598	1.838	1.289	0.767
	0.125	0.669	0.744	0.589	1.076	0.932	0.685	1.502	1.255	0.922
	0.250	0.739	0.822	0.673	1.098	1.013	0.819	1.378	1.321	1.155
	0.375	0.813	0.901	0.760	1.131	1.100	0.964	1.298	1.395	1.413
	0.500	0.882	0.972	0.840	1.158	1.176	1.104	1.228	1.452	1.670
	0.625	0.944	1.035	0.912	1.183	1.243	1.233	1.172	1.487	1.896
	0.750	0.990	1.080	0.966	1.195	1.291	1.334	1.128	1.498	2.052
	0.875	1.016	1.106	0.997	1.199	1.319	1.396	1.102	1.495	2.126
	1.000	1.027	1.117	1.011	1.200	1.327	1.420	1.094	1.490	2.141
1	0.000	0.997	1.140	0.917	1.351	1.240	0.907	1.720	1.421	0.988
	0.125	0.957	1.122	0.919	1.238	1.209	0.965	1.475	1.361	1.109
	0.250	0.936	1.082	0.923	1.161	1.155	1.019	1.297	1.275	1.217
	0.375	0.930	1.061	0.936	1.109	1.124	1.075	1.171	1.220	1.320
	0.500	0.931	1.046	0.950	1.071	1.101	1.125	1.073	1.176	1.400
	0.625	0.933	1.038	0.963	1.041	1.087	1.166	1.001	1.145	1.451
	0.750	0.935	1.034	0.974	1.019	1.078	1.197	0.951	1.123	1.475
	0.875	0.936	1.029	0.979	1.004	1.070	1.212	0.922	1.105	1.470
	1.000	0.938	1.027	0.981	0.997	1.067	1.213	0.912	1.100	1.465
2	0.000	0.612	0.763	0.615	0.736	0.782	0.596	0.849	0.823	0.602
	0.125	0.623	0.755	0.636	0.746	0.774	0.656	0.836	0.806	0.698
	0.250	0.608	0.716	0.625	0.719	0.731	0.677	0.775	0.755	0.748
	0.375	0.595	0.677	0.610	0.690	0.689	0.685	0.712	0.707	0.774
	0.500	0.574	0.637	0.588	0.651	0.646	0.679	0.643	0.659	0.772
	0.625	0.547	0.595	0.561	0.606	0.603	0.659	0.577	0.612	0.746
	0.750	0.516	0.554	0.529	0.561	0.560	0.629	0.519	0.566	0.700
	0.875	0.486	0.516	0.499	0.522	0.521	0.595	0.475	0.525	0.648
	1.000	0.473	0.499	0.484	0.506	0.504	0.580	0.457	0.507	0.625

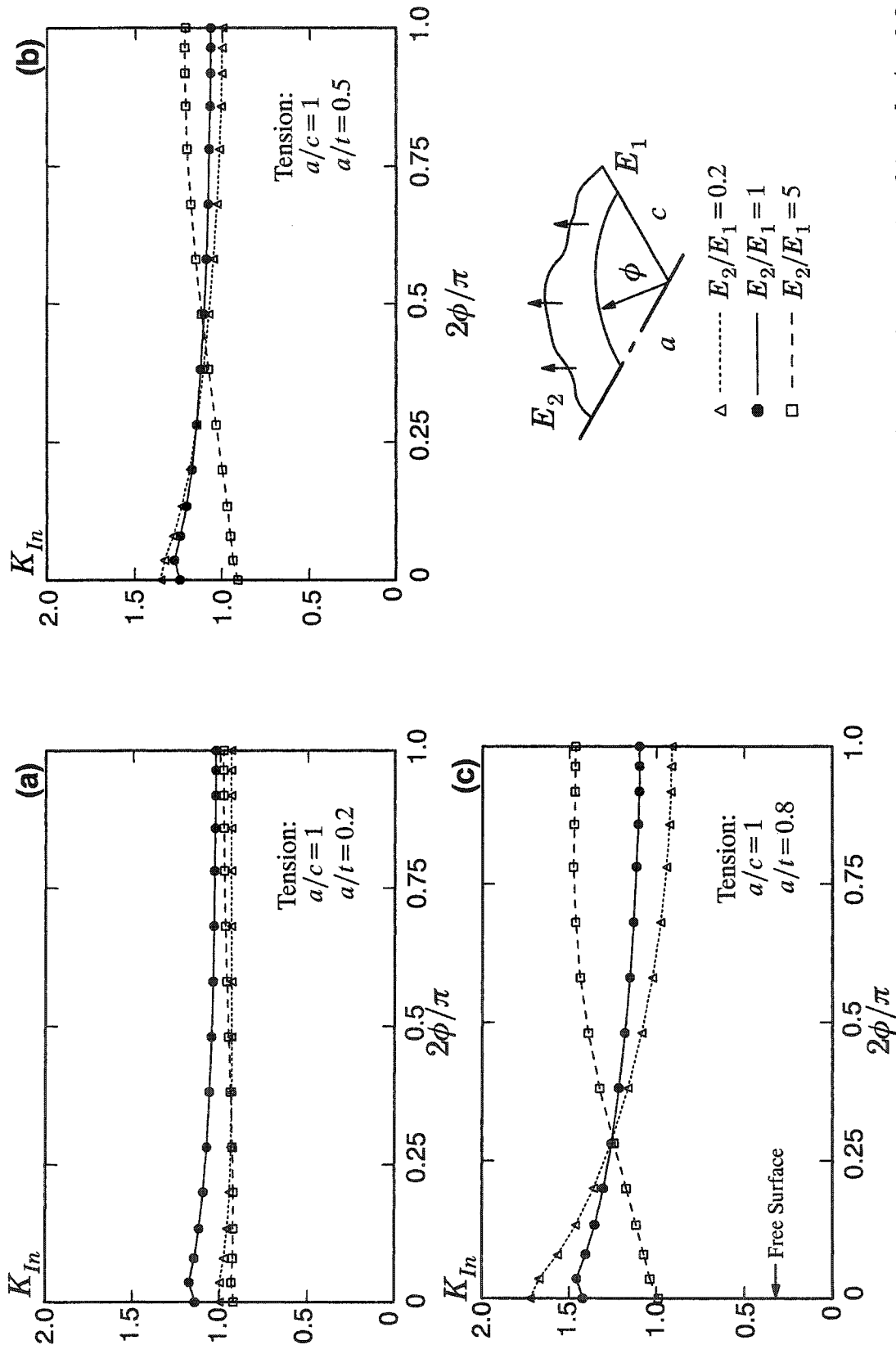


Fig. 2.20. (a) Normalized K_I -values along a crack front loaded in remote tension, with $a/c = 1$, $E_2/E_1 = 0.2, 5$ and 1 , and $a/t = 0.2$, (b) $a/t = 0.5$, and (c) $a/t = 0.8$.

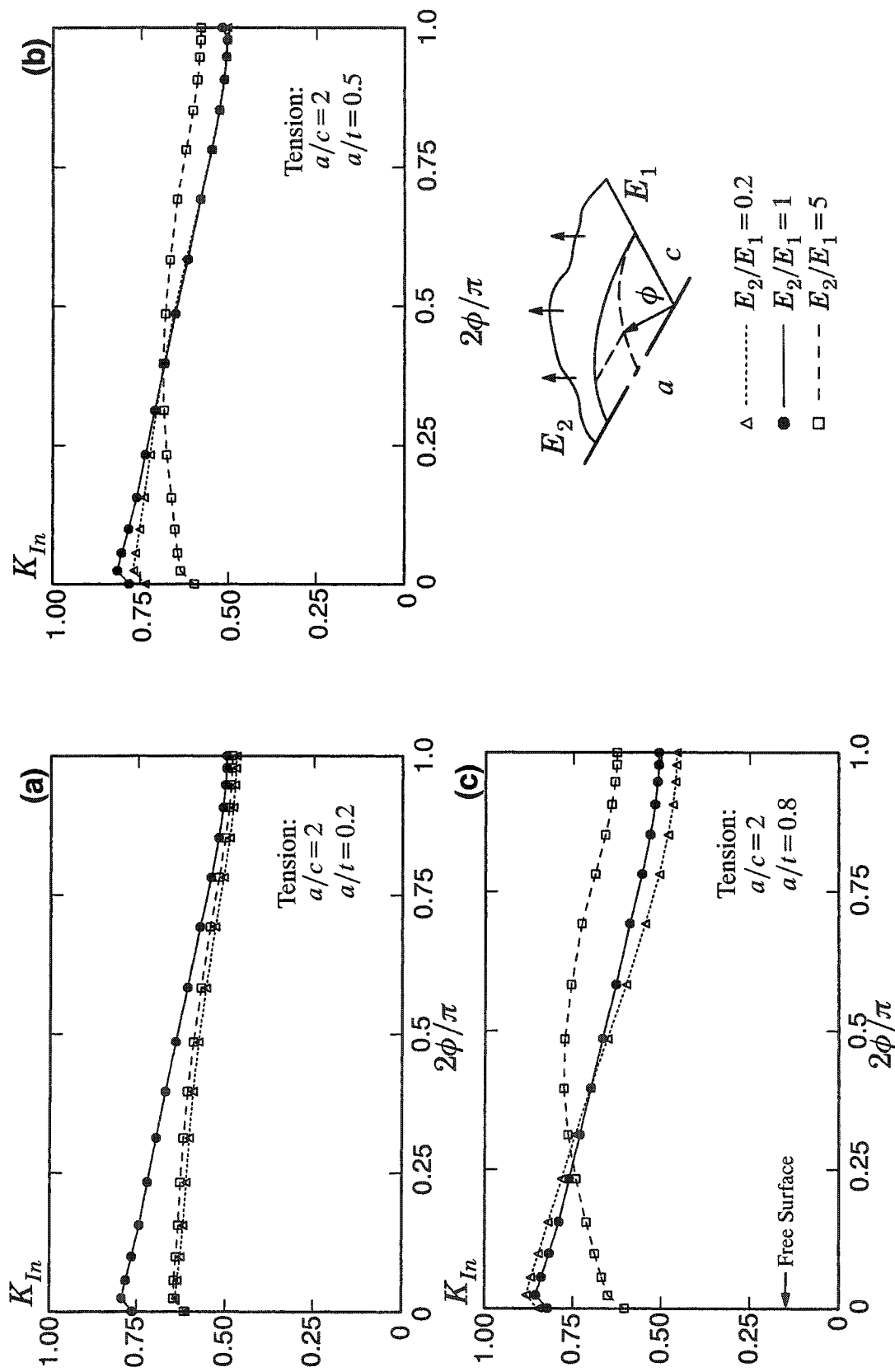


Fig. 2.21. (a) Normalized K_I -values along a crack front loaded in remote tension, with $a/c=2$, $E_2/E_1=0.2, 5$ and 1 , and $a/t=0.2$, (b) $a/t=0.5$, and (c) $a/t=0.8$.

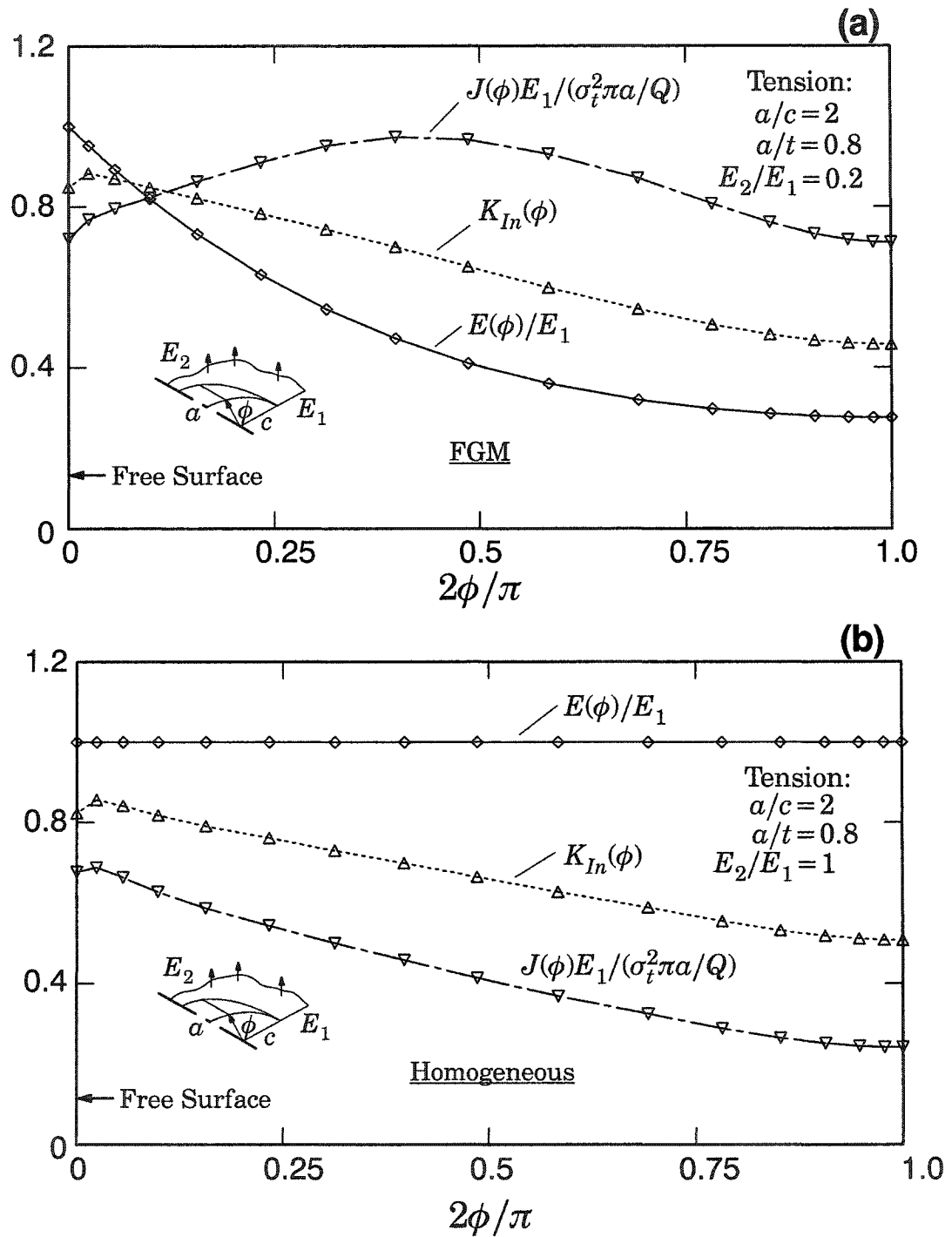


Fig. 2.22. Comparison of trends in J , K_{In} and E along a crack front under tensile loading for the geometry $\alpha/c = 2$ and $\alpha/t = 0.8$, in material where (a) $E_2/E_1 = 0.2$ and (b) $E_2/E_1 = 1$. In FGMs, the location, ϕ , of maximum J along the curved crack front does not necessarily correspond to the location of maximum K_{In} .

2.8.2 Bending loading

Figures 2.23-2.25 show K_{In} -values for selected crack geometries under remote through-bending load. For some crack geometries, bending causes crack-face nodes to penetrate the crack plane, thereby producing negative stress intensity factors. Figures and tables for specimens under bending omit the unrealistic negative values.

Figures 2.23-2.25 show that an increase in crack depth causes stress intensity factors at the deepest part of the crack to decrease, which reflects the decreased stress from bending. As expected, the decrease in K_{In} is most pronounced in the soft material, and smallest in the stiff material. For crack geometry $a/c = 1/3$ (Fig. 2.23), the stress intensity factor near the cracked surface increases slightly as crack depth increases. The increase is largest in the soft material, and smallest in the stiff material. When $a/c = 1$ (Fig. 2.24) and $a/c = 2$ (Fig. 2.25), the stress intensity factor near the cracked surface decreases slightly with crack depth. The decrease is again largest in the soft material, and smallest in the stiff material.

In Figs. 2.23-2.25, for a constant value of a/t , the variation in stress intensity factor near the cracked surface is not monotonic with increasing a/c , whereas K_{In} at the deepest point of the crack decreases monotonically with increasing a/c . Near the cracked surface, the stress intensity increases when the crack geometry changes from $a/c = 1/3$ to 1 (from Fig. 2.23 to Fig. 2.24), but decreases when the geometry changes from $a/c = 1$ to 2 (from Fig. 2.24 to Fig. 2.25). At the deepest point of the crack, the value of K_{In} decreases for each increase in crack depth, i.e. from $a/c = 1/3$ to 1 to 2 (Figs. 2.23-2.25). When $a/c = 1/3$ and $a/t = 0.8$ (Fig. 2.23(c)), the stress intensity factor reaches its maximum value at a point along the crack front between the cracked surface and the deepest point on the crack front.

Table 2.6 lists normalized K_I -values for the selected surface crack/material combinations under bending load. Dashes in the table replace otherwise negative stress intensity factors. Cubic-spline interpolation again yields estimates of K_{In} at evenly-spaced (ϕ) crack-front locations in the range $0 \leq \phi \leq \pi/2$.

Table 2.6. Normalized stress intensity factors, K_{In} , along the crack front for bending loads. Dashes replace negative stress intensity factors caused by interpenetration of crack faces.

		Bending								
a/c	$2\phi/\pi$	$a/t=0.2$			$a/t=0.5$			$a/t=0.8$		
		E_2/E_1			E_2/E_1			E_2/E_1		
		0.2	1.0	5.0	0.2	1.0	5.0	0.2	1.0	5.0
1/3	0.000	1.261	0.684	0.364	1.461	0.758	0.377	1.572	0.856	0.433
	0.125	1.160	0.680	0.387	1.141	0.710	0.417	1.028	0.752	0.494
	0.250	1.141	0.721	0.434	0.939	0.699	0.476	0.682	0.676	0.570
	0.375	1.136	0.762	0.482	0.787	0.687	0.533	0.442	0.597	0.635
	0.500	1.121	0.793	0.525	0.651	0.661	0.579	0.250	0.494	0.667
	0.625	1.104	0.816	0.562	0.537	0.629	0.612	0.098	0.375	0.656
	0.750	1.086	0.830	0.588	0.453	0.597	0.632	—	0.263	0.605
	0.875	1.073	0.837	0.603	0.403	0.576	0.641	—	0.181	0.546
	1.000	1.068	0.838	0.608	0.384	0.565	0.643	—	0.143	0.510
1	0.000	1.884	1.067	0.607	1.805	1.025	0.570	1.712	1.001	0.568
	0.125	1.614	1.012	0.599	1.286	0.908	0.582	0.984	0.815	0.594
	0.250	1.380	0.934	0.591	0.878	0.762	0.581	0.480	0.592	0.581
	0.375	1.210	0.876	0.589	0.603	0.643	0.576	0.187	0.405	0.543
	0.500	1.070	0.827	0.587	0.398	0.535	0.560	0.054	0.232	0.465
	0.625	0.968	0.788	0.586	0.259	0.447	0.539	—	0.087	0.359
	0.750	0.899	0.762	0.585	0.171	0.385	0.520	—	—	0.251
	0.875	0.853	0.743	0.583	0.117	0.341	0.502	—	—	0.155
	1.000	0.838	0.735	0.582	0.098	0.324	0.494	—	—	0.113
2	0.000	1.211	0.723	0.409	1.121	0.675	0.380	1.047	0.637	0.362
	0.125	1.057	0.683	0.415	0.792	0.587	0.397	0.569	0.496	0.381
	0.250	0.881	0.615	0.400	0.511	0.474	0.384	0.240	0.334	0.354
	0.375	0.727	0.548	0.381	0.298	0.364	0.357	0.049	0.180	0.293
	0.500	0.601	0.487	0.359	0.156	0.270	0.321	—	0.060	0.206
	0.625	0.504	0.434	0.336	0.068	0.198	0.283	—	—	0.115
	0.750	0.430	0.389	0.312	0.015	0.145	0.247	—	—	0.030
	0.875	0.378	0.352	0.291	—	0.109	0.217	—	—	—
	1.000	0.358	0.337	0.281	—	0.097	0.205	—	—	—

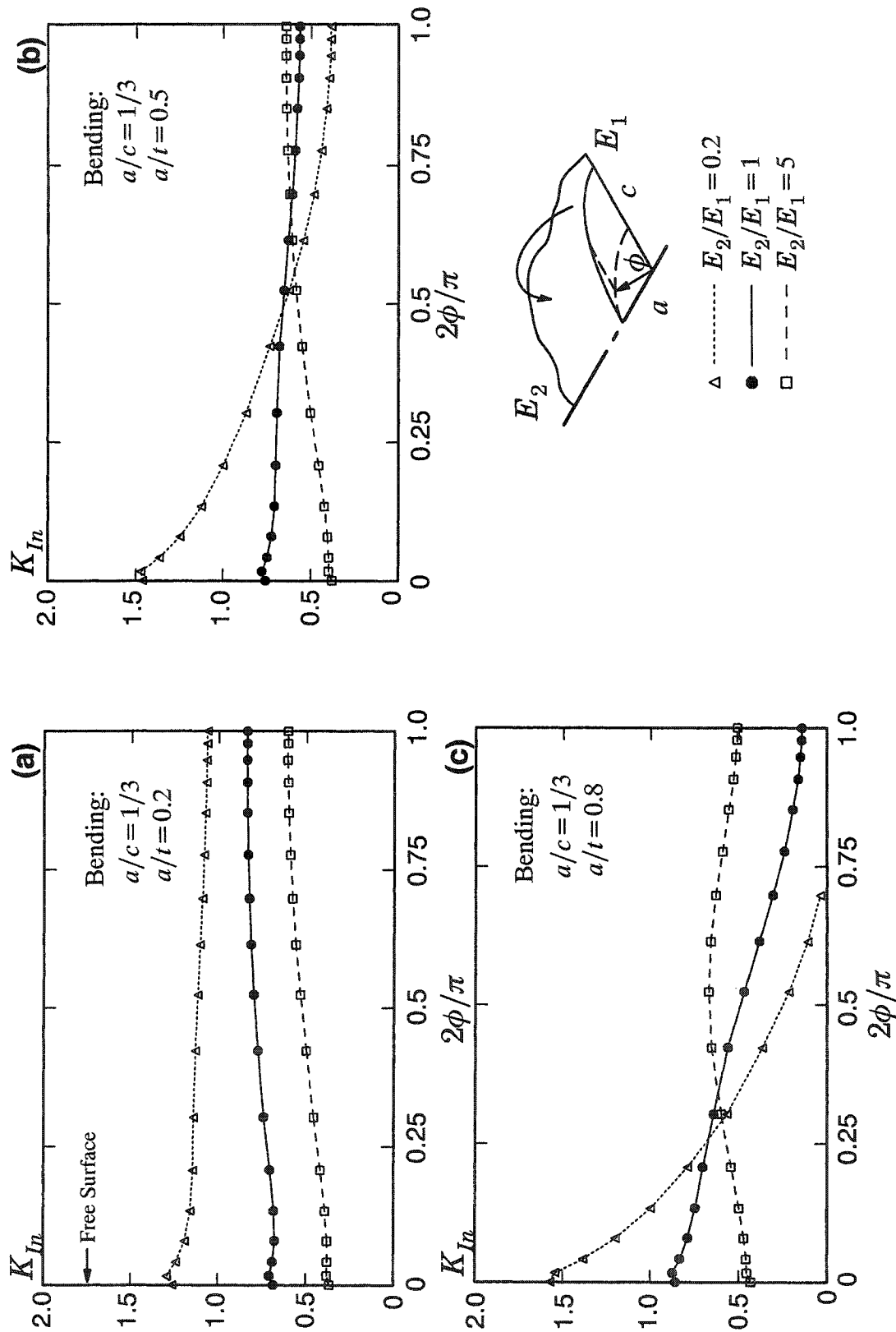


Fig. 2.23. (a) Normalized K_I -values along a crack front loaded in remote bending, with $a/c = 1/3$, $E_2/E_1 = 0.2, 5$ and 1 , and $a/t = 0.2$, (b) $a/t = 0.5$, and (c) $a/t = 0.8$.

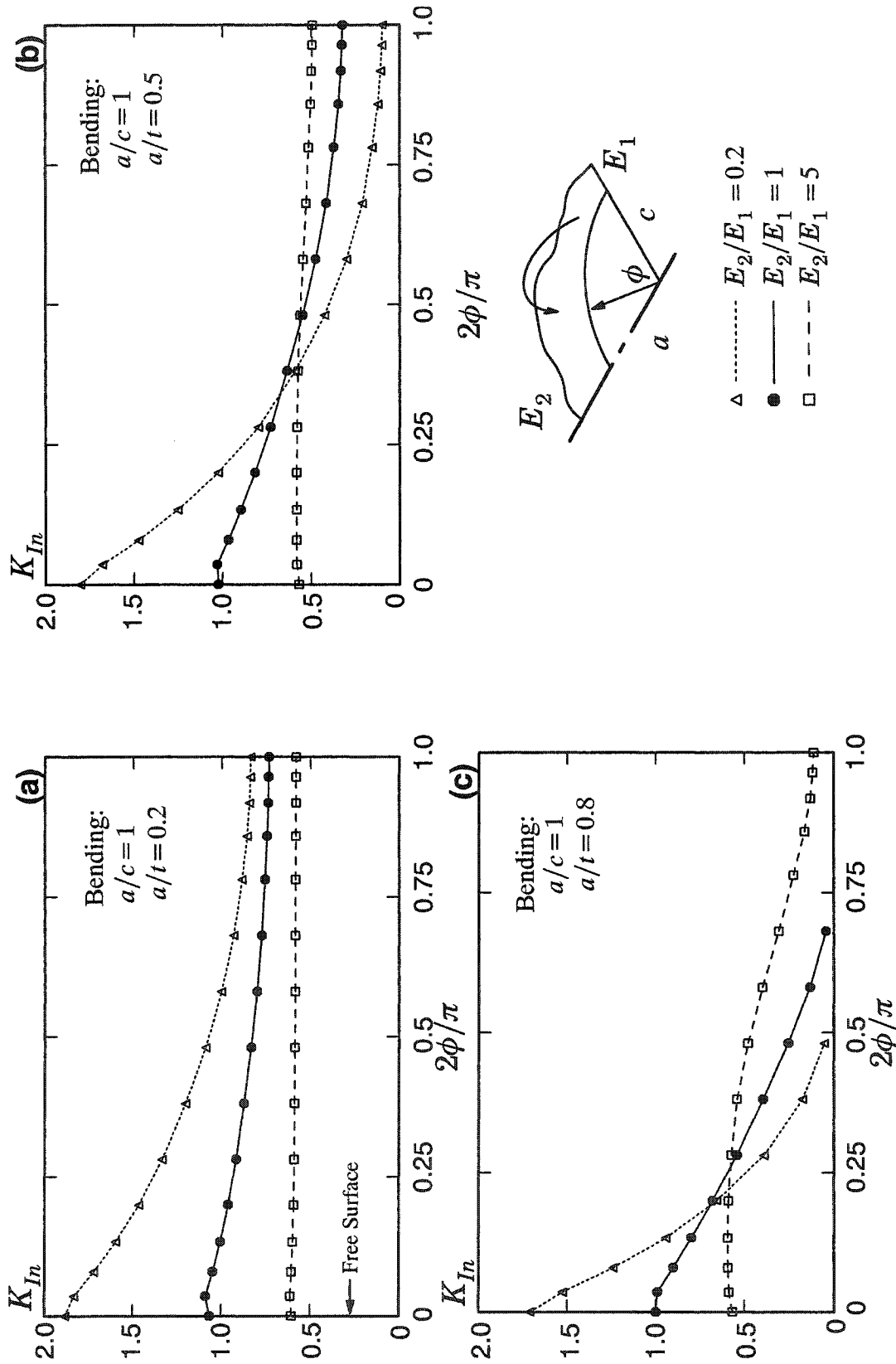


Fig. 2.24. (a) Normalized K_I -values along a crack front loaded in remote bending, with $a/c=1$, $E_2/E_1=0.2, 5$ and 1 , and $a/t=0$ (b) $a/t=0.5$, and (c) $a/t=0.8$.

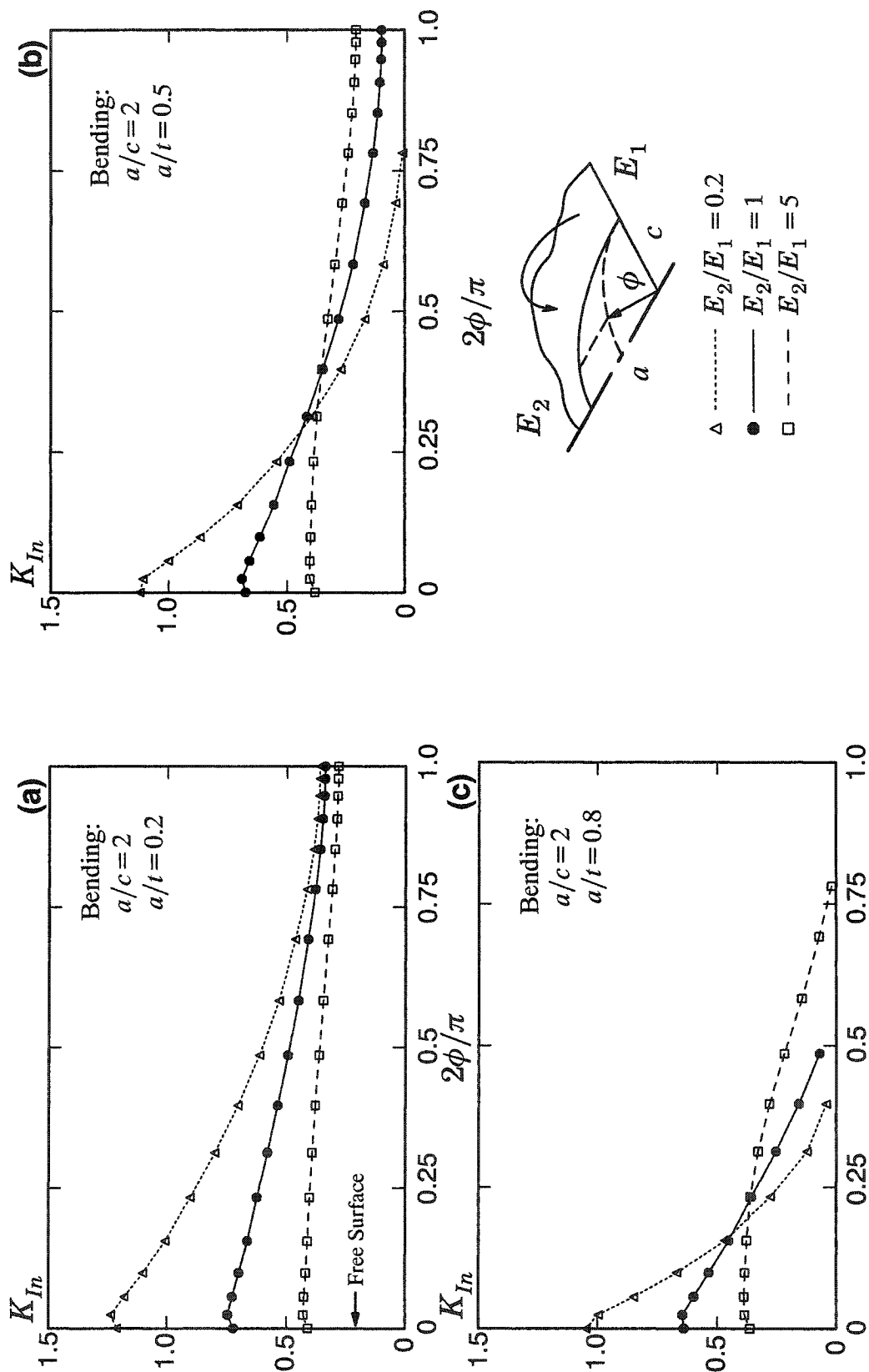


Fig. 2.25. (a) Normalized K_I -values along a crack front under remote bending, with $a/c=2$, $E_2/E_1=0.2$, 5 and 1, and $a/t=0.2$, (b) $a/t=0.5$, and (c) $a/t=0.8$.

2.8.3 Thermal loading

The material properties and thermal boundary conditions for analyses performed here follow those used by Erdogan and Wu [60] as described in Section 2.2. At crack-front locations interior to the specimen, Eqs. (40) and (42) here produce normalized K_I -values using the plane-strain conversion. We omit stress intensity factors at the free surface ($\phi = 0$) (see discussion in Section 2.7.3).

Figures 2.26(a)-(c) show normalized stress intensity factors, K_{In} , for surface cracks under thermal loading, where the crack geometry includes three ratios of a/c , and a fixed crack depth of $a/t = 0.2$. Table 2.4 lists the material properties, and Fig. 2.8 illustrates the thermal gradient where the temperature at the cracked surface, T_1 , equals 5, 10 and 20 times the temperature at the uncracked face, T_2 . As the ratio of crack depth to crack length, a/c , becomes larger, the variation in stress intensity factor drops more steeply from a maximum near $\phi = 0$ to a minimum at $2\phi/\pi = 1$. As a/c increases from 1/3 to 1 to 2, the magnitude of K_{In} at the deepest point of the crack, $2\phi/\pi = 1$, decreases monotonically. The value of K_{In} near the cracked surface increases as a/c grows from 1/3 to 1, and then decreases as a/c grows from 1 to 2. Table 2.7 lists normalized K_I -values for the selected surface crack/material combinations under thermal loads.

Table 2.7. Normalized stress intensity factors, K_{In} , along the crack front for thermal loading. Table 2.4 lists material properties, and Fig. 2.8 shows a schematic of the temperature distribution. Dashes replace stress intensity factors in the boundary layer (see Section 2.7.3).

		Thermal Loading								
a/t	$2\phi/\pi$	$a/c = 1/3$			$a/c = 1$			$a/c = 2$		
		T_1/T_2			T_1/T_2			T_1/T_2		
		5	10	20	5	10	20	5	10	20
	0.000	—	—	—	—	—	—	—	—	—
	0.125	0.393	0.884	1.866	0.582	1.309	2.765	0.395	0.888	1.874
	0.250	0.377	0.847	1.789	0.476	1.072	2.264	0.310	0.698	1.473
	0.375	0.362	0.814	1.719	0.394	0.888	1.874	0.231	0.520	1.097
0.2	0.500	0.341	0.767	1.619	0.324	0.730	1.541	0.168	0.377	0.796
	0.625	0.318	0.716	1.513	0.270	0.609	1.286	0.122	0.274	0.577
	0.750	0.299	0.673	1.420	0.234	0.526	1.111	0.089	0.201	0.424
	0.875	0.287	0.645	1.361	0.210	0.472	0.997	0.068	0.154	0.325
	1.000	0.281	0.633	1.336	0.201	0.453	0.957	0.062	0.139	0.292

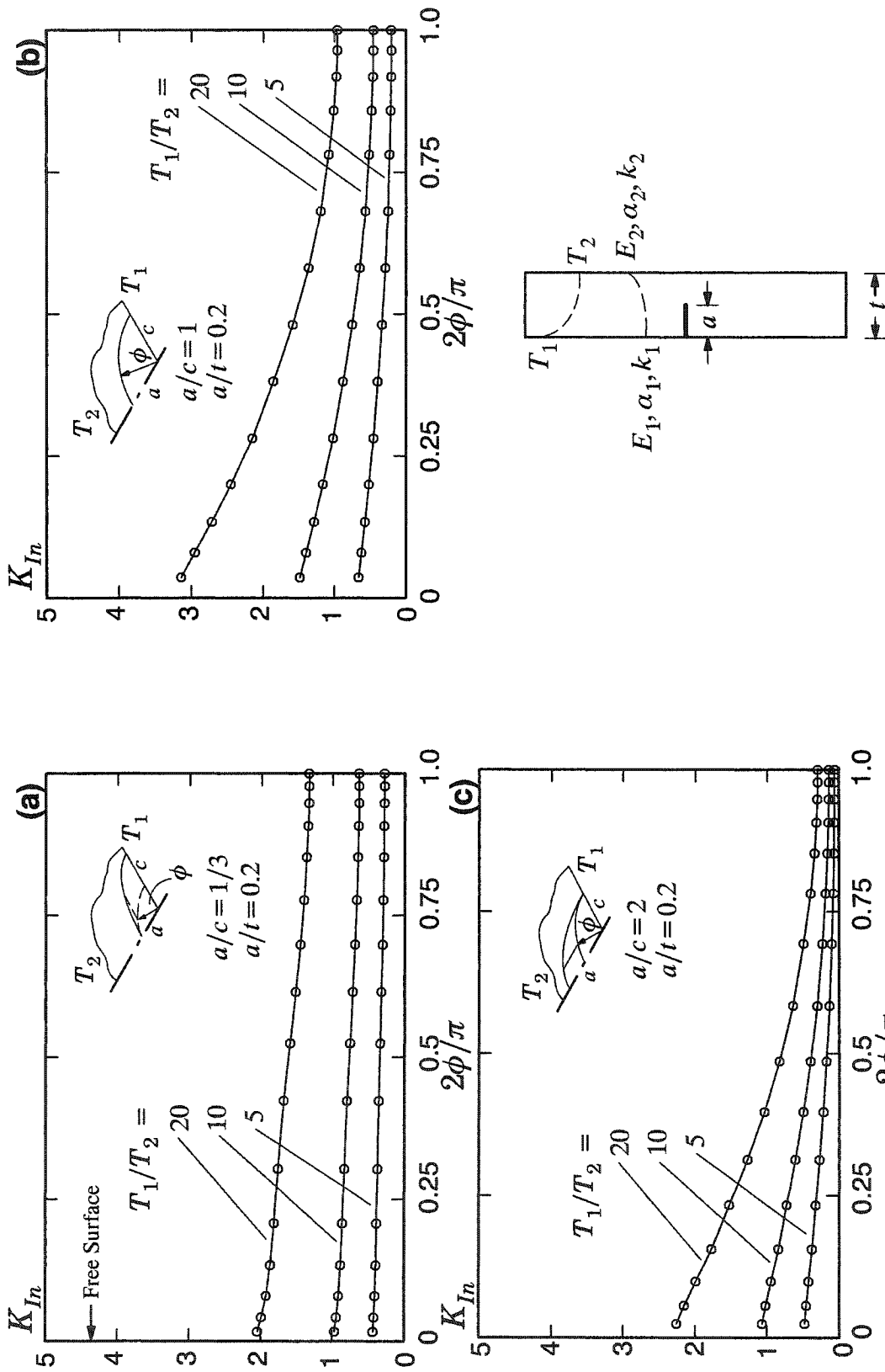


Fig. 2.26. Normalized K_I -values for a specimen under thermal loading with $\alpha/t=0.2$, $T_1/T_2=5, 10$ and 20 , and (a) $\alpha/c=1/3$, (b) $\alpha/c=1$, and (c) $\alpha/c=2$. Material properties are listed in Table 2.4.

2.9 Summary and Conclusions

This chapter describes a domain integral formulation suitable to compute J -integral values along 3-D crack fronts in fracture specimens and components constructed of isotropic, functionally graded materials (FGMs). Within a finite element setting, material property values are specified at the model nodes with standard isoparametric interpolations to define integration point values. This approach coupled with the proposed domain integral thus accommodates effectively arbitrary, smooth gradations of material properties. The proposed numerical procedures to evaluate the domain integral use conventional quantities generated in a finite element solution and may thus be implemented in a post-processor. The present study explores the numerical implementation with applications to mode-I configurations in 2-D and 3-D having linear-elastic response and subjected to thermomechanical loading. For simple 2-D configurations, the available analytical solutions for an edge crack loaded remotely by tension and by temperature gradients support verification of stress intensity factors derived from J -values computed with the proposed domain integral. In 3-D surface crack configurations, the displacement correlation technique yields pointwise values of stress intensity factors along crack fronts for verification of corresponding factors computed with the domain integral procedure. The discussions also address mesh refinement levels required to resolve the solution gradients ahead of the crack front in FGMs, to obtain path independence of the J -values, and to evaluate various contributions of the domain integral. These results demonstrate the utility and accuracy of using the proposed domain integral to compute 2-D and 3-D stress intensity factors for FGMs.

A parametric study provides stress intensity factors along crack fronts derived using the proposed domain integral for plates containing semi-elliptical surface cracks. This initial set of 3-D stress intensity factors covers a practical range of crack sizes, aspect ratios and gradations of isotropic material properties (elastic modulus and coefficient of thermal expansion). Loadings considered include remote tension, bending and through-thickness temperature gradients. All configurations reflect mode-I conditions (geometry, boundary conditions and loadings) with material properties that vary only in the thickness direction. The computed stress intensity factors are presented in a standard non-dimensional form for surface cracks using both graphical and tabular formats. The presence of the material property gradations introduces some unusual trends in K_I -values along the crack fronts (compared to those for surface cracks in homogenous materials as characterized by the Newman-Raju solutions). Moreover, unlike configurations with homogenous material properties, the locations of maximum J and maximum K_I do not necessarily coincide in the presence of material property gradations. The present set of 3-D solutions, while not exhaustive, does provide insights into the expected complexities of surface crack behavior in FGMs.

Our ongoing work considers applications of the proposed domain integral to compute J -values in surface cracks for metal-ceramic FGMs that undergo elastic-plastic deformations. The preliminary results again show good path independence of the J -values. Such J -values may prove useful to characterize the intensity of elastic-plastic crack-front fields in FGM specimens.

Chapter 3

Interaction-Integral Procedures for Curved Cracks With Surface Traction

3.1 Introduction

The determination of accurate stress-intensity factors for mixed-mode loading in complex, 3-D configurations remains a significant challenge in computational fracture mechanics. Defect assessments of industrial structures require reliable estimates of stress-intensity factors—especially for fatigue life predictions that adopt a damage tolerance philosophy. Finite element models of complex components must have sufficient refinement to resolve strong gradients in the near-tip fields along curved crack fronts and must be coupled with robust numerical methods to extract the mixed-mode stress-intensity factors from the solutions pointwise along the front. Interaction-integral methods have emerged as perhaps the most accurate and readily implementable approach to extract mixed-mode, stress-intensity factors. These methods post-process the computed displacements, strains and stresses from the finite element model that are taken to represent the correct equilibrium state for the specified boundary-value problem. Another selected equilibrium state supplies auxiliary near-tip fields defined in terms of the mixed-mode stress intensity factors. For this purpose, Williams' [221] solution for the 2-D asymptotic stress and displacement fields in the vicinity of a crack represents a widely-used auxiliary field. A linear combination of finite element fields (commonly termed the “actual” fields) with auxiliary fields constitutes a third, superimposed, equilibrium state. One class of interaction integrals arises from an interpretation of the J -integral [181]—the computation of J for the superimposed state leads to a conservation integral composed of interacting actual and auxiliary terms that permits direct computation of stress intensity factors [34]. Numerical evaluation of this interaction integral fits conveniently into existing domain-integral procedures for J -computation [192], thereby providing a readily implemented, robust and accurate tool for linear-elastic analyses.

Through post-processing of finite-element results, Yau et al. [226] evaluate an interaction integral to determine mixed-mode stress intensity factors for 2-D cracks in specimens under mechanical loading. Studies of interaction-integral procedures for 3-D cracks include analyses of plates under in-plane loading [145] and elastic-plastic interface cracks [190]. Dhondt [48] examines the variation in crack-front singularity along quarter-circular corner cracks. Krysl and Belytschko [125] employ the element free Gal-

erkin method to analyze the dynamic propagation of arbitrary 3-D cracks in homogeneous material. Most prior works provide interaction-integral solutions for cracks with traction-free faces in homogeneous or bi-material specimens under quasi-static, isothermal loading. Nakamura and Parks [146] discuss the formulation of an interaction integral for thermal and body-force loads, and Cho et al. [37] analyze 2-D interface cracks with surface tractions that interact with additional singularities caused by point forces or dislocations. Other interaction integrals follow from the application of Betti's reciprocal work theorem [203, 208], or the M - and L -integrals of Knowles and Sternberg [122, 88, 38]. Kim et al. [121] compute stress intensity factors along curved cracks in homogeneous 3-D solids using an interaction integral derived from the M -integral [122].

This study examines a J -integral based, interaction-integral procedure to compute mixed-mode stress intensity factors for curved, planar cracks in three-dimensional homogeneous solids under remote mechanical loading and/or applied crack-face tractions. For cracked, axisymmetric configurations and for curved 3-D cracks, the 2-D Williams' [221] solutions do not satisfy equilibrium or strain-displacement compatibility when expressed in curvilinear coordinates, thereby leading to additional terms in the interaction integral [142]. Nahta and Moran [142] include these curvature effects to study axisymmetric interface cracks. They suggest that inclusion of the curvature effects generally should improve the interaction-integral values for a particular level of mesh refinement. Gosz et al. [74] and Gosz and Moran [75] also include the effects of local crack-front curvature to analyze 3-D curved interface cracks and non-planar 3-D cracks, respectively. Krysl and Belytschko [125], however, omit curvature terms from interaction-integral computations in their analyses of curved, 3-D cracks. For straight and curved 3-D cracks in homogeneous materials, our present work investigates the accuracy of stress intensity factors obtained using the simplified interaction integral without curvature terms. We compare values from the simplified interaction integral with J -integral values and with analytical solutions using models that have reasonable levels of mesh refinement in the crack front region.

Shih et al. [192] describe a domain integral procedure to evaluate the J -integral along a 3-D crack front that incorporates a surface integral over traction-bearing crack faces (needed to maintain path independence). A crack-face integral also becomes necessary to preserve path independence of the interaction-integral method. Cho et al. [37] employ such an integral in their study of cracks with surface tractions in 2-D bodies. Gosz and Moran [75] integrate over crack surfaces to compute stress intensity factors for traction-free, non-planar cracks. The necessary surface integral, however, does not appear in some other interaction-integral treatments of traction-bearing cracks. This study examines the importance of the crack-face integral and presents a simple, exact integration procedure applicable for one class of 3-D finite elements.

The plan of this paper is as follows: Section 3.2 reviews the domain-integral technique that forms the basis of current numerical procedures. Section 3.3 discusses the interaction-integral procedure to compute mixed-mode stress intensity factors along curved 3-D cracks in homogeneous solids under quasi-static, mechanical loads including applied crack-face tractions. A description of numerical procedures follows in Section 3.4. Section 3.5 describes a 3-D analysis of a 2-D plane-strain problem that provides insight into the influence of the crack-face-traction integral and the improvement offered by its exact integration. Section 3.6 presents mixed-mode stress intensity factors computed using the interaction integral without curvature terms, and compares them to values obtained from analytical solutions. Some observations conclude the work in Section 3.8.

3.2 A domain integral for 3-D cracks with surface tractions

Shih et al. [192] develop the domain-integral method as a powerful numerical procedure to evaluate the J -integral for 3-D cracks. The domain-based, interaction-integral methods build upon this approach. An expression for the J -integral at location s along a 3-D crack front is [192]

$$J(s) = \lim_{\Gamma \rightarrow 0} \int_{\Gamma} (W\delta_{1i} - \sigma_{ij}u_{j,1})n_i d\Gamma, \quad (52)$$

where W is strain energy density, σ_{ij} represents stress components, u_j denotes displacement components, and δ_{ij} is the Kronecker delta. Latin subscripts range from 1 to 3, and unless noted otherwise, repeated indices imply summation. The partial derivative $(\cdot)_{,i} = \partial(\cdot)/\partial X_i$ indicates the spatial derivative of (\cdot) with respect to direction X_i of the local coordinate system defined at crack front position s as shown in Fig. 2.5. The contour, Γ , with normal-vector components n_i , lies in the X_1 - X_2 plane of the local coordinate system, and extends from the bottom crack face to the top crack face. When the contour shrinks to the crack front at s , Eq. (52) equals Rice's J -integral [181] and remains valid in the presence of general material behavior, body forces, crack-face tractions and thermal strains.

Shih et al. [192] transform Eq. (52) into volume and surface integrals suitable for numerical evaluation in a 3-D finite-element context. They derive an expression for $\bar{J}(s)$, the energy released per unit advance of crack-front segment L_C (see Fig. 2.5). This expression may be written as

$$\begin{aligned} \bar{J}(s) = & \int_V (\sigma_{ij}u_{j,1} - W\delta_{1i})q_{,i}dV + \int_V (\sigma_{ij}u_{j,1} - W\delta_{1i})_{,i}qdV \\ & - \int_{S^+ + S^-} t_j u_{j,1} q dS, \end{aligned} \quad (53)$$

where t_j are components of traction acting on the crack face. Here, surfaces S^+ , S^- , S_1 , S_t , S_2 , and S_3 , shown in Fig. 2.5, enclose the simply-connected volume V , and surface S_t shrinks to the crack front (i.e. $r \rightarrow 0$). The scalar weight-function, q , varies smoothly within V . A simple form for q assigns it a smooth variation from zero on surfaces S_1 , S_2 and S_3 , to a value of 1.0 at location s on S_t [192].

For elastic, homogeneous materials under quasi-static, isothermal loading with no body forces or crack-face tractions, the second and third integrals in Eq. (53) vanish. The second integral in Eq. (53) gives rise to interaction-integral terms that are non-zero for curved cracks. The third integral in Eq. (53) reflects the contribution of applied crack-face tractions. Shih et al. [192] assume that the energy release rate varies slowly along crack segment L_C , and thus obtain the approximate expression

$$J(s) = \frac{\bar{J}(s)}{\int_{L_C} q(s) ds}, \quad (54)$$

for the energy release rate, $J(s)$, at location s along a 3-D crack front.

3.3 An interaction integral procedure for curved 3-D cracks with surface tractions

This section reviews the formulation of an interaction integral for isothermal, quasi-static loading of planar, 3-D curved cracks in homogeneous materials under remote loads and crack-face tractions. We discuss a formulation that includes the effects of crack-front curvature, and then describe the computational procedure to obtain stress intensity factors.

3.3.1 Auxiliary fields

Williams' solution [221] for auxiliary stress and displacement in the vicinity of a crack has the form:

$$\sigma_{ij}^{aux} = \frac{K_I^{aux}}{\sqrt{2\pi r}} f_{ij}^I(\theta) + \frac{K_{II}^{aux}}{\sqrt{2\pi r}} f_{ij}^{II}(\theta) + \frac{K_{III}^{aux}}{\sqrt{2\pi r}} f_{ij}^{III}(\theta), \quad (55)$$

$$u_j^{aux} = \frac{K_I^{aux}}{2\mu} \sqrt{\frac{r}{2\pi}} g_j^I(\theta, \nu) + \frac{K_{II}^{aux}}{2\mu} \sqrt{\frac{r}{2\pi}} g_j^{II}(\theta, \nu) + \frac{2K_{III}^{aux}}{\mu} \sqrt{\frac{r}{2\pi}} g_j^{III}(\theta, \nu), \quad (56)$$

where superscript “aux” denotes auxiliary fields. Appendix A provides the expressions for $f_{ij}(\theta)$ as well as the plane-stress and plane-strain forms for $g_j(\theta, \nu)$. The symmetric gradient of displacements defines the auxiliary strain components:

$$\varepsilon_{ij}^{aux} = \frac{1}{2} (u_{i,j}^{aux} + u_{j,i}^{aux}). \quad (57)$$

These 2-D auxiliary fields are a function of location r and θ , and shear modulus μ . Most interaction-integral studies use the plane-strain form of these auxiliary fields to analyze cracks in 3-D solids, with the assumption that plane-strain conditions exist (asymptotically) near the crack front at locations away from free surfaces. The excellent accuracy of reported stress intensity factors supports the adequacy of this approximation. In an alternative approach, Kim et al. [121] demonstrate the use of numerically-generated auxiliary fields to obtain stress intensity factors.

Nahta and Moran [142], Gosz et al. [74] and Gosz and Moran [75] develop interaction-integral procedures that use the 2-D auxiliary fields based on Eqs. (55)-(57) for axisymmetric interface cracks, curved 3-D interface cracks, and 3-D cracks with non-planar surfaces, respectively. In a finite-element context, values of r and θ in these expressions describe the position of an element integration point in curvilinear coordinates, relative to a curved crack front. Definition of the auxiliary fields in curvilinear coordinates gives rise to additional terms in the gradients of auxiliary displacements [74,75,142]. To quantify the accuracy of interaction-integral computations without terms for crack curvature, numerical studies here use curvilinear coordinates to compute r and θ for auxiliary fields, but omit these additional, auxiliary-field gradients during evaluation of the interaction integral.

3.3.2 Interaction-integral formulation

By superimposing actual (computed) equilibrium fields and auxiliary fields, $\bar{J}(s)$ for the superimposed state, \bar{J}^S , from Eq. (53) becomes

$$\begin{aligned} \bar{J}^S(s) = & \int_V \left[(\sigma_{ij} + \sigma_{ij}^{aux})(u_{j,1} + u_{j,1}^{aux}) - W^S \delta_{1i} \right] q_{,i} dV \\ & + \int_V \left[(\sigma_{ij} + \sigma_{ij}^{aux})(u_{j,1} + u_{j,1}^{aux}) - W^S \delta_{1i} \right]_{,i} q dV \\ & - \int_{S^+ + S^-} (t_j + t_j^{aux})(u_{j,1} + u_{j,1}^{aux}) q dS. \end{aligned} \quad (58)$$

Here, superscript S denotes the superimposed state. For a linear-elastic material, the strain energy density for the superimposed state, W^S , is

$$W^S = \frac{1}{2} (\sigma_{ij} + \sigma_{ij}^{aux})(\varepsilon_{ij} + \varepsilon_{ij}^{aux}),$$

$$= W + W^{aux} + W^I, \quad (59)$$

where W^I is

$$W^I = \frac{1}{2} \left(\sigma_{ij} \varepsilon_{ij}^{aux} + \sigma_{ij}^{aux} \varepsilon_{ij} \right). \quad (60)$$

With Eq. (59), \bar{J}^S separates into three parts:

$$\bar{J}^S(s) = \bar{J}(s) + \bar{J}^{aux}(s) + \bar{I}(s), \quad (61)$$

where $\bar{J}(s)$ equals Eq. (53), the domain integral for the actual state; $\bar{J}^{aux}(s)$ is the domain integral for the auxiliary state; and $\bar{I}(s)$ is an integral with interacting actual and auxiliary terms, written as

$$\begin{aligned} \bar{I}(s) = & \int_V \left[\sigma_{ij} u_{j,1}^{aux} + \sigma_{ij}^{aux} u_{j,1} - \frac{1}{2} \left(\sigma_{jk} \varepsilon_{jk}^{aux} + \sigma_{jk}^{aux} \varepsilon_{jk} \right) \delta_{1i} \right] q_{,i} dV \\ & + \int_V \left[\sigma_{ij} u_{j,1}^{aux} + \sigma_{ij}^{aux} u_{j,1} - \frac{1}{2} \left(\sigma_{jk} \varepsilon_{jk}^{aux} + \sigma_{jk}^{aux} \varepsilon_{jk} \right) \delta_{1i} \right]_{,i} q dV \\ & - \int_{S^+ + S^-} \left(t_j u_{j,1}^{aux} + t_j^{aux} u_{j,1} \right) q dS. \end{aligned} \quad (62)$$

The third integral of Eq. (62) vanishes for crack faces without applied tractions. For straight cracks, the second integral vanishes for quasi-static, isothermal loading of homogeneous materials in the absence of body forces. Auxiliary fields based on Williams' 2-D solution do not satisfy equilibrium or compatibility in curvilinear coordinates [142], however, and the second integral remains non-zero for curved cracks.

The interaction-integral procedure here assumes that the same constitutive tensor, C_{ijkl} , couples actual and auxiliary stress and strain components, i.e.

$$\sigma_{ij} = C_{ijkl} \varepsilon_{kl}, \text{ and } \sigma_{ij}^{aux} = C_{ijkl} \varepsilon_{kl}^{aux}. \quad (63)$$

With appropriate definitions of auxiliary strain components (see Appendix E), the constitutive tensor is the same for the 3-D actual fields and for the 2-D auxiliary fields. Equation (63) leads to the useful relationships

$$\sigma_{ij} \varepsilon_{ij}^{aux} = C_{ijkl} \varepsilon_{kl} \varepsilon_{ij}^{aux} = C_{klij} \varepsilon_{ij}^{aux} \varepsilon_{kl} = \sigma_{ij}^{aux} \varepsilon_{ij}, \quad (64)$$

which enable simplification of the stress-strain terms in the first and second integrals of Eq. (62). Expansion of the second integral in Eq. (62) simplifies because $\sigma_{ij,i} u_{j,1}^{aux} \equiv 0$ due to equilibrium (assumed to be exact) of the actual stresses, and Eq. (64) leads to the cancellation of two additional terms:

$$\begin{aligned}
\sigma_{ij}^{aux} u_{j,1i} - \sigma_{ij,1} \varepsilon_{ij}^{aux} &= \sigma_{ij}^{aux} u_{j,1i} - C_{ijkl,1} \varepsilon_{kl} \varepsilon_{ij}^{aux} + C_{ijkl} \varepsilon_{kl,1} \varepsilon_{ij}^{aux} \\
&= \sigma_{ij}^{aux} u_{j,1i} - C_{klj} \varepsilon_{ij}^{aux} \varepsilon_{kl,1} \\
&= \sigma_{ij}^{aux} u_{j,1i} - \sigma_{ij}^{aux} \varepsilon_{ij,1} = 0.
\end{aligned} \tag{65}$$

Nahta and Moran [142] observe that 2-D auxiliary fields based on Williams' solution do not satisfy strain-displacement compatibility and equilibrium when defined in curvilinear coordinates. Therefore,

$$\sigma_{ij} \left(u_{j,1i}^{aux} - \varepsilon_{ij,1}^{aux} \right) \neq 0, \text{ and } \sigma_{ij,i}^{aux} \neq 0. \tag{66}$$

Because auxiliary fields correspond to an arbitrarily-specified equilibrium state, the third integral in Eq. (62) simplifies with the assumption that the auxiliary state has crack faces without applied tractions. As a result of the preceding arguments, Eq. (62) reduces to

$$\begin{aligned}
\bar{I}(s) &= \int_V \left(\sigma_{ij} u_{j,1i}^{aux} + \sigma_{ij}^{aux} u_{j,1i} - \sigma_{jk} \varepsilon_{jk}^{aux} \delta_{li} \right) q_{,i} dV \\
&\quad + \int_V \left[\sigma_{ij} \left(u_{j,1i}^{aux} - \varepsilon_{ij,1}^{aux} \right) + \sigma_{ij,i}^{aux} u_{j,1i} \right] q dV \\
&\quad - \int_{S^+ + S^-} t_j u_{j,1i}^{aux} q dS,
\end{aligned} \tag{67}$$

The terms $\sigma_{ij} \left(u_{j,1i}^{aux} - \varepsilon_{ij,1}^{aux} \right)$ and $\sigma_{ij,i}^{aux} u_{j,1i}$ that arise here due to crack-front curvature also appear in the interaction-integral formulations for straight cracks in functionally-graded materials [53,117].

The crack-face integral,

$$\int_{S^+ + S^-} t_j u_{j,1i}^{aux} q dS, \tag{68}$$

contributes significantly to stress intensity factors, but is occasionally neglected. None of the quantities in Eq. (68) depend upon the finite element solution of the boundary-value problem—an exact evaluation of this integral thus ensures that it does not contribute error to numerical results. Section 3.4.3 and Appendix B describe a simple, exact numerical integration procedure for Eq. (68) when element edges along the crack front are straight.

With the value of $\bar{I}(s)$ generated using Eq. (67), computation of a pointwise value of the interaction integral at location s , along a 3-D crack front follows Eq. (54):

$$I(s) = \frac{\bar{I}(s)}{\int_{L_c} q(s) ds} . \quad (69)$$

3.3.3 Extraction of stress intensity factors

An expression for the energy release rate in terms of mixed-mode stress intensity factors K_I , K_{II} and K_{III} , is

$$J(s) = \frac{K_I^2 + K_{II}^2}{E^*} + \frac{1 + \nu}{E} K_{III}^2 , \quad (70)$$

where $E^* = E/(1 - \nu^2)$ for plane-strain, $E^* = E$ for plane-stress conditions, and stress intensity factors refer to crack-front location s . For the superimposed state, Eq. (70) becomes

$$\begin{aligned} J^S(s) &= \frac{1}{E^*} \left[(K_I + K_I^{aux})^2 + (K_{II} + K_{II}^{aux})^2 \right] + \frac{1 + \nu}{E} (K_{III} + K_{III}^{aux})^2 , \\ &= J(s) + J^{aux}(s) + I(s) , \end{aligned}$$

where

$$I(s) = \frac{1}{E^*} (2K_I K_I^{aux} + 2K_{II} K_{II}^{aux}) + \frac{1 + \nu}{E} (2K_{III} K_{III}^{aux}) . \quad (71)$$

Equations (69) and (71) provide the sought-after relationship between stress intensity factors and the interaction integral in Eq. (67). With the assigned values $K_I^{aux} = 1.0$ and $K_{II}^{aux} = K_{III}^{aux} = 0$, Eq. (71) yields

$$K_I = \frac{E^*}{2} I(s) . \quad (72)$$

To obtain the actual mode-I stress intensity factor from (72), we: 1) assume either plane-stress or plane-strain conditions (based on the nature of the boundary-value problem) for E^* and for the auxiliary fields; 2) compute $\bar{I}(s)$ by evaluating the interaction integral in Eq. (67) using the values $K_I^{aux} = 1.0$, $K_{II}^{aux} = 0.0$, and $K_{III}^{aux} = 0$; 3) compute $I(s)$ from Eq. (69) for use in Eq. (72).

The selection $K_{II}^{aux} = 1.0$, $K_I^{aux} = K_{III}^{aux} = 0$, and the selection $K_{III}^{aux} = 1.0$, $K_I^{aux} = K_{II}^{aux} = 0$ in Eq. (71) leads to relationships between K_{II} , K_{III} and $I(s)$:

$$K_{II} = \frac{E^*}{2} I(s) , \text{ and } K_{III} = \frac{E}{2(1 + \nu)} I(s) . \quad (73)$$

To obtain values of K_{II} and K_{III} from Eq. (73), we evaluate Eqs. (67), (69), and (73) with appropriate values of K_I^{aux} , K_{II}^{aux} , and K_{III}^{aux} . Five distinct evaluations of the interaction integral in Eq. (67) thus lead to values of K_I and K_{II} for plane-stress and plane-strain

conditions, and to a value of K_{III} for anti-plane-shear conditions. Section 3.4 discusses the numerical evaluation of Eq. (67).

3.4 Numerical procedures

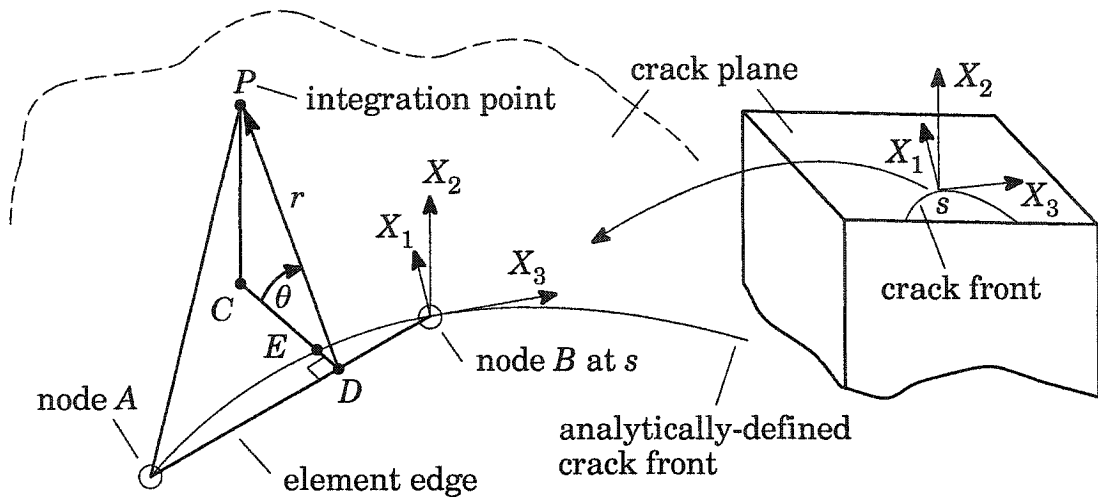
Within a finite-element framework, numerical procedures to evaluate the interaction integral parallel those used in conventional, element-level computations. This section describes numerical evaluation of the integrals, discusses computation of r and θ for the auxiliary-fields and reviews procedures to evaluate the surface-traction integral in Eq. (68). All procedures employed in this work are implemented in WARP3D, a general-purpose, open-source finite-element code [78].

3.4.1 Numerical evaluation of volume and surface integrals

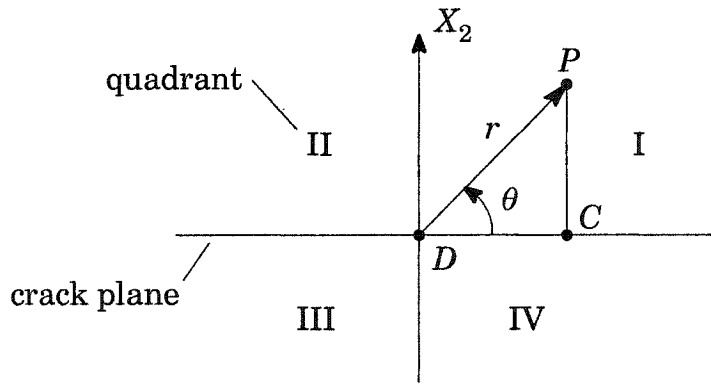
Evaluation of the integrals in Eq. (67) follows the same Gauss-quadrature procedures employed for the computation of element stiffnesses [41]:

$$\begin{aligned}
\bar{I}(s) = & \sum_V \sum_p^{elems \ gpts} \left[\left(\sigma_{ij} u_{j,1}^{aux} + \sigma_{ij}^{aux} u_{j,1} - \sigma_{jk} \varepsilon_{jk}^{aux} \delta_{li} \right) q_{,i} \det \mathbf{J} \right]_p w_p \\
& + \sum_V \sum_p^{elems \ gpts} \left\{ \left[\sigma_{ij} \left(u_{j,1i}^{aux} - \varepsilon_{ij,1}^{aux} \right) + \sigma_{ij,i}^{aux} u_{j,1} \right] q \det \mathbf{J} \right\}_p w_p \\
& - \sum_S \sum_p^{faces \ gpts} \left(t_j u_{j,1}^{aux} q \det \mathbf{J} \right)_p w_p , \tag{74}
\end{aligned}$$

where the sum over volume V includes all elements in the domain, and the sum over surface S includes each traction-bearing element face on the boundary of domain V which lies on the crack surface. The sum over p includes all integration points, and w_p denotes the corresponding weight for that point. All quantities included in the summation must be expressed in the local, orthogonal coordinate system at location s on the crack front (see Fig. 2.5). Here, $\det \mathbf{J}$ denotes the determinant of the coordinate Jacobian matrix in two or three dimensions, depending upon surface or volume domains. Repeated indices imply summation. We employ a simple ‘‘plateau’’ function for the variation of q [192], and Gauss quadrature based on the two-point rule for linear- and quadratic-displacement elements. Evaluation of these terms in the first domain of elements that surround the crack front includes a singularity in the auxiliary fields. Standard Gaussian integration of the singular auxiliary fields within these elements will not yield good accuracy. However, for homogeneous material, the plateau function employed for the q -function enables these elements to be omitted from larger domains of integration that include only elements further from the crack front.



(a)



(b)

Fig. 3.1 (a) Computation of r and θ values to determine auxiliary fields at integration point P for interaction integral evaluation at crack-front location s . In meshes with straight element edges, distance r spans point P and the element edge between nodes A and B , and angle PDC defines θ . Point C is the projection of P onto the X_1 - X_3 plane. (b) Quadrants I-IV in the plane PDC for computation of θ .

3.4.2 Computation of r and θ for auxiliary fields

Evaluation of the auxiliary fields at an integration point requires the distance r from the crack front to the point, and the angle, θ , measured from the crack plane ahead of the crack to the integration point (see Fig. 3.1). For curved crack fronts, Gosz et al. [74] define the distance r between an integration point and the analytically-defined crack front using a curvilinear coordinate system. They first project an integration point, P ,

onto the crack plane as point C in Fig. 3.1(a), and then formulate an expression for the distance between C and the analytical definition of the curved crack front. Minimization of this distance through a Newton procedure determines the point E along the analytically-defined crack front closest to C (see Fig. 3.1(a)). Distance r is finally measured from E to P , and angle $P-E-C$ determines θ .

The present work considers two different approaches to compute r and θ . For curved crack fronts discretized using quadratic elements with curved edges, i.e. elements with nodes that lie on the analytically-defined curve, computation of r and θ follows the above procedure employed by Gosz et al. [74]. For curved crack fronts discretized with linear elements (straight edges), r is the distance $D-P$ from line segment $A-B$ defined by element nodes, to integration point P , as illustrated in Fig. 3.1(a). Figures 3.1(a)-(b) and Appendix C describe a procedure to compute r and θ for this case. For a curved crack represented by straight-edged elements, this approach to define r and θ remains consistent with the discretization of the body into finite elements. It also avoids inaccurate computation of r and θ when the distance from the analytically-defined crack front to the mesh-defined crack front, distance $D-E$ in Fig. 3.1(a), becomes significant compared to the width of elements in the domain of integration. Figure 3.2(a) shows one quarter of a cylindrical mesh for an embedded penny-shaped crack discretized by elements with straight edges. Figure 3.2(b) illustrates the potentially significant deviation of an analytical curve that describes a circular crack from the crack front defined by the mesh elements. The (actual) analytical curve in Fig. 3.2(b) extends into the fourth ring of elements surrounding the crack front, and does not correspond to the discontinuity in the mesh that defines the crack. Within the first few rings of elements that surround the crack front, r and θ values computed from the analytical curve locate incorrectly the position of integration points, thereby leading to auxiliary-fields inconsistent with actual fields generated by the mesh. This necessitates the use of local orthogonal coordinates to compute values of r and θ when elements with straight edges define the crack front. Numerical examples considered in this study employ finite-element meshes with curved crack fronts discretized using both straight and curved element edges.

3.4.3 Numerical evaluation of the crack-face-traction integral

Consider now integration of the surface-traction integral in Eq. (67) over the surface of an element incident on the crack front. Values of $K_1^{aux} = 1.0$, and $t_2 = 1.0$ correspond to a mode-I crack-opening surface pressure, and lead to an integrable, inverse square-root singularity:

$$\lim_{r \rightarrow 0} \int_S t_j u_{j,1}^{aux} q dS = \lim_{r \rightarrow 0} \int_0^Z \int_{x=0}^{x=r} \pm \frac{\mu}{\sqrt{x}} dx dz \approx \lim_{r \rightarrow 0} O(r^{1/2}) = 0, \quad (75)$$

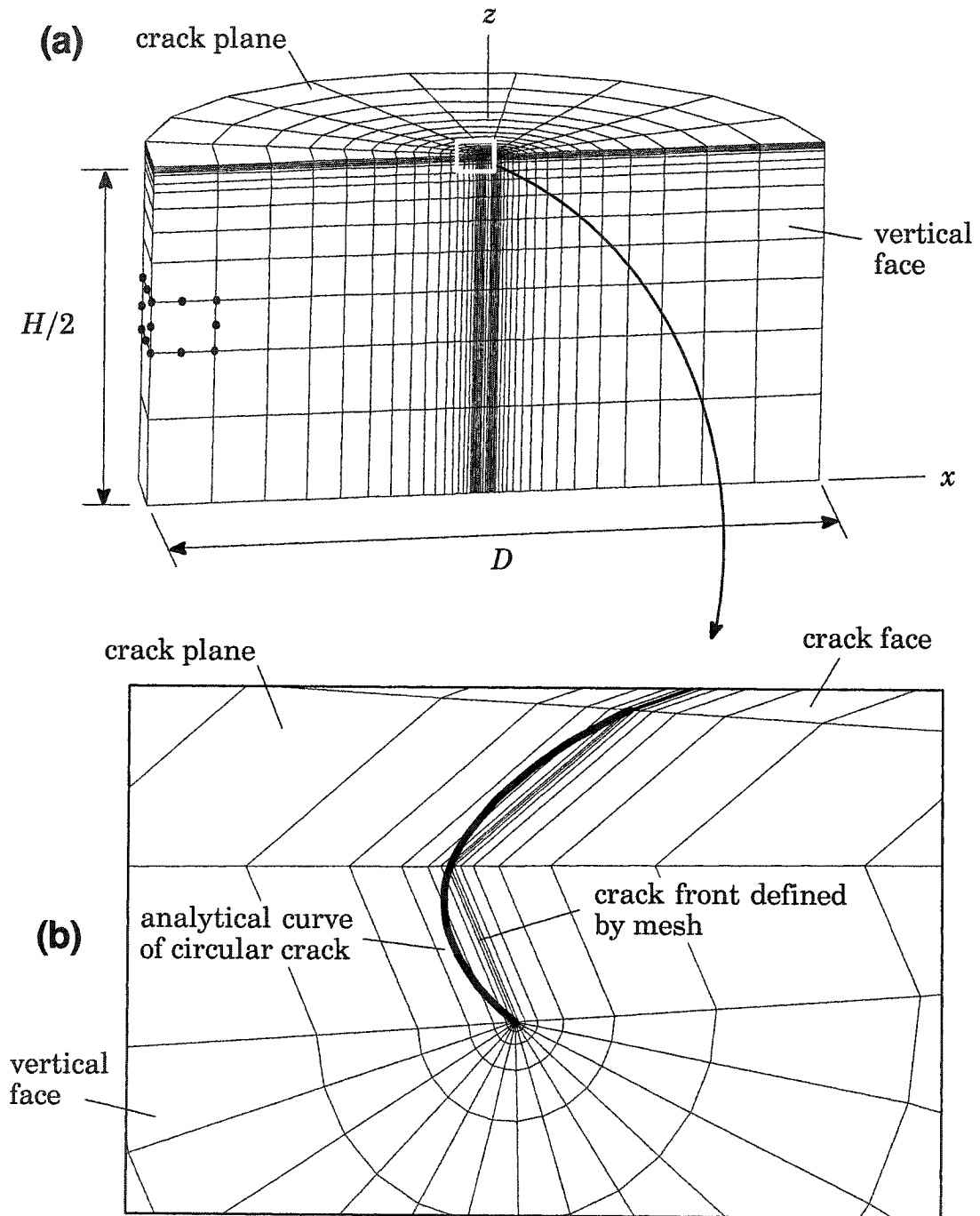


Fig. 3.2. (a) Quarter section of a circular cylindrical mesh with an embedded penny-shaped crack used for some examples in Section 3.7. (b) View of crack front discretized by elements with straight edges, showing difference between crack front defined by the mesh and by an analytical expression.

where $q = 1.0$ for simplicity, and where the sign of the integrand depends upon the sign of $u_{j,1}^{aux}$ at $\theta = \pm\pi$. The terms in Eq. (68) have no dependence on the solution to the boundary-value problem—crack-face tractions, auxiliary-displacement derivatives, q -values and the domain of integration are defined entirely by the analyst. During numerical evaluation, as the number of integration points increases, standard Gauss quadrature converges slowly toward the exact value for a function with a singularity at one end point [65]. A simple change of variables, detailed in Appendix B, leads to exact integration of Eq. (68) for elements with straight edges incident on the crack front, and requires only minor modifications to the standard Gauss-quadrature procedure. The modified Gauss integration, based on a 2×2 rule, leads to exact values of Eq. (68) for elements with four and eight nodes on each face. For quadratic elements with quarter-point nodes and straight edges, standard 2×2 Gauss quadrature integrates Eq. (68) exactly, and the change of variables becomes unnecessary. The exact integration procedure described in Appendix B is used here only for linear elements with loaded faces and incident on the crack front—standard 2×2 quadrature yields accurate values for elements with loaded faces not incident on the crack front. Standard quadrature, based on a four-point rule is adopted to evaluate Eq. (68) for elements with curved edges. Table 3.1 summarizes the various integration schemes used to evaluate Eq. (68). Numerical results presented here demonstrate that exact evaluation of Eq. (68) over elements incident on the crack front increases noticeably the accuracy of stress intensity factors.

Table 3.1. Integration schemes used in this study to evaluate the crack-face-traction integral in Eq. (68).

hex element geometry	number of nodes on element face	integration for face of element incident on crack	integration for faces of elements remote from crack
straight edges	4	modified 2×2 (exact)	standard 2×2
	8	modified 2×2 (exact)	standard 2×2
	8 (with quarter-point nodes)	standard 2×2 (exact)	standard 2×2
curved edges	8 (with quarter-point nodes)	standard 4×4	standard 4×4

3.5 3-D analyses of plane-strain and plane-stress configurations

This section discusses verification of the 3-D numerical procedures to evaluate Eq. (67) for through-crack configurations with straight crack fronts. Finite element solutions for a standard boundary-layer model [144] (details omitted for brevity) verify the correct computation of mixed-mode stress intensity factors in homogeneous materials under plane-stress, plane-strain and anti-plane-shear conditions. The present finite element

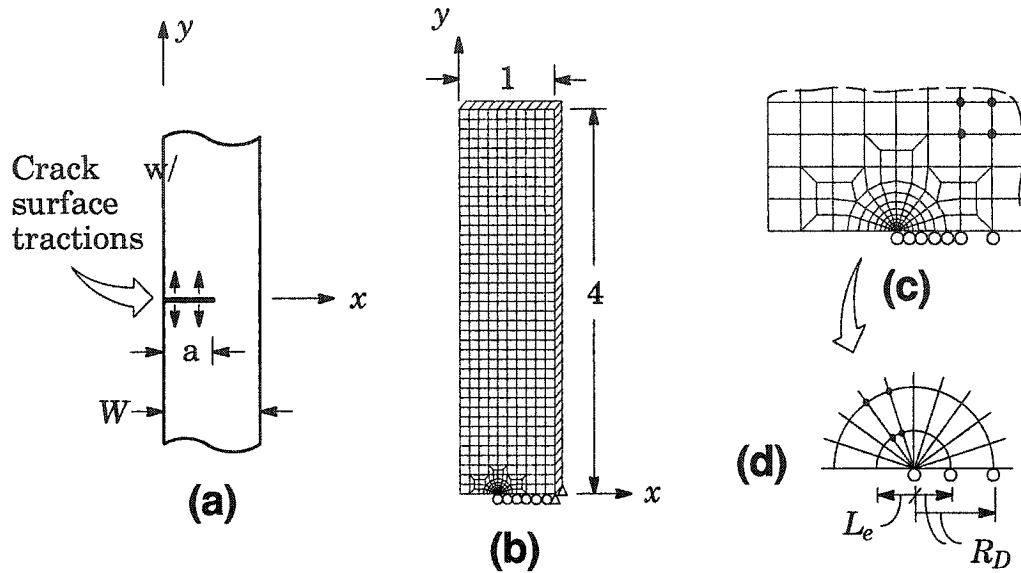


Fig. 3.3. (a) Schematic of a SE(T) specimen with crack-face tractions. (b) Symmetric mesh representing the cracked strip where $a/W = 0.4$. (c) Detail of mesh in crack-front region showing 10 semi-circular rings and 10 sectors of elements. (d) Elements incident on the crack front each have one collapsed face. Here, L_e describes the size of elements incident on the crack front, and R_D indicates domain size.

procedures yield the identical K_I , K_{II} and K_{III} values imposed on the remote boundary of the model. Here, we focus on the analysis of a single-edge-notch tension, SE(T), specimen under plane-strain conditions to illustrate the influence of the crack-face traction integral, Eq. (68).

Figure 3.3(a) illustrates a semi-infinite strip subjected to crack-face tractions. Symmetry permits the analysis of one-half of the specimen. The finite-element mesh shown in Fig. 3.3(b) discretizes the model with 8-noded brick elements. Ten rings of elements surround the crack front, and 10 sectors of elements discretize the crack-front region in the hoop direction as shown in Fig. 3.3(c). Figure 3.3(d) shows the collapsed elements incident on the crack front; L_e describes the size of elements incident on the crack front, and R_D describes the size of domains. For the domain of integration comprising the 10 elements immediately surrounding the crack front in the current model, only one element of size $L_e/a = 0.0177$ contributes to Eq. (68). With a 2×2 Gauss-quadrature rule, the ratio of numerical and exact values obtained from Eq. (68) for this element reflects an error greater than 25%. Figure 3.4 illustrates the very slow convergence of standard quadrature toward the exact value of Eq. (68) with an increase in the number of quadrature points.

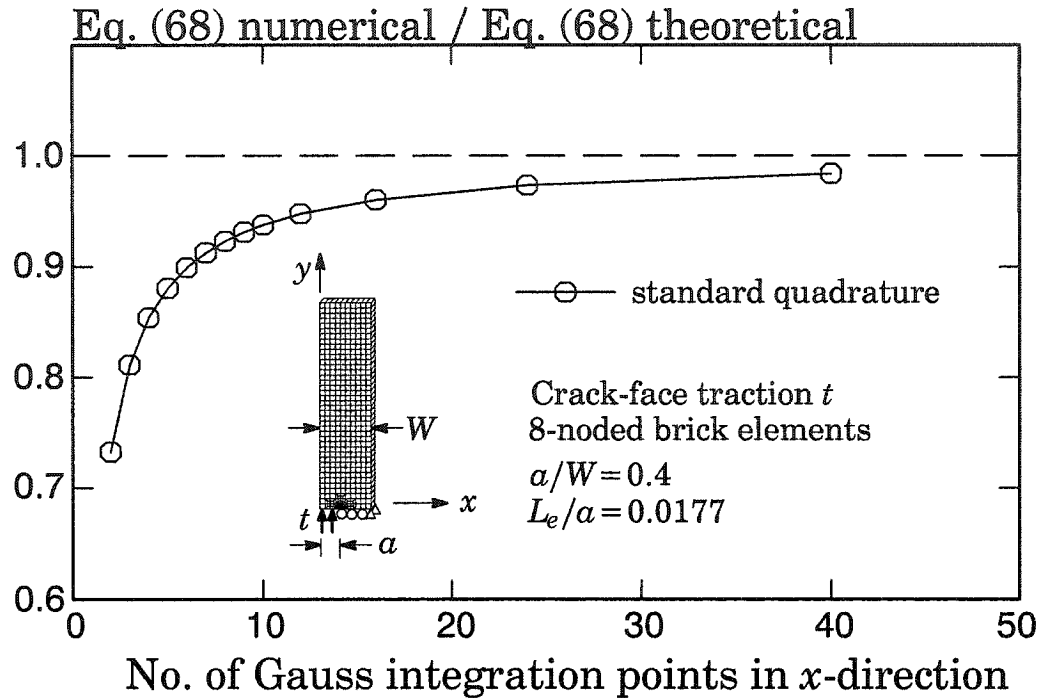


Fig. 3.4. Convergence of standard Gauss quadrature for evaluation of the crack-face traction integral, Eq. (68), for the element incident on the crack front in the SE(T) model.

Figure 3.5(a) shows the contribution to $\bar{I}(s)$ from each term in Eq. (67); recall that the second integral vanishes for a straight crack front. The error introduced by using standard 2×2 quadrature to evaluate Eq. (68) for the element incident on the crack front remains significant for large domains, as shown in Fig. 3.5(b). Current results obtained using “standard” quadrature match closely the stress intensity factor values obtained from ABAQUS 6.4-3 [1], also shown in Fig. 3.5(b). This figure shows that by following the procedure in Appendix B to evaluate Eq. (68) exactly over the element incident on the crack front, the accuracy of the stress intensity factor improves by about 1%. The lowest curve in Fig. 3.5(b) illustrates the impact of omitting the crack-face-traction contribution on the computed stress intensity factor values.

3.6 Curved cracks modeled with piecewise-linear fronts

Gosz et al. [74] and Kim et al. [121] compare stress intensity factors computed with and without the terms in the second integral of Eq. (67). Stress intensity factors computed by Gosz et al. [74] for a flat, elliptical crack embedded in an infinite homogeneous body under remote mode-I loading improve significantly when crack-front-curvature terms are included. Kim et al. [121] demonstrate an improvement in stress intensity factors

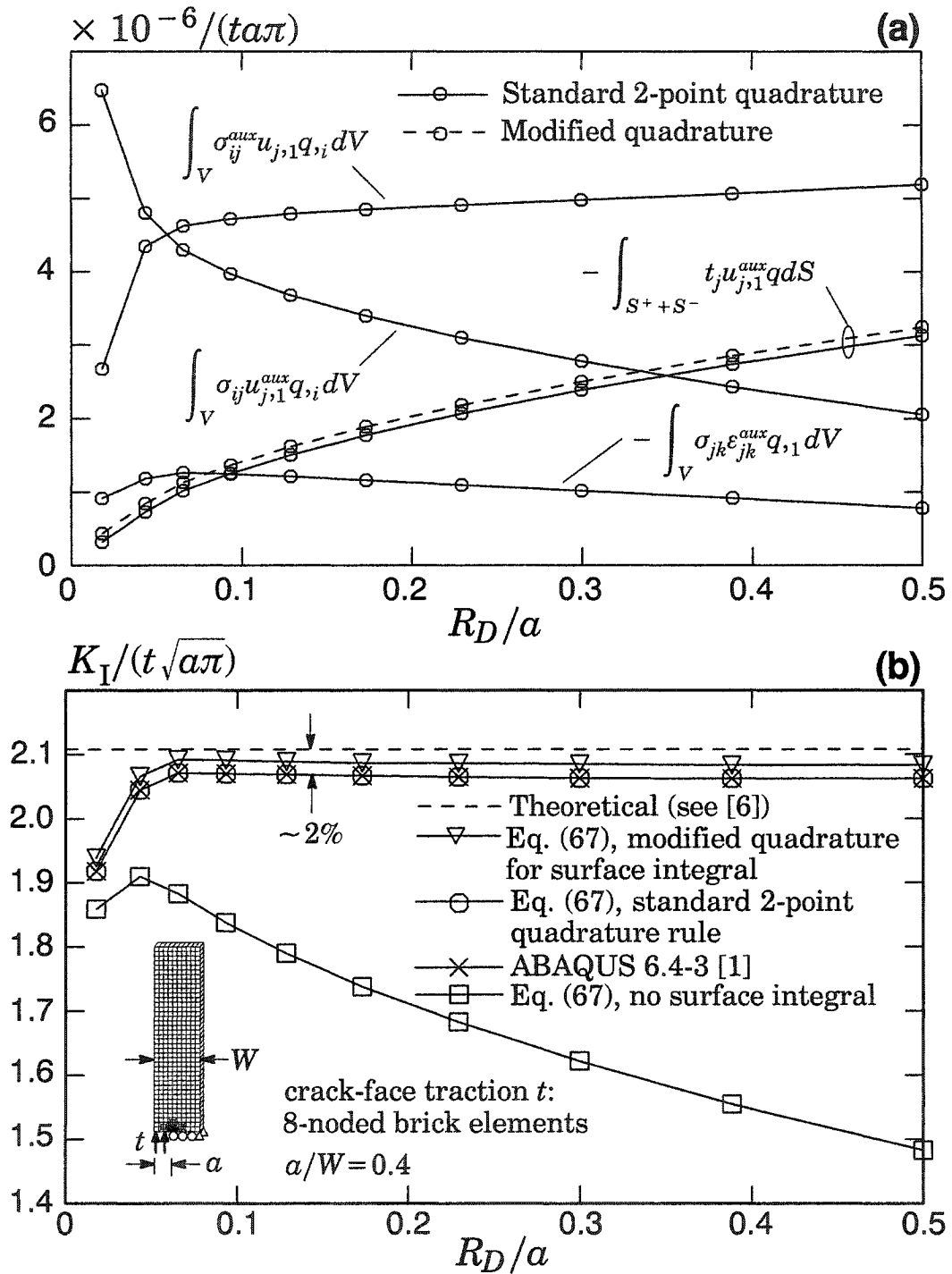


Fig. 3.5. (a) Normalized terms of the interaction-integral vs. normalized domain size for the SE(T) specimen loaded by crack-face tractions. (b) Normalized stress intensity factors vs. domain size for the SE(T) specimen obtained using standard and modified quadrature for the surface integral, theoretical results and ABAQUS 6.4-3 [1].

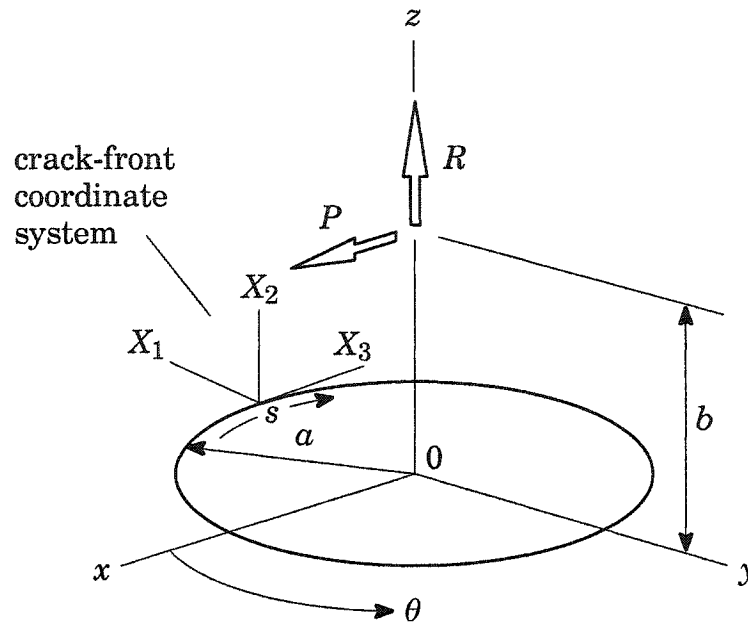


Fig. 3.6. (after Kassir and Sih [103]) A penny-shaped crack in an infinite homogeneous solid loaded by point forces P and R acting at point $x=0, y=0, z=b$, and directed parallel to the x and z axes, respectively. For the ABAQUS 6.4-3 [1] benchmark model, $P=R=400.0E+6$, and $b=0.33$.

when they employ the method of Gosz et al. [74] for a penny-shaped crack in a homogeneous cylinder loaded through remote displacements.

This section employs the interaction-integral procedure described in Section 3.3 to compute mixed-mode stress intensity factors along penny-shaped and elliptical cracks in homogeneous solids. Meshes used for examples in this section have either linear or quadratic elements with *straight* edges along the front (often produced by mesh generation programs). For domain-integral computations, local crack-front curvature in the numerical model vanishes, and computations of r and θ values in a local orthogonal coordinate system follow the descriptions in Section 3.4.2, Appendix C and Figs. 3.1(a)-(b). With this approach, gradients in the auxiliary field due to curvilinear coordinates do not appear, and the second integral of Eq. (67) vanishes because it arises from the definition of 2-D auxiliary fields in a curvilinear coordinate system. This section explores the accuracy of this simplified approach for the computation of mixed-mode stress intensity factors.

3.6.1 Penny-shaped crack in an infinite solid under mixed-mode loading

Figure 3.6 shows the problem of a circular crack in an infinite solid loaded by point forces above the crack plane. Kassir and Sih [103] provide analytical stress intensity factor solutions for this problem (see Appendix D.1), and the ABAQUS 6.4-3 benchmark

manual contains mesh data and loading conditions which we use here. Figure 3.7(a) shows a cross-section of the mesh obtained from the ABAQUS 6.4-3 input file, which defines 10,260 8-noded hexagonal elements. Boundary conditions consist of one fixed node at each end of the cylinder axis; nodal forces P and R in Fig. 3.6 act with magnitude 400 MN at distance 0.33 above the crack plane. Young's modulus and Poisson's ratio equal 200 GPa, and 0.3, respectively, and the ratio of cylinder height, H , and diameter, D , to crack radius, a , are $H/a = D/a = 80$. Figure 3.7(b) shows domains of 24 radial sectors that discretize the crack-front. Elements of size $L_e/a = 0.00129$ having one collapsed face surround the crack front, and the largest domain on which we compute values (domain five) has dimension $R_D/a = 0.04$. Thirty sectors discretize the cylinder in the radial direction about the z -axis, and we report stress intensity factors computed at element corner nodes on the crack front.

At each crack-front location, an average of the interaction-integral values obtained from domains two through five yields stress intensity factors normalized as

$$K_n = \frac{Ka^{3/2}}{P\sqrt{\pi}}. \quad (76)$$

Figure 3.8(a) shows normalized stress intensity factors along one-half of the crack front, obtained from present computations and from the analytical solutions listed in Appendix D.1. Stress intensity factors generated by the ABAQUS 6.4-3 interaction-integral routines match current values to three or more significant digits for this case and do not appear in the figure. We also examine stress intensity factors obtained using the mesh shown in Fig. 3.7(a) following conversion to 20-noded hexagonal elements. Here again, element edges are straight, and thus local crack-front curvature is zero. Computations employ reduced $2 \times 2 \times 2$ integration and collapsed elements with quarter-point nodes incident on the crack-front. For this problem, our stress intensity factors compare to within 1.0% of the values generated by ABAQUS 6.4-3. Figure 3.8(a) shows the variation in stress intensity factors obtained using the higher-order elements.

Figure 3.8(b) compares energy release rate values generated using the interaction integral, the J -integral formulation described by Eq. (53), and the analytical solutions contained in Appendix D.1. Equation (70) converts stress intensity factors to equivalent J -values. Normalization of J -integral values shown in Figure 3.8(b) follows

$$J_n = \frac{JEa^3}{P^2}. \quad (77)$$

The mesh of 20-noded elements leads to improved accuracy. This figure demonstrates that the accuracy of interaction-integral computations along a curved crack front using a model with zero local curvature matches the high accuracy of J -integral computations which here do not include effects from crack-front curvature. Close agreement between results computed using the interaction integral, the J -integral, and analytical expres-

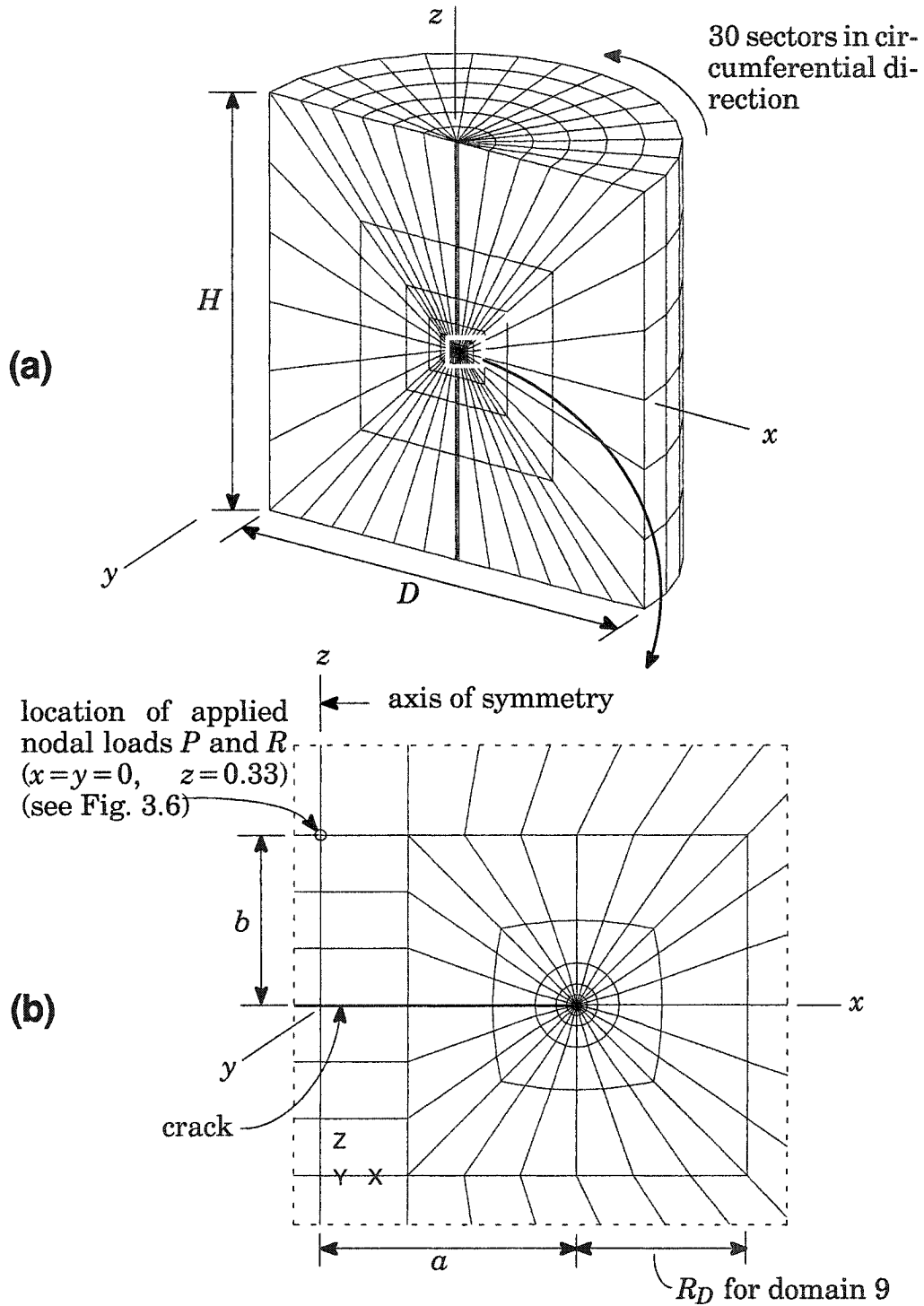


Fig. 3.7. (a) Section view of cylindrical mesh representing an infinite body with an embedded penny-shaped crack (from ABAQUS 6.4-3 benchmark library [1]). Dimension ratios are $H/a = D/a = 80$. (b) View of mesh discretization in crack-front region. Seven cylindrical domains with 24 sectors surround the crack front. For domain 1, $L_e/a = R_D/a = 0.00129$. For domain 5, $R_D/a = 0.04$.

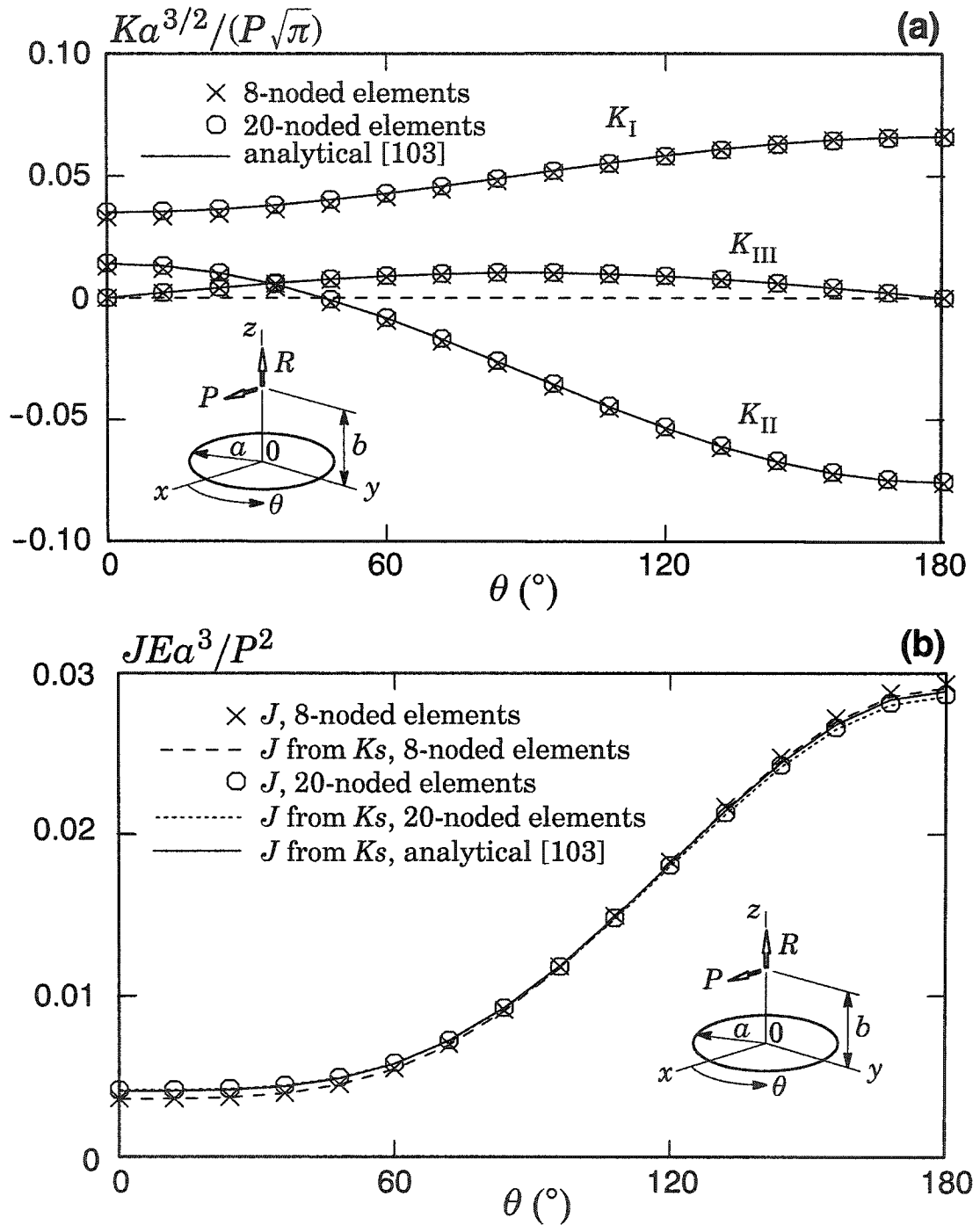


Fig. 3.8. (a) Normalized stress intensity factor values along the front of a penny-shaped crack under mixed-mode loading due to point forces P and R . (b) Normalized values of energy release rate determined from the J -integral, interaction-integral values and analytical solutions.

sions indicates that excellent accuracy for this problem may be achieved by measuring r and θ from straight element edges as described in Section 3.4.2.

Table 3.2 describes the error between numerical results and analytical results through the following quantities:

$$\epsilon = \frac{1}{|h^e|_{max}} \sqrt{\frac{1}{D} \sum_{i=1}^D (h_i^e - h_i^n)^2}, \quad (78)$$

$$\Delta_{min} = \frac{|h_i^e - h_i^n|_{min}}{|h^e|_{max}}, \quad (79)$$

$$\Delta_{max} = \frac{|h_i^e - h_i^n|_{max}}{|h^e|_{max}}, \quad (80)$$

$$\Delta_{ave} = \frac{1}{D} \sum_{i=1}^D \frac{|h_i^e - h_i^n|}{|h^e|_{max}}. \quad (81)$$

Here, ϵ represents the global error, h is a normalized stress intensity factor (K) or energy release rate (J) obtained using exact (superscript e) or numerical (superscript n) solutions, and D is the number of points on each curve. Quantities Δ_{min} , Δ_{max} and Δ_{ave} describe the minimum, maximum and average variation of calculated values from the maximum analytical value. The accuracy of stress intensity factors as demonstrated by Table 3.2 suggests that mesh refinement or use of higher-order elements (h or p refinement) should permit the interaction integral to yield arbitrarily accurate stress intensity factors without the curvature terms.

Table 3.2. Error measures of normalized stress intensity factors and energy release rates (see Figs. 3.8(a)-(b)) with respect to analytical solutions.

mesh	value	global error ϵ	Δ_{min} (%)	Δ_{max} (%)	Δ_{ave} (%)
8-noded elements	K_{In}	0.019	0.00	3.06	1.50
	$K_{II n}$	0.012	0.06	1.66	1.10
	$K_{III n}$	0.033	0.00	4.59	2.93
	J_n from Ks	0.010	0.04	1.70	0.86
	J_n	0.012	0.12	1.65	1.05
20-noded elements	K_{In}	0.003	0.00	0.54	0.28
	$K_{II n}$	0.004	0.23	0.57	0.40
	$K_{III n}$	0.012	0.00	1.64	1.04
	J_n from Ks	0.006	0.05	1.16	0.46
	J_n	0.004	0.00	0.74	0.31

3.6.2 An infinite solid with a flat elliptical crack under tension

Curvature effects may be more significant for elliptical cracks than for penny-shaped cracks. In this section, the computation of mode-I stress intensity factors along the front of a flat elliptical crack in a homogeneous solid supports a comparison between interaction-integral results by Gosz et al. [74], J -integral results, and analytical values. Crack-face pressure provides loading conditions for the present analysis, giving additional insight into the influence of the surface-traction integral in Eq. (68). This example, and the corresponding problem in Gosz et al. [74], employ linear, 8-noded hexagonal elements. Gosz et al. [74] compute r and θ from an *analytically*-defined curve that describes the crack front; and thus include auxiliary field terms reflecting local curvilinear coordinates that appear in the second integral of Eq. (67). Here, computations of r and θ values use local orthogonal coordinates as described in Section 3.4.2 with crack front geometry defined by the element mesh.

The large rectangular specimen contains an embedded elliptical crack. The crack has a semi-minor-axis to semi-major-axis ratio of $a/c = 0.4$. To allow for arbitrary crack-face tractions, a full mesh is used here and consists of 26,504 8-noded brick elements. Figure 3.9(a) shows one eighth of this mesh of size $L/c = 10$. Along the crack front shown in Fig. 3.9(b), evaluation of the interaction integral occurs over domains including elements incident on corner nodes along the crack front. Elements with collapsed faces surround the crack front, and have dimension $L_e/a = 0.0165$. Ten sectors and seven rings of elements discretize the region surrounding the crack. Here, we report the average of stress intensity factors computed using domains two through five at each crack-front location.

Irwin [91] derives an analytical expression for the mode-I stress intensity factor along the front of an elliptical crack in an infinite solid under tension:

$$K_I = \sigma_0 \sqrt{\frac{\pi}{Q}} \left(\frac{a}{c}\right) (a^2 \cos^2 \phi + c^2 \sin^2 \phi)^{1/2}, \quad (82)$$

where σ_0 is the remote uniform tensile stress, $2c$ and $2a$ are the major and minor axis lengths of the ellipse, parametric angle ϕ defines the crack-front location as described in Fig. 3.10, and \sqrt{Q} is a complete elliptic integral of the second kind equal to $\ell/4c$, where ℓ is the arc length of the ellipse. Merkle [136] discusses a commonly-used approximate expression for Q , which for $a/c \leq 1$ is [6]

$$Q = 1 + 1.464 \left(\frac{a}{c}\right)^{1.65}. \quad (83)$$

The standard normalization of stress intensity factors for elliptical cracks follows

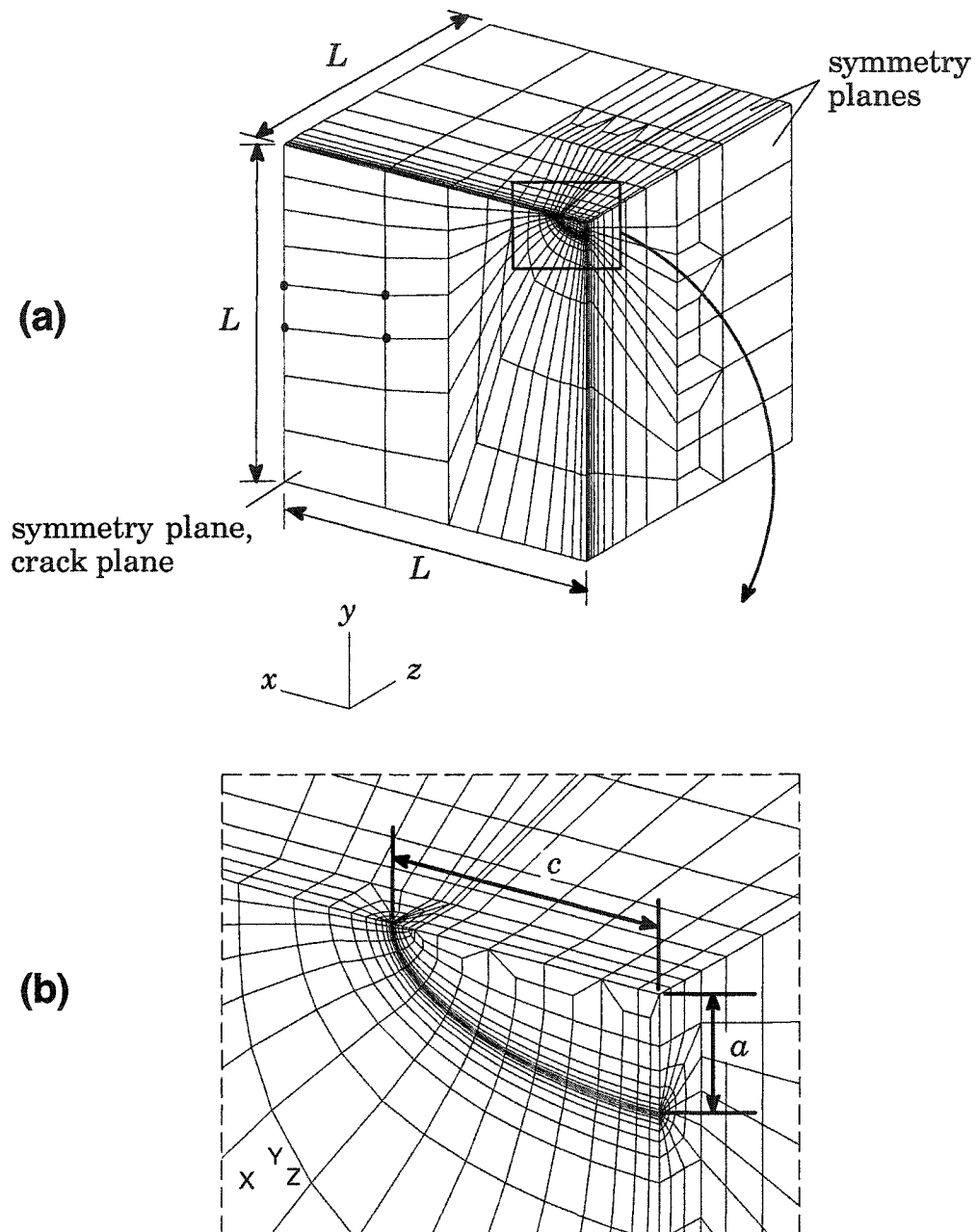


Fig. 3.9. (a) One eighth of the mesh defined to model a planar, elliptical crack in an infinite solid. Loading includes crack-face pressure and crack-face shear. The full mesh includes 26,504 8-noded brick elements. (b) View of mesh in crack-front region, where 7 rings divided into 20 sectors surround the crack front. Ratios $L/c=10$, and $a/c=0.4$.

$$K_{In} = \frac{K_I}{S \sqrt{\frac{\pi a}{Q}}}, \quad (84)$$

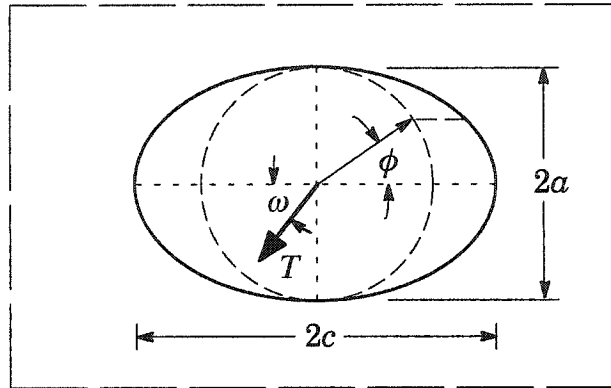


Fig. 3.10. Description of parametric angle ϕ , on an elliptical crack front where $a/c \leq 1.0$. Angle ω describes the direction of crack-face shear loading, represented by T .

where $S = \sigma_0$ for tension loading.

Figure 3.11(a) shows the normalized mode-I stress intensity factors obtained from Eqs. (67) and (82) for crack-face pressure loading. With exact integration of the crack-face traction integral over the element incident on the crack front, the numerical result at all crack-front locations agrees to within 1% of the analytical expression. With standard Gauss quadrature evaluation of Eq. (68), results are within 2.5% of theoretical values, and agree very closely with values generated by ABAQUS 6.4-3 [1]. Numerical results are accurate even along the more highly-curved portion of the crack front, whereas better path-independence of stress intensity factors occurs in areas of smaller curvature.

Figure 3.11(b) compares K_I -values computed with the interaction integral to J -values computed using Eq. (53). Excellent agreement exists between interaction-integral and J -integral values. Here, J -integral computations do not involve curvilinear coordinates as in Fernlund et al. [67]. Excellent overall accuracy and good correspondence between J -integral and interaction-integral results for this problem imply that the use of straight-edged elements to discretize curved cracks essentially eliminates the influence of local crack-front curvature on interaction-integral computations. Straight element edges enable simple computations of r and θ from local orthogonal coordinate systems, eliminate auxiliary-field gradients that arise due to curvilinear coordinates, and cause the second integral in Eq. (67) to vanish. Results in Figs. 3.11(a)-(b) demonstrate the accuracy that can be achieved through this approach, and an additional example further illustrates its usefulness for mixed-mode loading cases.

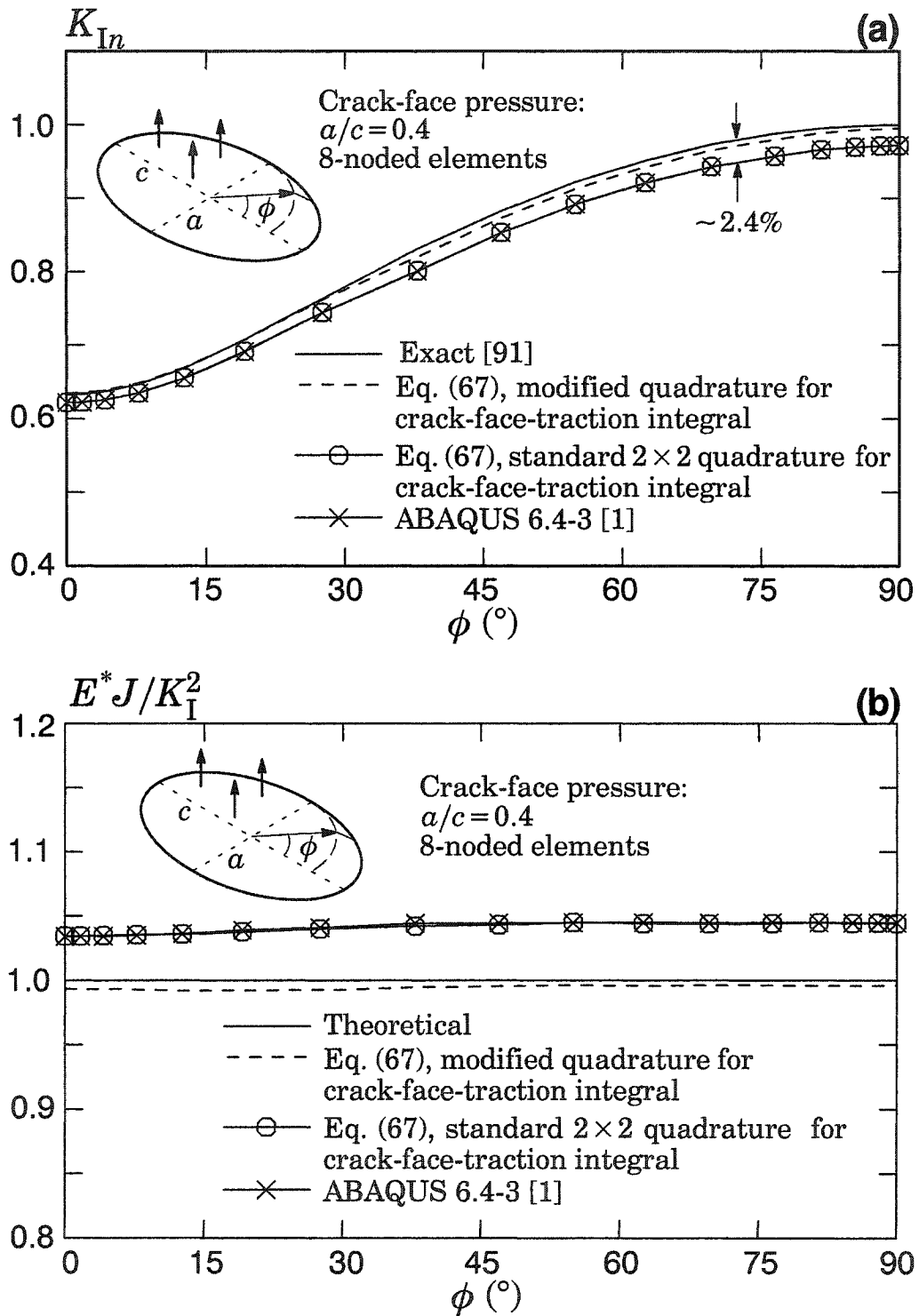


Fig. 3.11. (a) Comparison of numerical and analytical mode-I stress intensity factors along a flat elliptical crack loaded by crack-surface pressure in an infinite solid. (b) Comparison of J -integral values with energy release-rate values computed from interaction integral.

3.6.3 An infinite solid with a flat elliptical crack under shear

Application of tractions parallel to the faces of the elliptical crack described in Section 3.6.2 generates mode-II and mode-III loading. Computed stress intensity factors verify the accuracy of interaction-integral procedures for mixed-mode loading of a curved crack modeled with straight finite elements along the front. Evaluation of the interaction integral at each crack-front location again leads to reported values obtained from the average of domains two through five.

Kassir and Sih [102] derive analytical expressions for stress intensity factors along the front of elliptical cracks under uniform shear loading, included here in Appendix D.2 for convenience. Figure 3.10 illustrates the orientation of crack-face shear according to angle ω . At the ends of the major axis, mode-II stress intensity factors vary most rapidly for $\omega = 0$, and mode-III stress intensity factors vary most rapidly when $\omega = 90^\circ$. We therefore examine stress intensity factors for these two cases.

Figures 3.12(a)-(b) show the variation of normalized stress intensity factors along the crack front from $\phi = 0$ to $\phi = 90^\circ$. Normalization of the stress intensity factors follows Eq. (84), where S equals the magnitude of the uniform shear stress. Stress intensity factors show a maximum deviation of approximately 2.5% from theoretical values for standard quadrature evaluation of the crack-face traction integral over the elements incident on the crack front. Exact integration over these elements improves significantly the accuracy of stress intensity factors. This example demonstrates again that the interaction integral can yield very accurate results for curved cracks with zero local curvature in the model when the computation of r and θ values refers to local orthogonal coordinates. We now examine interaction integral results computed for curved cracks with non-zero local curvature in the model.

3.7 Analysis of cracks modeled with curved elements along front

When elements with curved edges discretize the crack front, non-zero local curvature in the model requires the use of curvilinear coordinates to compute accurate values of r and θ to evaluate the auxiliary fields. In these cases, the second integral of Eq. (67) is non-zero, and the gradients of some auxiliary fields involve terms that reflect explicitly the local curvature of the crack front [74]. This section examines the effects of omitting curvature terms during computations of the interaction integrals.

3.7.1 An infinite solid with a flat penny-shaped crack under tension

A cylindrical mesh with a penny-shaped crack under tension represents a standard problem to explore the influence of crack-curvature terms on the interaction integral. Figure 3.13(a) shows the cross section of a mesh composed of 16,480 20-noded brick ele-

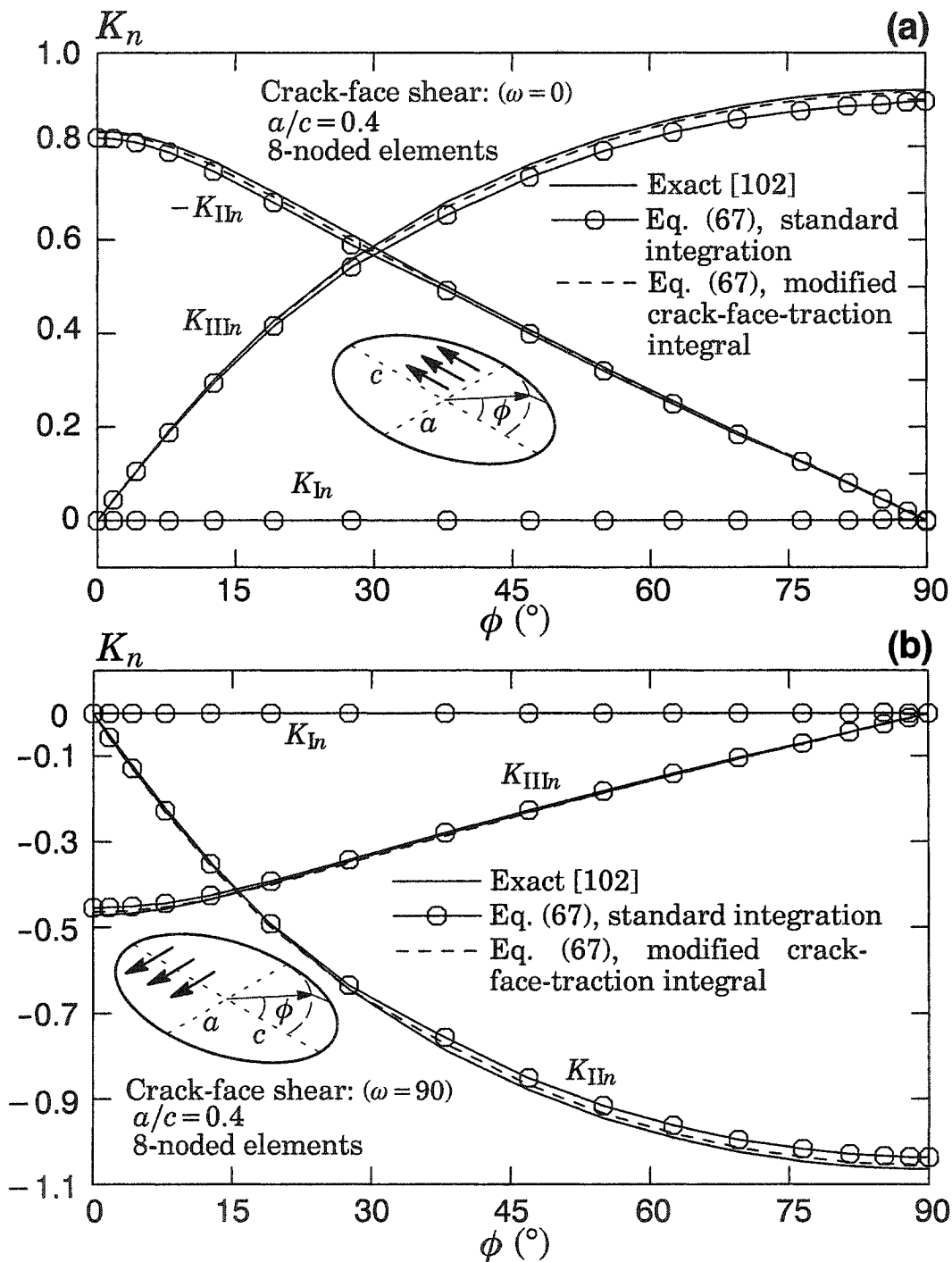


Fig. 3.12. Normalized analytical and numerical stress intensity factor values along the front of a flat elliptical carrying crack-face shear in an infinite solid. Crack-face shear induces loading in modes II and III for (a) shear parallel to the major axis ($\omega = 0$); (b) shear parallel to the minor axis ($\omega = 90$).

ments. A Young's modulus of 30,000 and Poisson's ratio of 0.3 describe material proper-

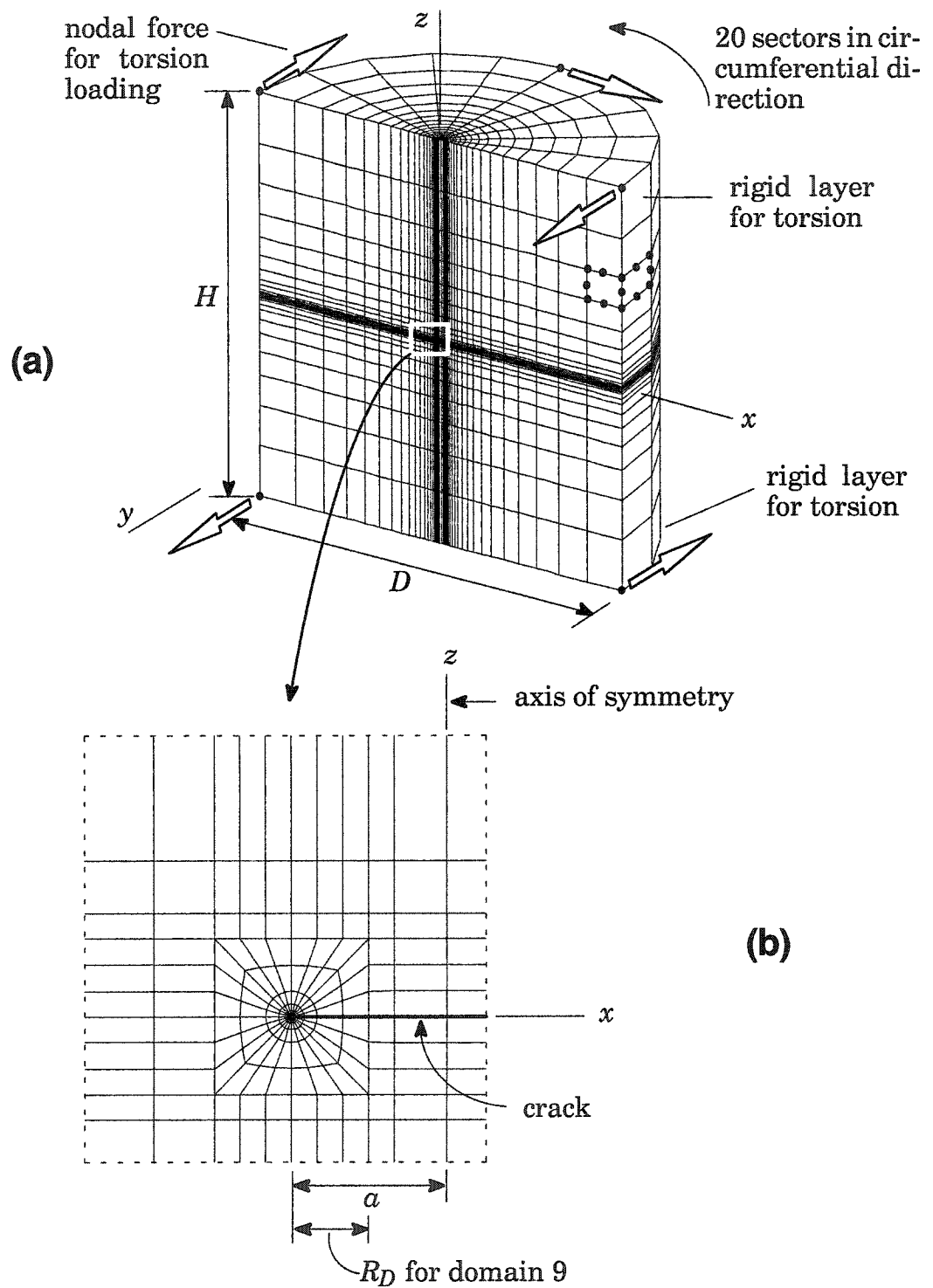


Fig. 3.13. (a) Section view of cylindrical mesh representing an infinite body with a penny-shaped crack. 16,480 20-noded hexagonal elements comprise the mesh. Dimensions are $H/a = D/a = 80$. (b) View of mesh in crack-front region.

ties. The ratios of mesh height H and diameter D to crack radius a are $H/a = D/a = 80$. This cylindrical mesh has 20 sectors of elements surrounding the axis of symmetry, and domains surrounding the crack front are divided into 24 sectors, as seen in Fig. 3.13(b). Elements surrounding the crack-front have a size of $L_e/a = 0.00129$ with one collapsed face and quarter-point nodes on edges normal to the front. Two models following the above description provide insight into the difference between stress intensity factors generated using a mesh with straight and curved elements incident on the crack front. For the mesh with straight edges, computations of r and θ in this section follow the procedure described in Appendix C which uses local orthogonal coordinates. For the mesh with curved elements, computations of r and θ use curvilinear coordinates along the analytically-defined curve representing the crack front.

Uniform crack-face pressure σ_0 imposes mode-I loading, and stress intensity factors computed at each crack-front location lead to reported stress intensity factor values obtained by averaging values from domains two through five. Normalization of stress intensity factors follows as

$$K_{In} = \frac{K_I}{\sigma_0 \sqrt{\pi a}}. \quad (85)$$

Table 3.3 shows very good agreement among stress intensity factors obtained using the interaction integral in Eq. (67), the standard J -integral (Eqs. (53), (70)), analytical solutions for an infinite body, and asymptotic expressions for a finite cylinder. The asymptotic expression for stress intensity factors corresponds to a penny-shaped crack of radius a in a finite homogeneous cylinder of radius $b = D/2$ loaded in tension. The asymptotic solution is [21]

$$K_I = \frac{2N \sqrt{a(1 - a/b)}}{\pi^{3/2}(b^2 - a^2)} \left(1 + \frac{1a}{2b} - \frac{5a^2}{8b^2} + 0.421 \frac{a^3}{b^3} \right), \quad (86)$$

where N is the normal force acting on the cylinder. When the crack size shrinks to zero, i.e. $a/b \rightarrow 0$, this expression reduces to the stress intensity factor for a penny-shaped crack in an infinite body under tension [103]:

$$K_I = \frac{2}{\pi} \sigma_0 \sqrt{\pi a}, \quad (87)$$

where σ_0 is the remote tensile stress, equal to $N/\pi b^2$ for the finite cylinder, or the crack-face-opening pressure for an infinite cylinder.

The mesh with curved elements yields more accurate interaction integral and J -integral results than the mesh with straight-edged elements. The straight-edge mesh includes zero error from the crack-face traction integral, while the value from the mesh with curved edges includes some error due to the inexact 4×4 quadrature employed to integrate Eq. (68). A comparison of numerical results generated from the two meshes

indicates that the combined influence of the curvature terms in the auxiliary field and the second integral of Eq. (67) must be less than $\approx 1.0\%$ for this problem.

Table 3.3. Normalized stress intensity factors for a penny-shaped crack in an infinite homogeneous solid under torsion and tension, illustrated in Figs. 3.2 and 3.13. Normalization follows $K_{In} = K_I/(\sigma_0\sqrt{\pi a})$ for tension, and for torsion, $K_{IIIIn} = K_{III}/(\tau_0\sqrt{\pi a})$, where $\tau_0 = 2T\alpha/(\pi b^4)$.

loading	source	result	% difference
tension K_{In}	infinite body [103]	0.6366	—
	finite cylinder [21]	0.6366	0.00
	interaction integral (straight edges)	0.6299	-1.05
	from J -integral (straight edges)	0.6309	-0.90
	interaction integral (curved edges)	0.6316	-0.79
	from J -integral (curved edges)	0.6348	-0.28
torsion K_{IIIIn}	infinite body [103]	0.4244	—
	finite cylinder [21]	0.4244	0.00
	interaction integral (straight edges)	0.4268	+0.57
	from J -integral (straight edges)	0.4307	+1.48
	interaction integral (curved edges)	0.4194	-1.18
	from J -integral (curved edges)	0.4228	-0.38

3.7.2 An infinite solid with a flat penny-shaped crack under torsion

The meshes employed in Section 3.7.1 also enable computation of mode-III stress intensity factors for cracks in a homogeneous cylinder under torsion. Boundary conditions for torsion loading include nodal loads and one fixed node at each end of the cylinder (see Fig. 3.13(a)). Assignment of a high Young's modulus to the layer of elements at both ends of the cylinder ensures a uniform distribution of torsional stresses. Other regions of the mesh have a Young's modulus of 30,000 and a Poisson's ratio of 0.3. We again report stress intensity factor values obtained from the average of domains two through five.

Table 3.3 shows good agreement between stress intensity factors obtained from the interaction integral, the J -integral, analytical solutions for an infinite body and asymptotic expressions for a finite cylinder. An expression for the mode-III stress intensity factor along a penny-shaped crack of radius a , in a finite homogeneous cylinder of radius $b = D/2$, loaded in torsion is [21]

$$K_{\text{III}} = \frac{8T\alpha^{3/2}\sqrt{(1-a/b)}}{3\pi^{3/2}(b^4-a^4)} \left(1 + \frac{1a}{2b} + \frac{3a^2}{8b^2} + \frac{5a^3}{16b^3} - \frac{93a^4}{128b^4} + 0.038\frac{a^5}{b^5} \right), \quad (88)$$

where T is total torque. When the crack size shrinks to zero, i.e. $a/b \rightarrow 0$, this expression reduces to

$$K_{\text{III}} = \frac{4}{3\pi} \frac{2T\alpha}{\pi b^4} \sqrt{\pi a}. \quad (89)$$

For torque T applied to an uncracked cylinder of radius $b = D/2$, the quantity $\tau_0 = 2T\alpha/\pi b^4$ equals the magnitude of the linearly-varying shear stress, τ , at distance $r = a$ from the longitudinal axis. For the perturbed problem, in which loading conditions consist of crack-face tractions rather than far-field loads, $\tau = 2Tr/\pi b^4$ defines the linearly-varying shear tractions applied to the crack faces between $r = 0$ and $r = a$. For a linearly-varying traction applied on the crack face to generate torsional loading (magnitude τ_0 at a), the stress intensity factor for a penny-shaped crack in an infinite body is [103]

$$K_{\text{III}} = \frac{4}{3\pi} \tau_0 \sqrt{\pi a}. \quad (90)$$

Normalization of K_{III} follows

$$K_{\text{III}n} = \frac{K_{\text{III}}}{\tau_0 \sqrt{\pi a}}. \quad (91)$$

As Table 3.3 shows, the stress intensity factor computed from the interaction integral is slightly more accurate when the model crack front has straight elements, but computations from the J -integral improve in accuracy for the mesh with curved front elements. The curvature terms omitted from the interaction integral may play a greater role for the torsion loading here than for the tension loading. Nevertheless, errors introduced by approximate evaluations of the interaction-integral (that omit curvature terms) remain less than 2% for this example.

3.8 Summary and conclusions

This work describes an interaction-integral formulation and computational procedure applicable to compute mixed-mode, stress-intensity factors for curved 3-D cracks in homogeneous solids under remote mechanical loading and applied crack-face tractions. The described procedures adapt readily into existing 3-D codes that utilize a domain-integral formulation to compute J -integral values. The commonly adopted, 2-D Williams solutions for the mixed-mode, auxiliary field in the interaction integral does not satisfy equilibrium or strain-displacement compatibility when expressed in curvilinear coordinates used for curved crack fronts, thereby leading to additional terms in the interac-

tion integral. A potentially significant contribution to the interaction-integral arises when the otherwise traction-free crack faces have applied loads. Through numerical solutions for several 3-D crack configurations, this work explores the significance of the additional (curvature) terms on computed stress-intensity factors relative to the various techniques often employed to mesh the cracked geometry (linear *vs.* quadratic elements, straight *vs.* curved elements along the crack front). These examples also explore the significance on stress-intensity factors of loadings (tractions) applied directly on the crack faces.

Evaluation of the interaction integral requires values for the auxiliary fields at integration points for elements within a domain defined at a crack-front location. The singular nature of the auxiliary fields at the crack front necessitates highly accurate values for the crack tip coordinates (r, θ) of the integration points—otherwise auxiliary field values become grossly incorrect. The use of straight or curved finite elements along the crack front dictates the choice of algorithms to compute the (r, θ) values. For curved front elements, an iterative Newton procedure, coupled with an analytical definition for the local crack-front geometry, is often adopted. We show here that such a procedure may introduce unacceptable errors for crack fronts modeled with straight elements, and thus describe an alternative procedure to compute accurate values for (r, θ) using a local, orthogonal coordinate system for each straight element incident on the crack front.

The use of elements with straight edges (linear or quadratic) along the crack front, coupled with the new procedure to compute (r, θ) values at integration points, eliminates the additional terms appearing in the interaction integral formulation for curvilinear coordinates. Numerical evaluation of the interaction integral becomes identical to that for an entirely straight crack front. The stress intensity factors computed here for models constructed with straight elements along curved crack fronts agree very closely with corresponding values obtained through the J -integral and with available analytical solutions. The use of quadratic elements (with straight edges) provides some additional increase in the solution quality compared to an identical mesh of linear elements.

The examples here using curved (quadratic) elements along the crack front omit terms in the interaction integral that arise from the definition of auxiliary fields in curvilinear coordinates. Comparisons of computed stress-intensity factors with corresponding J -integral values and with analytical solutions demonstrate that this simpler interaction-integral method yields highly accurate values for curved cracks with reasonable levels of mesh refinement that also provide accurate J -values.

The curvature terms appearing in the interaction integral appear to have an effect similar to the use of higher-order interpolation functions (p -version mesh refinement). Higher-order elements may improve the accuracy of a solution for a boundary-value problem by representing more realistically the gradients in field quantities. Similarly,

auxiliary-field terms that arise due to curvilinear coordinates represent a more accurate description along a curved crack, and thus improve interaction integral results. However, as normal mesh refinement reduces element size (h -version mesh refinement), linear elements represent accurately the gradients present in the actual fields, and the relative influence of curvature terms must diminish. The incorporation of curvature terms in the interaction integral would appear most beneficial with coarse meshes when reasonable mesh refinement is not a viable option. The analyses described here demonstrate that omission of auxiliary-field and interaction-integral terms arising from crack-front curvature simplifies the computation of interaction integrals and yields accurate stress intensity factors with reasonable levels of mesh discretization.

Finally, the numerical examples demonstrate clearly the strong significance of the crack-face integral contribution for models containing loaded crack faces. The term must be included and must be evaluated accurately. The special, exact integration procedure developed here for use with straight-sided, crack-front elements provides a simple approach to increase the accuracy of computed stress-intensity factors.

Chapter 4

Computation of Mixed-Mode Stress Intensity Factors

4.1 Introduction

A significant body of experimental work has been performed to observe crack behavior in functionally-graded materials (FGMs), and numerical methods have been developed to complement these experimental investigations, as well as to assist in the development of engineered FGM systems [206, 168]. FGMs employed in applications such as thermal barrier coatings, are exposed to severe stress gradients induced by thermal and/or mechanical loading. These harsh conditions frequently lead to the formation of surface cracks, which are a significant failure mechanism in FGM coatings [39, 178]. Many works develop numerical techniques to analyze cracks in two-dimensional (2-D) FGM specimens [59, 124, 77, 7, 31, 32, 43, 53, 109, 112, 116, 84], but few establish methods to analyze three-dimensional (3-D) fractures such as the surface crack.

Analysis capabilities and understanding of 3-D crack behavior in FGMs are improving, however. Ozturk and Erdogan [161, 162] solve integral equations to obtain stress intensity factors for axisymmetric cracks in infinite solids with a graded interface. Li and Zou [129, 130] and Li et al. [131] perform axisymmetric finite-element analyses of circumferentially-cracked FGM cylinders. They compute mode-I stress intensity factors using a displacement correlation technique (DCT) which links computed crack-face displacements with Williams' [221] stress-intensity-factor expressions for near-tip displacements. Jin et al. [98, 99] investigate quasi-static and elastic-plastic mode-I crack growth in 3-D FGMs using a cohesive-zone model. Forth et al. [68] simulate mixed-mode fatigue growth of surface cracks in FGMs using the DCT in conjunction with boundary-element analysis. Walters et al. [212] use a form of the domain integral described by Shih et al. [192], as well as the DCT, to compute mode-I stress intensity factors along surface cracks in FGM plates under thermal and mechanical loading. Jin and Dodds [96] employ the same domain integral to investigate crack-growth-resistance behavior in 3-D FGM specimens under mode-I loading. Established methods for computing mixed-mode stress intensity factors in 3-D FGMs currently seem limited to the DCT [68]. The present work investigates a robust and accurate, domain-based interaction-integral method for the computation of mixed-mode stress intensity factors along 3-D cracks in FGMs.

Two-state interaction integrals are a powerful tool for the analysis of cracks under mixed-mode loading [203, 34]. Interaction integrals involve numerical procedures simi-

lar to those necessary to evaluate the J -integral [181, 226], and are a convenient and accurate tool used widely to analyze cracks in 3-D solids [143, 48, 49, 50, 125, 217]. Curvature of 3-D crack fronts and crack surfaces imposes special requirements on the interaction-integral formulation. By including curvature effects, Nahta and Moran [142], Gosz et al. [74] and Gosz and Moran [75] develop formulations of the interaction integral for axisymmetric cracks, curved 3-D interface cracks and non-planar 3-D cracks, respectively. Dolbow and Gosz [75] extend the interaction-integral technique to FGMs by including additional terms to incorporate material gradients. Their work and subsequent studies employ interaction integrals to analyze cracks in 2-D FGMs [179, 113-116]. The present work extends existing capabilities to assess the significance of crack-like defects in FGMs by investigating the interaction-integral method as a tool for computing mixed-mode stress intensity factors along curved, planar 3-D cracks in graded solids under mechanical loading.

The organization of remaining sections is as follows: Section 4.2 presents the domain integral that underlies current FGM interaction-integral formulations including the one employed in this study. Section 4.3 reviews the interaction-integral procedure for quasi-static, mechanical loading of FGMs, and Section 4.4 describes related numerical procedures. Section 4.5 demonstrates the accuracy of interaction-integral computations for 3-D FGMs through analyses of cracks in thin specimens under mixed-mode, in-plane loading, and of fully 3-D specimens with cracks loaded in all three modes. Some observations and inferences conclude the work in Section 4.6.

4.2 A domain integral for 3-D cracks in FGMs

Shih et al. [192] develop the domain-integral method as a convenient, numerical procedure to evaluate the J -integral [181] for 3-D crack fronts. Because the domain integral procedure underlies the interaction integral method employed here, this section reviews key details of the derivation as found in Shih et al. [192].

An expression for the J -integral at location s along a 3-D crack front is [192]

$$J(s) = \lim_{\Gamma \rightarrow 0} \int_{\Gamma} (W\delta_{1i} - \sigma_{ij}u_{j,1})n_i d\Gamma, \quad (92)$$

where W is strain energy density, σ_{ij} represents stress components, u_j denotes displacement components, and δ_{ij} is the Kronecker delta. Latin subscripts range from 1 to 3, and unless otherwise noted, repeated indices imply summation. The partial derivative $(\cdot)_{,i} = \partial(\cdot)/\partial X_i$ indicates the spatial derivative of (\cdot) with respect to direction X_i of the coordinate system defined at crack front position s . The contour Γ with normal \mathbf{n} lies in the X_1 - X_2 plane and extends from the bottom crack face to the top crack face as shown

in Fig. 2.3. Equation (92) remains path-independent for elastic material behavior in the absence of body forces, crack-face tractions and thermal strains, and equals the standard J -integral [181] when the contour of integration shrinks to the crack front, i.e. $r \rightarrow 0^+$.

Shih et al. [192] integrate Eq. (92) along a crack-front segment of length L_C , illustrated in Fig. 2.4. This yields an expression for $\bar{J}(s)$, the approximate energy released when crack segment L_C advances by a prescribed X_1 -displacement $l(s)$, drawn schematically in Fig. 2.4:

$$\bar{J}(s) = \lim_{r \rightarrow 0} \int_{S_t} (\sigma_{ij} u_{j,1} - W \delta_{i1}) l(s) m_i dS. \quad (93)$$

Figure 4.1 shows the tubular surface S_t obtained by sweeping contour $\Gamma(s)$ along the crack front through distance L_C . On $\Gamma(s)$ and S_t , $\mathbf{m} = -\mathbf{n}$ as shown in Fig. 2.3. For nonhomogeneous materials and general loading conditions, Eq. (93) is valid only when the radius r of surface S_t shrinks to zero.

To transform Eq. (93) into a volume integral for convenient numerical evaluation, Shih et al. (1986) construct a simply-connected volume, V , enclosed by surfaces S^+ , S^- , S_1 , S_t , S_2 , and S_3 , shown in Fig. 4.1. They then define a continuous, vector-valued function q_k that varies within V according to

$$q_k = \begin{cases} l(s) & \text{on } S_t, \\ 0 & \text{on } S_1, S_2, S_3, \\ \text{arbitrary elsewhere.} & \end{cases} \quad (94)$$

In the local crack-front coordinate system, X_i , $q_2 = 0$ everywhere. Hereafter, we define $q_k = q_1 = q$, and employ a plateau function for q (Shih et al., 1986). With these definitions of q and with surface S defined as $S = S^+ + S^- + S_1 - S_t + S_2 + S_3$, Eq. (93) becomes

$$\begin{aligned} & \lim_{r \rightarrow 0} \int_{S_t} (\sigma_{ij} u_{j,1} - W \delta_{i1}) q m_i dS \\ &= \int_S (\sigma_{ij} u_{j,1} - W \delta_{i1}) q m_i dS - \int_{S^+ + S^-} (\sigma_{ij} u_{j,1} - W \delta_{i1}) q m_i dS, \end{aligned} \quad (95)$$

where the q -function eliminates the integrals over surfaces S_1 , S_2 , and S_3 . An application of the divergence theorem to the first integral in Eq. (95) yields a volume integral:

$$\bar{J}(s) = \int_V (\sigma_{ij} u_{j,1} - W \delta_{i1}) q_{,i} dV + \int_V (\sigma_{ij} u_{j,1} - W \delta_{i1})_{,i} q dV. \quad (96)$$

For homogeneous materials under elastic, quasi-static, isothermal loading with no body forces, the second integral in Eq. (96) vanishes. For flat cracks lying in the X_1 - X_3 plane, $m_1 = m_3 = 0$ on surfaces S^+ and S^- , respectively, and since $t_j = \sigma_{ij} m_i$, Eq. (95) becomes

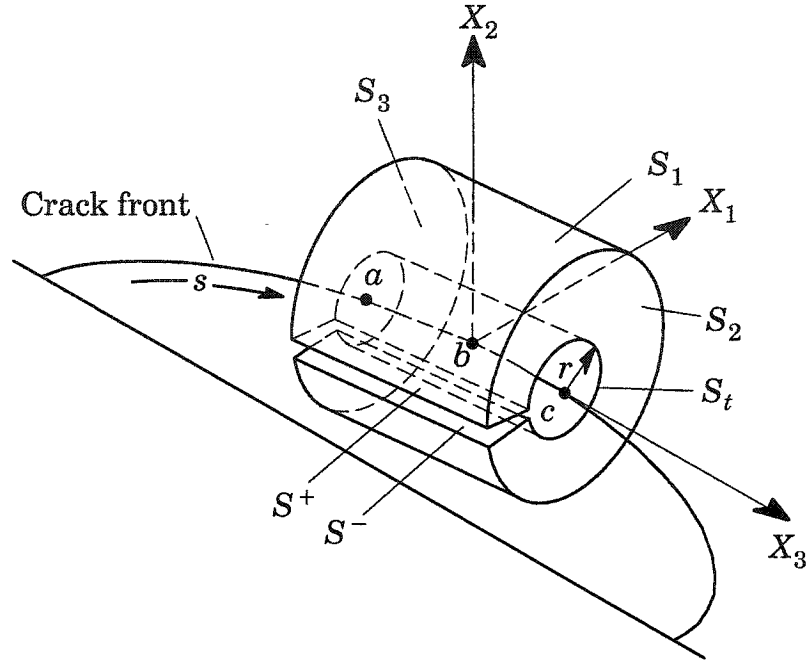


Fig. 4.1. Surfaces enclosing volume domain for computation of $\bar{J}(s)$ at location $s=b$ along a curved crack front. For functionally-graded material, S_t must shrink to the crack front, i.e. $r \rightarrow 0^+$.

$$\int_{S^+ + S^-} t_j u_{j,1} q dS. \quad (97)$$

Hence the energy release rate at location s equals

$$\begin{aligned} \bar{J}(s) = & \int_V (\sigma_{ij} u_{j,1} - W \delta_{1i}) q_{,i} dV + \int_V (\sigma_{ij} u_{j,1} - W \delta_{1i})_{,i} q dV \\ & - \int_{S^+ + S^-} t_j u_{j,1} q dS. \end{aligned} \quad (98)$$

Through the definition of W , Eq. (98) accounts for elastic, thermomechanical loading of FGMs, and remains path-independent when loading conditions do not include body forces or inertia. If the energy release rate varies little along crack segment L_C , $J(s)$ may be approximated by [192]

$$J(s) = \frac{\bar{J}(s)}{\int_{L_C} l(s) ds}. \quad (99)$$

The energy release rate for cracks in 3-D specimens corresponds approximately to stress intensity factors for opening, sliding and anti-plane modes, (K_I , K_{II} and K_{III} , respectively) according to

$$J(s) = \frac{K_I^2 + K_{II}^2}{E^*(s)} + \frac{1 + \nu(s)}{E(s)} K_{III}^2, \quad (100)$$

where $E^*(s) = E(s)/(1 - \nu(s)^2)$ for plane-strain, and $E^*(s) = E(s)$ for plane-stress. For FGMs, this expression requires material properties at crack-front location s , i.e. the asymptotic behavior of crack-front fields is identical in homogeneous and nonhomogeneous materials [59]. Walters, et al. [212] employ Eqs. (98)-(130) to calculate stress intensity factors along semi-elliptical surface cracks with traction-free faces in 3-D FGM specimens under mode-I thermomechanical loading. Nikishkov and Atluri [152] demonstrate how to decompose $J(s)$ into three orthogonal components, enabling calculation of the three stress intensity factor components. The domain form of the interaction integral employs Eqs. (98)-(130) to directly determine the stress intensity factors.

4.3 An interaction integral for 3-D cracks in FGMs

Interaction-integral procedures generally are performed as a post-processing step after the solution of a boundary-value problem. The method typically requires the superposition of actual, computed equilibrium fields, with corresponding fields from an auxiliary equilibrium state selected by the analyst. Evaluation of a conservation integral for this superimposed state leads to expressions that comprise interacting actual and auxiliary terms. Interaction integrals have been developed from Betti's reciprocal theorem [203] the J -integral [34], and the L - and M -integrals of Knowles and Sternberg [122, 38, 106]. The present section describes an interaction-integral procedure to compute stress intensity factors along cracks in 3-D FGMs under mechanical loading, and discusses terms that arise due to material nonhomogeneity and crack-front curvature. We discuss three formulations that account for material gradient effects, the asymptotic behavior of the integrals, and the computational procedure to obtain stress intensity factors.

4.3.1 A domain integral for two superimposed equilibrium states

The interaction integral method constitutes a post-processing step that utilizes the stresses, strains and displacements generated during the solution of a boundary-value problem. We refer to numerically-calculated quantities as *actual* fields. By superimposing *actual* fields with *auxiliary* fields corresponding to a second, arbitrary equilibrium state, we obtain fields for the *superimposed* state. For this superimposed state, Eq. (98) becomes

$$\begin{aligned}
\bar{J}^{(S)}(s) &= \int_V \left[(\sigma_{ij} + \sigma_{ij}^{aux})(u_{j,1} + u_{j,1}^{aux}) - W^{(S)}\delta_{1i} \right] q_{,i} dV \\
&+ \int_V \left[(\sigma_{ij} + \sigma_{ij}^{aux})(u_{j,1} + u_{j,1}^{aux}) - W^{(S)}\delta_{1i} \right]_{,i} q dV \\
&- \int_{S^+ + S^-} (t_j + t_j^{aux})(u_{j,1} + u_{j,1}^{aux}) q dS .
\end{aligned} \tag{101}$$

Here, superscripts (1) and (2) indicate actual and auxiliary fields, respectively, and (S) denotes the superimposed state. We must now examine the strain energy density for the superimposed state, $W^{(S)}$, to separate Eq. (101) into useful components.

The strain energy density, W , is a function of position $\mathbf{x} = (x_1, x_2, x_3)$, and a function of strain components ε_{ij} . For a linear-elastic, nonhomogeneous material, $W^{(S)}$ is

$$\begin{aligned}
W^{(S)}(\mathbf{x}) &= \frac{1}{2} (\sigma_{ij} + \sigma_{ij}^{aux}) (\varepsilon_{ij} + \varepsilon_{ij}^{aux}) \\
&= \frac{1}{2} \sigma_{ij} \varepsilon_{ij} + \frac{1}{2} \sigma_{ij}^{aux} \varepsilon_{ij}^{aux} + \frac{1}{2} (\sigma_{ij} \varepsilon_{ij}^{aux} + \sigma_{ij}^{aux} \varepsilon_{ij}) \\
&= W + W^{aux} + W^{(I)} ,
\end{aligned} \tag{102}$$

where $W^{(I)}$ is

$$W^{(I)} = \frac{1}{2} (\sigma_{ij} \varepsilon_{ij}^{aux} + \sigma_{ij}^{aux} \varepsilon_{ij}) . \tag{103}$$

4.3.2 The interaction integral

Equation (102) permits the separation of Eq. (101) into three parts:

$$\bar{J}^{(S)}(s) = \bar{J}(s) + \bar{J}^{aux}(s) + \bar{I}(s) , \tag{104}$$

where $\bar{J}^{(S)}(s)$ becomes the domain integral for the superimposed state, $\bar{J}(s)$ equals Eq. (98), the domain integral for the actual state, $\bar{J}^{aux}(s)$ is the domain integral for the auxiliary state, and $\bar{I}(s)$ is the domain form of the interaction integral, written as

$$\begin{aligned}
\bar{I}(s) &= \int_V \left[\sigma_{ij} u_{j,1}^{aux} + \sigma_{ij}^{aux} u_{j,1} - \frac{1}{2} (\sigma_{jk} \varepsilon_{jk}^{aux} + \sigma_{jk}^{aux} \varepsilon_{jk}) \delta_{1i} \right] q_{,i} dV \\
&+ \int_V \left[\sigma_{ij} u_{j,1}^{aux} + \sigma_{ij}^{aux} u_{j,1} - \frac{1}{2} (\sigma_{jk} \varepsilon_{jk}^{aux} + \sigma_{jk}^{aux} \varepsilon_{jk}) \delta_{1i} \right]_{,i} q dV \\
&- \int_{S^+ + S^-} (t_j u_{j,1}^{aux} + t_j^{aux} u_{j,1}) q dS .
\end{aligned} \tag{105}$$

For quasi-static, isothermal loading of homogeneous specimens in the absence of body forces and crack-face tractions, the second and third integrals of Eq. (105) vanish. Be-

cause auxiliary fields correspond to an arbitrary equilibrium state, Eq. (105) simplifies with the assumption that the auxiliary state includes no crack-face tractions. The surface integral in Eq. (105) thus becomes

$$\int_{S^+ + S^-} t_j u_{j,1}^{aux} q dS . \quad (106)$$

Equation (106) defines the term apparently neglected in earlier works, as discussed in Section 4.3.1. We now discuss choices for auxiliary fields that lead to the calculation of stress intensity factors.

4.3.3 Auxiliary fields

A common approach to introduce stress intensity factors into the interaction integral is to define auxiliary fields according to the asymptotic fields near a crack [221]:

$$\sigma_{ij}^{aux} = \frac{K_I^{aux}}{\sqrt{2\pi r}} f_{ij}^I(\theta) + \frac{K_{II}^{aux}}{\sqrt{2\pi r}} f_{ij}^{II}(\theta) + \frac{K_{III}^{aux}}{\sqrt{2\pi r}} f_{ij}^{III}(\theta) , \quad (107)$$

$$u_j^{aux} = \frac{K_I^{aux}}{2\mu(s)} \sqrt{\frac{r}{2\pi}} g_j^I(\theta, \nu(s)) + \frac{K_{II}^{aux}}{2\mu(s)} \sqrt{\frac{r}{2\pi}} g_j^{II}(\theta, \nu(s)) \\ + \frac{2K_{III}^{aux}}{\mu(s)} \sqrt{\frac{r}{2\pi}} g_j^{III}(\theta, \nu(s)) , \quad (108)$$

$$\varepsilon_{ij}^{aux} = \frac{1}{2} (u_{ij}^{aux} + u_{ji}^{aux}) , \quad (109)$$

where r and θ are polar coordinates measured from the crack front, and $\mu(s)$ and $\nu(s)$ are respectively the shear-modulus and Poisson-ratio values at crack front location s . For convenience, Appendix E supplies expressions for the angular functions $f_{ij}(\theta)$ and the plane-stress and plane-strain forms for $g_j(\theta, \nu(s))$. Eischen [59] proves that the asymptotic crack-tip fields in homogeneous and graded materials are identical in form, which means that Eqs. (107)-(109) are valid for FGMs. Anlas et al. [8] study the zone of dominance of these expressions in FGMs.

These 2-D auxiliary fields are a function of location r and θ , and shear modulus μ . Nakamura and Parks [144] and Gosz et al. [74] use these fields to analyze cracks in 3-D solids by assuming that near-plane-strain conditions exist near the crack front. Their accurate results for stress intensity factors demonstrate the adequacy of this approximation. Kim et al. [106] demonstrate the use of numerically-generated auxiliary fields to obtain stress intensity factors. Near-tip fields in homogeneous and graded materials exhibit similar asymptotic behavior [59], and therefore Eqs. (107)-(108) are useful auxiliary fields for FGMs. For FGMs, the displacements in Eq. (108) depend upon the value of the shear modulus at crack-front location s :

$$\mu(s) = \frac{E(s)}{2(1 + \nu(s))} . \quad (110)$$

4.3.4 Constant constitutive tensor interaction-integral formulation

Auxiliary fields defined by Eqs. (107)-(109) satisfy equilibrium, compatibility, and constitutive relations at crack-front location s where the asymptotic functions maintain validity for both homogeneous and graded material. A constant constitutive tensor, employing material properties at crack-front location s in the FGM specimen, relates auxiliary stresses and strains at s as $\sigma_{ij}^{aux} = C_{ijkl}(s)\varepsilon_{ij}^{aux}$. If the auxiliary fields follow this constitutive relation, they represent equilibrium in a homogeneous material with properties described everywhere by $\mu(s)$. Actual fields, however, represent equilibrium in a material with spatially-varying properties described by $\mu(\mathbf{x})$. This is apparent from Eq. (102) written in terms of the constitutive tensors:

$$\begin{aligned} W^{(S)} &= W + W^{aux} + W^{(I)} \\ &= \frac{1}{2} \left(C_{ijkl}(\mathbf{x})\varepsilon_{kl}\varepsilon_{ij} + C_{ijkl}(s)\varepsilon_{kl}^{aux}\varepsilon_{ij}^{aux} + C_{ijkl}(\mathbf{x})\varepsilon_{kl}\varepsilon_{ij}^{aux} + C_{ijkl}(s)\varepsilon_{kl}^{aux}\varepsilon_{ij} \right). \end{aligned} \quad (111)$$

With the auxiliary fields described above, Eq. (105) becomes

$$\begin{aligned} \bar{I}(s) &= \int_V \left[\sigma_{ij} u_{j,1}^{aux} + \sigma_{ij}^{aux} u_{j,1} - \frac{1}{2} (\sigma_{jk} \varepsilon_{jk}^{aux} + \sigma_{jk}^{aux} \varepsilon_{jk}) \delta_{1i} \right] q_{,i} dV \\ &+ \int_V \left[\frac{1}{2} (\sigma_{ij} \varepsilon_{ij,1}^{aux} + \sigma_{ij}^{aux} \varepsilon_{ij,1}) - \frac{1}{2} (\sigma_{ij,1} \varepsilon_{ij}^{aux} + \sigma_{ij,1}^{aux} \varepsilon_{ij}) \right] q dV \\ &- \int_{S^+ + S^-} t_j u_{j,1}^{aux} q dS. \end{aligned} \quad (112)$$

In Eq. (112), the $\sigma_{ij,j} u_{j,1}^{aux}$ and $\sigma_{ij,j}^{aux} u_{j,1}$ terms cancel due to equilibrium, and other terms combine because $\sigma_{ij} u_{j,1i}^{aux} = \sigma_{ij} \varepsilon_{ij,1}^{aux}$ and $\sigma_{ij}^{aux} u_{j,1i} = \sigma_{ij}^{aux} \varepsilon_{ij,1}^t$. All terms in Eq. (112) correspond to the expressions in Eqs. (107)-(109) and their derivatives, and material-property values at crack-front location s . Standard finite-element procedures enable numerical calculation of actual stress and strain derivatives [41]. Rao and Rahman [179] employ Eq. (112) to calculate stress intensity factors for cracks in 2-D FGMs under remote mechanical loading, and we adopt the nomenclature of Kim and Paulino [115] who describe Eq. (112) and its associated auxiliary fields as the ‘‘constant constitutive tensor’’ formulation.

4.3.5 Non-equilibrium interaction-integral formulation

Another choice for auxiliary fields includes displacements and strains defined according to Eqs. (108)-(109), and stresses derived from the FGM constitutive tensor (see Appendix E):

$$\sigma_{ij}^{aux} = C_{ijkl}(\mathbf{x})\varepsilon_{kl}^{aux}, \quad (113)$$

so that

$$\begin{aligned}\sigma_{ij,i}^{aux} &= 0 & : \mathbf{x} &= 0 \\ \sigma_{ij,i}^{aux} &\neq 0 & : \mathbf{x} &\neq 0.\end{aligned}\quad (114)$$

At $\mathbf{x} = s$, material properties for the FGM are valid for use in the auxiliary fields of Eqs. (107)-(109). Kim and Paulino [115] refer to the interaction integral based on this choice of auxiliary fields as the “non-equilibrium” formulation. Equation (113) leads to the useful relationship

$$\sigma_{ij} \varepsilon_{ij}^{aux} = C_{ijkl}(\mathbf{x}) \varepsilon_{kl} \varepsilon_{ij}^{aux} = C_{klij}(\mathbf{x}) \varepsilon_{ij}^{aux} \varepsilon_{kl} = \sigma_{ij}^{aux} \varepsilon_{ij}, \quad (115)$$

where the same constitutive tensor, $C_{ijkl}(\mathbf{x})$, operates on both actual (3-D) and auxiliary (2-D) fields (see Appendix E):

$$\sigma_{ij} = C_{ijkl}(\mathbf{x}) \varepsilon_{kl} \text{ and } \sigma_{ij}^{aux} = C_{ijkl}(\mathbf{x}) \varepsilon_{kl}^{aux}. \quad (116)$$

Equation (64) enables the expression of Eq. (103) as

$$W^I = \sigma_{ij} \varepsilon_{ij}^{aux} = \sigma_{ij}^{aux} \varepsilon_{ij}. \quad (117)$$

Either expression for W^I in Eq. (117) is suitable for numerical evaluation, and each may be used to verify the other. With auxiliary fields defined according to Eqs. (108), (109) and (113), Eq. (105) becomes

$$\begin{aligned}\bar{I}(s) &= \int_V \left(\sigma_{ij} u_{j,1}^{aux} + \sigma_{ij}^{aux} u_{j,1} - \sigma_{jk} \varepsilon_{jk}^{aux} \delta_{1i} \right) q_{,i} dV \\ &+ \int_V \left(\sigma_{ij} u_{j,1i}^{aux} + \sigma_{ij,i}^{aux} u_{j,1} + \sigma_{ij}^{aux} \varepsilon_{ij,1} - \sigma_{ij,1} \varepsilon_{ij}^{aux} - \sigma_{ij} \varepsilon_{ij,1}^{aux} \right) q dV \\ &- \int_{S^+ + S^-} t_j u_{j,1}^{aux} q dS.\end{aligned}\quad (118)$$

Here, we employ Eq. (117), and eliminate $\sigma_{ij,j} u_{j,1}^{aux}$ due to equilibrium of actual stresses. The definition of auxiliary stresses in Eq. (113) implies that in general, $\sigma_{ij,j}^{aux} u_{j,1} \neq 0$. To avoid calculating numerical derivatives of strain and stress in the second integral, we may rewrite the stress-derivative term as

$$\begin{aligned}\sigma_{ij,1} \varepsilon_{ij}^{aux} &= C_{ijkl,1}(\mathbf{x}) \varepsilon_{kl} \varepsilon_{ij}^{aux} + C_{ijkl}(\mathbf{x}) \varepsilon_{kl,1} \varepsilon_{ij}^{aux} \\ &= C_{ijkl,1}(\mathbf{x}) \varepsilon_{kl} \varepsilon_{ij}^{aux} + C_{klij}(\mathbf{x}) \varepsilon_{ij}^{aux} \varepsilon_{kl,1} \\ &= C_{ijkl,1}(\mathbf{x}) \varepsilon_{kl} \varepsilon_{ij}^{aux} + \sigma_{ij}^{aux} \varepsilon_{kl,1}.\end{aligned}\quad (119)$$

When these expressions combine with Eq. (118), the result becomes

$$\begin{aligned}
\bar{I}(s) = & \int_V \left(\sigma_{ij} u_{j,1}^{aux} + \sigma_{ij}^{aux} u_{j,1} - \sigma_{jk} \varepsilon_{jk}^{aux} \delta_{1i} \right) q_{,i} dV \\
& + \int_V \left[\sigma_{ij,i}^{aux} u_{j,1} - C_{ijkl,1}(\mathbf{x}) \varepsilon_{kl} \varepsilon_{ij}^{aux} \right] q dV \\
& - \int_{S^+ + S^-} t_j u_{j,1}^{aux} q dS, \tag{120}
\end{aligned}$$

where the relationships $\sigma_{ij} u_{j,1i}^{aux} = \sigma_{ij} \varepsilon_{ij,1}^{aux}$ and $\sigma_{ij}^{aux} u_{j,1i} = \sigma_{ij}^{aux} \varepsilon_{ij,1}^t$ eliminate some terms. Because Eq. (113) generates non-equilibrating auxiliary stresses remote from the crack front, $\sigma_{ij,i}^{aux} u_{j,1}$ is nonvanishing, and we have $\sigma_{ij,i}^{aux} = C_{ijkl,1}(\mathbf{x}) \varepsilon_{ij}^{aux} + C_{ijkl}(\mathbf{x}) \varepsilon_{ij,1}^{aux}$. In Eq. (120), auxiliary displacements and strains employ material properties at crack-front location s . Eq. (120) contains fewer terms than Eq. (118), and does not include derivatives of actual stresses or strains. Kim and Paulino [115] employ Eq. (120) to calculate stress intensity factors for cracks in 2-D plane-stress and plane-strain problems with remote mechanical loading.

4.3.6 Incompatibility interaction-integral formulation

The two forms of the interaction integral discussed previously include the effects of FGM properties through assumptions regarding constitutive relations or stress equilibrium. The interaction integral for FGMs originally proposed by Dolbow and Gosz [75] accounts for material gradients through the definition of auxiliary strain. Strains defined by Eq. (109) are compatible with displacements described by Eq. (108). In what Kim and Paulino [115] refer to as the ‘‘incompatibility formulation,’’ however, auxiliary strains depend upon auxiliary stresses defined by Eq. (107) and the spatially-varying compliance tensor (see Appendix E):

$$\varepsilon_{ij}^{aux} = S_{ijkl}(\mathbf{x}) \sigma_{kl}^{aux}, \tag{121}$$

Auxiliary stresses in Eq. (107) satisfy equilibrium, but strain-displacement compatibility is satisfied only when material properties correspond to crack-front location s . At s , therefore, $\varepsilon_{ij}^{aux} = S_{ijkl}(s) \sigma_{kl}^{aux} = 0.5(u_{ij} + u_{j,i})$, but for $\mathbf{x} \neq s$,

$$\varepsilon_{ij}^{aux} = S_{ijkl}(\mathbf{x}) \sigma_{kl}^{aux} \neq \frac{1}{2}(u_{ij}^{aux} + u_{j,i}^{aux}). \tag{122}$$

This incompatibility causes additional terms to appear in the interaction-integral formulation because

$$\sigma_{ij} \left(u_{j,1i}^{aux} - \varepsilon_{ij,1}^{aux} \right) \neq 0. \tag{123}$$

The relationships expressed in Eqs. (64), (116) and (117) remain valid for this formulation, and Eq. (105) becomes

$$\begin{aligned}
\bar{I}(s) &= \int_V \left(\sigma_{ij} u_{j,1}^{aux} + \sigma_{ij}^{aux} u_{j,1} - \sigma_{jk} \varepsilon_{jk}^{aux} \delta_{1i} \right) q_{,i} dV \\
&+ \int_V \left(\sigma_{ij} u_{j,1i}^{aux} + \sigma_{ij}^{aux} \varepsilon_{ij,1} - \sigma_{ij,1} \varepsilon_{ij}^{aux} - \sigma_{ij} \varepsilon_{ij,1}^{aux} \right) q dV \\
&- \int_{S^+ + S^-} t_j u_{j,1}^{aux} q dS .
\end{aligned} \tag{124}$$

Here, $\sigma_{ij,i} u_{j,1}^{aux} = \sigma_{ij,i}^{aux} u_{j,1} = 0$ because actual and auxiliary stress fields satisfy equilibrium. Eq. (65) enables the removal of derivatives of actual stresses and strains from Eq. (124), yielding

$$\begin{aligned}
\bar{I}(s) &= \int_V \left(\sigma_{ij} u_{j,1i}^{aux} + \sigma_{ij}^{aux} u_{j,1} - \sigma_{jk} \varepsilon_{jk}^{aux} \delta_{1i} \right) q_{,i} dV \\
&+ \int_V \left[\sigma_{ij} \left(u_{j,1i}^{aux} - \varepsilon_{ij,1}^{aux} \right) - C_{ijkl,1}(\mathbf{x}) \varepsilon_{kl} \varepsilon_{ij}^{aux} \right] q dV \\
&- \int_{S^+ + S^-} t_j u_{j,1}^{aux} q dS ,
\end{aligned} \tag{125}$$

where the relations $\sigma_{ij} u_{j,1i}^{aux} = \sigma_{ij} \varepsilon_{ij,1}^{aux}$ and $\sigma_{ij}^{aux} u_{j,1} = \sigma_{ij}^{aux} \varepsilon_{ij,1}$ again simplify the expression. The term $\sigma_{ij} (u_{j,1i}^{aux} - \varepsilon_{ij,1}^{aux})$ results directly from the incompatibility between auxiliary strains and displacements, and the second integral of Eq. (128) vanishes for homogeneous material. Auxiliary displacements in this formulation require material properties at crack-front location s . Derivatives of auxiliary strain follow as

$$\varepsilon_{ij,1}^{aux} = S_{ijkl,1}(\mathbf{x}) \sigma_{kl}^{aux} + S_{ijkl}(\mathbf{x}) \sigma_{kl,1}^{aux} , \tag{126}$$

where Eq. (107) defines auxiliary stresses.

Dolbow and Gosz [53], Rao and Rahman [179] and Kim and Paulino [114] employ Eq. (128) to calculate stress intensity factors for cracks in 2-D FGM geometries under remote mechanical loading. Kim and Paulino also employ this formulation to calculate stress intensity factors for cracks in orthotropic FGMs [113]. The current study also employs Eq. (128) for numerical implementation.

4.3.7 Influence of crack-front curvature on the interaction integral

Computation r - and θ -values for the 2-D auxiliary fields in Eqs. (107)-(109) occurs in planes orthogonal to the crack front. For curved cracks, auxiliary fields must therefore be defined in curvilinear coordinates. Nahta and Moran [142] observe that in a curvilinear coordinate system, the 2-D auxiliary fields described by Williams' [221] solution, do not satisfy strain-displacement compatibility or stress equilibrium. Therefore,

$$\sigma_{ij}(u_{j,1i}^{aux} - \varepsilon_{ij,1}^{aux}) \neq 0, \text{ and } \sigma_{ij,i}^{aux} \neq 0. \quad (127)$$

For curved cracks, these non-vanishing terms appear in the interaction integral, and some auxiliary-field gradients also become non-zero (see [74]). Thus both crack-front curvature and material nonhomogeneity bear similar influences on interaction-integral expressions. However, crack-front curvature requires the interaction integral to include *both* expressions in Eq. (127), whereas for two of the previously described interaction-integral formulations for FGMs, material nonhomogeneity requires *either* the expression in Eq. (113) *or* that in Eq. (123).

4.3.8 An interaction integral for curved 3-D cracks in FGMs

Here, we will employ the incompatibility formulation to incorporate material gradients into the interaction-integral formulation. By combining the effects of both material nonhomogeneity and curvature as discussed previously, Eq. (105) may be expressed as

$$\begin{aligned} \bar{I}(s) = & \int_V \left(\sigma_{ij} u_{j,1}^{aux} + \sigma_{ij}^{aux} u_{j,1} - \sigma_{jk} \varepsilon_{jk}^{aux} \delta_{li} \right) q_{,i} dV \\ & + \int_V \left[\sigma_{ij} \left(u_{j,1i}^{aux} - \varepsilon_{ij,1}^{aux} \right) + \underline{\sigma_{ij,i}^{aux} u_{j,1}} - C_{ijkl,1}(\mathbf{x}) \varepsilon_{kl} \varepsilon_{ij}^{aux} \right] q dV \\ & - \int_{S^+ + S^-} t_j u_{j,1}^{aux} q dA, \end{aligned} \quad (128)$$

where equilibrium of actual stresses causes $\sigma_{ij,i} u_{j,1}^{aux}$ to vanish. For straight, traction-free cracks in homogeneous material, the second and third integrals of Eq. (128) vanish. For straight, traction-free cracks in FGMs, the third integral and the underlined terms in the second integral vanish, and Eq. (128) reduces to the interaction integral proposed by Dolbow and Gosz [53]. Kim [108] and Paulino and Kim [169] prove the existence of the interaction integral for FGMs by demonstrating that the second integral in Eq. (128) vanishes in the limit as the domain size shrinks to zero. A point-wise value of the interaction integral along a 3-D crack front follows from the procedure in Eq. (99), i.e.

$$I(s) = \frac{\bar{I}(s)}{\int_{L_c} q(s) ds}. \quad (129)$$

4.3.9 Extraction of stress intensity factors

As a function of the mixed-mode stress intensity factors K_I , K_{II} and K_{III} , the energy release rate may be expressed as [6]

$$J(s) = \frac{K_I^2 + K_{II}^2}{E^*(s)} + \frac{1 + \nu(s)}{E(s)} K_{III}^2, \quad (130)$$

where $E^*(s) = E(s)/(1 - \nu(s)^2)$ for plane-strain, and $E^*(s) = E(s)$ for plane-stress conditions. For FGMs, this expression requires material properties at crack-front location, s . From Eq. (130), superposition of actual and auxiliary states gives

$$\begin{aligned} J^S(s) &= \frac{1}{E^*(s)} \left[(K_I + K_I^{aux})^2 + (K_{II} + K_{II}^{aux})^2 \right] + \frac{1 + \nu(s)}{E(s)} (K_{III} + K_{III}^{aux})^2, \\ &= J(s) + J^{aux}(s) + I(s), \end{aligned}$$

where

$$I(s) = \frac{1}{E^*(s)} (2K_I K_I^{aux} + 2K_{II} K_{II}^{aux}) + \frac{1 + \nu(s)}{E(s)} (2K_{III} K_{III}^{aux}). \quad (131)$$

Equations (128), (129) and (131) provide the necessary relationship between the interaction integral and actual stress intensity factors. By alternately assigning a non-zero value to only one auxiliary stress intensity factor, Eq. (131) yields

$$K_I(s) = \frac{E^*(s)}{2} I(s), \quad K_{II}(s) = \frac{E^*(s)}{2} I(s), \quad \text{and} \quad K_{III}(s) = \mu(s) I(s). \quad (132)$$

4.3.10 Behavior of volume and area integrals

The singular auxiliary fields in Eq. (128) govern the existence of the integrals as the domain size shrinks to zero. For volume integrals, we consider a cylindrical domain and first examine a representative term in the first integral of Eq. (128) for a constant value of q_i :

$$\lim_{r \rightarrow 0} \int_V \sigma_{ij} u_{j,1}^{aux} q_i dV \approx \int_V O(r^{-1/2}) O(r^{-1/2}) r dr d\theta dz \approx \int_V dr d\theta dz = 0. \quad (133)$$

The behavior of the first two terms in the second integral of Eq. (128) can be observed by rewriting Eq. (126) as follows [108]:

$$\varepsilon_{ij,1}^{aux} = S_{ijkl,1}(\mathbf{x}) \sigma_{kl}^{aux} + (S_{ijkl}(\mathbf{x}) - S_{ijkl}(s)) \sigma_{kl,1}^{aux} + S_{ijkl}(s) \sigma_{kl,1}^{aux}. \quad (134)$$

According to the definitions of auxiliary stress and displacement used in the incompatibility formulation, $S_{ijkl}(s) \sigma_{ij,1}^{aux} = 0.5(u_{i,j1}^{aux} + u_{j,i1}^{aux})$, and therefore $\sigma_{ij}(u_{j,1i}^{aux} - S_{ijkl}(s) \sigma_{kl,1}^{aux}) = 0$. An expression for the first two terms of the second integral in Eq. (128) is then

$$\sigma_{ij} (u_{j,1i}^{aux} - \varepsilon_{ij,1}^{aux}) = \sigma_{ij} \left[-S_{ijkl,1}(\mathbf{x}) \sigma_{kl}^{aux} - (S_{ijkl}(\mathbf{x}) - S_{ijkl}(s)) \sigma_{kl,1}^{aux} \right]. \quad (135)$$

Asymptotic fields in homogeneous and functionally graded material have the same form when the functions describing material-property variations are bounded, continu-

ous and differentiable. Material property variation in this case may be described by a Maclaurin series expansion about crack-front position s ($r=0$) [59]:

$$S_{ijkl}(\mathbf{x}) = S_{ijkl}(r, \theta, z) = S_{ijkl}(s) \left(1 + rS_{ijkl}^a(\theta, z) + \frac{r^2}{2}S_{ijkl}^b(\theta, z) + O(r^3) + \dots \right), \quad (136)$$

where $S_{ijkl}^a(\theta, z)$ and $S_{ijkl}^b(\theta, z)$ are bounded, continuous and differentiable functions of θ and z . This definition of the compliance tensor implies that $S_{ijkl,1}(\mathbf{x}) \approx O(r^\beta)$, where $\beta \geq 0$, and $(S_{ijkl}(\mathbf{x}) - S_{ijkl}(s)) \approx O(r^\gamma)$, where $\gamma \geq 1$. In the limit as domain size r approaches zero, for a constant q -value, $\beta = 0$, and $\gamma = 1$, the second integral of Eq. (128) behaves as

$$\begin{aligned} & \lim_{r \rightarrow 0} \int_V \left[\sigma_{ij} \left(u_{j,1i}^{aux} - \varepsilon_{ij,1}^{aux} \right) - C_{ijkl,1}(\mathbf{x}) \varepsilon_{kl} \varepsilon_{ij}^{aux} \right] q dV, \\ & \approx \int_V \left\{ O(r^{-1/2}) \left[O(r^{-1/2}) + O(r)O(r^{-3/2}) \right] + O(r^{-1/2})O(r^{-1/2}) \right\} q r dr d\theta dz, \\ & \approx \int_V dr d\theta dz = 0. \end{aligned} \quad (137)$$

The integrands of the first two integrals in Eq. (128) are therefore well-behaved.

Integration over the surface of an element adjacent to a crack front enables us to observe the behavior of the surface-traction integral in Eq. (128). Values of $K_I^{aux} = 1.0$, $t_2 = 1.0$ and $q(r, z) = 1.0$ correspond to a mode-I crack-opening surface pressure, and lead to an integrable, inverse square-root singularity:

$$\lim_{r \rightarrow 0} \int_S t_j u_{j,1}^{aux} q dS = \int_0^z \int_0^r \pm \frac{\mu(s)}{\sqrt{r}} dr dz \approx O(r^{1/2}) = 0, \quad (138)$$

where the sign of the integrand depends upon the sign of $u_{j,1}^{aux}$ at $\theta = \pm \pi$. All terms in Eq. (138) are independent of the solution to the boundary-value problem because crack-face tractions, auxiliary-displacement derivatives, q -values and the domain of integration are defined a-priori by the user. Section 3.4.3 describes a simple transformation that enables standard Gauss quadrature procedures to integrate exactly the surface-traction term which generally contains an inverse-square root singularity in elements adjacent to the crack.

4.4 Numerical aspects

Evaluation of the interaction integral using the finite-element method employs numerical techniques similar to those used to solve the boundary-value problem. This section provides a description of some relevant procedures. All computations in this study uti-

lize WARP3D, a freely-distributed, open-source finite-element code with extensive fracture-analysis capabilities, developed at the University of Illinois at Urbana-Champaign [78].

4.4.1 Numerical evaluation of volume and surface integrals

In a finite-element context, standard Gauss quadrature procedures permit the evaluation of Eq. (128) (e.g. [41]):

$$\begin{aligned} \bar{I}(s) = & \sum_V \sum_p^{elems \ gpts} \left[\left(\sigma_{ij} u_{j,1}^{aux} + \sigma_{ij}^{aux} u_{j,1} - \sigma_{jk} \varepsilon_{jk}^{aux} \delta_{li} \right) q_{,i} \det \mathbf{J} \right]_p w_p \\ & + \sum_V \sum_p^{elems \ gpts} \left\{ \left[\sigma_{ij} \left(u_{j,1i}^{aux} - \varepsilon_{ij,1}^{aux} \right) + \frac{\sigma_{ij}^{aux} u_{j,1}}{i} - C_{ijkl,1}(\mathbf{x}) \varepsilon_{kl} \varepsilon_{ij}^{aux} \right] q \det \mathbf{J} \right\}_p w_p \\ & - \sum_S \sum_p^{faces \ gpts} \left(t_j u_{j,1}^{aux} q \det \mathbf{J} \right)_p w_p, \end{aligned} \quad (139)$$

where the summations include all integration points on the interior or on the face of elements included in volume V . Weight w_p scales the function at each integration point, and $\det \mathbf{J}$ represents the determinant of the coordinate Jacobian for 2-D surface or 3-D volume coordinates. In this study, the q -function follows the plateau variation described by Shih et al. [192], and varies from zero on surfaces A_1 , A_2 and A_3 , to 1.0 at crack-front position s on A_t (see Fig. 4.1). Quadrature over element volumes employs a $2 \times 2 \times 2$ rule. The surface integral in Eq. (128) has an inverse-square-root singularity and comprises only terms defined a-priori by the analyst. For elements with straight edges, we compute this integral exactly, according to the simple procedure described by Walters et al. (2004b). For elements with curved edges, we employ standard 4×4 Gauss quadrature.

4.4.2 Computation of material-property derivatives

Numerical evaluation of Eq. (139) requires derivatives at element integration points of the compliance- and constitutive-tensor components. We interpolate specified nodal material properties $E(\mathbf{x})$ and $\nu(\mathbf{x})$ and compute their X_1 -derivatives at integration points using standard isoparametric interpolation (e.g. [132, 110]):

$$(E(\mathbf{x}))_p = \sum_{I=1}^n N_I(E(\mathbf{x}))_I, \quad (E(\mathbf{x}),_1)_p = \sum_{I=1}^n \sum_{k=1}^3 \frac{\partial N_I}{\partial \eta_k} \frac{\partial \eta_k}{\partial X_1} (E(\mathbf{x}))_I, \quad (140)$$

$$(\nu(\mathbf{x}))_p = \sum_{I=1}^n N_I(\nu(\mathbf{x}))_I, \quad \text{and} \quad (\nu(\mathbf{x}),_1)_p = \sum_{I=1}^n \sum_{k=1}^3 \frac{\partial N_I}{\partial \eta_k} \frac{\partial \eta_k}{\partial X_1} (\nu(\mathbf{x}))_I, \quad (141)$$

where $(E(\mathbf{x}))_p$ and $(\nu(\mathbf{x}))_p$ denote material properties at integration points, n is the number of element nodes, $(E(\mathbf{x}))_I$ and $(\nu(\mathbf{x}))_I$ are material properties at node I , N_I is the element shape function for node I evaluated at integration point p , and η_k are parent coordinates.

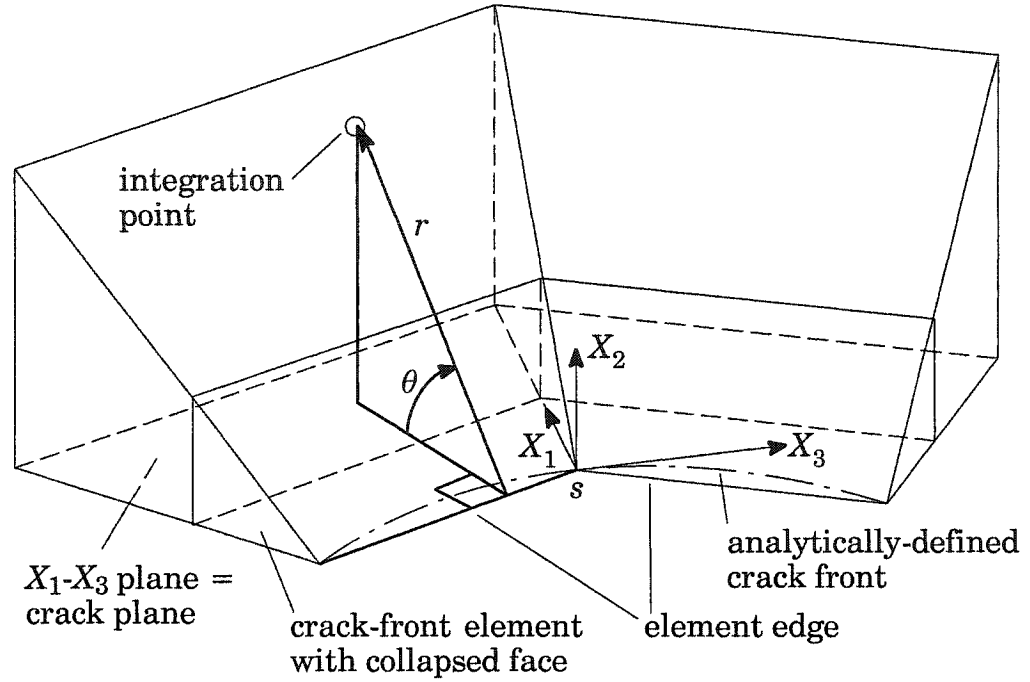


Fig. 4.2. Computation of r and θ for an integration point in a domain of four straight-edged elements. $\bar{I}(s)$ values lead to stress intensity factors at crack-front location s .

dinates. Integration-point values of $E(\mathbf{x})_{,1}$ and $\nu(\mathbf{x})_{,1}$ enable the direct computation of constitutive-tensor derivatives as

$$C_{ijkl}(\mathbf{x})_{,1} = \frac{\partial C_{ijkl}(\mathbf{x})}{\partial E(\mathbf{x})} E(\mathbf{x})_{,1} + \frac{\partial C_{ijkl}(\mathbf{x})}{\partial \nu(\mathbf{x})} \nu(\mathbf{x})_{,1}, \quad (142)$$

where the quantities $\partial(\cdot)/E(\mathbf{x})$ and $\partial(\cdot)/\nu(\mathbf{x})$ denote explicit derivatives of (\cdot) with respect to $E(\mathbf{x})$ and $\nu(\mathbf{x})$. The same process yields $S_{ijkl}(\mathbf{x})_{,1}$.

4.4.3 Computation of r and θ for auxiliary fields

Auxiliary stresses and strains of order $O(r^{-1/2})$ are extremely sensitive to small errors in r when r is small. It is therefore important to compute r - and θ -values in curvilinear coordinates. Gosz et al. [74] and Gosz and Moran [75] provide thorough details for this procedure. For curved cracks discretized by finite elements with straight edges, it is more appropriate to compute r and θ using local Cartesian coordinates defined on each segment of the crack-front, as illustrated in Fig. 4.2 and described with more detail in Walters et al. [213].

4.5 Numerical examples

This section presents examples that include the computation of mode-I and mode-II stress intensity factors in thin, 3-D FGM specimens under in-plane loading, as well as in fully 3-D configurations.

4.5.1 Boundary-layer model (homogeneous material)

A boundary-layer model enables verification of the current interaction integral implementation for cracks in homogeneous media. Here, discretization of a thin circular disk of radius R consists of one layer of 20-noded hexagonal elements. The ratio of thickness t to model radius, R , is $t/R = 0.018$ (see Fig. 4.3). Elements form 36 “sectors” in the circumferential direction, and 43 concentric “rings” around the crack front. Thirty-six elements with collapsed faces and quarter-point nodes surround the crack front. Displacement boundary conditions corresponding to William’s solution (Eqs. (A7)-(A9)) induce pure mode-I, mode-II and mode-III conditions in three separate analyses. For pure mode-I loading, nodes at the model boundary (at distance R from the crack front) undergo imposed displacements u_1 and u_2 , as defined in Eqs. (A7)-(A8) where K_I equals an assigned value, and $K_{II} = 0$. Similarly, Eqs. (A7)-(A8) produce boundary displacements u_1 and u_2 for pure mode-II loading when K_{II} equals an assigned value, and $K_I = 0$. Use of plane-stress auxiliary fields (Appendix A) in the interaction integral yields stress intensity factors for the plane-stress state. For plane-strain conditions, we assign $u_3 \equiv 0$ everywhere and employ the plane-strain auxiliary fields to obtain stress intensity factors from the interaction integral. Pure mode-III loading results from the assignment of displacements $u_1 = 0$, $u_2 = 0$ to all nodes in the model, where Eq. (A9) defines u_3 for an assigned value of K_{III} . Displacements of all nodes in the model according to nonzero values of K_I , K_{II} and K_{III} test the fully mixed-mode case.

Evaluation of the interaction integral for the cases described above, i.e. modes I and II for plane stress and plane strain, and anti-plane shear for mode III, yield stress intensity factors that match to within four or more digits the stress intensity factors used to generate displacement loading conditions. These results verify the correct implementation of the first integral in Eq. (128) for analyses of 3-D homogeneous solids with cracks under plane and anti-plane loading. Shim et al. [193] develop a novel boundary-layer technique that permits verification of numerically-computed stress intensity factors, but here, we employ results from numerical studies in the literature. We now examine a problem to verify the second integral of Eq. (128) that includes effects of material non-homogeneity.

4.5.2 3-D analyses simulating plane-stress and plane-strain conditions

The interaction-integral procedure enables computation of stress intensity factors in thin 3-D configurations under in-plane loading (e.g. [220, 145]). Analyses of a middle-

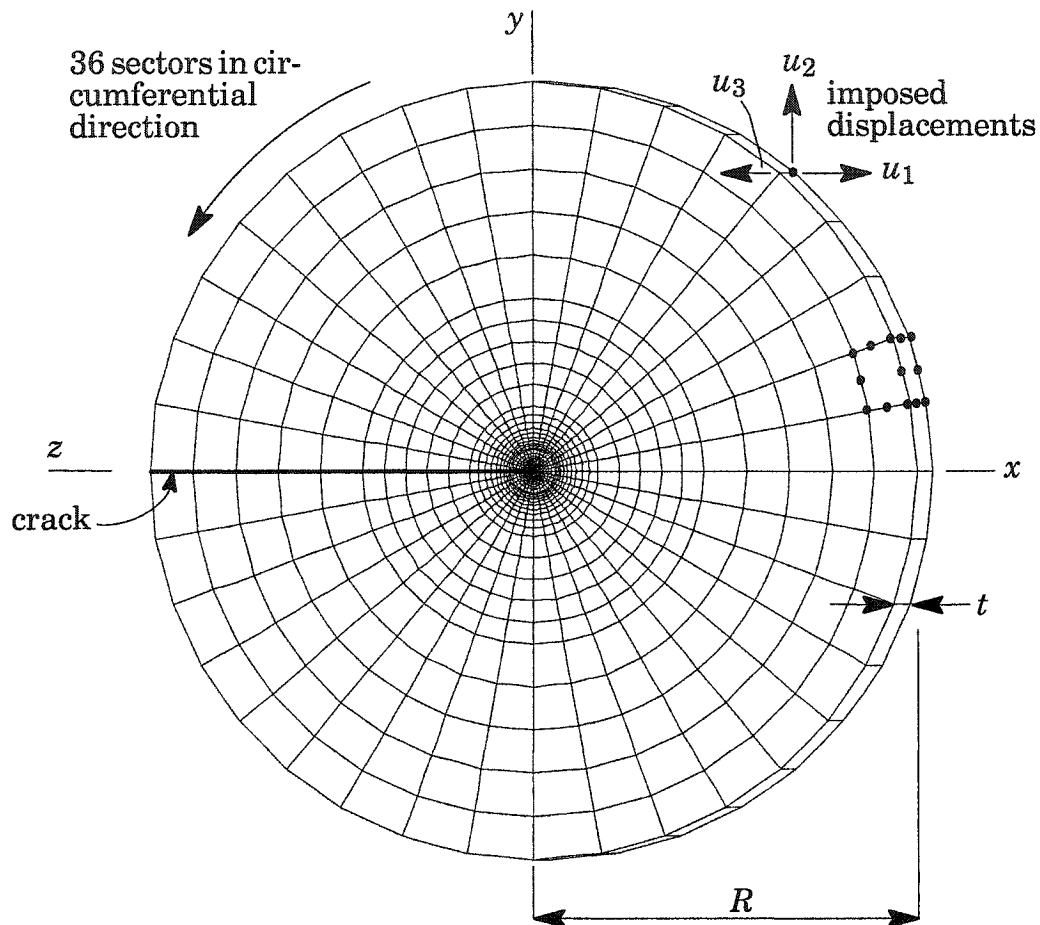


Fig. 4.3. Boundary-layer model used to verify correct calculation of stress intensity factors in a cracked homogeneous solid under plane (modes I-II, plane-stress, plane-strain) and anti-plane (mode-III) deformations. Dimension $t/R = 0.018$. Mesh has 11,054 nodes and 1548 20-noded hexagonal elements arranged in 36 circumferential sectors and 43 rings in the radial direction. 36 collapsed elements with quarter-point nodes surround the crack front.

crack tension specimen with an inclined crack permit useful observations regarding the simulation of plane-stress and plane-strain conditions with 3-D FGM models. Figure 4.4(a) shows the 3-D mesh with a crack inclined at 36° , used to model this problem. A study of mesh-refinement levels for domain-integral computations in 2-D FGMs is found in Kim and Paulino [115]. In the present model, twenty elements with collapsed faces and quarter-point nodes surround the crack front as shown in Fig. 4.4(b). Length L_e indicates the size of the element adjacent to the crack front, and dimension R_D describes the radius of a domain of elements that surround the crack front. Model height H , width W , and thickness t , have values relative to crack length $2a$ given by $H = W = 20a$, and $t = 0.125a$. Crack-front elements are of size $L_e/a = 0.0177$. In this example, Young's modulus varies in the x -direction as $E(x) = E_0 e^{\beta x}$, where $E_0 = E(x = 0)$,

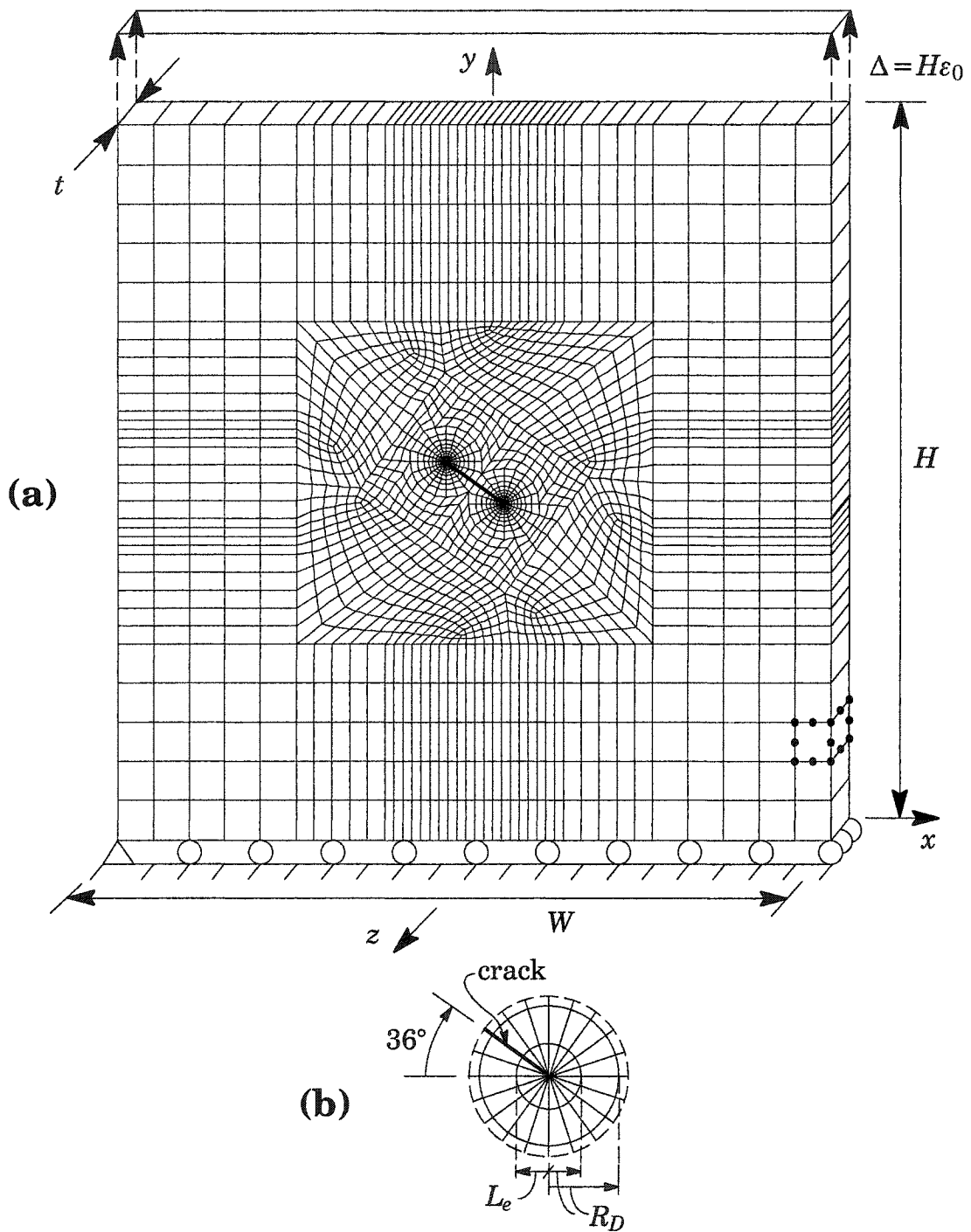


Fig. 4.4. (a) Mesh for fixed-grip displacement of a specimen with a crack inclined at 36° (see Table 4.1). Distance between crack fronts = $2a$. (b) 20 collapsed crack-front elements of size $L_e/a = 0.0177$ surround each crack front. Ratio R_D/a describes domain size in this work.

$\beta\alpha = 0.5$ and $\nu = 0.3$. For loading, all nodes along $y = H$ have an imposed displacement $\Delta = H\epsilon_0$, where ϵ_0 is an assigned strain value. For plane-stress simulations, the model

permits through-thickness deformations. Constrained through-thickness displacements impose plane-strain conditions.

For simulated plane-stress conditions, the model employed here generates non-zero through-thickness stresses, σ_{33} , when $\nu \neq 0$. Williams' [221] solution for plane-stress conditions leads to a non-zero value for the gradient of through-thickness strain:

$$\varepsilon_{33,1}^{aux} = \left[-\frac{\nu(\mathbf{x})}{E(\mathbf{x})}(\sigma_{11}^{aux} + \sigma_{22}^{aux}) \right]_{,1} \neq 0. \quad (143)$$

Consequently, the product $\sigma_{33}\varepsilon_{33,1}^{aux}$ appearing in the second integral of Eq. (128) introduces error into computed stress intensity factors for simulated plane-stress conditions. Two analyses demonstrate the magnitude of this error. The first analysis allows non-zero σ_{33} -values caused by through-thickness Poisson contraction, and for the second analysis, $\sigma_{33}\varepsilon_{33,1}^{aux} \equiv 0$. Table 4.1 lists normalized stress intensity factors computed for the left and right crack fronts in this model. Normalization of stress intensity factors follows

$$K_n = \frac{K}{E_0\varepsilon_0\sqrt{\pi a}}. \quad (144)$$

When $\sigma_{33}\varepsilon_{33,1}^{aux} \equiv 0$, computed stress intensity factors compare well with those of Konda and Erdogan [124], Dolbow and Gosz [53], Kim and Paulino [115] and Dong and Paulino [54]. These results recommend assigning a zero value to the product $\sigma_{33}\varepsilon_{33,1}^{aux}$ when Eq. (128) is used for 3-D simulations of plane-stress configurations. Alternative formulations of the interaction integral for FGMs may not require such a modification (see e.g. [179, 169]). An analysis of the current model for plane-strain conditions leads to computed stress intensity factors that match closely the results obtained by Dong and Paulino [54] (see Table 4.1).

The interaction integral formulation incorporates material nonhomogeneity through the second integral of Eq. (128). Figure 4.5(a)-(b) illustrate the influence of the components of this integral on computed stress intensity factors for this 2-D problem. The plots show relative contributions to computed values of $\bar{I}(s)$ from the various components of Eq. (128), for each of the domains surrounding the right crack tip. In the figure, Eq. (128) is separated into the following components:

$$\bar{I}_1 = \int_V \left(\sigma_{ij}u_{j,1}^{aux} + \sigma_{ij}^{aux}u_{j,1} - \sigma_{jk}\varepsilon_{jk}^{aux}\delta_{1i} \right) q_{,i} dV \quad (145)$$

$$\bar{I}_2 = \int_V \sigma_{ij} \left(u_{j,1i}^{aux} - \varepsilon_{ij,1}^{aux} \right) q dV \quad (146)$$

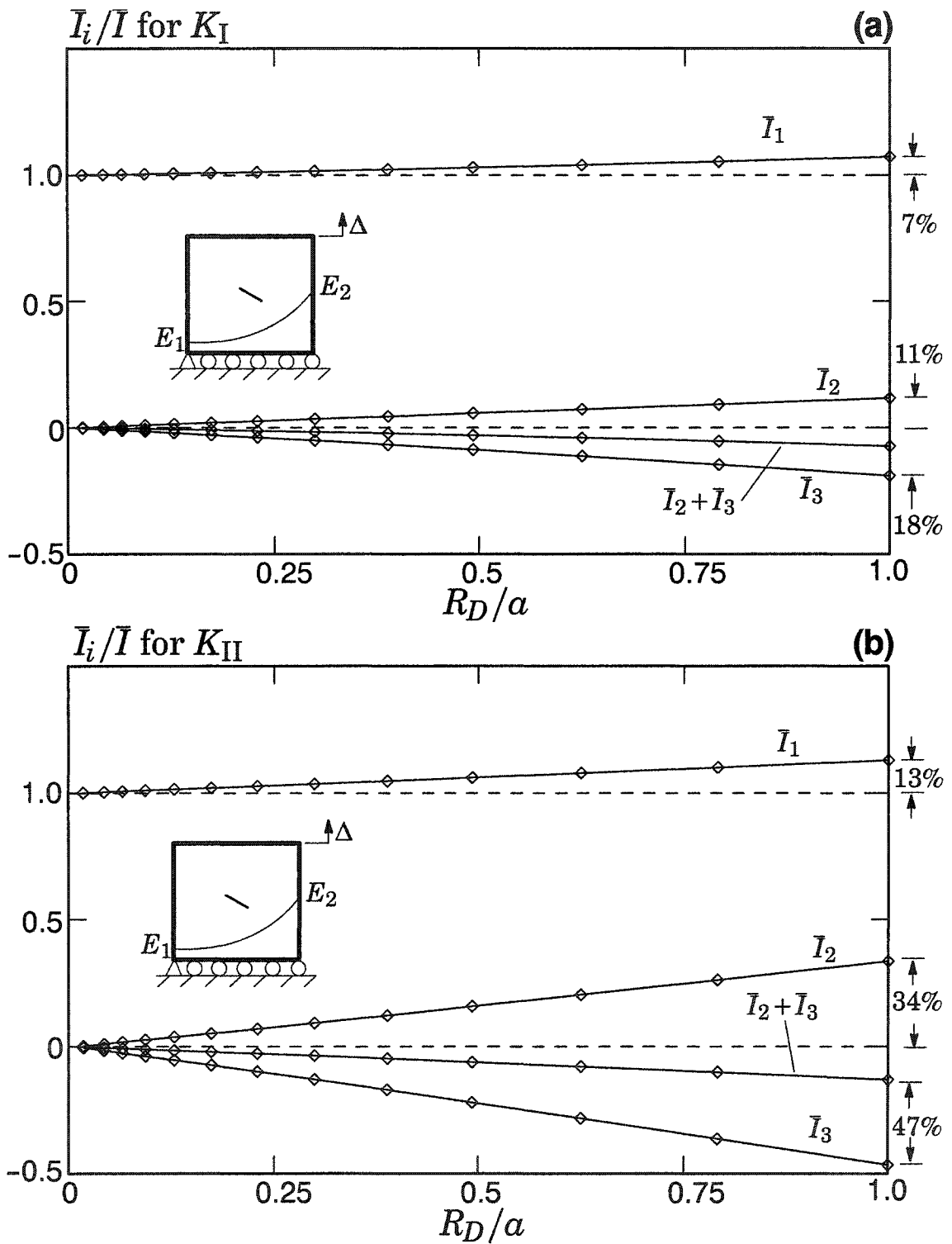


Fig. 4.5. Relative contribution of interaction-integral terms vs. increasing domain size for (a) K_I and (b) K_{II} for an inclined crack in an exponentially-graded M(T) specimen under plane-strain, fixed-grip loading.

$$\bar{I}_3 = \int_V - C_{ijkl,1}(\mathbf{x}) \varepsilon_{kl} \varepsilon_{ij}^{aux} q dV \quad (147)$$

$$\bar{I}_4 = \int_{S^+ + S^-} - t_j u_{j,1}^{aux} q dA. \quad (148)$$

Influence of the second integral in Eq. (128) ($\bar{I}_2 + \bar{I}_3$) increases with domain size, thus maintaining the path independence of $\bar{I}(s)$. Percentages shown on the right of each plot indicate the relative contribution to values of $\bar{I}(s)$ from domain-integral components for the domain of size $R_D/a = 1.0$. These 2-D examples demonstrate the accuracy of 3-D interaction-integral computations for thin FGM specimens.

Table 4.1. Normalized stress intensity factors for in-plane displacement loading of a plate with a through crack inclined at 36° (see Fig. 4.4).

analysis	source	K_{In} left	K_{In} right	K_{IIIn} left	K_{IIIn} right
plane stress	Konda & Erdogan [124]	0.460	0.925	-0.365	-0.548
	present	0.446	0.902	-0.367	-0.556
	present modified*	0.457	0.922	-0.362	-0.551
	Dolbow & Gosz [53]	0.467	0.930	-0.364	-0.560
	Kim & Paulino [115]	0.456	0.922	-0.362	-0.551
	Dong & Paulino [54]	0.457	0.923	-0.363	-0.550
plane strain	present	0.504	1.02	-0.398	-0.605
	Dong & Paulino [54]	0.505	1.02	-0.399	-0.605

$$* \sigma_{33} \varepsilon_{33,1}^{aux} \equiv 0$$

4.5.3 Analysis of planar, curved 3-D cracks in FGMs

This section examines four boundary-value problems involving mixed-mode loading of planar, curved cracks in FGMs. All examples in this section employ plane-strain auxiliary fields, with the assumption that near-plane-strain conditions exist near the crack front. Gosz et al. [74] demonstrate that interaction-integral formulations incorporating the influence of crack-front curvature as described in Sections 4.3.3 and 4.3.8, can greatly improve computed stress intensity factors for cracks in homogeneous and bi-material specimens. Kim et al. [106] also show differences between numerical results that employ and omit corrective terms due to crack curvature. Walters et al. [213] show that for a variety of mixed-mode crack problems in homogeneous material, the influence of curvature terms depends significantly upon mesh discretization, and becomes very small with mesh-refinement levels that permit accurate computation of J -integral val-

ues. In this study we omit all terms from the interaction integral procedure that arise solely from the influence of crack-front curvature. Omitted terms include those underlined in Eq. (128), and auxiliary-field quantities that reflect crack curvature [74]. Use of the terms in Eq. (123) is dictated by material nonhomogeneity and not by crack-front curvature. Computation of r and θ values in curvilinear coordinates as described in Section 4.4.3, is necessary for good accuracy, however, when curved elements align the crack front. In the sequel, comparisons of computed values with analytical solutions demonstrate that good accuracy can be achieved using these approximations.

4.5.4 Mode-I and mode-II loading of a penny-shaped crack in a graded interfacial layer

This example compares numerical and semi-analytical stress intensity factors for a penny-shaped crack under mixed mode-I, mode-II loading conditions in an infinite solid, with a functionally-graded interfacial layer. In this configuration, a semi-infinite solid with Young's modulus E_1 occupies the half-space $z \leq 0$, and another half-space with modulus E_3 occupies the region $z \geq h$. A graded interfacial layer lying in the region $0 \leq z \leq h$ has a Young's modulus described by $E_2(z) = E_1 e^{\beta z}$, $E_2(z = h) = E_3$. Material properties at $z = 0$ and $z = h$ are continuous, but material gradients are not. Poisson's ratio remains constant at 0.3 throughout the body.

When Poisson's ratio is non-zero, tension loading of this FGM specimen generates mode-I and mode-II crack-front loading. This illustrates why for cracks in FGMs, stress intensity factors induced by remote loading generally do not correspond, through superposition, to stress intensity factors generated by crack-face tractions of the same direction and magnitude. The current numerical example employs uniform tractions acting normal to the crack surfaces. This allows a direct comparison between present results and the solutions provided by Ozturk and Erdogan [162], who solve integral equations to obtain stress intensity factors for the axisymmetric crack problem.

A cylindrical mesh with a penny-shaped crack shown in Fig. 4.6(a) comprises 16,480 20-noded brick elements. Cylinder height H and diameter D compare to crack radius a as $H/a = D/a = 80$. Figure 4.6(b) shows the mesh near the crack-front, and illustrates schematically the material variation. The cylinder is formed by 20 sectors of elements that surround the longitudinal axis, and the crack is surrounded by 24 sectors of elements, as shown in Fig. 4.6(b). Elements incident on the crack front have quarter-point nodes and collapsed faces, and are of size $L_e/a = 0.00129$. Two such meshes allow a comparison between interaction-integral results obtained using either straight-edged or curved quadratic elements along the crack front. At any location along the crack, the average of interaction-integral values computed for domains two through five produces stress intensity factors normalized as

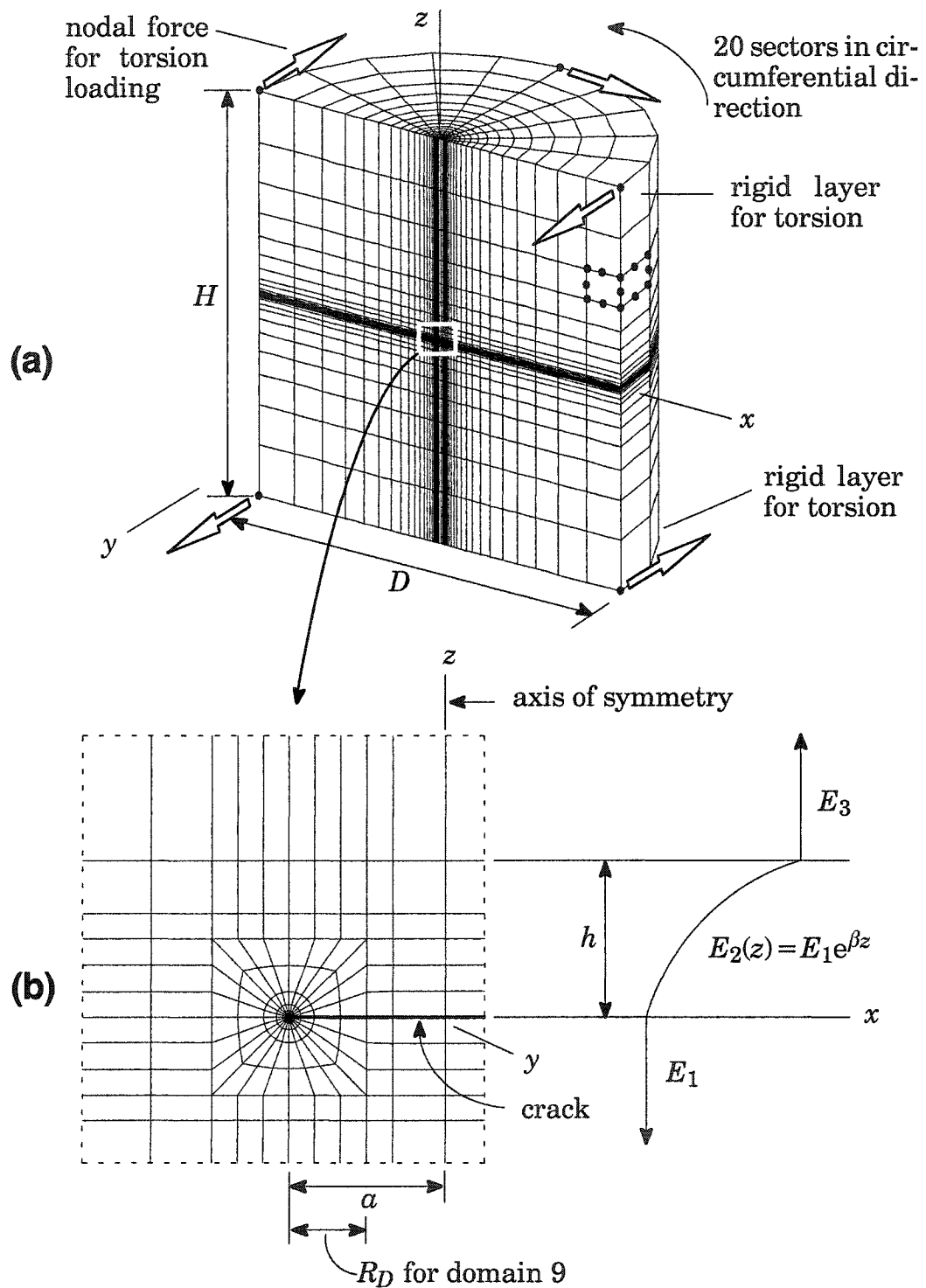


Fig. 4.6. (a) Mesh for infinite body with a penny-shaped crack on the boundary of a graded interfacial layer. (b) View of mesh in crack-front region showing schematic of material variation in interfacial layer for $h/a = 1.0$. Twenty-four sectors of elements of size $L_e/a = 0.00129$ surround the crack front.

$$K_n = \frac{K}{t_0 \sqrt{\pi a}}, \quad (149)$$

where t_0 is the magnitude of the crack-face traction. Table 4.2 lists present numerical results as well as stress intensity factors computed by Ozturk and Erdogan [162] for different interfacial-layer thicknesses and material gradients. Stress intensity factor values obtained using curved crack-front elements are more accurate than those obtained from the mesh with straight crack-front segments despite the error introduced by inexact evaluation of the crack-face-traction integral in Eq. (128). For this crack configuration, accuracy of the numerical results depends heavily upon mesh refinement within and near the graded region, which in this example includes only 3 layers of elements for $h/a = 0.5$, and 5 layers of elements for $h/a = 1.0$ (see Fig. 4.6(b)). Values in Table 4.2 agree well with Ozturk and Erdogan [162] for moderate material gradients in the interfacial layer. A finer mesh discretization would permit computation of accurate results for more severe material gradients within the interfacial layer.

Table 4.2. Normalized stress intensity factors for a penny-shaped crack at the edge of a graded interface between two semi-infinite solids under tension (see Fig. 4.6).

h/a	$\beta\alpha$	E_3/E_1	result	K_{In}	% diff.	K_{IIIn}	% diff.
—	0.0	1.0	Ozturk & Erdogan [162]	0.6366	—	—	—
			straight edges	0.6299	-1.05	—	—
			curved edges	0.6316	-0.79	—	—
0.5	0.5	1.28	Ozturk & Erdogan [162]	0.6079	—	0.0149	—
			straight edges	0.6035	-0.72	0.0146	-2.01
			curved edges	0.6048	-0.51	0.0148	-0.67
1.0	0.5	1.65	Ozturk & Erdogan [162]	0.5955	—	0.0201	—
			straight edges	0.5913	-0.71	0.0196	-2.49
			curved edges	0.5924	-0.52	0.0199	-1.0

We now examine the effect of domain size on path independence of computed stress intensity factors for this problem, using the mesh with curved edges, in which element nodes lie on a circular crack front. For the homogeneous problem, normalized K_I -values are compared with normalized K_I -values obtained from computed J -integral values using the plane-strain conversion:

$$K_I = \sqrt{\frac{JE^*}{1-\nu^2}}. \quad (150)$$

The ratio of the maximum domain size R_D , to crack radius a , is 0.66 for this problem. Figure 4.7 illustrates a very small variation between the computed K_I -values for small

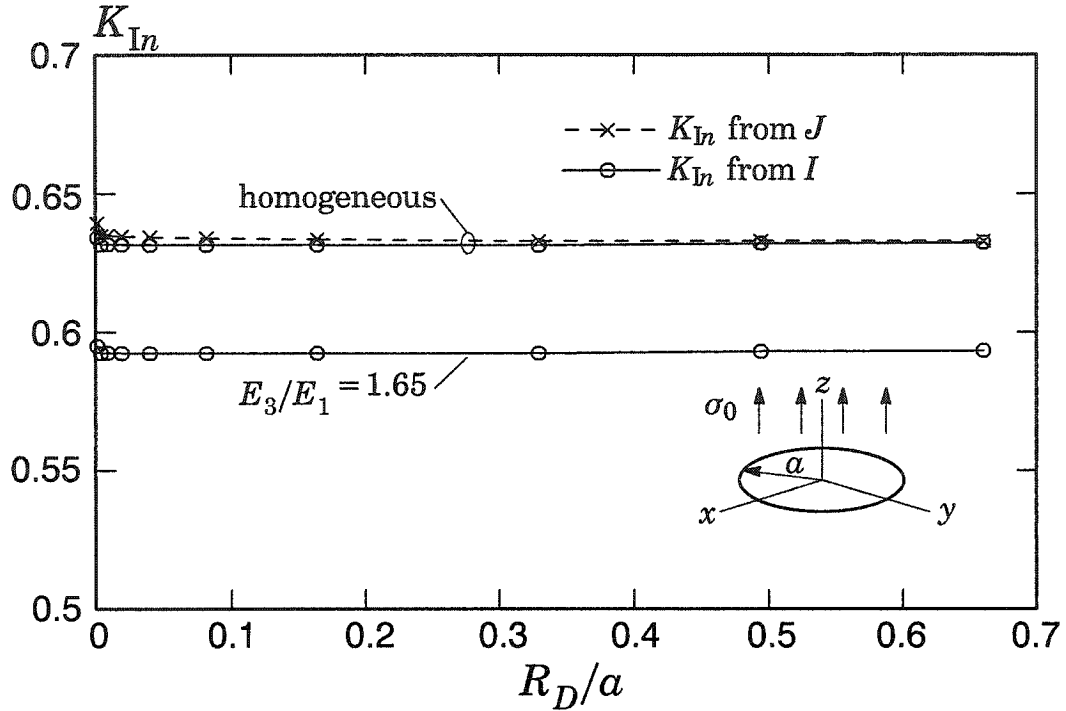


Fig. 4.7. Normalized values of K_I vs. domain size R_D/a , for a penny-shaped crack in an infinite solid under remote tension. The FGM case is for a graded layer illustrated in Figs. 4.6(a)-(b) where $h/a = 1$ and $E_3/E_1 = 1.65$.

and large domains, both for the homogeneous case and the FGM case. This indicates that the effect of curvature terms omitted from Eq. (128) does not appear to change significantly within the range of domain sizes employed for this problem. Whether this trend holds for larger domains ($R_D/a > 1$) or for coarser meshes is uncertain.

Again using the mesh with curved edges, the influence of terms in Eq. (128) included for nonhomogeneity (i.e. \bar{I}_2 and \bar{I}_3 in Eq. (146) and Eq. (147)) can be observed. Figures 4.8(a)-(b) illustrate relative contributions to K_I and K_{II} from terms \bar{I}_1 - \bar{I}_4 in Eqs. (145)-(148). For mode-I computations, the FGM term \bar{I}_2 contributes roughly 2% for the largest domain, and the contribution from \bar{I}_3 is numerically insignificant, while the homogeneous term \bar{I}_1 and the crack-face traction term \bar{I}_4 largely determine the computed K_I -value. For mode-II computations, \bar{I}_1 and \bar{I}_2 dominate, while \bar{I}_3 is negligible, and \bar{I}_4 is zero. The contribution from \bar{I}_3 for this problem is negligible because it involves the derivative of material gradients in the local X_1 -direction, while the actual material gradient is in the X_2 -direction.

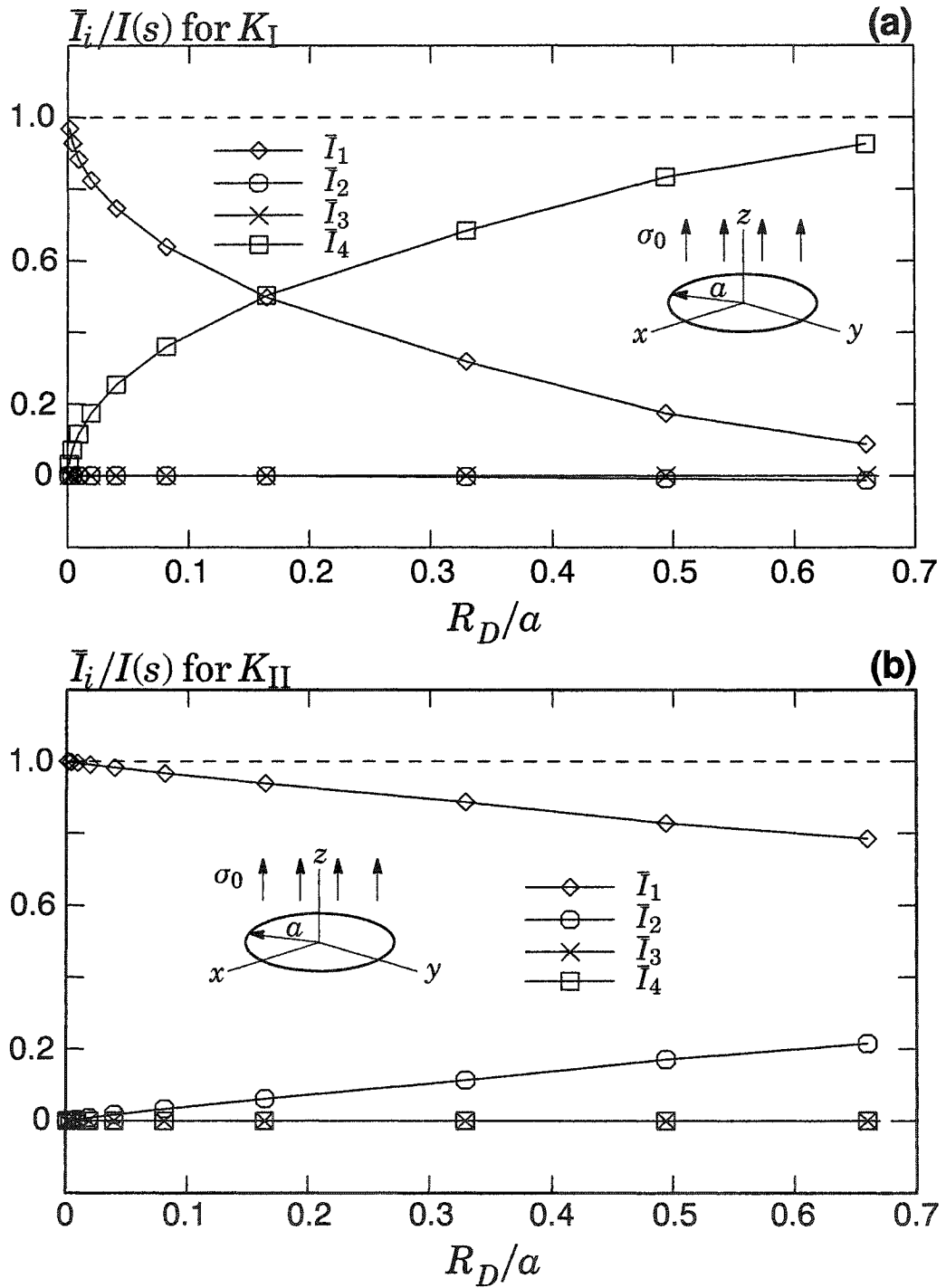


Fig. 4.8. Contributions to $\bar{I}(s)$ from components \bar{I}_1 - \bar{I}_4 for a penny-shaped crack subjected to surface pressure in a graded interlayer ($h/a = 1$, $E_3/E_1 = 1.65$) for (a) K_I and (b) K_{II} computations.

4.5.5 Contribution of crack-face-traction integral to mixed-mode stress intensity factors

On the surfaces of a planar crack, where $\theta = \pm\pi$, auxiliary displacements based on Williams' [221] solution (Appendix A) yields the following derivatives for each loading mode:

$$\text{mode I: } \underline{K_{II}^{aux} = K_{III}^{aux} = 0}$$

$$u_{1,1}^{aux} = u_{3,1}^{aux} = 0; u_{2,1}^{aux} = \frac{K_I^{aux}(\kappa + 1)}{4\mu(s)\sqrt{2\pi r}} \cos(\theta) \sin\left(\frac{\theta}{2}\right), \quad (151)$$

$$\text{mode II: } \underline{K_I^{aux} = K_{III}^{aux} = 0}$$

$$u_{2,1}^{aux} = u_{3,1}^{aux} = 0; u_{1,1}^{aux} = \frac{K_{II}^{aux}(\kappa + 1)}{4\mu(s)\sqrt{2\pi r}} \cos(\theta) \sin\left(\frac{\theta}{2}\right), \quad (152)$$

$$\text{mode III: } \underline{K_I^{aux} = K_{III}^{aux} = 0}$$

$$u_{1,1}^{aux} = u_{2,1}^{aux} = 0; u_{3,1}^{aux} = \frac{K_{III}^{aux}}{\mu(s)\sqrt{2\pi r}} \cos(\theta) \sin\left(\frac{\theta}{2}\right). \quad (153)$$

These expressions demonstrate complete uncoupling of the loading modes in the crack-face-traction integral. Consequently, if a crack-face traction acts parallel to one of the three axes of the local crack-front coordinate system illustrated in Fig. 4.1, Eq. (106) generates no contribution from crack-loading modes that correspond to the other two axis directions. For example, take the case of an FGM specimen in which material gradients cause an applied crack-face pressure (t_2) to induce mixed-mode loading along the crack front. In this example, the crack-face-traction integral in Eq. (128) is non-zero only for mode-I interaction-integral computations, and therefore contributes no error to the computed mode-II stress intensity factor. To evaluate the mode-I stress intensity factor K_I in this case, $K_I^{aux} = 1.0$, and $K_{II}^{aux} = K_{III}^{aux} = 0$. For $\theta = \pm\pi$, the integrand of Eq. (106) includes the product

$$t_j u_{j,1}^{aux} = \left[(0.0)(0.0) \pm \frac{t_2(\kappa(s) + 1)}{4\mu(s)\sqrt{2\pi r}} + (0.0)(0.0) \right], \quad (154)$$

which includes the crack-surface traction, t_2 . For mode-II interaction-integral computations, $K_{II}^{aux} = 1.0$, $K_I^{aux} = K_{III}^{aux} = 0$, and the crack-face-traction integral includes

$$t_j u_{j,1}^{aux} = \left[\pm (0.0) \frac{(\kappa(s) + 1)}{4\mu(s)\sqrt{2\pi r}} \pm (t_2)(0.0) + (0.0)(0.0) \right] = 0, \quad (155)$$

meaning that the crack-surface-traction integral does not contribute to $\bar{I}(s)$ for mode-II calculations, as witnessed in Fig 4.8(b). The integrand of Eq. (106) for mode-III com-

putations similarly vanishes for loading caused by t_2 . This example demonstrates that for problems where crack-face tractions induce mixed-mode loading, Eq. (106) contributes to $\bar{I}(s)$ for only one of the modes. The surface-traction integral is non-zero only when crack-face tractions have a non-zero component in the direction of crack opening represented by the non-zero auxiliary stress intensity factor.

4.5.6 Mode-III loading of a penny-shaped crack in a graded interfacial layer

This third example of a 3-D configuration demonstrates the accuracy of interaction-integral computations of mode-III stress intensity factors along cracks in a 3-D FGM. The crack geometry, material variation and finite-element meshes for this problem follow the descriptions in Section 4.5.4 and Fig. 4.6. Nodal loads at opposite ends of the cylinder apply torsion loading, and fixed nodes at the center of each cylinder face supply constraints (see Fig. 4.6(a)). The element layer at each end of the cylinder is assigned a high value of Young's modulus in order to ensure a uniform distribution of torsional stresses throughout the model.

At locations along the crack front where interaction-integral computations are performed, the average of stress intensity factors obtained from domains two through five is again the reported value. Normalization of the mode-III stress intensity factor follows Eq. (149), where $t_0 = 2T\alpha/\pi b^4$, in which T is the total applied torque, and $b = D/2$ is the cylinder radius. In the case of torsion applied through crack-face tractions, t_0 would be the magnitude of the traction at $r = \alpha$.

Table 4.3 compares stress intensity factors computed for this problem with those obtained by Ozturk and Erdogan [161], who solve integral equations for an axisymmetric crack with torsion applied to the crack faces. Computed stress intensity factors show excellent agreement with the semi-analytical results even when material gradients are severe. For a similar material gradient, the mode-III problem shows very good accuracy compared to the mode-I, mode-II problem. This is likely due to the fact that for pure torsion, the governing equations of elasticity reduce to the Laplace equation, enabling the same mesh to approximate the solution more accurately. In this example, stress intensity factor values obtained using the mesh with straight element edges are more accurate than those obtained from the mesh with curved elements, which may be an effect of omitting crack-front curvature terms from the interaction integral.

Table 4.3. Normalized stress intensity factors for a penny-shaped crack at the edge of a graded interface between two semi-infinite solids under torsion (see Fig. 4.6).

h/a	E_3/E_1	result	K_{III_n}	% difference
—	1.0	Ozturk & Erdogan [161]	0.424	—
		straight element edges	0.427	+0.71
		curved element edges	0.419	-1.18
1.0	1/22	Ozturk & Erdogan [161]	0.483	—
		straight element edges	0.483	+0.0
		curved element edges	0.475	-1.66
1.0	22	Ozturk & Erdogan [161]	0.383	—
		straight element edges	0.386	+0.78
		curved element edges	0.379	-1.04
0.5	0.1	Ozturk & Erdogan [161]	0.509	—
		straight element edges	0.510	+0.20
		curved element edges	0.501	-1.57
0.5	3.0	Ozturk & Erdogan [161]	0.395	—
		straight element edges	0.398	+0.76
		curved element edges	0.390	-1.27

Domain independence of computed stress intensity factors for mode-III computations is very good, as illustrated in Fig. 4.9 for the mesh with curved edges. For both the homogeneous and FGM cases, the two largest domains shown in Fig. 4.9 yield K_{III_n} -values that increase very slightly from values of smaller domains. This small variation may be due to the curvature terms omitted from Eq. (128), because a similar variation does not occur in normalized K_{III} -values obtained through J -integral computations according to

$$K_{III} = \sqrt{\frac{JE}{1+\nu}}. \quad (156)$$

Contributions to computed K_{III_n} -values from individual components of Eq. (128) are illustrated in Fig. 4.10 for the mesh with curved edges. Once again, component \bar{I}_1 dominates the other terms. Term \bar{I}_2 contributes approximately 5% for the largest domain, and \bar{I}_3 is zero everywhere because the material gradient is in the X_2 -direction. This example provides useful comparisons with a semi-analytical solution, and demonstrates that good accuracy can be achieved when the interaction-integral formulation omits curvature terms. In the above example of a penny-shaped crack under tension and torsion loading, it is apparent that the strength and direction of the material gradient in-

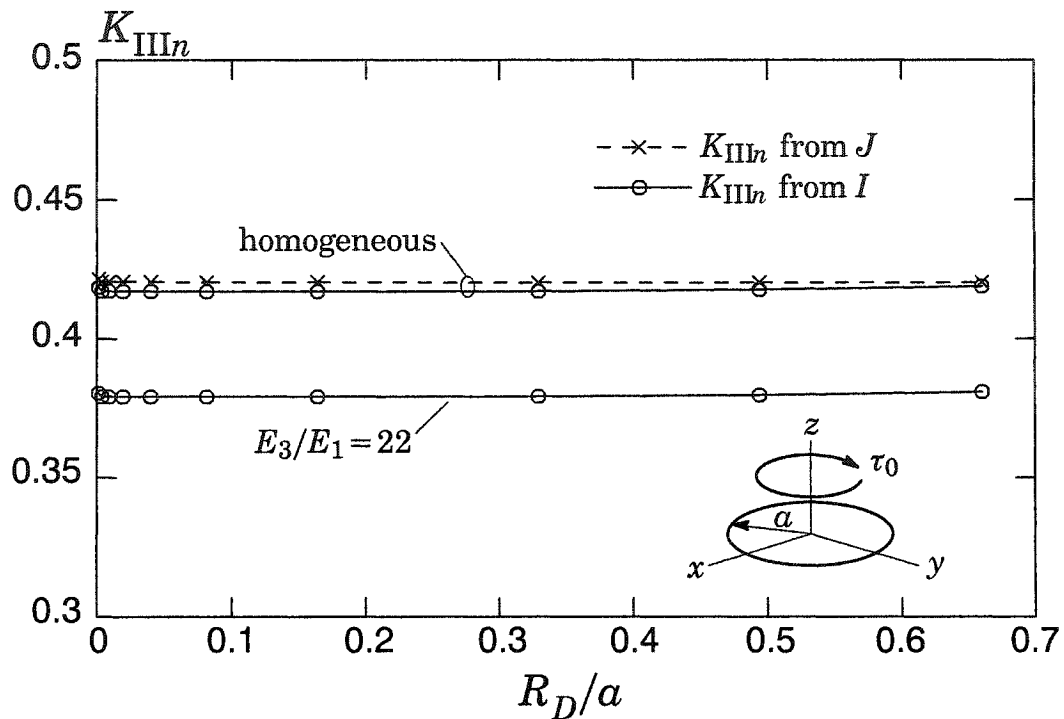


Fig. 4.9. Normalized values of K_{III} vs. domain size R_D/a , for a penny-shaped crack in an infinite solid under remote torsion. The FGM case is for a graded layer illustrated in Figs. 4.6(a)-(b) where $h/a = 1$ and $E_3/E_1 = 22$.

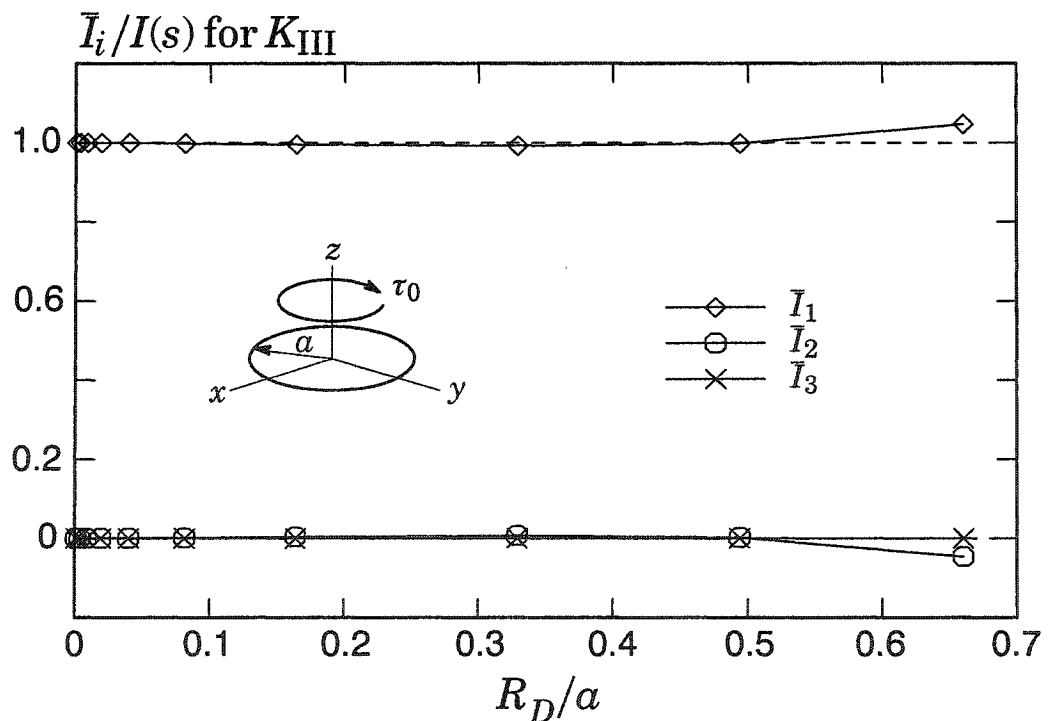


Fig. 4.10. Contribution to $\bar{I}(s)$ from components \bar{I}_1 - \bar{I}_3 for a penny-shaped crack in a graded interlayer in an infinite solid under torsion, where $h/a = 1$, $E_3/E_1 = 22$.

fluences strongly the contribution of FGM terms in Eq. (128). A material gradient in the

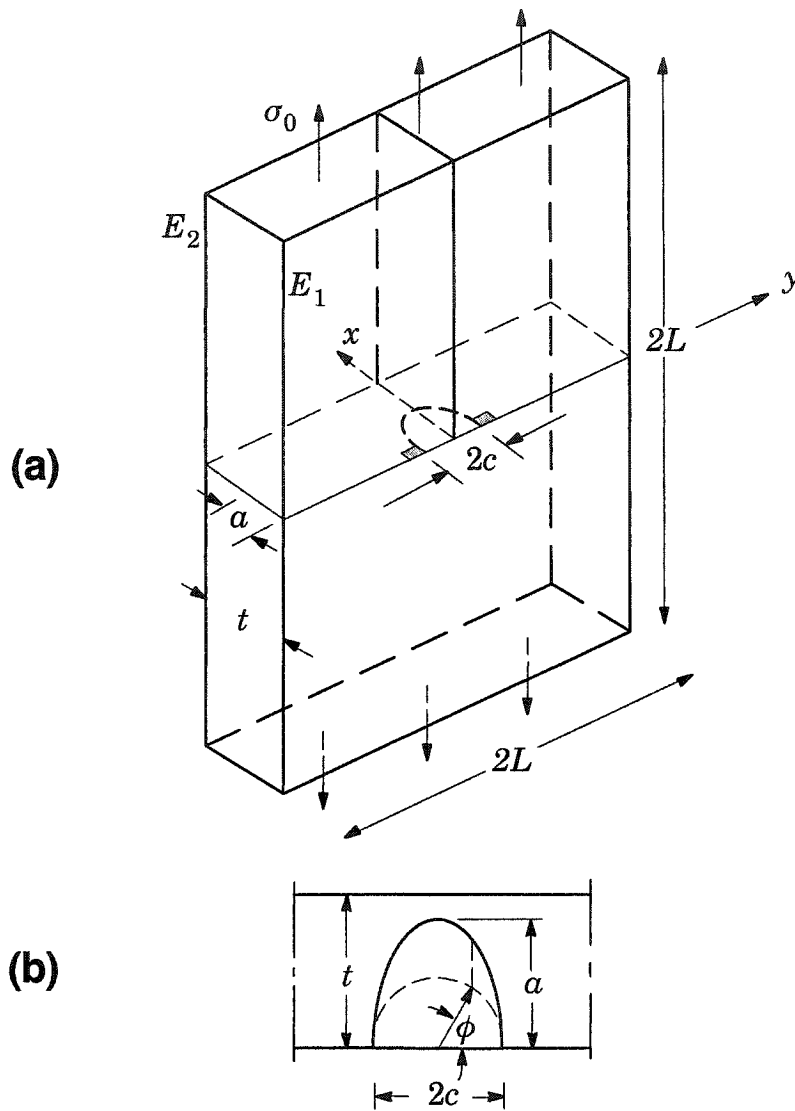


Fig. 4.11. (a) Infinite plate with semi-elliptical surface crack under remote tension. Stress intensity factors decrease to zero in shaded “boundary-layer” region. **(b)** Parametric angle ϕ indicates location along the crack front.

plane of the crack would engage the I_3 term in Eq. (147). It is therefore useful to examine another 3-D crack geometry in order to investigate the influence of all FGM terms in the presence of different material gradients.

4.5.7 Mode-I loading of a semi-elliptical surface crack in an FGM plate

This analysis compares stress intensity factors obtained through interaction-integral and J -integral computations for a semi-elliptical surface crack in a functionally-graded plate under remote tension (see Fig. 4.11(a)). Poisson’s ratio is constant at 0.25, through-thickness gradients in Young’s modulus vary according to $E(x) = E_1 e^{\beta x}$,

$E_1 = E(x=0)$, $E_2 = E(x=t)$, and E_2/E_1 equals 0.05, 1 and 20. The ratio of crack width c , to crack depth a , is $a/c = 2$, and the ratio of crack depth to plate thickness t , is $a/t = 0.8$. Other plate dimensions are $L = 2t$. Parametric angle ϕ describes location along the crack front, as shown in Fig. 4.11(b). Symmetry of the problem permits reduction of the analysis model to one-quarter of the plate, discretized with a mesh of 13,556 20-noded hexagonal elements generated using FEACrack [66] software, shown in Fig. 4.12(a). Figure 4.12(b) shows the mesh discretization in the crack-front region, where 8 collapsed elements of size $L_e/a = 0.00267$ surround the crack front, and are in turn surrounded by semi-circular rings of elements. The high level of mesh refinement apparent in Fig. 4.12(b) ensures good accuracy of computed J -integral and stress intensity factor values. Element edges along the crack front are straight, such that local crack-front curvature is zero, and computation of r and θ employs local Cartesian coordinates as described previously.

At each of 73 crack-front locations, twenty semi-circular rings of elements enable computation of stress intensity factors using twenty different domains. Interaction-integral computations yield highly path-independent K_{In} -values, which, for nearly all crack-front locations, were identical up to four significant figures for domains 2-20. Standard normalization of stress intensity factors for elliptical cracks follows

$$K_{In} = \frac{K_I}{\sigma_0 \sqrt{\frac{\pi a}{Q}}}, \quad (157)$$

where σ_0 is the uniform remote tensile stress, and where Q may be approximated by

$$Q = 1 + 1.464 \left(\frac{c}{a} \right)^{1.65} \quad (158)$$

for $a/c > 1$ [6]. Figure 4.12(c) shows the variation along the crack of normalized stress intensity factor values obtained through Eq. (128). Comparison in the figure is made with stress intensity factors obtained from computations using a domain form of the J -integral for FGMs described by Walters et al. [212]. In this example, mesh refinement near the free surface ($\phi = 0^\circ$) does not permit computations to reflect the true variation in stress intensity factor values, which decrease to zero within a boundary layer shown schematically in Fig. 4.11(a) [171]. Values for the domain at the free surface are therefore omitted from Fig. 4.12(c). Due to inaccuracy of values computed using domains adjacent to the plane of symmetry ($\phi = 90^\circ$), these values are also omitted from Fig. 4.12(c). Values computed using the J -integral and the interaction integral agree very well. For the homogeneous case, the plotted lines cannot be distinguished from one another, because the maximum difference between data points is less than 0.1%. For all three cases of material variation, the maximum difference between the J -integral and interaction-integral curves is less than 0.75%. Figure 4.12(c) also shows values of K_{In} computed using the interaction integral computed without the FGM terms \bar{I}_2 and \bar{I}_3 in Eqs.

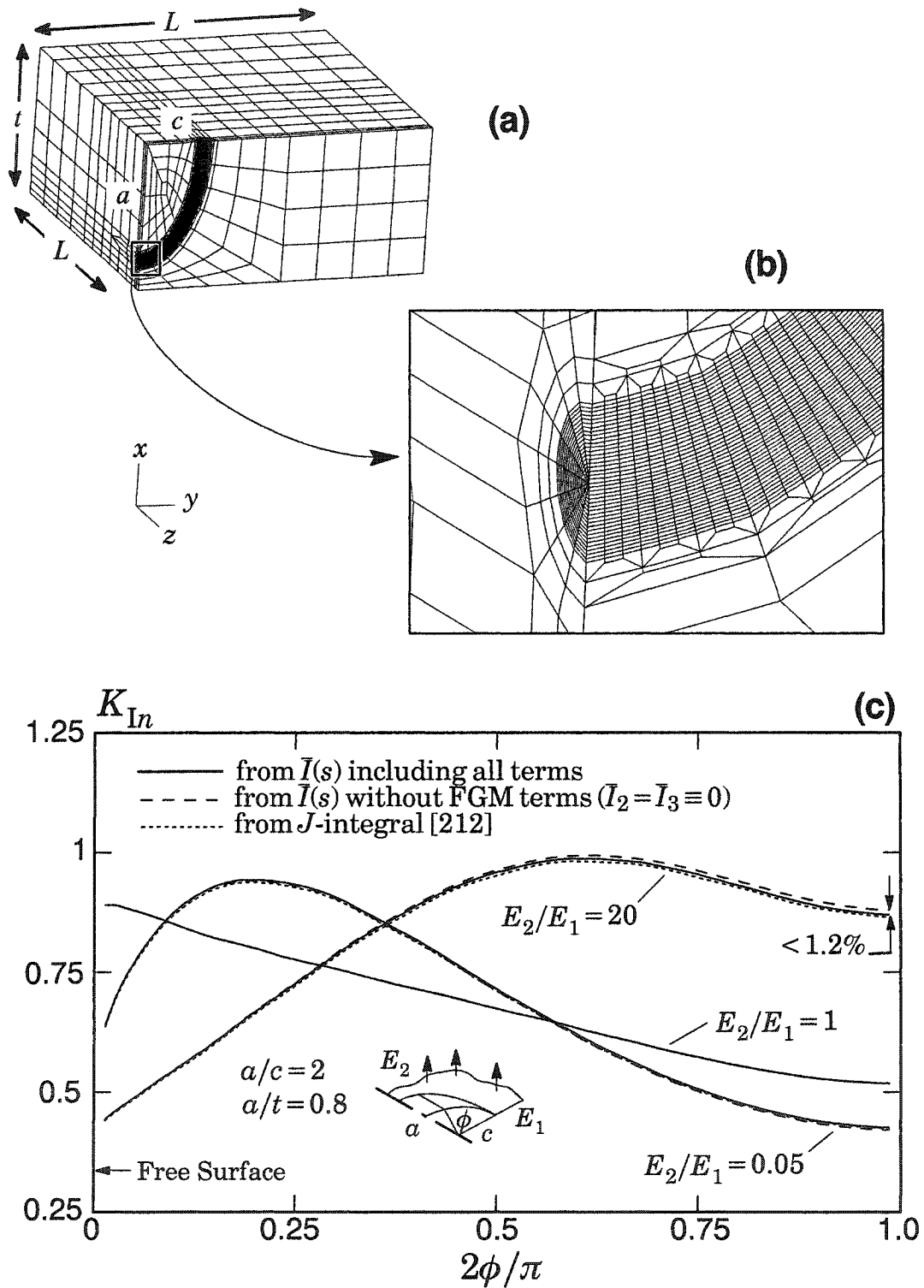


Fig. 4.12. (a) Quarter-symmetric mesh of semi-elliptical surface crack in plate under remote tension. (b) Detail of discretization in crack-front region. (c) Normalized K_I -values along crack.

(146)-(147). Despite large material gradients in the FGM cases, the maximum contribution of these omitted terms for any data point occurs at the point closest to $\phi = 90^\circ$, and is less than 1.2% of the total value. The difference between the interaction-integral curves with and without FGM terms becomes greatest toward $\phi = 90^\circ$ because the exponentially-varying material gradients are the steepest in that region.

Specimen and crack geometries may limit the domain size that can be employed practically for interaction-integral computations. The largest domain employed in this example was of size $R_D/a = 0.053$. This domain size can be compared to domain sizes shown in Figs. 4.5(a)-(b), 4.8(a)-(b) and 4.10, to give an idea of the expected contribution of FGM terms. In each of these example problems, the contribution of FGM terms is very small for the smallest domains. The plots in Fig. 4.12(c) therefore indicate that for mode-I loading of FGMs, a highly refined mesh with domain sizes small compared to the crack geometry, yields stress intensity factors that do not depend significantly upon the FGM terms, and that show no noticeable dependence upon the omitted curvature terms. The former observation has been made by various others (e.g. [77]), and the latter observation agrees with numerical examples in Walters et al. [213].

4.5.8 Mixed-mode loading of a semi-elliptical surface crack in an FGM plate

A final example illustrates the variation of computed stress intensity factors for a surface crack under mixed-mode loading. The plate geometry, crack aspect ratio, material variation, loading conditions and mesh refinement level in the crack-front region are identical with those in the previous example in Section 4.5.7. In this example, however, the crack inclines at $\omega = 45^\circ$ to the plate-thickness direction, as illustrated in Fig. 4.13(a). Therefore, though the ratio $a/t = 0.8$ remains unchanged from the previous example, the inclined crack extends only to a depth of 0.57 of the plate thickness. FEA-Crack [66] software again generated the mesh, which is shown in Figs. 4.13(a)-(b). Excellent path independence of computed stress intensity factors is apparent in Fig. 4.13(c), which shows values computed for each of the twenty domains at crack-front location $\phi = 85^\circ$, for each mode of loading and for each material variation. However, as in the previous example of a surface crack under mode-I loading, the small size of the domains with respect to the crack size, severely limits the influence of the FGM terms \bar{I}_2 and \bar{I}_3 . The small domain size may also limit the potential influence of curvature terms, which have no influence on at least the first four significant digits in the computed values shown in Fig. 4.13(c). Figures 4.14-4.16 show total contributions from \bar{I}_2 and \bar{I}_3 to the stress intensity factor values computed along the crack front for each mode of loading. The maximum contribution of these FGM terms occurs in the region of steepest material variation, yet represents a very small portion of the computed values in each case. Figures 4.17-4.19 illustrate the contributions of terms \bar{I}_1 - \bar{I}_3 for each of the twenty domains used to compute stress intensity factors at crack-front location $\phi = 85^\circ$.

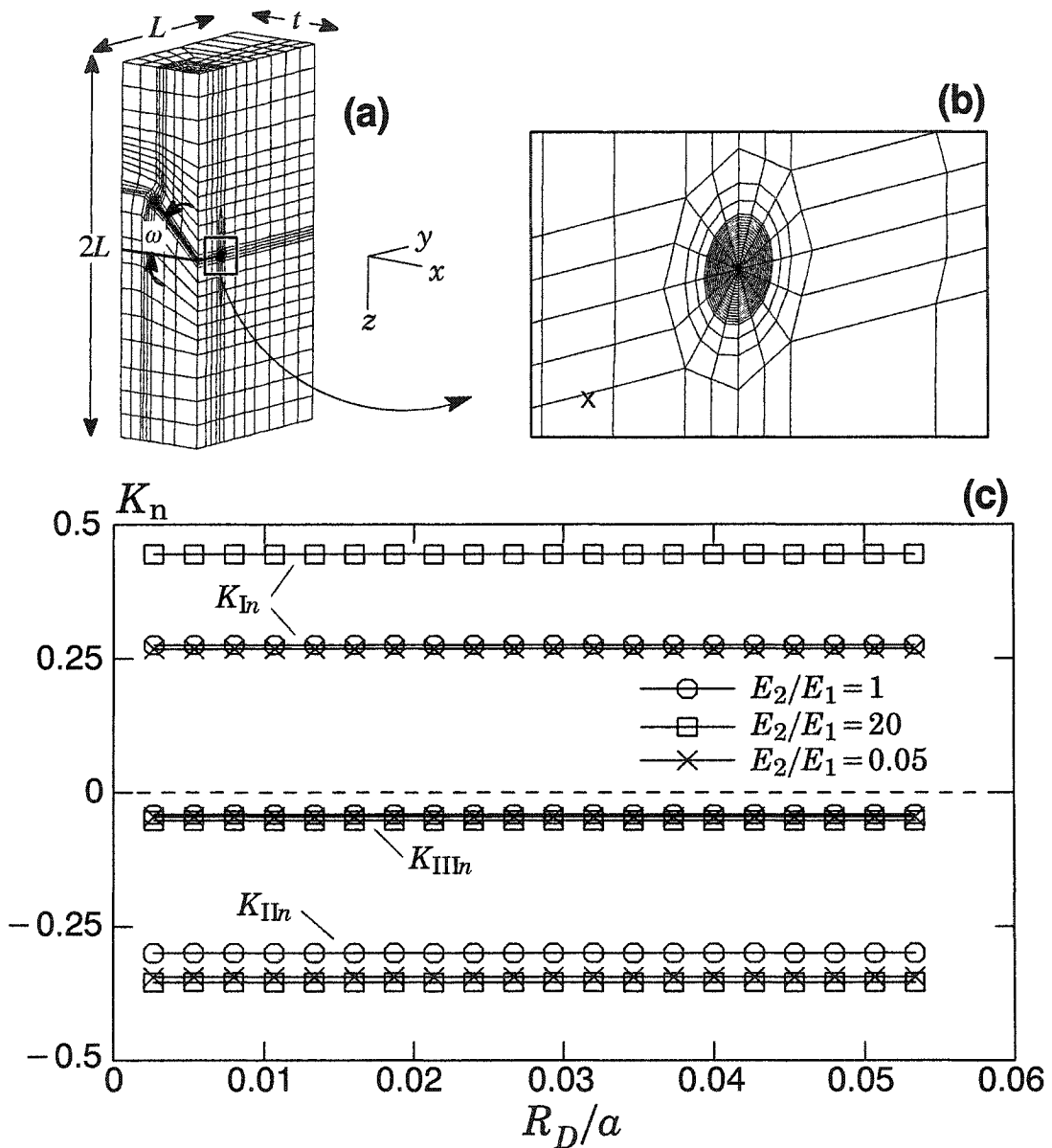


Fig. 4.13. (a) Mesh of semi-elliptical crack, inclined at $\omega = 45^\circ$, in plate under remote tension. (b) Detail of discretization in crack-front region. (c) Normalized K -values vs. domain size for twenty domains at crack-front location $\phi = 85^\circ$.

Terms \bar{I}_2 and \bar{I}_3 do become significant for this problem, but they largely cancel each other, making their combined contribution quite small.

4.6 Discussion and conclusions

This work examines interaction-integral procedures for planar, curved cracks in 3-D functionally-graded solids under remote mechanical loading and applied crack-face tractions. Computations omit auxiliary-field and interaction-integral terms that arise

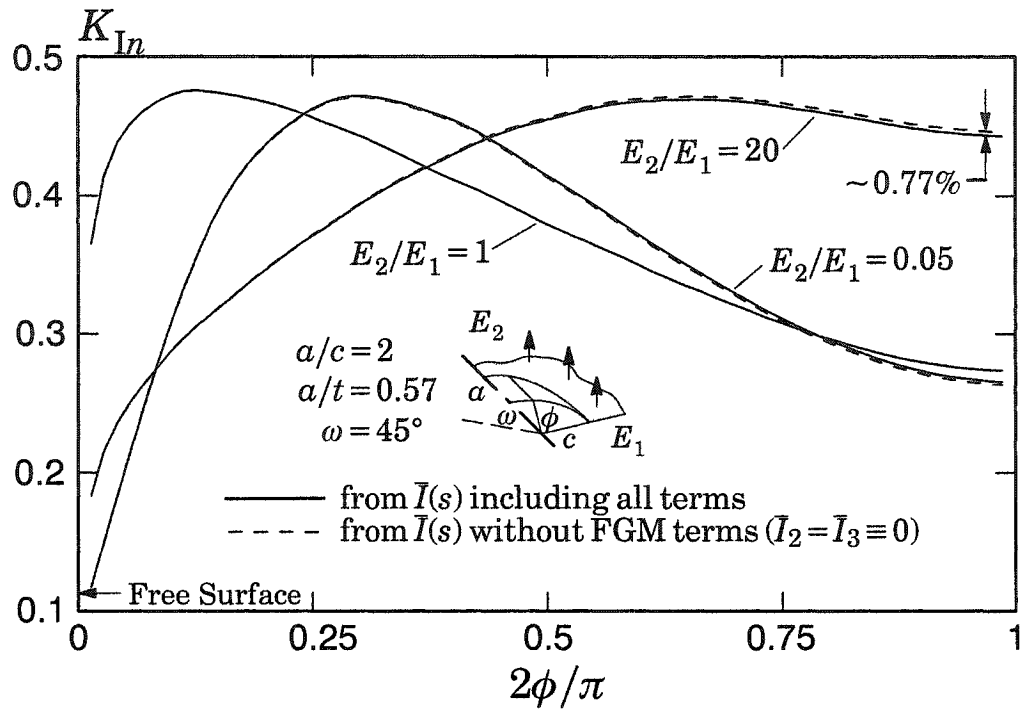


Fig. 4.14. Variation of K_{In} along front of surface crack inclined at 45° in FGM plate under tension.

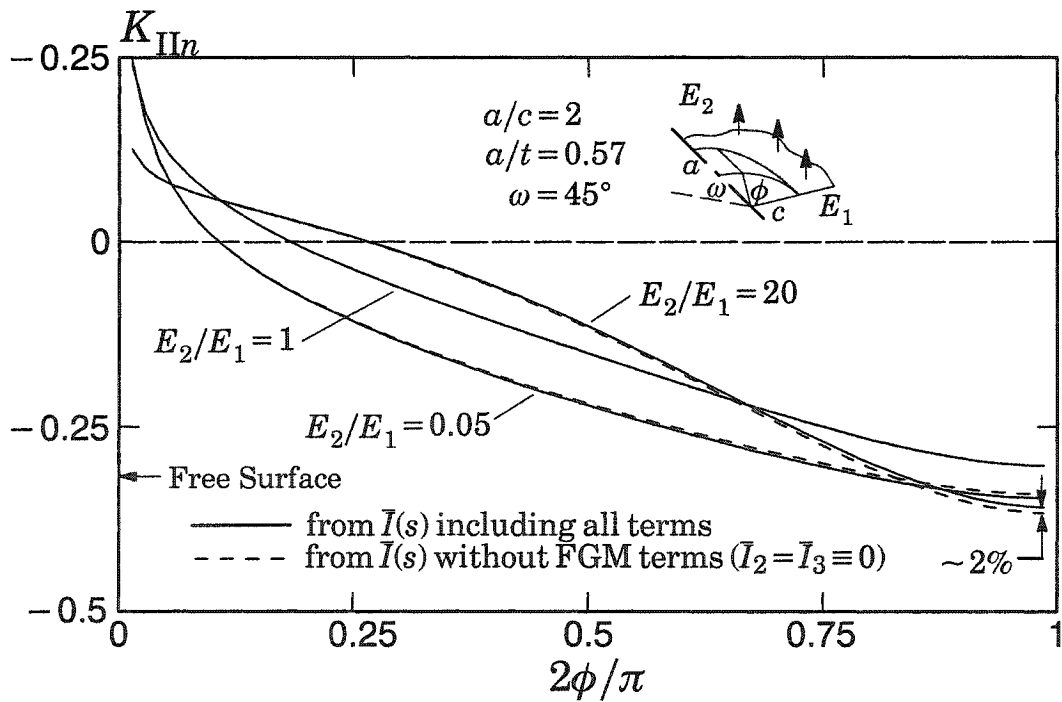


Fig. 4.15. Variation of $K_{II,n}$ along front of surface crack inclined at 45° in FGM plate under tension.

due to the effects of crack-front curvature. The excellent potential accuracy of computed

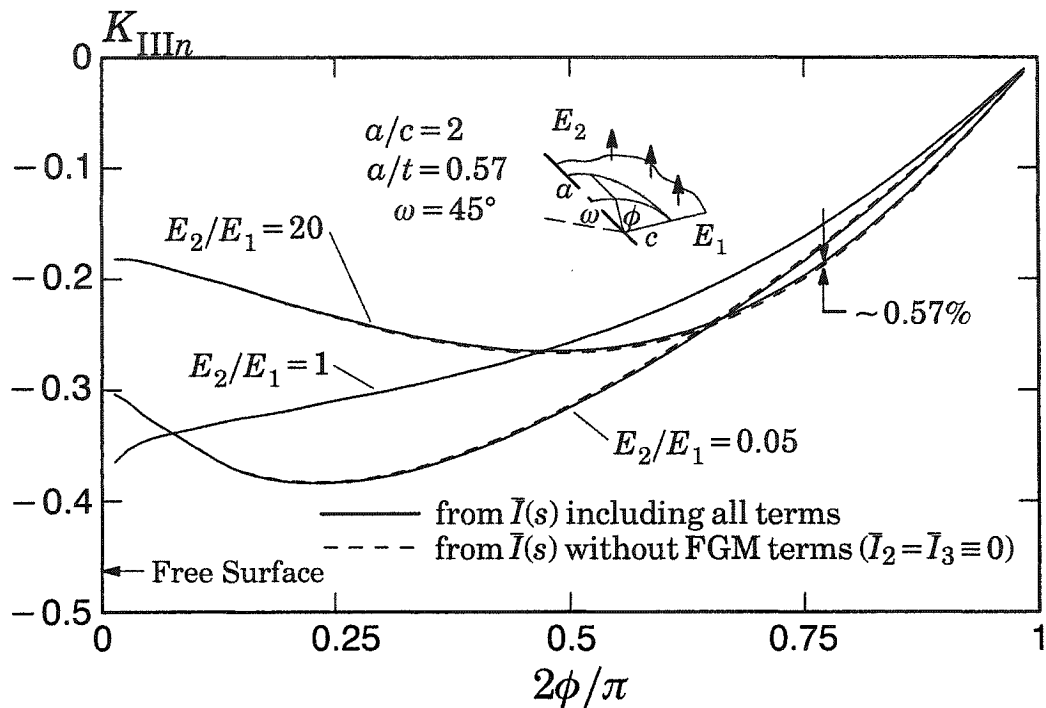


Fig. 4.16. Variation of K_{III} along front of surface crack inclined at 45° in FGM plate under tension.

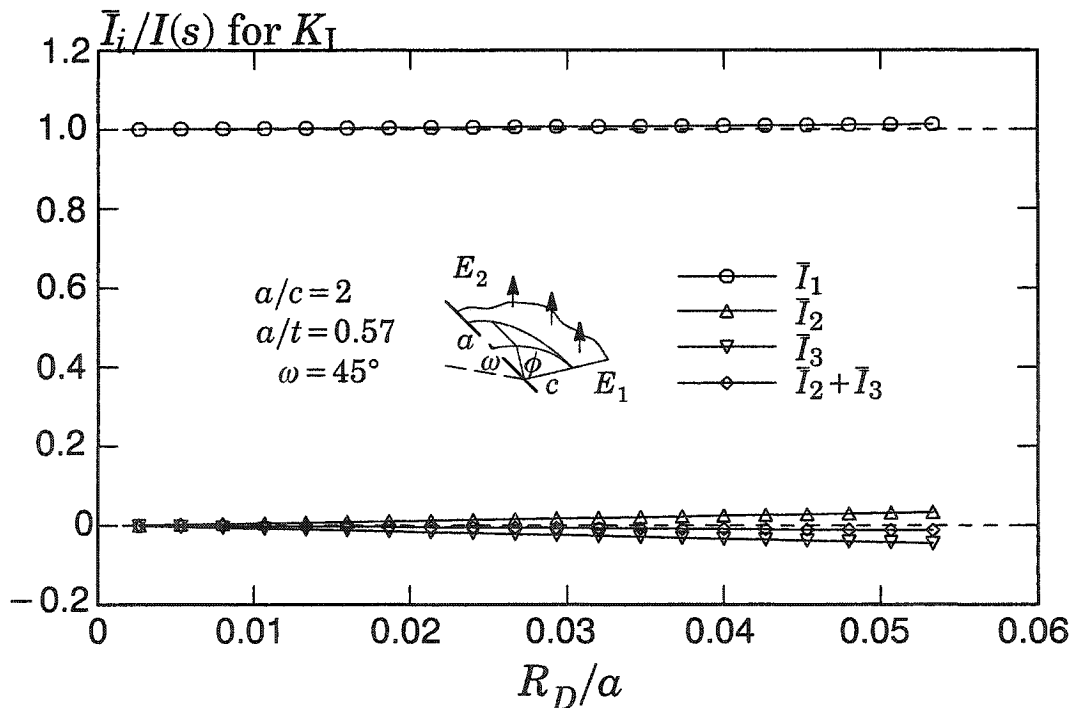


Fig. 4.17. Components of $\bar{I}(s)$ for K_I computations at $\phi = 85^\circ$ along semi-elliptical crack inclined at 45° in FGM plate under remote tension where $E_2/E_1 = 20$.

stress intensity factors indicates that the influence of these terms is small for the prob-

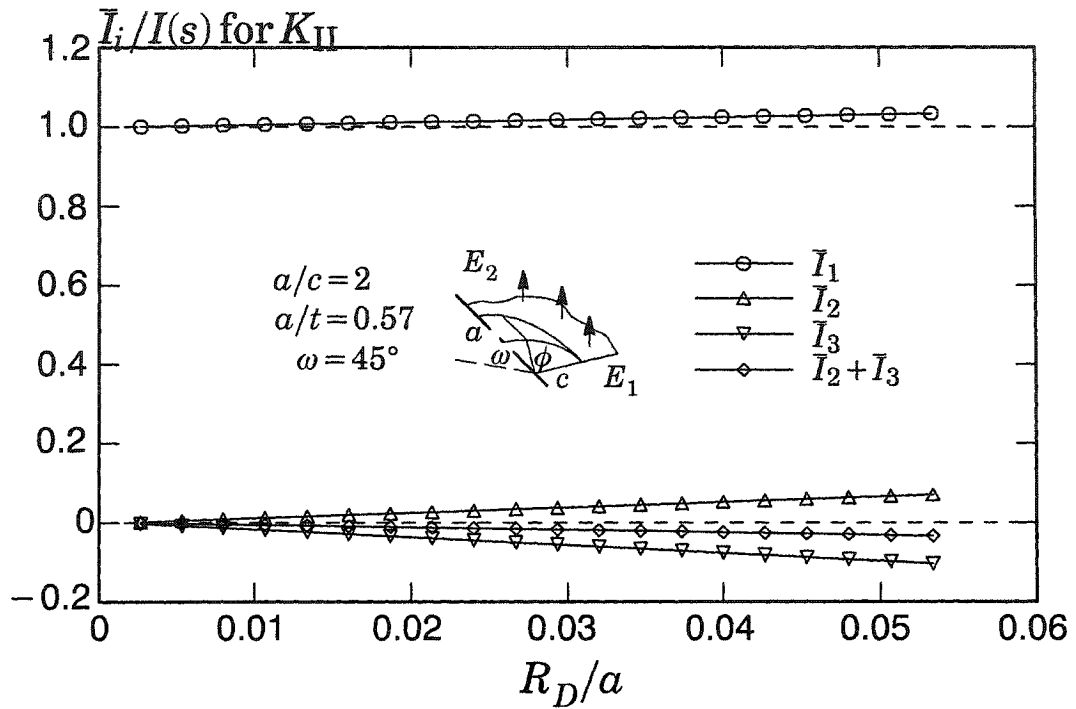


Fig. 4.18. Components of $\bar{I}(s)$ for K_{II} computations at $\phi = 85^\circ$ along semi-elliptical crack inclined at 45° in FGM plate under remote tension where $E_2/E_1 = 20$.

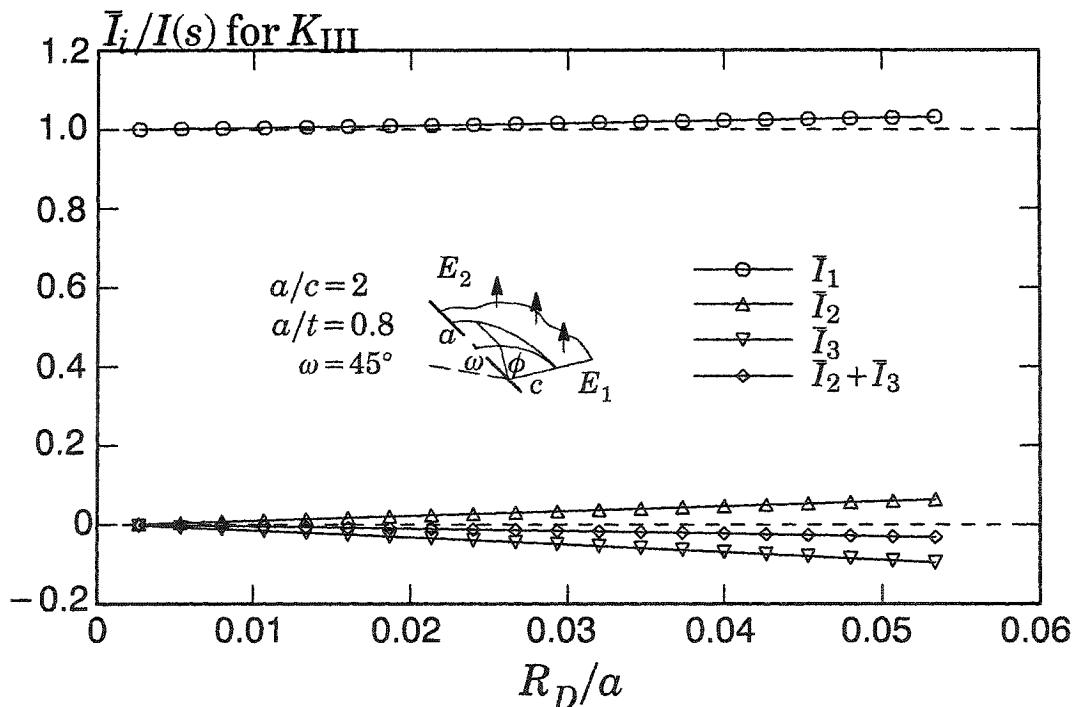


Fig. 4.19. Components of $\bar{I}(s)$ for K_{III} computations at $\phi = 85^\circ$ along semi-elliptical crack inclined at 45° in FGM plate under remote tension where $E_2/E_1 = 20$.

lems considered, and that the proposed approach may yield very accurate stress intensi-

ty factors with sufficient mesh refinement. Comparisons of computed stress intensity factors with existing semi-analytical solutions demonstrate that the interaction integral is an accurate and useful tool for the analysis of cracks in 3-D FGM configurations. The interaction-integral terms included to incorporate material gradients also contribute very little to stress intensity factor computations when the ratio of the domain size to the crack size is small. This suggests a methodology to employ interaction-integral codes that do not include FGM terms (e.g. ABAQUS [1]) to compute stress intensity factors for cracks in FGMs. First, in order to solve the boundary-value problem for the FGM, material properties may be assigned to nodes through an input file, or to integration points through a user subroutine. Then, a figure such as 4.5(a)-(b), generated from a simple 2-D configuration having similar material gradients, can suggest a domain size for acceptable error in stress intensity factors computed without FGM terms in the interaction integral.

In the future, interaction-integral computations might complement experimental investigations of mixed-mode crack growth in 3-D FGMs. Also, the anisotropy inherent to some FGM systems may encourage development of presented techniques to extend the work of Dhondt [50] who employs the interaction integral method to analyze anisotropic 3-D specimens, and Kim and Paulino [114], who employ it for the analysis of 2-D orthotropic FGM specimens. Analysis of cracks near the interface of an FGM coating with a homogeneous substrate would require a combination of the approach developed by Gosz et al. [74] and that employed herein. Interaction-integral terms to include thermal-strain effects would add the important capability to analyze cracks in FGM thermal barrier coatings. T -stresses are another parameter easily computed using interaction integrals which may prove useful for analyzing constraint effects in metallic FGMs.

Chapter 5

Computation of T -Stresses for Mixed-Mode Loading

5.1 Introduction

The elastic T -stresses are the constant terms in the asymptotic expansion of Williams [221] for stresses in the vicinity of a crack tip. The first two terms in this expansion are

$$\begin{bmatrix} \sigma_{11}(r, \theta) & \sigma_{12}(r, \theta) & \sigma_{13}(r, \theta) \\ & \sigma_{22}(r, \theta) & \sigma_{23}(r, \theta) \\ \text{symm} & & \sigma_{33}(r, \theta) \end{bmatrix} = \frac{K}{\sqrt{2\pi r}} \begin{bmatrix} f_{11}(\theta) & f_{12}(\theta) & f_{13}(\theta) \\ & f_{22}(\theta) & f_{23}(\theta) \\ \text{symm} & & f_{33}(\theta) \end{bmatrix} + \begin{bmatrix} T_{11} & 0 & T_{13} \\ & 0 & 0 \\ \text{symm} & & T_{33} \end{bmatrix}, \quad (159)$$

where stresses are a function of polar coordinates r and θ originating at the crack tip, and the angular functions $f_{ij}(\theta)$ depend only upon the angle θ . The three non-zero components of T -stresses act tangent to the crack plane. Larsson and Carlsson [126] demonstrate that T -stress influences strongly the size of the near-tip plastic-zone under small-scale yielding conditions in two-dimensions (2-D). Parks [167] and Wang [218] make the same observation for cracks in three-dimensional (3-D) bodies. Results from these studies encourage the use of T -stress as a parameter to describe stress biaxiality and crack-tip plasticity.

A variety of methods have been developed to compute stress intensity factors for 2-D and 3-D bodies. The most widely used numerical methods for determining T -stresses include direct stress and direct displacement methods, through which T -stresses are deduced from computed values of stress and K [126, 3, 219, 83, 225, 11, 16], and interaction-integral methods, which employ a path-independent integral constructed from the J -integral.

Cardew et al. [29] and Kfoury [105] employ a theorem due to Eshelby, to obtain a path-independent interaction integral whose value is directly proportional to The T -stress normal to the crack, T_{11} . Their integral derives from the J -integral written for the superimposition of two equilibrium states: one is that of the actual boundary value problem, and the other comprises the analytical expressions for stresses, strains and displacements near the tip of a wedge loaded by a point force. Nakamura and Parks [146] extend this procedure to the 3-D case. Most works in the literature that employ the interaction-integral method to compute T -stresses derive from this procedure. Sladek and Sladek [197] develop an interaction integral using the Betti-Rayleigh recipro-

cal theorem, which Chen et al. [33] prove to be analytically equivalent to the integral of Cardew et al. [29] and Kfoury [105].

Because of their robustness and accuracy, interaction integrals have been developed to compute T -stresses for a variety of materials and loading conditions. Sladek and Sladek study cracks in homogeneous material under static, dynamic and thermal loading, and isotropic bimetals [195-200]. Jayadevan et al. [92] also compute T -stress for dynamic loading. Yang and Yuan [227] compute the singular and non-singular terms in the Williams' expansion [221] for anisotropic solids. Jeon and Im [93] compute higher-order terms in the expansion for elastic-plastic cracks. Without solving the boundary-value problem, Beom and Earmme [23] and Cho et al. [37] use the interaction integral as a tool to derive analytical expressions for the stress intensity factors and T -stress in isotropic homogeneous and bimaterial solids carrying surface tractions and interacting with singularities. Moon and Earmme [139] and Kim et al. [107] similarly derive analytical expressions for in-plane (T_{11}) and out-of-plane (T_{13}) T -stresses for interface cracks in isotropic and anisotropic solids under in-plane and anti-plane loading. Kim and Paulino [113, 116, 117] employ interaction-integrals to compute T -stress in 2-D isotropic and orthotropic FGMs. The purpose of this work is to investigate the interaction-integral procedure for cracks in 3-D homogeneous and FGM under mixed-mode loading. Further work involving the anti-plane T -stress T_{13} can be found in the paper by Walters et al. [215]

The organization of remaining sections in this study proceeds as follows: Section 5.2 reviews the interaction-integral formulation for generally-curved, 3-D cracks in functionally-graded material. Section 5.3 describes computation of T -stresses using the interaction integral. Details of the numerical implementation follow in Section 5.4. Section 5.5 includes example problems that partially verify 3-D computations for analyses of cracks in 2-D homogeneous and functionally-graded specimens. Analyses of T -stresses for 3-D cracks in homogeneous and functionally-graded specimens follow in Section 5.6. Concluding remarks in Section 5.7 discuss the potential of presented methods and describe future possibilities for investigation.

5.2 Interaction-integral formulation

This section reviews interaction-integral procedures that enable the computation of stress intensity factors and T -stresses in this study.

5.2.1 An interaction integral for FGMs including surface tractions

The interaction integral employed in this work derives from the evaluation of Rice's [181] J -integral for two superimposed equilibrium states, and was first developed by

Chen and Shield [34]. Typically, the *actual* state refers to the solution of the boundary-value problem in question, and the superimposed *auxiliary* state describes quantities selected by the analyst to involve desired quantities. The J -integral formulated for the superimposed state separates into three integrals: one integral comprises only actual quantities, another only auxiliary quantities, and the third—the interaction integral—comprises interacting quantities which are the product of actual and auxiliary terms. Rice [182] demonstrates that although the T -stress influences the plastic zone size, it has no effect upon energy release rates computed using the J -integral. This indicates that the standard J -integral may be employed in the construction of the interaction integral.

Crack-front curvature, surface tractions and material inhomogeneity all influence the formulation of the interaction integral, and their combined effects lead to the following expression [214]:

$$\begin{aligned} \bar{I}(s) = & \int_V \left(\sigma_{ij} u_{j,1}^{aux} + \sigma_{ij}^{aux} u_{j,1} - \sigma_{jk} \varepsilon_{jk}^{aux} \delta_{1i} \right) q_{,i} dV \\ & + \int_V \left[\sigma_{ij} \left(u_{j,1i}^{aux} - \varepsilon_{ij,1}^{aux} \right) + \frac{\sigma_{ij}^{aux} u_{j,1}}{i} - C_{ijkl,1}(\mathbf{x}) \varepsilon_{kl} \varepsilon_{ij}^{aux} \right] q dV \\ & - \int_{S^+ + S^-} t_j u_{j,1}^{aux} q dS, \end{aligned} \quad (160)$$

where $\bar{I}(s)$ represents the interaction-energy release rate per unit advance of crack-front segment L_C , shown in Fig. 5.1. The volume integrals refer to the simply-connected domain enclosed by surfaces S_1, S_2, S_3, S_t, S^+ and S^- , also illustrated in Fig. 5.1. Surface S_t shrinks to the crack front, and surfaces S^+ and S^- correspond to the upper and lower crack faces, respectively. As denoted in Eq. (160), q is a scalar-valued function that here follows the plateau variation described by Shih et al. [192], varying from zero on surfaces S_1, S_2 , and S_3 , to a value of unity on surface S_t at location s along the crack front where evaluation of the interaction integral occurs. Components of stress σ_{ij} , displacement u_j , strain ε_{ij} , and traction t_j , reflect actual quantities when no superscript is present, and refer to auxiliary quantities with the superscript *aux*. For a nonhomogeneous material, constitutive tensor $C_{ijkl}(\mathbf{x})$ depends upon spatial location $\mathbf{x} = (X_1, X_2, X_3)$ according to the coordinate system shown in Fig. 5.1. The Kronecker delta is δ_{ij} , and $(\cdot)_{,i}$ indicates the partial derivative $\partial(\cdot)/X_i$ with respect to direction X_i .

For cracks with traction-free faces, the surface integral in Eq. (160) vanishes. The second volume integral in Eq. (160) arises due to the influence of crack-front curvature and material nonhomogeneity, as described originally by Nahta and Moran [142], Gosz

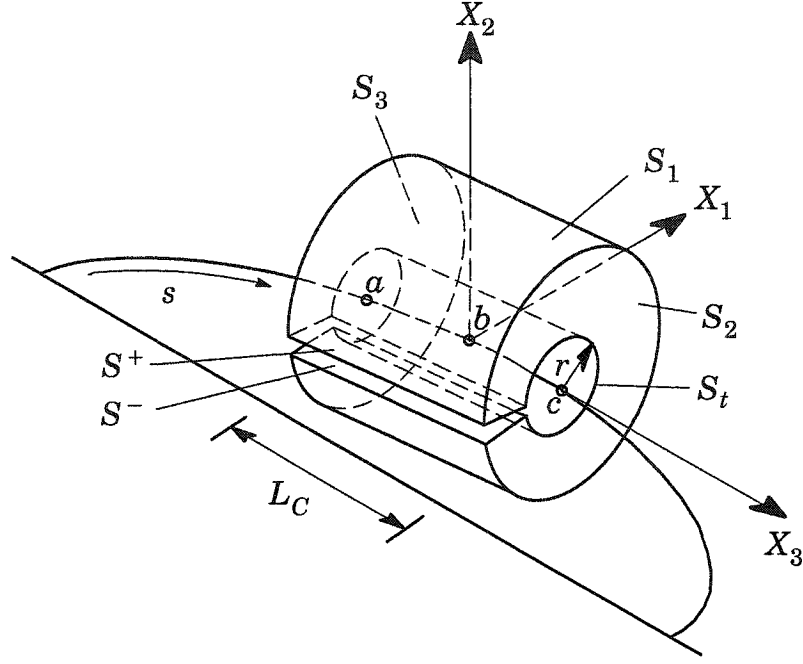


Fig. 5.1. Domain of integration used to evaluate $\bar{I}(s)$ at crack-front location $s = b$. Surfa S_1 , S_2 , S_3 , S^+ , and S^- enclose a simply-connected volume. Surface S_t shrinks crack front, i.e. $r \rightarrow 0^+$, and surfaces S^+ and S^- represent the top and bottom crack respectively.

et al. [74], and Dolbow and Gosz [53]. Material gradients are incorporated through the following terms [53]:

$$\int_V \left[\sigma_{ij} \left(u_{j,1i}^{aux} - \varepsilon_{ij,1}^{aux} \right) - C_{ijkl,1}(\mathbf{x}) \varepsilon_{kl} \varepsilon_{ij}^{aux} \right] q dV, \quad (161)$$

which vanish in homogeneous material. The effects of crack-front curvature are represented by the following terms [142, 74, 75]:

$$\int_V \left[\sigma_{ij} \left(u_{j,1i}^{aux} - \varepsilon_{ij,1}^{aux} \right) + \underline{\sigma_{ij,i}^{aux} u_{j,1}} \right] q dV. \quad (162)$$

Walters et al. [213, 214] observe that the influence of curvature effects on computed stress intensity factors can be very small ($< 1\%$) when mesh discretization permits computation of converged J -integral values. Therefore, in this study, we omit the underlined terms in Eq. (162), as well as auxiliary-field gradients that are non-zero in curvilinear coordinates (see [74]). The value of $\bar{I}(s)$ obtained from Eq. (160) leads to a point-wise value of the interaction integral along the crack front, $I(s)$, through the assumption that $I(s)$ is nearly constant along crack-front segment L_C :

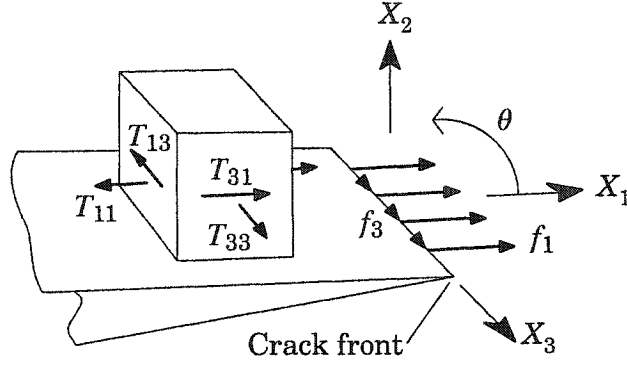


Fig. 5.2. Line loads f_1 and f_3 normal and tangent to the crack front, and T -stresses on a differential element at $\theta = \pi$.

$$I(s) = \frac{\bar{I}(s)}{\int_{L_c} q(s) ds}. \quad (163)$$

5.3 Computation of T -stresses using interaction integrals

This section discusses interaction procedures for the computation of T -stresses for 2-D and 3-D cracks in specimens under mixed-mode, remote mechanical loading. Subsections 5.3.1 and 5.3.2 review procedures for in-plane, mixed-mode loading of thin specimens. The following subsection describes a current procedure to compute T -stresses along 3-D cracks in specimens under mode-I loading. Subsection 5.3.4 investigates the use of this procedure for T -stress computations along 3-D cracks under mixed-mode loading. The consideration of T_{13} is addressed in the paper by Walters et al. [215].

5.3.1 Auxiliary fields for computation of $T_{11}(s)$

To compute T -stress T_{11} in 2-D homogeneous specimens, Cardew et al. [29] and Kfoury [105] select as auxiliary fields the solution by Michell [137] for the stress distribution generated by a line load acting normal to the apex of a wedge, as illustrated in Fig. 5.2. For a crack, where the included angle of the wedge equals 2π , the stresses for plane-strain conditions are [137, 210]:

$$\begin{aligned} \sigma_{11}^{aux} &= -\frac{f_1}{\pi r} \cos^3 \theta, \quad \sigma_{22}^{aux} = -\frac{f_1}{\pi r} \cos \theta \sin^2 \theta, \quad \sigma_{12}^{aux} = -\frac{f_1}{\pi r} \cos^2 \theta \sin \theta, \\ \sigma_{33}^{aux} &= \nu(\sigma_{11}^{aux} + \sigma_{22}^{aux}) = -\frac{\nu f_1}{\pi r} \cos \theta, \quad \sigma_{13}^{aux} = \sigma_{23}^{aux} = 0. \end{aligned} \quad (164)$$

Here, f_1 indicates the force per unit length of the line load applied along the crack front in the local X_1 direction. Displacements derived from Eq. (164) are

$$u_1^{aux} = -\frac{f_1(1+\kappa)}{8\pi\mu} \ln \frac{r}{d} - \frac{f_1}{4\pi\mu} \sin^2 \theta, \quad (165)$$

$$u_2^{aux} = -\frac{f_1(\kappa-1)}{8\pi\mu} \theta + \frac{f_1}{4\pi\mu} \sin \theta \cos \theta, \quad (166)$$

$$u_3^{aux} = 0, \quad (167)$$

$$\varepsilon_{ij}^{aux} = S_{ijkl}(x) \sigma_{ij}^{aux}, \quad (168)$$

where $\kappa = (3-\nu)/(1+\nu)$ for plane stress, $\kappa = (3-4\nu)$ for plane strain, and coordinate $x_1 = d$ specifies a point at a fixed distance from the crack front. For FGMs, we use material properties that correspond to the crack tip at $r = 0$, with the assumption that the fields expressed by Eqs. (164)-(167) have the same asymptotic form in both homogeneous and functionally-graded materials. Auxiliary strains for homogeneous material are the symmetric gradient of displacements. Equation (168) defines auxiliary strains (see [53]).

5.3.2 Extraction of $T_{11}(s)$ from interaction integral for in-plane loading

Cardew et al. [29] obtain a relationship between the interaction integral and T_{11} by assuming that *actual* fields follow Williams' [221] asymptotic solution including the non-singular T -stress:

$$\sigma_{ij} = \frac{K_I}{\sqrt{2\pi r}} f_{ij}^I(\theta) + \frac{K_{II}}{\sqrt{2\pi r}} f_{ij}^{II}(\theta) + T_{11} \delta_{1i} \delta_{1j} \quad (169)$$

$$u_1 = \frac{K_I}{2\mu} \sqrt{\frac{r}{2\pi}} g_1^I(\theta, \nu) + \frac{K_{II}}{2\mu} \sqrt{\frac{r}{2\pi}} g_1^{II}(\theta, \nu) + \frac{Tr}{E'} \cos \theta, \quad (170)$$

$$u_2 = \frac{K_I}{2\mu} \sqrt{\frac{r}{2\pi}} g_2^I(\theta, \nu) + \frac{K_{II}}{2\mu} \sqrt{\frac{r}{2\pi}} g_2^{II}(\theta, \nu) - \frac{\nu' Tr}{E'} \sin \theta, \quad (171)$$

$$\varepsilon_{ij} = \frac{1}{2} (u_{ij} + u_{ji}), \quad (172)$$

where $i, j = 1 \dots 2$, $E' = E$ and $\nu' = \nu$ for plane-stress conditions, and $E' = E/(1-\nu^2)$ and $\nu' = \nu/(1-\nu)$ for plane-strain conditions. Appendix A lists expressions for $f_{ij}(\theta)$ and $g_j(\theta, \nu)$. Also,

$$\begin{aligned} T_{33} &= 0 && : \text{plane stress} \\ T_{33} &= \nu T_{11} && : \text{plane strain.} \end{aligned} \quad (173)$$

These expressions are identical in form for homogeneous and FGMs (Eischen [59]). For FGMs, the shear modulus, μ , and Poisson's ratio, ν , must reflect material-property values at the crack tip. Cardew et al. [29] combine the auxiliary fields in Eqs. (164)-(166) with actual fields defined by Eqs. (169)-(172), and evaluate a 2-D line integral analogous to the first integral in Eq. (160):

$$I = \lim_{r \rightarrow 0} \int_{\Gamma} \left\{ \sigma_{jk} \varepsilon_{jk}^{aux} \delta_{1i} - (\sigma_{ij} u_{j,1}^{aux} + \sigma_{ij}^{aux} u_{j,1}) \right\} n_i d\Gamma. \quad (174)$$

Integration from $-\pi$ to π along a circular contour, Γ , that shrinks to zero, simplifies this integral to an expression that links T_{11} , f_1 , and I . Simplification occurs because higher-order terms ($O(r^\beta)$, $\beta > 0$) in the actual fields represented by Eqs. (169)-(172) vanish asymptotically close to the crack tip, and singular actual-field terms, $O(r^{-1/2})$, cancel each other out, leaving only one non-zero actual stress:

$$\sigma_{11} = T_{11}, \quad (175)$$

which leads to stress-strain and strain-displacement relationships given by

$$u_{1,1} = \varepsilon_{11} = \frac{1 + \kappa}{8\mu} T_{11}, \quad u_{2,2} = \varepsilon_{22} = \frac{\kappa - 3}{8\mu} T_{11}, \quad u_{1,2} = u_{2,1} = 0. \quad (176)$$

Auxiliary fields that interact with these terms are

$$u_{1,1}^{aux} = \varepsilon_{11}^{aux} = \frac{1 + \kappa}{8\mu} \sigma_{11}^{aux} + \frac{\kappa - 3}{8\mu} \sigma_{22}^{aux}. \quad (177)$$

With these actual and auxiliary fields, Eq. (174) reduces to

$$I = - \lim_{r \rightarrow 0} \int_{\Gamma} \sigma_{ij}^{aux} u_{j,1} n_i d\Gamma = - \frac{T_{11}}{E^*} \lim_{r \rightarrow 0} \int_{\Gamma} \sigma_{ij}^{aux} n_i d\Gamma. \quad (178)$$

Tractions $\sigma_{ij}^{aux} n_i$ on contour Γ equilibrate auxiliary force f_1 , and so Eq. (178) gives [29]

$$T_{11} = \frac{E^* I}{f_1}. \quad (179)$$

Material nonhomogeneity also requires consideration of the second integral in Eq. (160) in order to observe any influence on the relationship between T_{11} and I . As the domain radius shrinks to zero, terms that arise due to strain-displacement incompatibility vanish because material properties approach material-property values at the crack tip, i.e. $S_{ijkl}(\mathbf{x}) \rightarrow S_{ijkl}(s)$ as $\mathbf{x} \rightarrow s$. Therefore,

$$\sigma_{ij} (u_{j,1i}^{aux} - \varepsilon_{ij,1}^{aux}) = 0. \quad (180)$$

If derivatives of terms in the FGM constitutive tensor are of the order $O(r^\beta)$, $\beta \geq 0$, remaining components in Eq. (161) behave as follows:

$$\lim_{r \rightarrow 0} \int_{\Gamma} C_{ijkl,1}(\mathbf{x}) \varepsilon_{kl} \varepsilon_{ij}^{aux} d\Gamma \approx \lim_{r \rightarrow 0} \int_{\Gamma} O(r^\beta) O(r^{-1/2}) O(r^{-1}) r d\theta = 0. \quad (181)$$

Therefore, Eq. (179) is valid for both homogeneous and functionally-graded materials. Kim and Paulino [117] provide details regarding the behavior and existence of FGM integrals. Gosz et al. [74] observe that interaction-integral terms due to crack-front curvature are not sufficiently singular to affect the expression in Eq. (179). To observe the behavior of the crack-face traction integral, take a rectangular element on the crack face

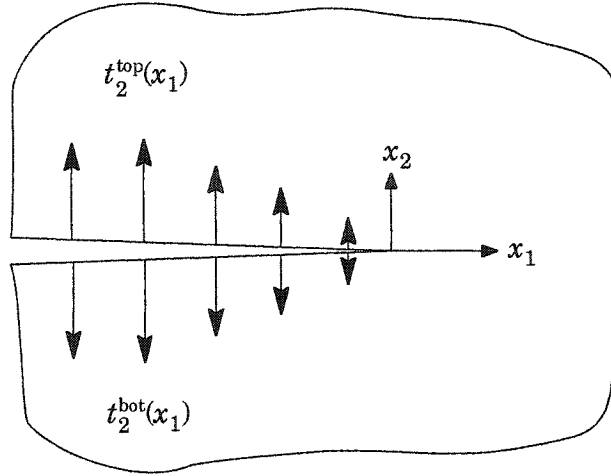


Fig. 5.3. Configuration studied by Cho et al. [37]: semi-infinite crack loaded with crack-face tractions that go to zero at the crack tip.

at $\theta = \pi$, and assume, for simplicity, that q is constant. The crack-face-traction integral in Eq. (160) then behaves as

$$\lim_{r \rightarrow 0} \int_S t_j u_{j,1}^{aux} q dS = \lim_{r \rightarrow 0} \int_0^Z \int_{r=0}^{r=x} t_1 \frac{f_1}{\pi E^* r} dr dz \approx \lim_{r \rightarrow 0} (\ln r) = -\infty, \quad (182)$$

where $u_{2,1}^{aux}$ and $u_{3,1}^{aux}$ are zero (see Eqs. (166)-(167)). In order for Eq. (182) to exist, it is necessary to assume that shear traction t_1 on the crack face is zero at $r = 0$ (see [37]). When mode-I crack-opening tractions, t_2 , act on the crack surface, and shear traction t_1 is zero, Eq. (182) vanishes. Cho et al., [37] derive an expression for T_{11} near the tip of a semi-infinite interface crack loaded by crack-face tractions, as illustrated in Fig. 5.3. Their expression for T_{11} reduces to the following for a homogeneous material:

$$T_{11} = \frac{1}{\pi} \int_{-\infty}^0 [t_1^{\text{top}}(x_1) + t_1^{\text{bot}}(x_1)] \frac{dx_1}{x_1}. \quad (183)$$

Here, $t_1^{\text{top}}(x_1)$ and $t_1^{\text{bot}}(x_1)$ describe tractions on the top and bottom crack faces, respectively, which vary as a function of coordinate x_1 , and which equal zero at the crack tip. The interface crack lies in the plane $x_2 = 0$ (see Fig. 5.3). The analogous 3-D expression for Eq. (183) may be obtained by equating the crack-face-traction integral in Eq. (160) to Eq. (179) and integrating over a semi-infinite crack surface. When only crack-opening tractions $t_2^{\text{top}}(x_1)$ and $t_2^{\text{bot}}(x_1)$ act on the crack faces, Eq. (183) implies that $T_{11} = 0$. But it is known that uniform remote stress, and by correspondence, crack-opening tractions, induce a non-zero value of T_{11} for this configuration. Equation (183) therefore implies that the auxiliary fields described by Eqs. (164)-(167) do not lead to a useful expression between T_{11} and I for loading induced by crack-opening tractions.

Evaluation of Eq. (160) with actual fields provided by the solution to the boundary-value problem, and auxiliary fields given by Eqs. (164)-(166), leads to a value of $I(s)$ and then $T_{11}(s)$ through Eq. (179). The procedures in this section for 2-D analyses are also valid for 3-D analyses of thin structures that simulate plane-stress or plane-strain conditions.

5.3.3 Computation of $T_{11}(s)$ along 3-D cracks under mode-I loading

Nakamura and Parks [146] extend the method of Cardew et al. [29] to the case of 3-D cracks under mode-I loading in homogeneous material. They assume that actual stresses follow Williams' [221] solution for plane strain:

$$\sigma_{ij} = \frac{K_I}{\sqrt{2\pi r}} f_{ij}^I(\theta) + T_{11} \delta_{1i} \delta_{1j}, \quad i, j = 1 \dots 2. \quad (184)$$

Functions $f_{ij}(\theta)$ appear in Appendix A, and out-of-plane stress components are

$$\sigma_{33} = \nu(\sigma_{11} + \sigma_{22}) = \frac{K_I}{\sqrt{2\pi r}} 2\nu(s) \cos \frac{\theta}{2} + T_{33}, \quad \sigma_{13} = 0, \quad \sigma_{23} = 0. \quad (185)$$

For plane-strain conditions, $T_{33}(s) = \nu(s)T_{11}(s)$, but for general 3-D conditions, Nakamura and Parks [146] define $T_{33}(s)$ as

$$T_{33}(s) = \sigma^* + \nu(s)T_{11}(s), \quad (186)$$

and identify σ^* with a state of simple tension tangent to the crack front which causes extensional strain ε_{33} , and Poisson contractions ε_{11} and ε_{22} , described by

$$\varepsilon_{33} = \frac{\sigma^*}{E(s)}, \quad \text{and} \quad \varepsilon_{11} = \varepsilon_{22} = -\nu(s)\varepsilon_{33} = -\frac{\nu(s)\sigma^*}{E(s)}. \quad (187)$$

With these additional strains, the plane-strain, strain-stress relationships in cylindrical coordinates become

$$\varepsilon_{rr} = \frac{1}{2\mu} [(1 - \nu)\sigma_{rr} - \nu\sigma_{\theta\theta}] - \frac{\nu\sigma^*}{E}, \quad (188)$$

$$\varepsilon_{\theta\theta} = \frac{1}{2\mu} [(1 - \nu)\sigma_{\theta\theta} - \nu\sigma_{rr}] - \frac{\nu\sigma^*}{E}, \quad (189)$$

$$\varepsilon_{zz} = \frac{\sigma^*}{E}, \quad \varepsilon_{r\theta} = \frac{\sigma_{r\theta}}{2\mu}, \quad (190)$$

where r and θ are measured in planes orthogonal to cylindrical axis z , and σ_{rr} , $\sigma_{\theta\theta}$ and $\sigma_{r\theta}$ are the polar forms of the stress components represented by Eq. (184). Integration of the polar form of the strain-displacement relationships, in which Eqs. (188)-(190) represent strain components, leads to the following displacements in Cartesian coordinates:

$$u_1 = \frac{K_I}{2\mu} \sqrt{\frac{r}{2\pi}} g_1^I(\theta, \nu) + \frac{(1 - \nu^2)T_{11}}{E} r \cos \theta - \frac{\nu\sigma^*}{E} r \cos \theta, \quad (191)$$

$$u_2 = \frac{K_I}{2\mu} \sqrt{\frac{r}{2\pi}} g_2^I(\theta, \nu) - \frac{\nu(1 + \nu)T_{11}}{E} r \sin \theta - \frac{\nu\sigma^*}{E} r \sin \theta, \quad (192)$$

$$u_3 = \int_{z_1}^{z_2} \frac{\sigma^*}{E} dz = \frac{\sigma^*}{E} (z_2 - z_1), \quad (193)$$

where functions $g_j(\theta, \nu)$ are the same here as in Eq. (170)-(171), and appear in Appendix A. When $\sigma^* = 0$, Eqs. (191)-(192) reduce to the plane-strain mode-I displacements defined in Eqs. (170)-(171). With the actual stresses described by Eqs. (184)-(186), actual displacements defined by Eqs. (191)-(193), actual strains that follow Eq. (172) where $\varepsilon_{33} = \sigma^*/E$, and auxiliary fields given by Eqs. (164)-(167), the line integral in Eq. (174) yields

$$I(s) = \frac{f_1}{E(s)} \left\{ T_{11}(s) [1 - \nu(s)^2] - \nu(s)\sigma^*(s) \right\}. \quad (194)$$

For a 3-D crack, $I(s)$ denotes a value obtained from Eq. (174) at crack-front position s , and $T_{11}(s)$ denotes the T -stress computed at that crack-front location. Rearrangement of Eq. (194) gives

$$T_{11}(s) = \frac{E(s)}{[1 - \nu(s)^2]} \left[\frac{I(s)}{f_1} + \nu(s)\varepsilon_{33}(s) \right]. \quad (195)$$

Evaluation of Eq. (160) with actual fields defined by the numerical solution to the boundary-value problem, and auxiliary fields defined by Eqs. (164)-(167), leads to a value of $\bar{I}(s)$ with which Eq. (163) and Eq. (195) produce a value of $T_{11}(s)$. Tangential strain $\varepsilon_{33}(s)$, computed numerically at crack-front location s , enables the computation $\sigma^* = E\varepsilon_{33}(s)$, and then $T_{33}(s)$ through Eq. (186). For an FGM, material properties in Eq. (195) must reflect values at crack-front location s . A comparison of Eq. (195) with Eq. (179) shows that $\nu\varepsilon_{33}(s)$ acts as a penalty term that reduces $T_{11}(s)$ when contraction tangent to the crack front, $-\varepsilon_{33}(s)$, lowers the stresses induced by strain ε_{11} . When $\varepsilon_{33}(s) = \sigma^* = 0$, Eq. (195) reduces to the plane-strain form of Eq. (179). Therefore, Eq. (195) is valid for mode-I loading of cracks in homogeneous or functionally-graded material, and yields values of $T_{11}(s)$ that either increase or decrease from plane-strain values, depending upon the sign of $\varepsilon_{33}(s)$. Section 5.4 discusses numerical computation of tangential strain at the crack front, $\varepsilon_{33}(s)$. The next section explores the relationship between $I(s)$ and $T_{11}(s)$ when mixed-mode loading exists.

5.3.4 Computation of $T_{11}(s)$ for 3-D cracks under mixed-mode loading

This section examines the approach of Nakamura and Parks [146] for mixed-mode loading conditions. Here, actual fields are again assumed to follow Williams' [221] solution including the three non-singular T -stresses:

$$\begin{aligned}\sigma_{ij} = & \frac{K_I}{\sqrt{2\pi r}} f_{ij}^I(\theta) + \frac{K_{II}}{\sqrt{2\pi r}} f_{ij}^{II}(\theta) + \frac{K_{III}}{\sqrt{2\pi r}} f_{ij}^{III}(\theta) \\ & + T_{11} \delta_{1i} \delta_{1j} + T_{33} \delta_{3i} \delta_{3j} + T_{13} (\delta_{1i} \delta_{3j} + \delta_{3i} \delta_{1j}),\end{aligned}\quad (196)$$

$$u_1 = \frac{K_I}{2\mu} \sqrt{\frac{r}{2\pi}} g_1^I(\theta, \nu) + \frac{K_{II}}{2\mu} \sqrt{\frac{r}{2\pi}} g_1^{II}(\theta, \nu) + \frac{(1-\nu^2)T_{11}}{E} r \cos \theta - \frac{\nu\sigma^*}{E} r \cos \theta, \quad (197)$$

$$u_2 = \frac{K_I}{2\mu} \sqrt{\frac{r}{2\pi}} g_2^I(\theta, \nu) + \frac{K_{II}}{2\mu} \sqrt{\frac{r}{2\pi}} g_2^{II}(\theta, \nu) - \frac{\nu(1+\nu)T_{11}}{E} r \sin \theta - \frac{\nu\sigma^*}{E} r \sin \theta, \quad (198)$$

$$u_3 = \frac{K_{III}}{2\mu} \sqrt{\frac{r}{2\pi}} g_3^{III}(\theta, \nu) + \frac{T_{13}}{\mu} r \cos \theta + \int_{z_1}^{z_2} \frac{\sigma^*}{E} dz. \quad (199)$$

Here, $i, j = 1 \dots 2$, the expressions for $f_{ij}(\theta)$ and $g_j(\theta, \nu)$ follow Appendix A, T_{33} follows Eq. (186) and actual strains follow Eq. (168). Equation (196) is simply a restatement of Eq. (159). When K_I , K_{II} and K_{III} are non-zero, Eq. (174) again leads to the relationship in Eq. (195). This indicates that Eq. (195) is valid for mixed-mode loading conditions, and that T_{11} and T_{33} are uncoupled from T_{13} in this procedure. When K_I , K_{II} and K_{III} are all zero, or for any combination of zero and non-zero stress intensity factors, Eq. (195) continues to describe the relationship between $T_{11}(s)$ and $I(s)$ obtained through Eq. (174). This independence of $T_{11}(s)$ and $I(s)$ from stress intensity factors is apparent with an examination of terms that contribute to Eq. (174). For any combination of non-zero K_I , K_{II} and K_{III} values, the only terms in Eq. (174) that do not vanish as $r \rightarrow 0$, and that do not cancel with other terms, are $\sigma_{11}^{aux} u_{1,1}$ and $\sigma_{21}^{aux} u_{1,1}$. In these two terms, all components containing K_I , K_{II} or K_{III} either vanish or cancel out, and the only remaining components contain T_{11} and σ^* . Thus Eq. (195) derives from Eq. (174) when T_{11} is non-zero.

5.3.5 Computation of $T_{13}(s)$ for cracks under anti-plane shear

Auxiliary fields generated by a uniform line load applied tangent to a crack front, lead to an expression that links $T_{13}(s)$ with $I(s)$. Moon and Earmme [139] determine the complex potentials for asymptotic stresses and displacements near the tip of an interface crack in a 2-D, bi-material specimen loaded by an out-of-plane force acting at the crack tip. By considering the single material as a particular case of the bimaterial by using the same properties for both materials, an auxiliary stress field is obtained from their potentials:

$$\sigma_{zr}^{aux} = -\frac{f_3}{2\pi r}, \text{ and } \sigma_{z\theta}^{aux} = 0, \quad (200)$$

in cylindrical coordinates, which can be converted to auxiliary fields in Cartesian coordinates. Here, f_3 is the out-of-plane force acting at the crack tip. Figure 5.2 illustrates the 3-D analog of this problem, where uniform line load f_3 acts tangent to a 3-D crack front. To obtain a relationship between $T_{13}(s)$ and $I(s)$, actual anti-plane fields are assumed to vary according to Williams' [221] solution for mode III:

$$\sigma_{13} = \frac{K_{\text{III}}}{\sqrt{2\pi r}} \left(-\sin \frac{\theta}{2} \right) + T_{13}, \quad \sigma_{23} = \frac{K_{\text{III}}}{\sqrt{2\pi r}} \cos \frac{\theta}{2}, \quad (201)$$

$$u_3 = \frac{2K_{\text{III}}}{\mu} \sqrt{\frac{r}{2\pi}} \sin \frac{\theta}{2} + \frac{T_{13}}{\mu} r \cos \theta, \quad (202)$$

$$\varepsilon_{13} = \frac{\sigma_{13}}{2\mu} = \frac{u_{3,1}}{2}, \quad \varepsilon_{23} = \frac{\sigma_{23}}{2\mu} = \frac{u_{3,2}}{2}. \quad (203)$$

Evaluation of the line integral in Eq. (174) with auxiliary and actual fields defined according to Eqs. (200)-(203), leads to the following relationship between $T_{13}(s)$ and $I(s)$ [139]:

$$T_{13}(s) = \frac{I(s)\mu(s)}{f_3}. \quad (204)$$

For 3-D cracks, $I(s) = I$ and $T_{13}(s) = T_{13}$ at crack-front position s . At $\theta = \pi$, the surface-traction integral in Eq. (160) becomes

$$\lim_{r \rightarrow 0} \int_S t_j u_{j,1}^{\text{aux}} q dS = \lim_{r \rightarrow 0} \int_0^Z \int_{r=0}^{r=x} t_3 \frac{f_3}{2\pi r \mu} dr dz \approx \lim_{r \rightarrow 0} (\ln r) = -\infty, \quad (205)$$

In order for Eq. (205) to exist, the shear traction t_3 must be zero at $r = 0$ (see Cho et al. [37]).

5.4 Numerical aspects

5.4.1 Numerical evaluation of the interaction integral

In this work, evaluation of volume integrals in Eq. (160) employs standard $2 \times 2 \times 2$ Gauss quadrature, and surface integration uses a 2×2 rule. Computation of r and θ values for auxiliary-field quantities employs a curvilinear coordinate system when element edges are curved, and is based on local Cartesian coordinates when element edges on the crack front are straight. Gosz et al. [74] and Walters et al. [213] discuss these two approaches in greater detail. Computations in this study follow Walters et al. [213] by omitting auxiliary-field terms and the underlined terms in Eq. (160), which are non-zero in curvilinear coordinates (see [74]).

5.4.2 Computation of strain tangent to crack front, $\varepsilon_{33}(s)$

Equation (195) indicates that the accuracy of computed $T_{11}(s)$ and $T_{33}(s)$ values may depend strongly upon the accuracy of computed tangential strain $\varepsilon_{33}(s)$. Nakamura and Parks [146] compute ε_{33} at location s , by using the u_3 displacement components of adjacent crack-front nodes and nodal shape functions. They discuss some of the potentially significant influences that $\varepsilon_{33}(s)$ -values may have on interaction-integral computation-

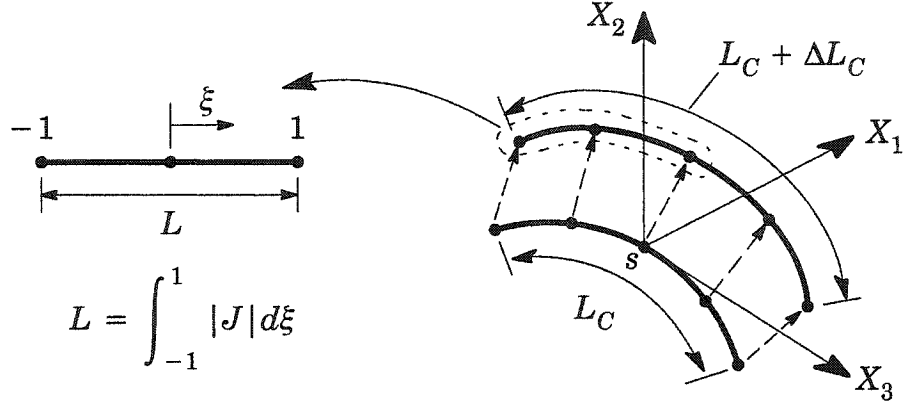


Fig. 5.4. Gauss quadrature in parent coordinates ξ , of the Jacobian J , yields the undeformed and deformed lengths of crack-front segment L_C . The ratio of the change in length to the undeformed length, $\Delta L_C/L_C$, provides an approximate value for strain ε_{33} tangent to the crack front at location s , i.e. $\varepsilon_{33}(s)$.

s . In the current study, we approximate $\varepsilon_{33}(s)$ -values as $\Delta L_C/L_C$, which is the change in length divided by the undeformed length of the crack-front segment enclosed within the domain of integration (see Fig. 5.4). This approximation is valid when $\varepsilon_{33}(s)$ varies little along crack-front segment L_C . Computation of the undeformed and deformed crack lengths follows

$$L_C = \int_{-1}^1 |J| d\xi, \quad (206)$$

where

$$|J| = \sqrt{\left(\frac{\partial X_1}{\partial \xi}\right)^2 + \left(\frac{\partial X_2}{\partial \xi}\right)^2 + \left(\frac{\partial X_3}{\partial \xi}\right)^2} \quad (207)$$

is the coordinate Jacobian. Integration occurs in parent (natural) coordinates, illustrated in Fig. 5.4, where X_i are actual coordinates of crack-front nodes in the local system shown in Fig. 5.4. For planar cracks in the undeformed configuration, $\partial X_2/\partial \xi$ equals zero in the local coordinate system, but it may be non-zero in the deformed state. Derivatives of the nodal shape functions, N_I , allow computation of partial derivatives as

$$\frac{\partial X_i}{\partial \xi} = \sum_{I=1}^n \frac{\partial N_I}{\partial \xi} (X_i)_I, \quad (208)$$

where n is the number of nodes on the element edge defining the crack front, and $(X_i)_I$ is the value of X_i at node I . Evaluation of Eq. (207) with Gauss quadrature follows

$$L_C = \sum_L \sum_p^{\text{edges gpts}} |J|_p w_p, \quad (209)$$

where the sum over edges L , includes element edges along the crack front within the current domain of integration. The sum over p includes integration points with weight w_p . For crack fronts discretized by elements with straight edges, one Gauss point is sufficient for exact integration because $|J|$ is constant in this case. For quadratic elements with curved edges, this study employs standard 4-point Gauss quadrature to integrate $|J|$, which is then the square root of a quadratic polynomial. Accuracy of computed $\Delta L_C/L_C$ values approaches the accuracy of the solution to the original boundary value problem, and therefore provides accurate estimates of $\varepsilon_{33}(s)$ when the tangential strain varies little along L_C .

5.4.3 Computation of stress intensity factors

Williams' [221] asymptotic solutions for stresses and displacements near a crack tip are auxiliary fields commonly employed in interaction-integral procedures to compute stress intensity factors (e.g. [226]). For homogeneous and non-homogeneous material, auxiliary fields defined by the singular stress terms in Williams' [221] series solution have the same form [59], but for nonhomogeneous material, Poisson's ratio ν , and shear modulus μ , must represent material-property values at crack-front location s . After evaluation of Eqs. (160) and (163), stress intensity factors follow immediately as (e.g. [143])

$$K_I(s) = \frac{E^*(s)}{2} I(s), \quad K_{II}(s) = \frac{E^*(s)}{2} I(s), \quad \text{and} \quad K_{III}(s) = \mu(s) I(s), \quad (210)$$

where $E^* = E/(1 - \nu^2)$ for plane-strain and $E^* = E$ for plane-stress problems.

5.5 Numerical simulations of thin specimens

In-plane loading of thin specimens enables simulation of 2-D problems using a 3-D numerical framework. In this section, available T -stress solutions for 2-D homogeneous and functionally-graded materials enable a partial verification of current numerical procedures.

5.5.1 Modified boundary-layer model

Boundary-layer models represent the region surrounding a 2-D crack tip or a 3-D crack front wherein Williams' [221] asymptotic solutions govern the behavior of stresses and displacements. In brittle materials or in metals under small-scale-yielding conditions, a process zone or plastic zone develops in the immediate vicinity of the crack front, and transitions to a zone of K -dominance where stress intensity factors expressed by Wil-

Williams' [221] solution describe field quantities. Boundary-layer models are typically circular (2-D) or cylindrical (3-D) models of the crack-front region, with traction or displacement boundary conditions prescribed by Williams' solution with a specified stress intensity factor. Stress intensity factors computed using such models should match the applied values, thus enabling verification of numerical solution methods [6].

Larsson and Carlsson [126] show that under small-scale yielding, imposed fields described by Williams' [221] solution generate plastic zones of different sizes in fracture specimens with differing geometries. They demonstrate that the non-singular T -stress term in Williams' [221] solution is a parameter that largely accounts for this discrepancy in plastic-zone size. Modified boundary-layer models include the effects of T -stress in the boundary conditions imposed on a traditional boundary-layer model. Assigned T -stress values enable verification of numerical procedures used to compute the non-singular stresses in the vicinity of a crack. Recently, Shim et al. [193] have developed a modified boundary-layer method for FGMs, but we do not employ their method here, depending, rather, upon available numerical solutions in the literature. Here, to verify interaction-integral computations of T -stress under mode-I and mode-II loading in homogeneous material, displacement boundary conditions applied to nodes on the perimeter of a modified boundary-layer model reflect either plane-stress or plane-strain conditions. Material behavior is linear elastic throughout the model. For mode-III loading and verification of T_{13} computations in homogeneous material, anti-plane-shear displacements apply to the nodes along the circumferential strip of the model (see Fig. 5.5(a)).

A boundary-layer model for this study, shown in Fig. 5.5(a), consists of 2000 8-noded hexagonal elements, and has one element layer through the thickness. Crack length, α , equals mesh radius, R , and mesh thickness, t , is described by $t/\alpha = 0.1$. Fifty circular rings of elements that surround the crack front are divided circumferentially into forty slices, or sectors. Elements surrounding the crack front each have one collapsed face, and a characteristic length, L_e , described by $L_e/\alpha = 0.000434$ (Fig. 5.5(b)). In this study, dimension R_D describes domain size, and R_D for domain 1 equals L_e . Table 5.1 lists imposed and computed stress intensity factors and T -stresses, and shows that computed T -stresses have accuracy similar to computed stress intensity factors for cases investigated. These modified-boundary-layer-model analyses verify interaction-integral procedures to compute T -stresses for cracks under mixed-mode loading in homogeneous material. Figure 5.6 illustrates the deformation of a boundary-layer model with displacements prescribed by Eq. (202) where $K_{III} = 1$, and $T_{13} = 0$. The figure also shows the deformation of a modified-boundary-layer model caused by displacements prescribed by Eq. (202), where $K_{III} = 0$, and $T_{13} = 1$.

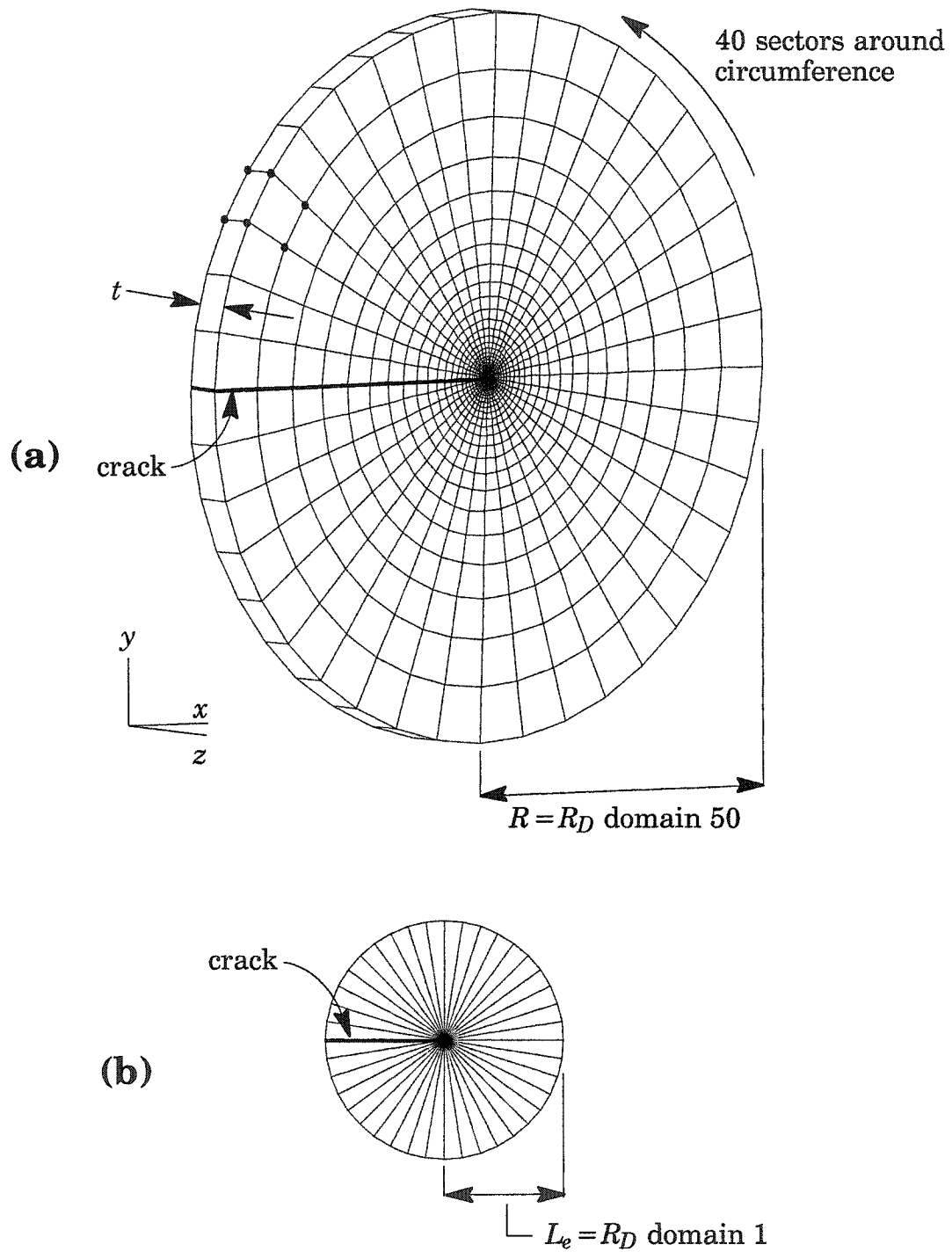


Fig. 5.5. (a) Modified boundary-layer model for verification of T -stress computations for homogeneous materials. Dimension $R/t = 10$. Mesh has 4102 nodes and 2000 8-noded hexagonal elements arranged in 50 circular rings divided into 40 sectors around the circumference. Dimension R_D describes domain size in this study. (b) Collapsed elements of size $L_e = 0.000434$ surround the crack front.

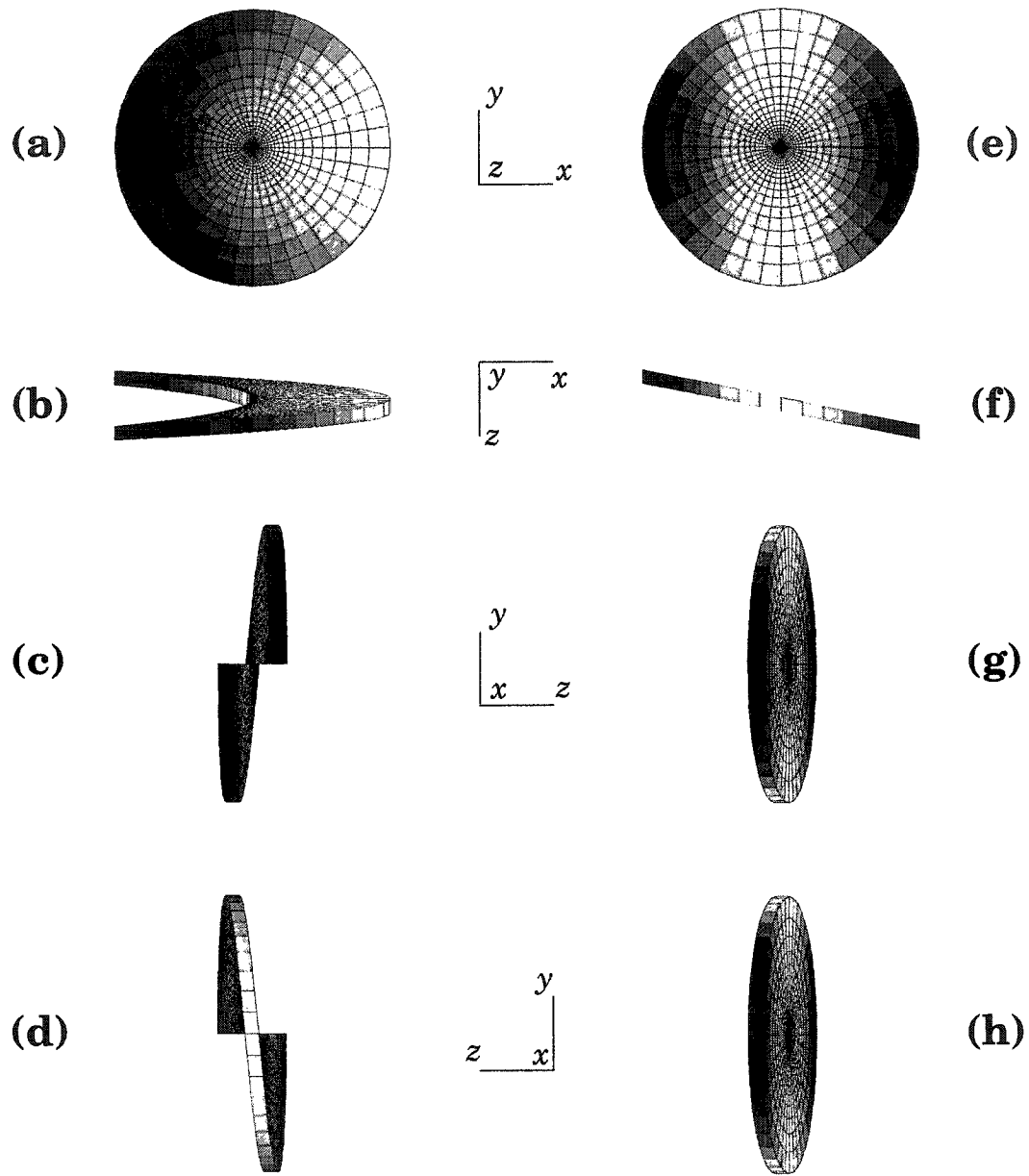


Fig. 5.6. Boundary-layer model with displacements prescribed by Eq. (202) where $K_{III} = 1.0$ and $T_{13} = 0.0$: (a) side view, (b) top view, (c) left view, (d) right view. Modified boundary-layer model with displacements prescribed by Eq. (202) where $K_{III} = 0.0$ and $T_{13} = 1.0$: (e) side view, (f) top view, (g) left view, (h) right view.

Table 5.1. Imposed and computed stress intensity factor and T -stress values for the crack front in a homogeneous, modified boundary-layer model (Fig. 5.5(a)).

loading conditions	quantity	imposed value	computed value
plane stress	K_I	1.000	0.9949
	K_{II}	1.000	1.003
	T_{11}	1.000	1.000
plane strain	K_I	1.000	1.004
	K_{II}	1.000	1.003
	T_{11}	1.000	1.000
	T_{33}	—	0.3000 ($=\nu T_{11}$)
uniform stress tangent to crack front	K_I	0.000	0.000
	K_{II}	0.000	0.000
	T_{11}	0.000	0.000
	T_{33}	1.000 ($=\sigma^*$)	1.000
anti-plane shear	K_{III}	1.000	1.001
	T_{13}	1.000	1.000

5.5.2 FGM plate with inclined center crack

Verification of T -stress computations for simulated 2-D conditions in FGMs follows from an analysis of a through-crack inclined at 30° from horizontal. Material variation follows

$$E(x) = E_0 e^{\beta x}, \quad (211)$$

according to the coordinate system illustrated in Fig. 5.7, and Poisson's ratio is constant at $\nu = 0.3$ throughout the model. The current finite-element model includes a crack of length $2a$, in a plate with height and width dimensions of $H = W = 20a$, and a thickness of $t = 0.125a$. The mesh consists of 2057 20-noded brick elements. Twenty elements of size $L_e/a = 0.0177$, having one collapsed face, surround each crack front. Reported T -stresses are the average of T -stress values computed using domains 2-10, which shows excellent path-independence.

Table 5.2 lists T_{11} -values computed for simulated plane-stress conditions, and a uniform remote displacement loading described by $\Delta = H/\epsilon_0$, where ϵ_0 is an assigned strain value. Normalized T -stress values follow as $T_{11n} = T_{11}/E_0\epsilon_0$, where E_0 is the value of Young's modulus at the crack front where values are reported. Because Poisson's ratio is non-zero, the current 3-D model has non-zero through-thickness stresses, and we set $\sigma_{33}\epsilon_{33,1}^{aux} = 0$ to improve the accuracy of interaction-integral computations for assumed plane-stress conditions [214]. Values in Table 5.2 show good agreement with T -stresses

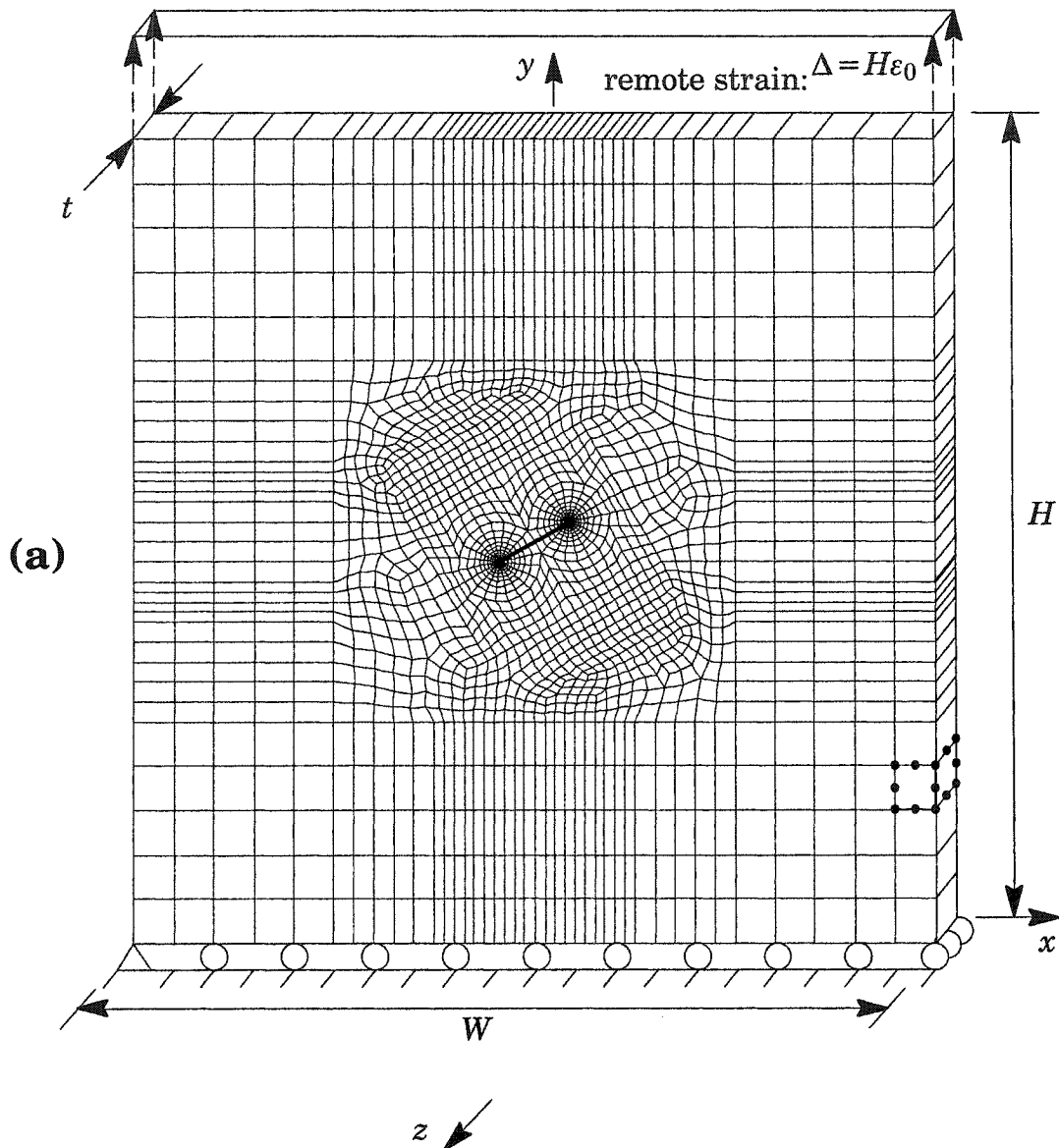


Fig. 5.7. Model for fixed-grip displacement (Δ) of an infinite FGM plate with a through-crack inclined 30° from horizontal. Distance between left and right crack fronts $= 2a$. Dimensions $H = W = 20a$, and $t = 0.125a$. The mesh discretization consists of 2057 20-noded brick elements. Twenty collapsed elements of size $L_e/a = 0.0177$ surround each crack front.

reported by Dong and Paulino [54] and Kim and Paulino [113, 117] for this crack specimen. Figures 5.8(a)-(b) show the relative contribution of interaction-integral components to the total value of \bar{I} computed for each domain. The second integral of Eq. (160) contributes a smaller proportion to \bar{I} for stress-intensity-factor computations ($\sim 6\%$ for the largest domain) than for T -stress computations ($\sim 17\%$ for the largest domain). However, the first two terms in the second integral of Eq. (160) have a much smaller

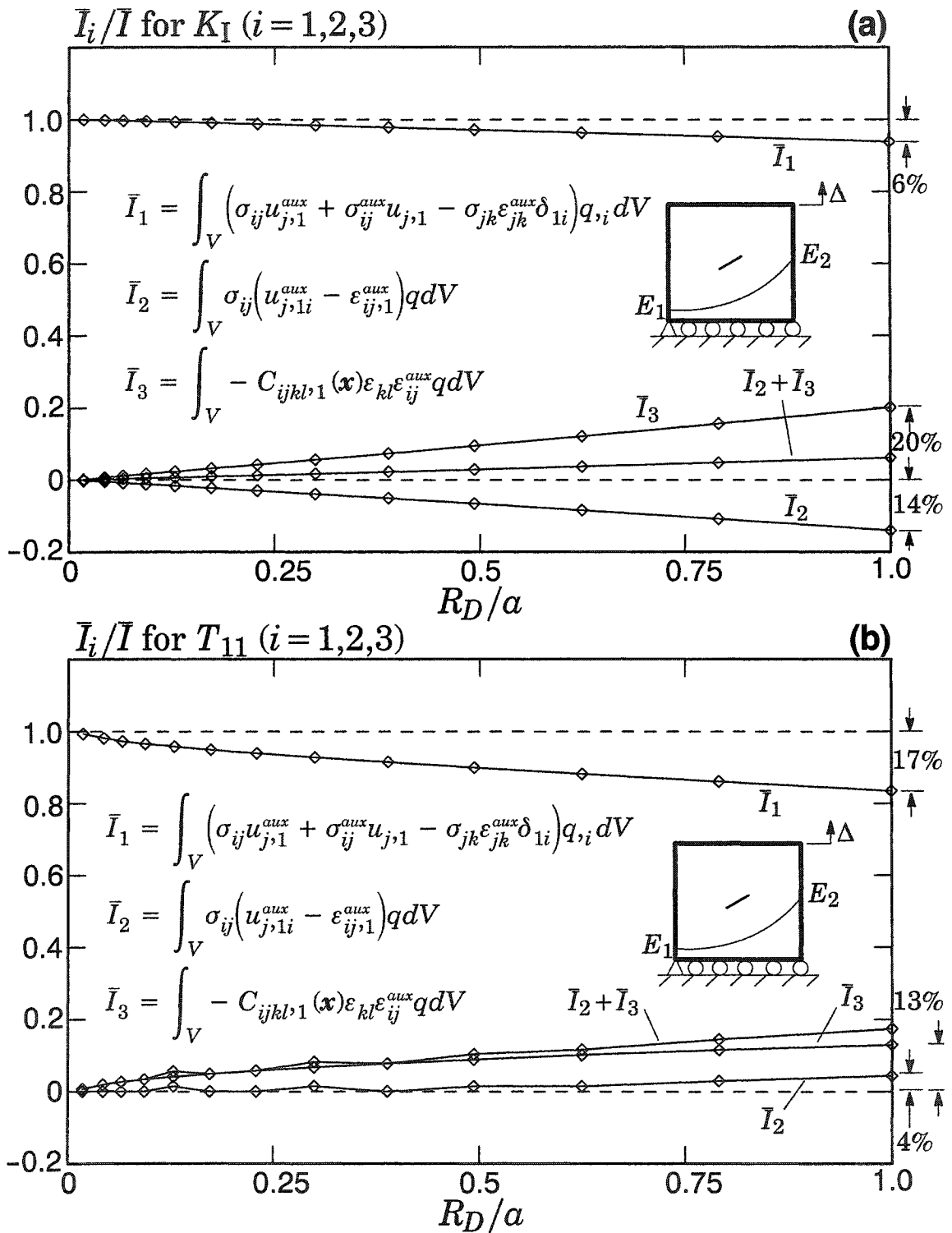


Fig. 5.8. Relative contribution of interaction-integral terms for various domain sizes used to compute values of (a) K_I and (b) T_{11} for an inclined crack in an exponentially graded M(T) specimen under plane-stress, fixed-grip loading. Percentages indicate relative contributions of individual terms at $R_D/a = 1.0$.

contribution to \bar{I} for T -stress computations than for stress-intensity-factor computations. For this problem, these terms contribute negligibly to the computed T -stress until the domain size becomes greater than $R_D/a = 0.5$.

Table 5.3 lists normalized T -stress values for the same FGM specimen under remote tension loading, and assumed plane-stress and plane-strain conditions. Constrained out-of-plane displacements lead to plane-strain conditions. Normalized T -stress values are obtained as $T_{11n} = T_{11}/\sigma_0$, where σ_0 is the magnitude of the remote tensile stress. For plane-strain conditions, $T_{33n} = \nu T_{11n}$. Stress intensity factors and T -stresses show close agreement between plane-stress and plane-strain conditions, which verifies interaction integral computations for these two loading conditions. The exact T -stress solution for the homogeneous configuration is found in Smith et al. [201].

Table 5.2. T -stress T_{11} at the left and right crack-fronts of a through crack inclined at 30° in an FGM plate under fixed-grip loading and assumed plane-stress conditions (see Fig. 5.7). Young's modulus varies as $E(x) = E_0 e^{\beta x}$, and Poisson's ratio is constant at $\nu = 0.3$. Normalization follows $T_{11n} = T_{11}/E_0 \varepsilon_0$.

reference	$\beta a = 0.0$		$\beta a = 0.25$		$\beta a = 0.5$	
	T_{11n} left	T_{11n} right	T_{11n} left	T_{11n} right	T_{11n} left	T_{11n} right
present	-0.5000	-0.5000	-0.4793	-0.4810	-0.4404	-0.4294
Paulino & Dong [54]	-0.5001	-0.5001	-0.4727	-0.4871	-0.4444	-0.4200
Paulino & Kim [169]	-0.4974	-0.4974	-0.4754	-0.4810	-0.4360	-0.4334
Kim & Paulino [113]	-0.4974	-0.4974	-0.4763	-0.4790	-0.4371	-0.4288

Table 5.3. T -stresses for the left and right fronts of an inclined crack in an FGM plate under remote tension loading (Fig. 5.7(a)). Normalization follows $T_n = T/\sigma_0$.

problem	value	$\beta a = 0.0$		$\beta a = 0.25$		$\beta a = 0.5$	
		left	right	left	right	left	right
plane stress	T_{11n}	-0.5083	-0.5110	-0.9760	-0.5870	-1.277	-0.4818
plane strain	T_{11n}	-0.5084	-0.5111	-0.9759	-0.5832	-1.293	-0.4811
	T_{33n}	-0.1525	-0.1533	-0.2928	-0.1750	-0.3879	-0.1443
exact	T_{11n}	-0.50	-0.50	—	—	—	—
	T_{33n}	-0.15	-0.15	—	—	—	—

5.6 Numerical simulations of 3-D specimens

In this section, numerical examples illustrate the accuracy of T -stress computations for cracks in 3-D configurations under mode-I and mixed-mode loading conditions. The examples also demonstrate that the magnitude of non-singular T -stress T_{13} can be significant in magnitude relative to T_{11} . All interaction-integral computations for 3-D problems employ plane-strain auxiliary fields, and the plane-strain assumption in Eq. (210).

5.6.1 Penny-shaped crack in an infinite body under uniform remote tension

Mode-I loading of a penny-shaped crack in an infinite solid under remote tension yields some useful observations regarding:

- accuracy of T_{11} values computed using Eq. (195),
- convergence of T_{11} values with p -version mesh refinement, and
- path-independence of computed values with changing domain size.

The geometry selected for this problem is a cylinder, whose height H and diameter D compare to the crack radius a through the ratios $H/a = D/a = 80$. The ABAQUS 6.4-3 [1] benchmark library provides a mesh for this problem which we use here. Figure 5.9 shows a cross-section of the mesh, comprising 8-noded hexagonal elements, and a view of mesh discretization in the crack-front region. Nine rings of elements, each divided into 24 sectors, surround the crack front. The first ring of elements has collapsed elements of size $L_e/a = 0.00129$. The ninth domain is of size $R_D/a = 0.66$.

Wang [217] derives a closed-form expression for T_{11} along a penny-shaped crack in an infinite solid under remote tension σ_0 :

$$T_{11} = -\frac{1+2\nu}{2}\sigma_0. \quad (212)$$

In this example, the T_{11} value normalized by the remote stress, is $T_{11}/\sigma_0 = 0.8$. Figure 5.10 shows a plot of the ratio of computed T_{11} values to this analytical value for the first 9 domains surrounding the crack front. Small domains show high inaccuracy, whereas domains 8 and 9 show very good agreement with the analytical value, and demonstrate both convergence and path-independence. Converged (path independent) domain-integral values generally indicate good accuracy of the numerical solution. Others (e.g. ABAQUS 6.4-3 [1], Kim and Paulino [117]) observe that for a given level of mesh refinement, computed T -stresses typically have greater path dependence than stress intensity factors computed using the interaction-integral, or J -integral values computed through the domain integral procedure. A comparison of domain-based computations for J -integral values, K_I values, and T -stress demonstrates an interesting difference in convergence behavior for this problem. Domain-integral computations (e.g. [192]) yield J -values for these domains, and interaction-integral computations yield K_I values. The analytical expression of K_I for this problem is [103]

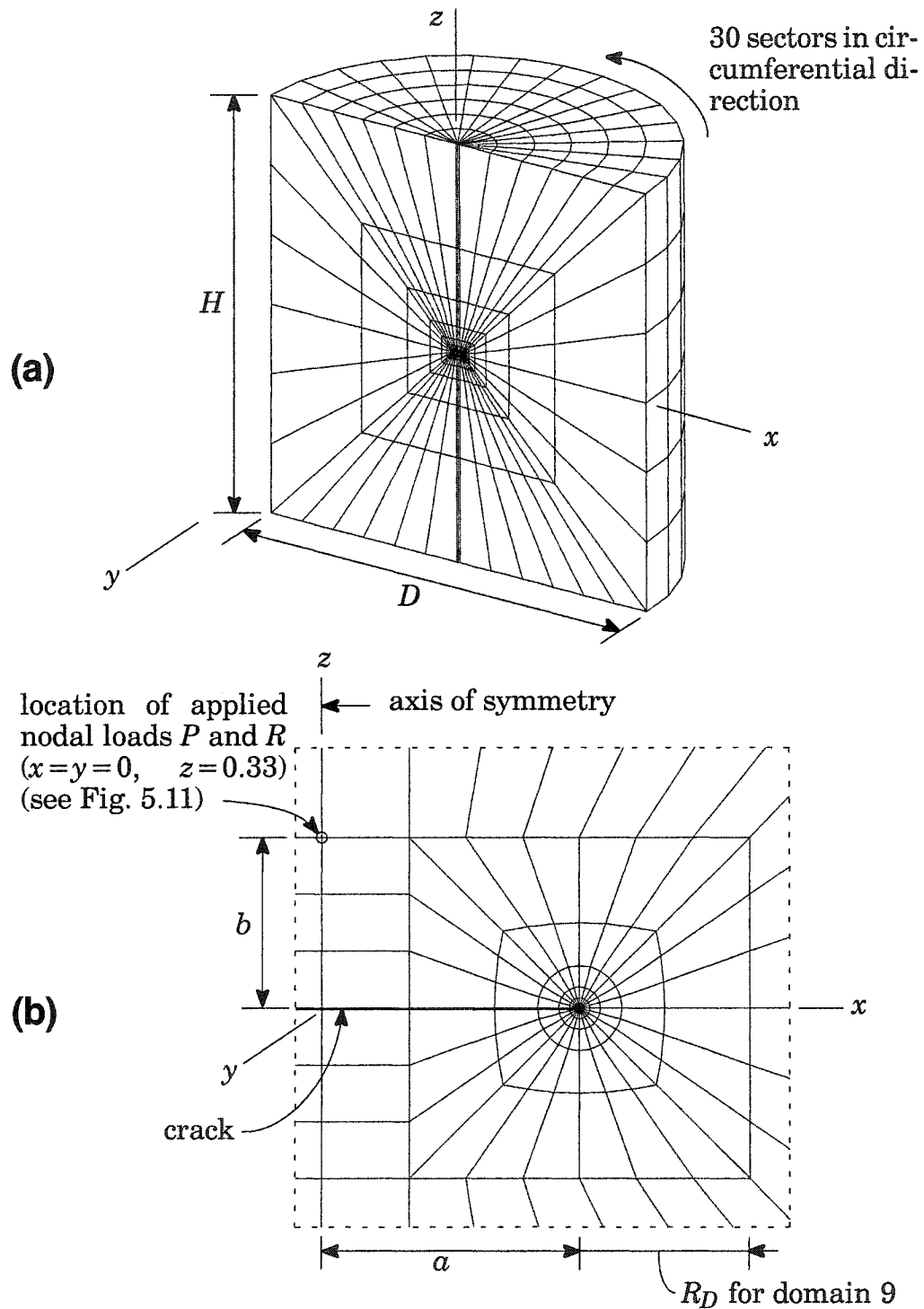


Fig. 5.9. (a) Section view of cylindrical mesh approximating an infinite body with a penny-shaped crack (from ABAQUS [1] benchmark library). Dimension ratios $H/a = D/a = 80$. (b) View of mesh discretization in crack-front region. Seven cylindrical domains with 24 sectors surround the crack front. For domain 1, $L_e/a = R_D/a = 0.00129$. For domain 9, $R_D/a = 0.66$.

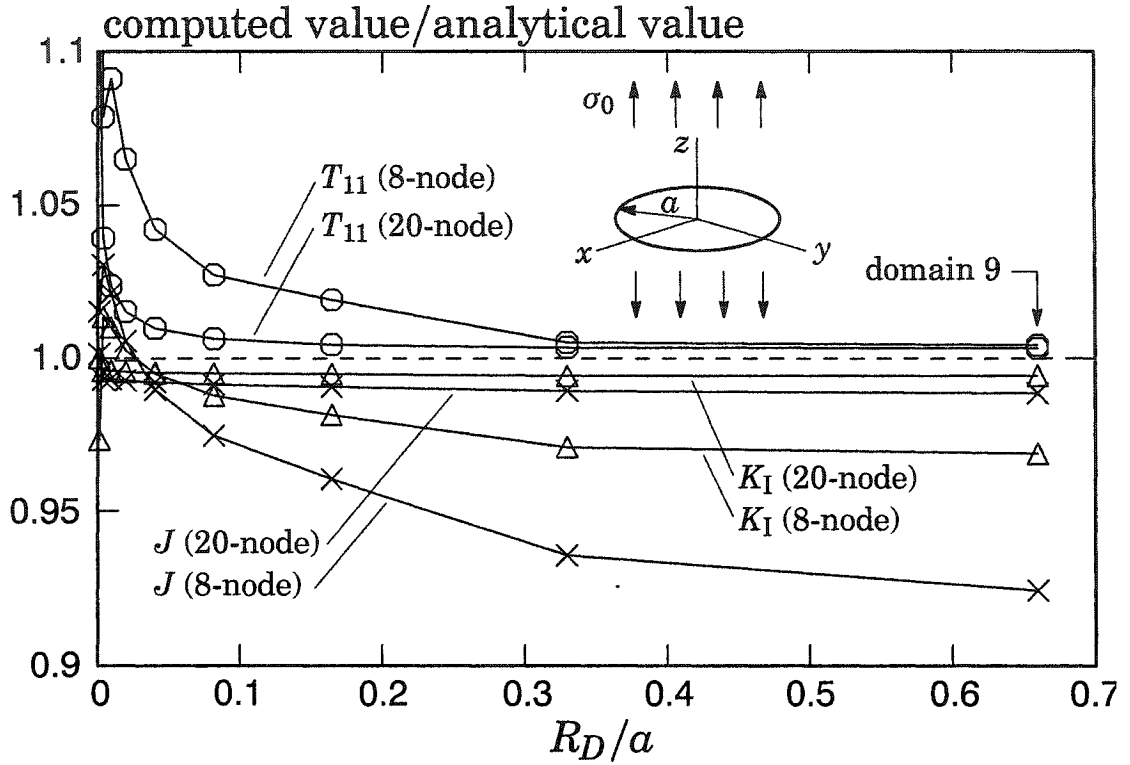


Fig. 5.10. Effect of mesh refinement and domain size on convergence of J , K_I and T_{11} values computed using the domain integral (J) and the interaction integral (K_I , T_{11}) for a penny-shaped crack in an infinite homogeneous solid under remote tension σ_0 . The finite-element mesh comprises either 8-noded or 20-noded hexagonal elements.

$$K_I = \frac{2}{\pi} \sigma_0 \sqrt{\pi a}. \quad (213)$$

The analytical value of K_I leads to an approximate J -value for 3-D problems through [91]

$$J = \frac{1 - \nu^2}{E} K_I^2. \quad (214)$$

Figure 5.10 shows that computed values of J and K_I are more accurate in the smaller domains, but become more path independent in the larger domains. This demonstrates that for a given mesh, it may be necessary to use different sets of domains to compute an accurate, averaged value of J , K_I or T_{11} . Upon refining the mesh of 8-noded bricks by converting the elements to 20-noded bricks, the convergence of computed values to the analytical solution becomes clear in Figure 5.10. All computed J and K_I values have high accuracy, and show excellent path independence over all domains. Computed values of T_{11} , however, become accurate and path independent only in the larger domains. The trends illustrated by these two meshes indicates that larger domains may be necessary to compute accurate values of T_{11} than are necessary to compute accurate values

of J or K_I . Because T -stresses computed here using Eq.(195) employ the same value of tangential strain, ε_{33} , for all domains, the accuracy of this strain does not play a role in the path independence of T_{11} values.

An examination of the terms in Eq. (195) further supports the approach of Nakamura and Parks [146], which begins with the definition of T_{33} described in Eq. (186). Table 5.4 shows the contribution to the computed T -stress from the term $E\nu\varepsilon_{33}/(1-\nu^2)$ in Eq. (195). Computed values shown in the table represent quantities obtained using domains 8 and 9 in the mesh comprising 8-noded elements. For this example, the standard, plane-strain computation of T -stress as $T_{11} = EI/[f_1(1-\nu^2)]$ (see Eq. (179)) would lead to a value of T_{11} with an error of approximately -23% . By including the effect of tangential strain according to Eq. (195), the computed value has an error of less than 0.5% . This illustrates the accuracy of the method of Nakamura and Parks [146] for problems involving mode-I loading. Table 5.4 also shows that for this loading and geometry, the computed value of T_{33} is nearly equal to the analytical value of T_{11} .

Table 5.4. Components of Eq. (195) for T_{11} , and of Eq. (186) for T_{33} , computed with the mesh of 8-noded brick elements shown in Fig. 5.9. Values demonstrate the contribution of tangential strain ε_{33} for a penny-shaped crack in an infinite solid under remote tension σ_0 .

component of Eq. (195)	value normalized by σ_0
$I/f_1 \times E/(1-\nu^2)$	-0.6188
$\nu\varepsilon_{33} \times E/(1-\nu^2)$	-0.1847
T_{11}	-0.8035
T_{11} (exact)	-0.8
component of Eq. (186)	value normalized by σ_0
$\sigma^* = E\varepsilon_{33}$	-0.5603
νT_{11}	-0.2410
T_{33}	-0.8013

5.6.2 Penny-shaped crack in an infinite body under mixed-mode loading induced by point forces

The finite-element mesh of 8-noded brick elements employed in section 5.6.1 (Fig. 5.9) enables the observation of T -stresses along a penny-shaped crack under mixed-mode loading conditions. The problem configuration, as provided by the ABAQUS 6.4-3 [1] benchmark library, includes two nodal forces acting on the axis of the cylinder, normal to the crack face and tangent to the crack face, at a distance of 0.33 above the plane of the crack, as illustrated in Fig. 5.11. The example problem employs forces P and $R = 400$

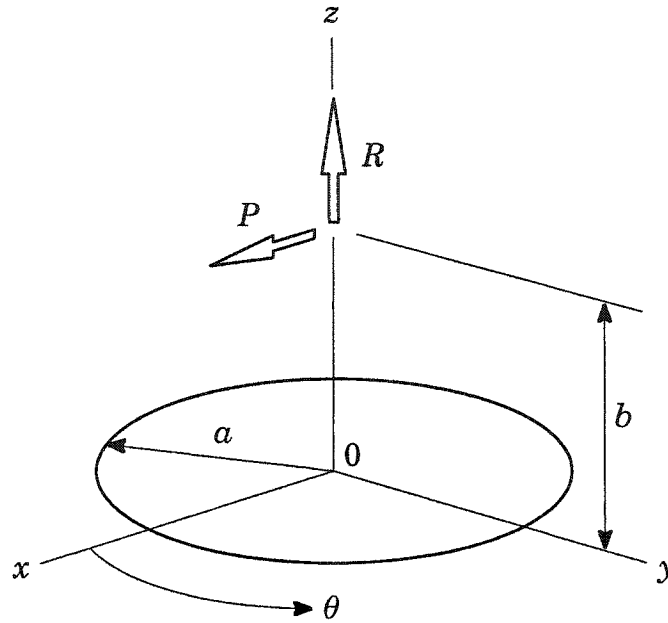


Fig. 5.11. (after Kassir and Sih, [103]) A penny-shaped crack in an infinite homogeneous solid loaded by point forces P and R acting at point $x=0, y=0, z=b$, and directed parallel to the x and z axes, respectively. For the ABAQUS [1] benchmark model, $P=R=400.0E+6$, and $b=0.33$.

MN, Young's modulus = 200 GPa, and Poisson's ratio = 0.3. Displacement boundary conditions in the ABAQUS problem include two fixed nodes, one at each end of the cylindrical axis. These boundary conditions are adequate to enable the computation of accurate stress intensity factors [213] and T_{11} values, but computed T_{13} values show an unsymmetric variation along the crack front. Therefore, the displacement boundary conditions were modified, and include the full constraint of all nodes on one end-face of the cylinder.

Path independence of computed T -stress values differs slightly for this loading condition compared to the case of remote tension, as shown in Fig. 5.12 for a randomly-selected location along the crack front. As with remote tension loading, values of T_{11} converge toward path independence in larger domains, but with the loading caused by concentrated forces, T_{11} values begin to diverge in domain 9. Preliminary computed values of T_{13} show higher path independence in smaller domains, and begin to diverge in domain 8. Figure 5.12 guides the selection of reported T -stress values which for T_{11} are the average of domains 6 through 8, and for T_{13} are the average of domains 4 through 7.

Figure 5.13(a) shows the variation of analytical stress intensity factors for this problem provided by Kassir and Sih [103]. These values, normalized as

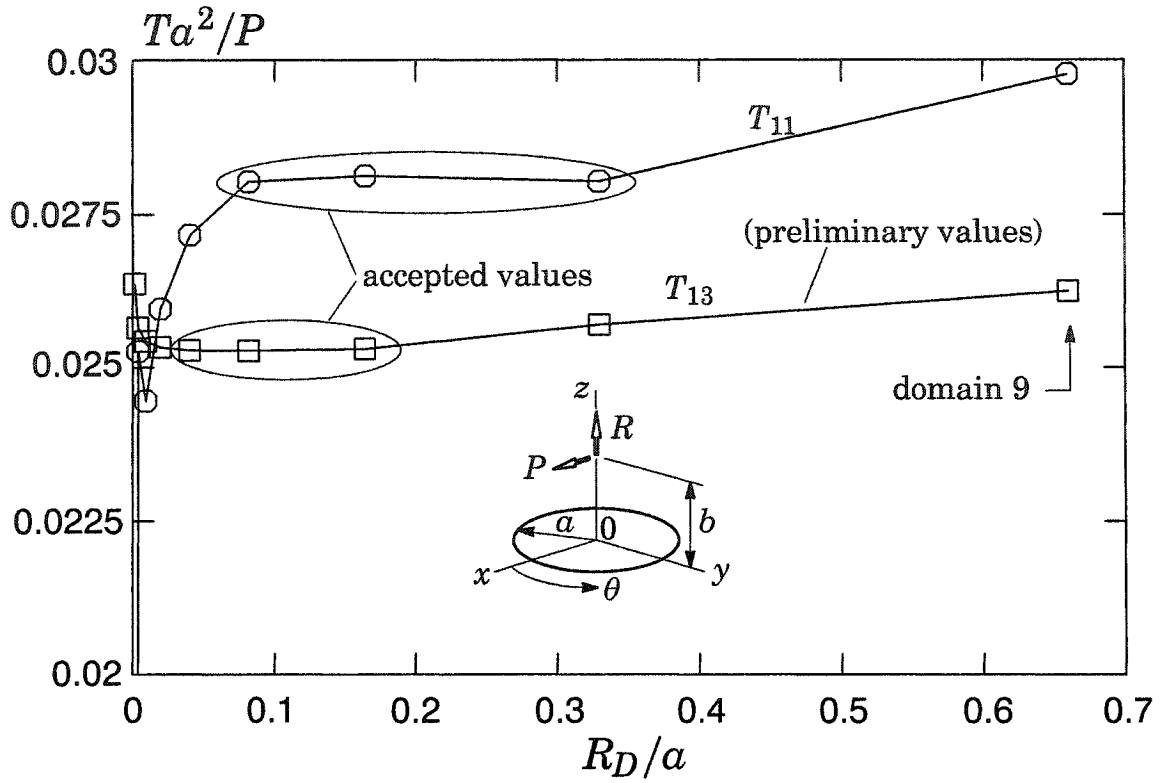


Fig. 5.12. Effect of increasing domain size on convergence of T -stress values at the randomly-selected location ($\theta = 84^\circ$) for a penny-shaped crack in an infinite homogeneous solid loaded by point forces P and R . The finite-element mesh employs 8-noded hexagonal elements.

$$K_n = \frac{K\alpha^{3/2}}{P\sqrt{\pi}}, \quad (215)$$

provide a reference to indicate the mixed-mode loading conditions that coincide with computed T -stresses. Figure 5.13(b) shows values of T -stresses computed along the crack front, normalized as

$$T_n = \frac{T\alpha^2}{P}. \quad (216)$$

5.6.3 Penny-shaped crack in an infinite body under bending

An additional numerical analysis of a penny-shaped crack under bending demonstrates the accuracy of the approach described in Section 5.4.2 to compute tangential strain ϵ_{33} using quadratic finite elements. Fig. 5.14 provides a schematic of the specimen geometry. Remote bending induces stress σ_{zz} normal to the crack plane, that varies along the crack front as

$$\sigma_{zz} = \sigma_b \frac{r}{a} \cos\theta, \quad (217)$$

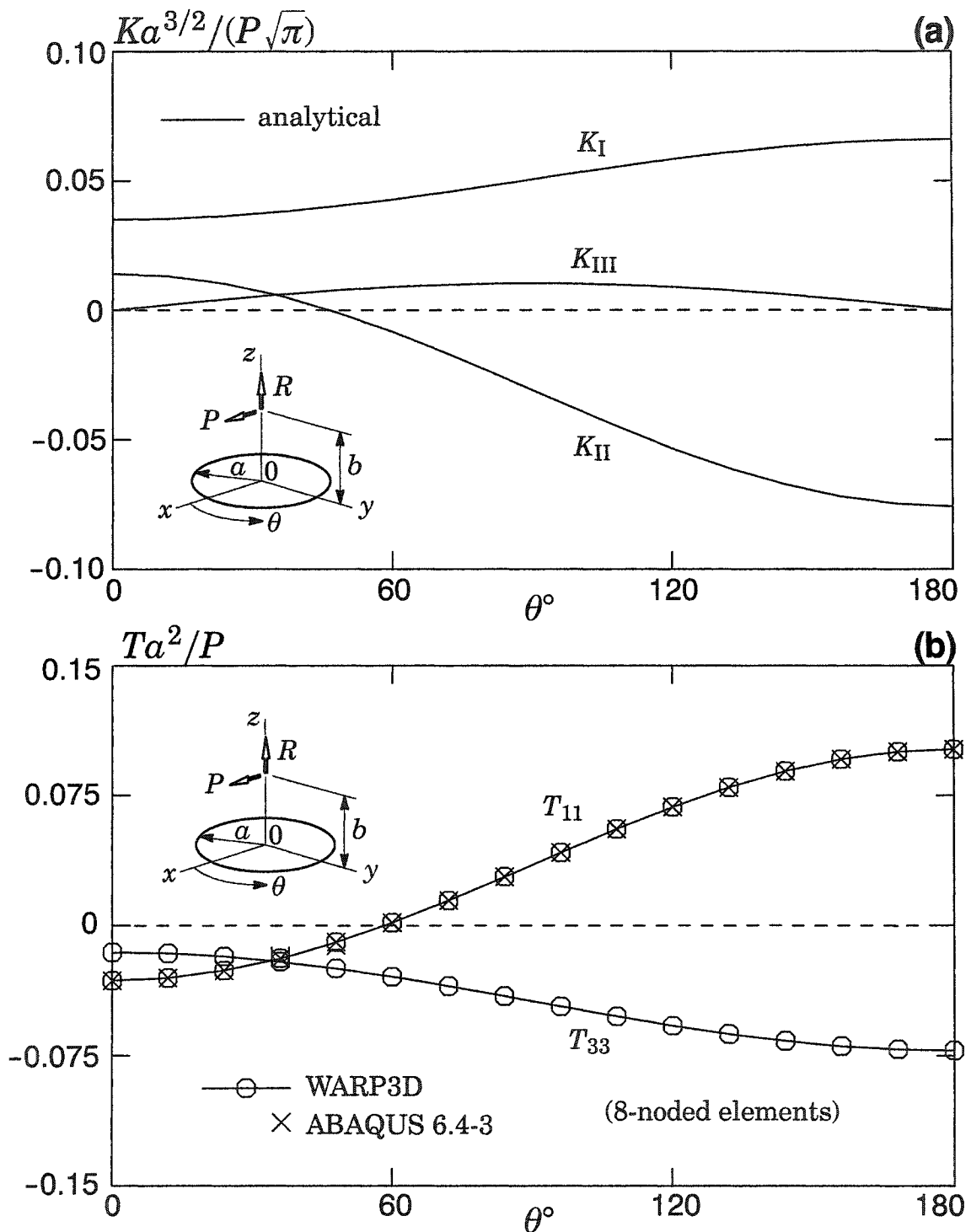


Fig. 5.13. (a) Normalized analytical stress intensity factor values along the front of a penny-shaped crack in an infinite solid loaded by point forces P and R . (b) Normalized T -stresses along the penny-shaped crack computed using the mesh of 8-noded brick elements obtained from the ABAQUS 6.4-3 benchmark library.

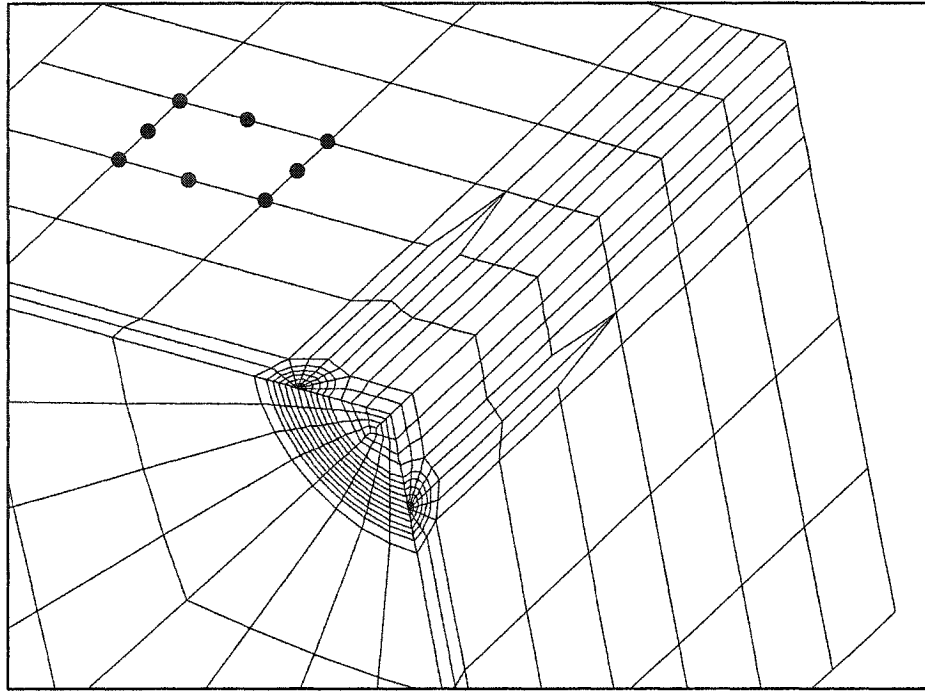


Fig. 5.14. View of one eighth of mesh generated by FEACrack [73] for analysis of a penny-shaped crack in an infinite solid under bending.

where θ indicates position along the crack front, a is the crack radius, r is the radial distance from the center of the crack, and σ_b is the magnitude of σ_{zz} on the crack front at $\theta=0$ and $\theta=\pi$. Figure 5.14 illustrates one eighth of the finite-element mesh employed to simulate this problem. The mesh of 7104 20-noded brick elements, generated using FEACrack [66] software, is a cube with sides equal in dimension to six times the crack radius a . Five rings of elements surround the crack front, which is discretized into 32 straight segments along the circumference (i.e. local crack curvature is zero). Hexagonal elements with one collapsed face and quarter-point nodes immediately surround the crack front. Bending loads applied to both ends of the full mesh consisted of a linearly-varying surface traction imposed by work-equivalent nodal loads. For this problem, Wang [217] derives a closed-form expression for T_{11} :

$$T_{11}(\theta) = \left(-\frac{3}{4} - \frac{\nu}{2} \right) \sigma_b \cos \theta. \quad (218)$$

Figure 5.15 illustrates the path independence of computed T_{11} values for the five domains at $\theta=45^\circ$, and demonstrates that good path independence does not necessarily indicate convergence to the exact solution.

To verify that the same boundary-value problem is being solved, Figure 5.16(a) compares K_I -values generated by interaction-integral computations in WARP3D and ABAQUS 6.4-3 [1], with analytical values reported in Kassir and Sih [103]. Figure

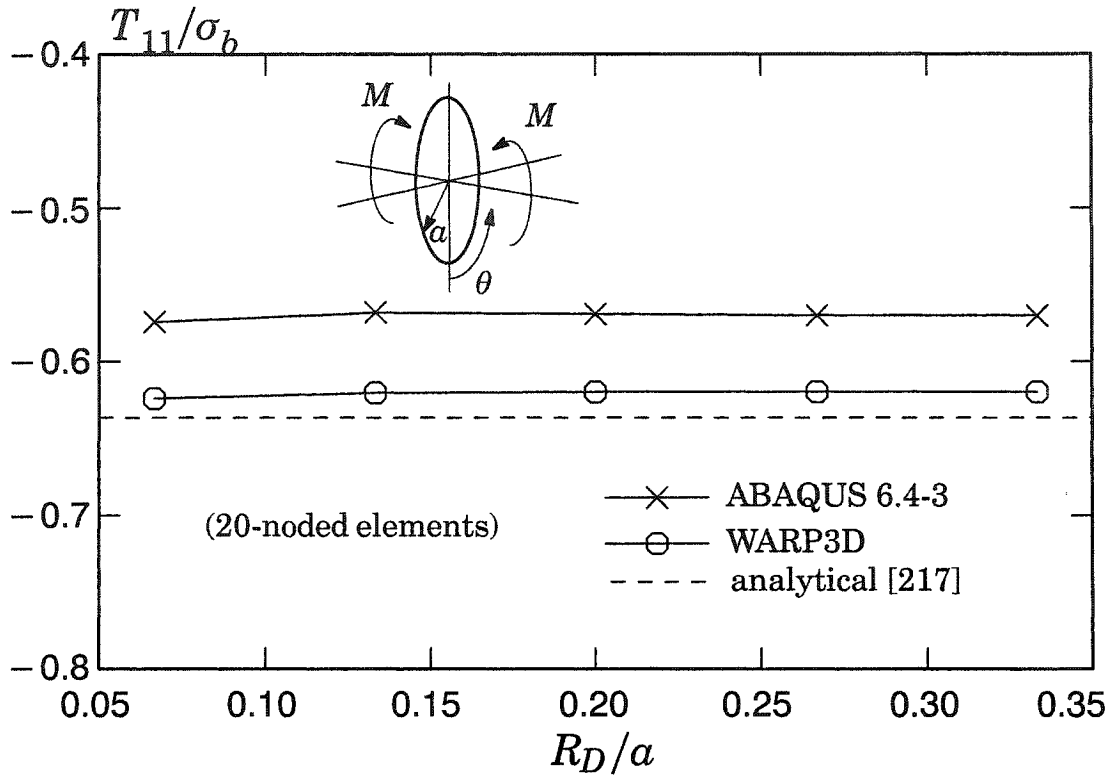


Fig. 5.15. Path independence of computed T_{11} values for penny-shaped crack in an infinite solid under bending. Plotted values were computed using 5 different domains at $\theta = 45^\circ$.

5.16(b) shows the normalized values $T_{11}(\theta)/\sigma_b$, for the range $\theta = 0$ to $\theta = 90^\circ$, obtained from Eq. (218), from present computations, and from ABAQUS 6.4-3. The close agreement between computed stress intensity factors in Eq. 5.16(a) suggests that the difference in accuracy of computed T -stress values in 5.16(b) is likely due to the method employed here to compute the crack-front tangential strain $\varepsilon_{33}(s)$. With further mesh refinement, T_{11} -values computed using ABAQUS 6.4-3 converge to the exact solution for this problem, as demonstrated by Wang [217].

5.6.4 Mode-I loading of a semi-elliptical surface crack in a graded plate

Tension loading of an FGM plate with a surface crack enables verification of computed T_{11} -values for 3-D cracks in FGMs. Figure 5.17(a) shows a quarter-symmetric mesh of the cracked plate, which has dimension ratios $a/c = 2$, $a/t = 0.8$ and $L/H = 2$. Selected ratios of through-thickness exponential material variation, following Eq. (211), are $E_2/E_1 = 1$, $E_2/E_1 = 20$ and $E_2/E_1 = 0.05$. Figure 5.17(b) shows plots of computed T_{11} -values along the length of the crack for each of these ratios. The plots also show the T_{11} -values computed without the terms in the second integral of Eq. (160). The plots omit values at the free surface and the plane of symmetry, due to inaccuracy at these locations.

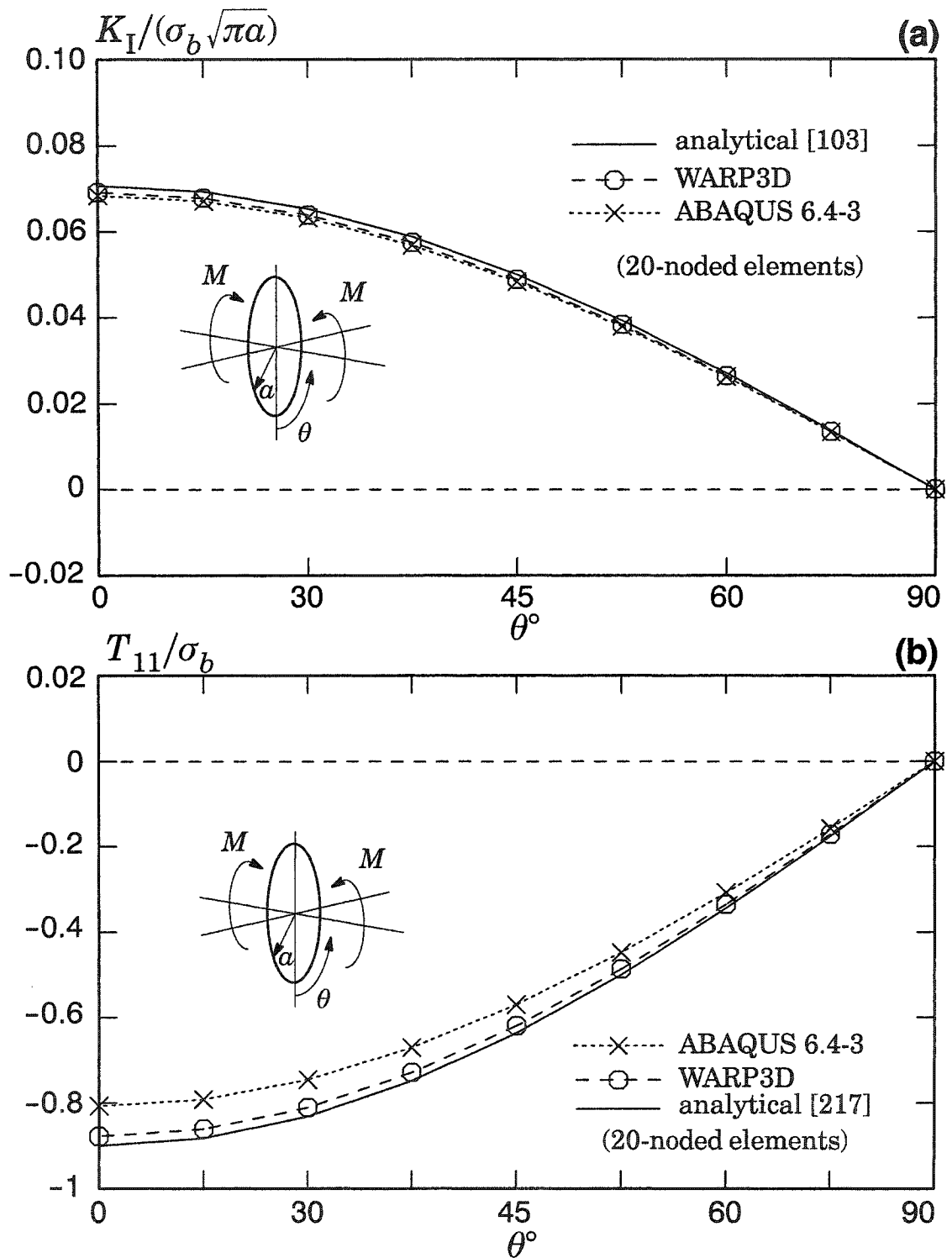


Fig. 5.16. (a) Normalized stress intensity factor values along the front of a penny-shaped crack in an infinite solid under bending. (b) Normalized T_{11} values.

Interaction-integral computations of stress intensity factors for the same problem,

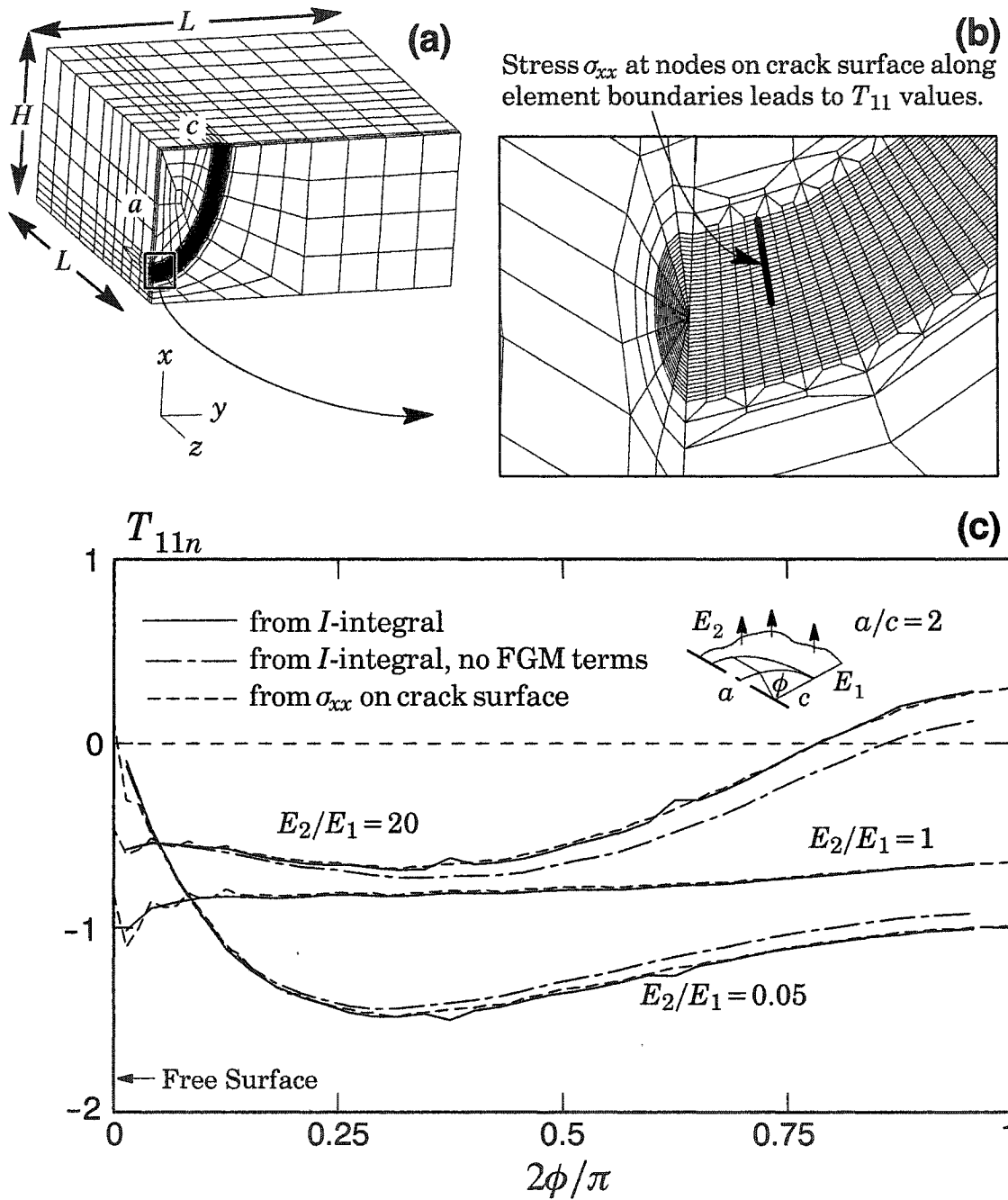


Fig. 5.17. (a) Quarter-symmetric mesh of a semi-elliptical surface crack in a plate under remote tension. (b) Detail of mesh discretization in crack-front region. (c) Normalized T -stress T_{11} computed from \bar{I} with and without FGM terms, and from values of σ_{xx} (stress in local crack-front coordinates) on the crack surface, $\theta = \pi$, extrapolated to $r = 0$.

shown in Fig. 4.12(c), show much weaker dependence upon the FGM terms, which contribute less than 2% to total values.

Ayatollahi et al. [11] discuss several simple methods to determine T_{11} -values for cracks under mode-I/mode-II loading, using computed stresses and displacements. For mode-I loading, the simplest of these methods is to determine the stress normal to the crack front, σ_{xx} , at an angle of $\theta = \pi$ (see Fig. 5.2). According to Eq. (159), this stress should be equal to T_{11} . For each crack-front location at which interaction-integral values are computed, we determine the value of σ_{xx} at nodes on the crack surface along element boundaries, as shown in Fig. 5.17(a). A linear least-squares curve fit of multiple values at each crack-front location then enables extrapolation of a σ_{xx} -value to the crack front. These extrapolated values of σ_{xx} at each location along the crack are the T_{11} -values shown plotted in Fig. 5.17(b), which agree very closely with the T_{11} -values computed using the interaction integral.

5.6.5 Mixed-mode loading of a semi-elliptical surface crack in an FGM plate

A final example illustrates the variation of computed stress intensity factors for a surface crack under mixed-mode loading. The plate geometry, crack aspect ratio, material variation, loading conditions and mesh refinement level in the crack-front region are identical with those in the previous example in Section 4.5.7. In this example, however, the crack inclines at $\omega = 45^\circ$ to the plate-thickness direction, as illustrated in Fig. 4.13(a). Therefore, though the ratio $a/t = 0.8$ remains unchanged from the previous example, the inclined crack extends only to a depth of 0.57 of the plate thickness. FEA-Crack [66] software again generated the mesh, which is shown in Figs. 4.13(a)-(b). Excellent path independence of computed stress intensity factors is apparent in Fig. 4.13(c), which shows values computed for each of the twenty domains at crack-front location $\phi = 85^\circ$, for each mode of loading and for each material variation. However, as in the previous example of a surface crack under mode-I loading, the small size of the domains with respect to the crack size, severely limits the influence of the FGM terms \bar{I}_2 and \bar{I}_3 . The small domain size may also limit the potential influence of curvature terms, which have no influence on at least the first four significant digits in the computed values shown in Fig. 4.13(c). Figures 4.14-4.16 show total contributions from \bar{I}_2 and \bar{I}_3 to the stress intensity factor values computed along the crack front for each mode of loading. The maximum contribution of these FGM terms occurs in the region of steepest material variation, yet represents a very small portion of the computed values in each case. Figures 5.20-5.21 illustrate the contributions of terms \bar{I}_1 - \bar{I}_3 for each of the twenty domains used to compute stress intensity factors at crack-front location $\phi = 85^\circ$. Terms \bar{I}_2 and \bar{I}_3 do become significant for this problem, but they largely cancel each other, making their combined contribution quite small.

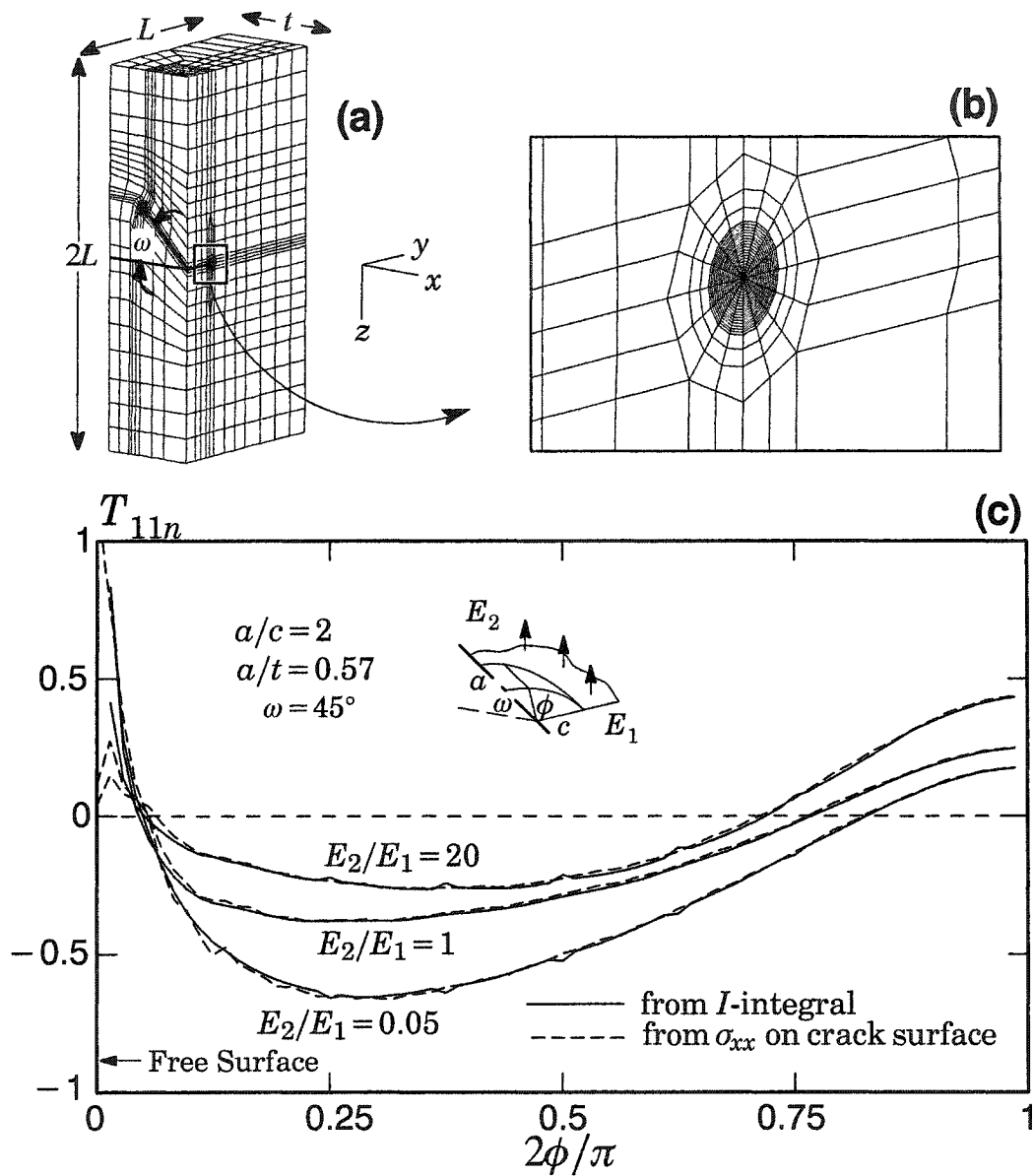


Fig. 5.18. (a) Mesh of semi-elliptical crack, inclined at $\omega = 45^\circ$, in plate under remote tension. (b) Detail of discretization in crack-front region. (c) Normalized T_{11n} -values along crack generated using interaction integral and local σ_{xx} stresses on crack faces.

5.7 Discussion and conclusions

This study has examined an interaction-integral procedure for planar, generally-curved cracks in 3-D FGMs under mixed-mode loading. The interaction-integral formulation for T -stress in homogeneous materials, proposed by Nakamura and Parks [146], has been demonstrated to be very accurate because it incorporates strain tangent

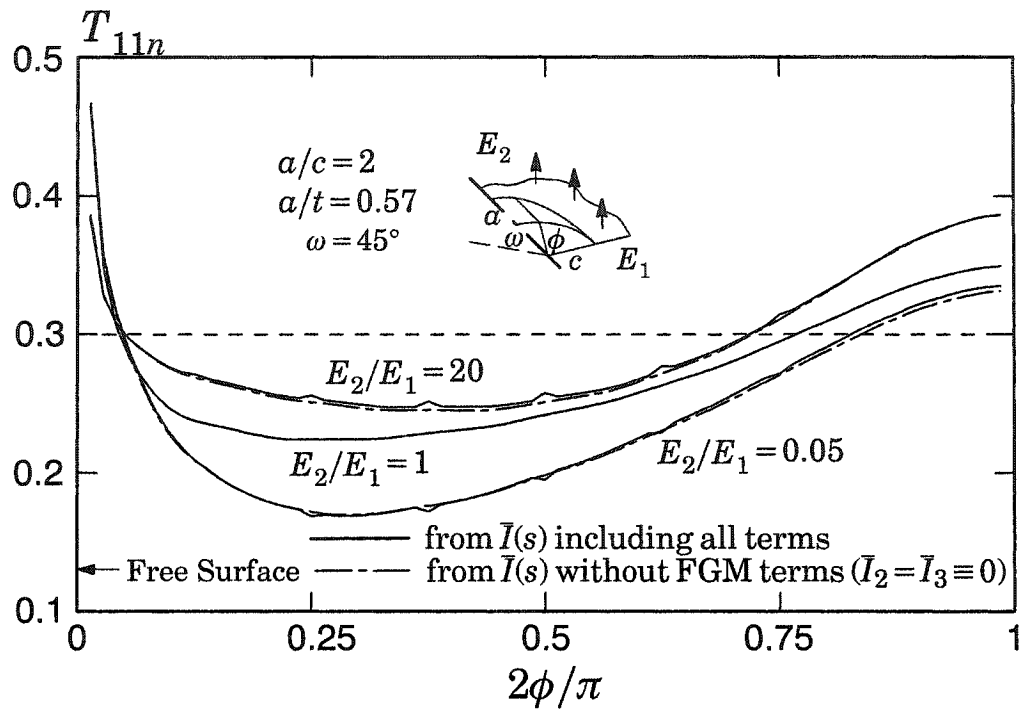


Fig. 5.19. Variation of T_{11n} values along inclined surface crack, computed with and without FGM terms.

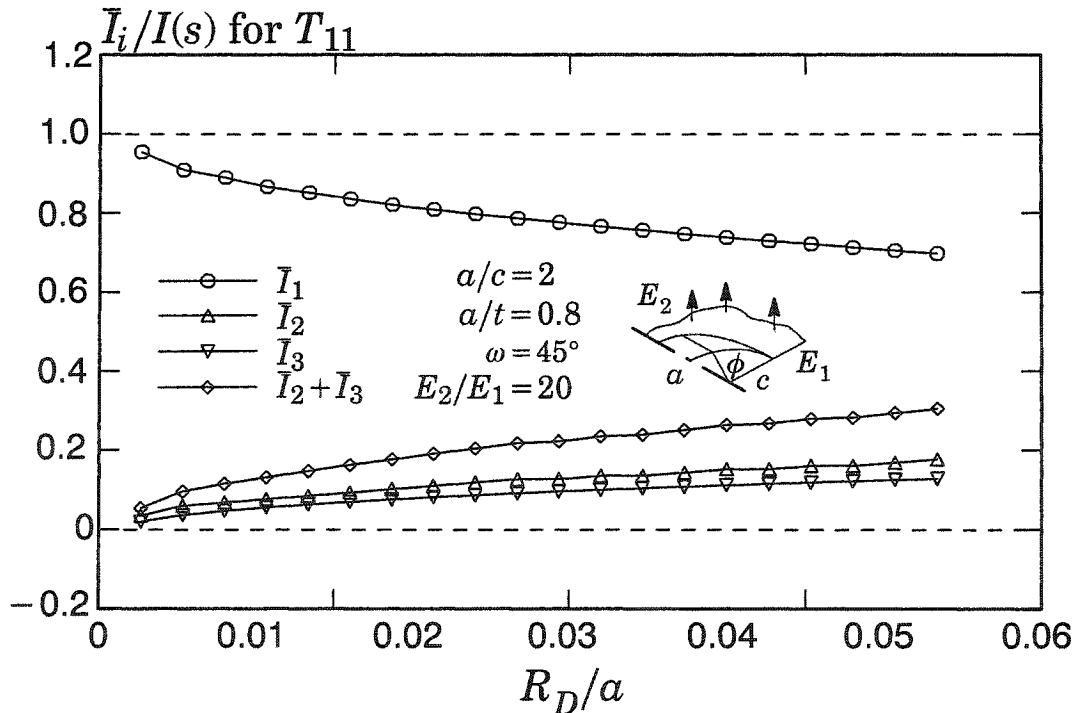


Fig. 5.20. Components of $\bar{I}(s)$ for T_{11} computations at $\phi = 85^\circ$ along a semi-elliptical surface crack under mode-I loading.

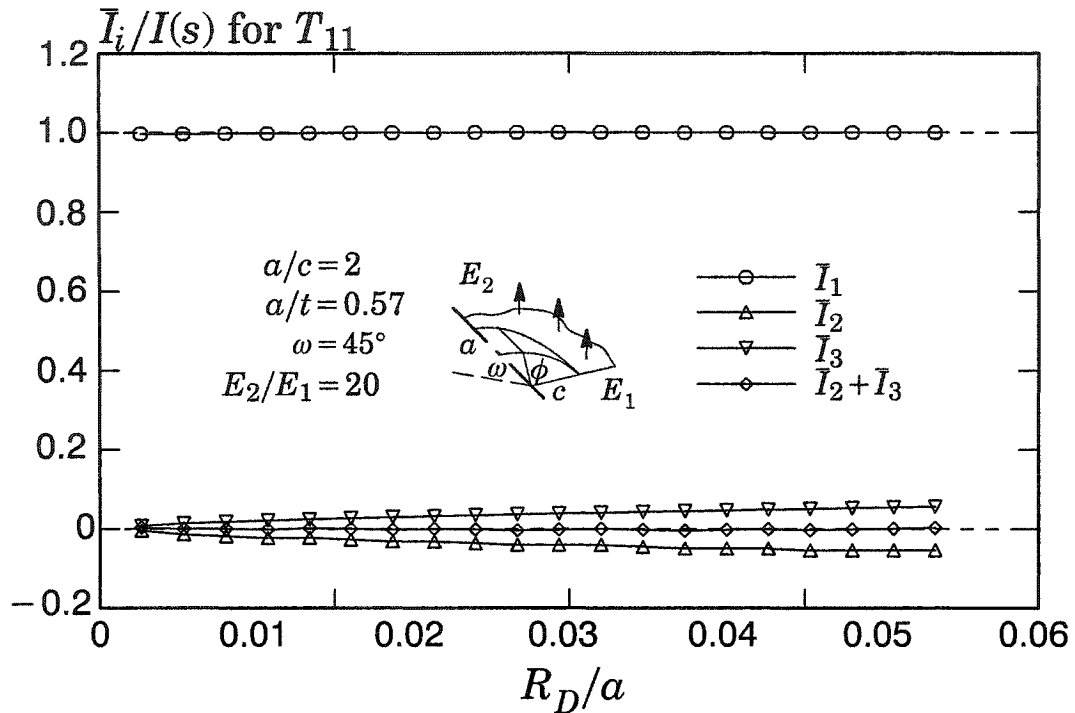


Fig. 5.21. Components of $\bar{I}(s)$ for T_{11} computations at $\phi = 85^\circ$ along an inclined, semi-elliptical surface crack under mixed-mode loading.

to the crack. The formulation has also been shown herein to remain valid for mixed-mode loading.

The interaction integral formulation proposed by Dolbow and Gosz [53] for computation of mixed-mode stress intensity factors in FGMs has been used successfully in conjunction with Eshelby's theorem to compute values for T_{11} in 2-D FGMs under plane loading [113, 116-118]. Here, this method has been explored for cracks in 3-D FGMs, and comparisons with alternative methods for T -stress computation demonstrate its good accuracy.

Anti-plane T -stress T_{13} has been treated in analytical works involving non-planar crack propagation [4, 224]. Some interesting problems involving mixed-mode loading indicate that T_{13} may contribute to crack behavior under constraint. An investigation of the plastic zone size in the presence of T_{13} may provide such insight.

Further work is needed to develop the interaction integral for the case when crack surfaces carry tractions. It was shown here that the derivation by Cho et al. [37] of an analytical expression for T -stress near traction-bearing cracks, actually proves that the contribution from the crack-face loading term is zero for tractions that induce mode-I opening. An alternative auxiliary field may be necessary to incorporate surface-traction effects.

The complexity of the interaction integral implementation, compared with the other, direct verification methods employed in this study, is offset for one primary reason. Direct-stress methods are not as well-defined as domain-integral methods. For example, the analyst must choose which nodes in a given mesh to employ when estimating T_{11} for an arbitrary crack. The domain approach, however, is somewhat more pre-defined for a given mesh, because there is a unique body of elements surrounding the crack front from which domain computations may be made. Another advantage typically attributed to domain-integral procedures—that of observable convergence to a path-independent value—is no longer such when compared to direct stress methods. At each crack-front location, it is possible to compute T -stress values at several nodes at varying distances from the crack. In this study, a curve-fitting procedure enabled the extraction of a single value. Therefore, when different nodes yield comparable T -stress values for a given crack-front location, this consistency is a strong indication of a good solution, just as path-independent values often signal accurate domain-integral computations. Perhaps the choice of a domain-integral method or a direct-stress technique to compute T -stresses will depend more upon available software or convenience rather than upon some inherent advantage of one technique over the other. In such a light, the contribution of this study is the substantiation of one more powerful tool which the analyst may use to compute T -stresses.

Chapter 6

Summary and Conclusions

Chapter 1 of the present work provides a background for domain and interaction-integral methods by reviewing the relationship between the energy release rate G , mixed-mode stress intensity factors K_I , K_{II} and K_{III} , and the J -integral. Then follows a brief review of the development of domain-based techniques to compute these parameters. An introduction to the significance of T -stresses follows next, and includes a thorough review of theoretical, numerical and experimental work in the literature.

Chapter 2 describes the development and application of a general domain integral method to obtain J -values along crack fronts in three-dimensional configurations of isotropic, functionally graded materials (FGMs). The present work considers mode-I, linear-elastic response of cracked specimens subjected to thermomechanical loading, although the domain integral formulation accommodates elastic-plastic behavior in FGMs. Finite element solutions and domain integral J -values for a two-dimensional edge crack show good agreement with available analytical solutions for both tension loading and temperature gradients. A displacement correlation technique provides pointwise stress-intensity values along semi-elliptical surface cracks in FGMs for comparison with values derived from the proposed domain integral. Numerical implementation and mesh refinement issues to maintain path independent J -values are explored. The paper concludes with a parametric study that provides a set of stress intensity factors for semi-elliptical surface cracks covering a practical range of crack sizes, aspect ratios and material property gradations under tension, bending and spatially-varying temperature loads.

Chapter 3 examines a two-state interaction integral for the direct computation of mixed-mode stress intensity factors along curved cracks under remote mechanical loads and applied crack-face tractions. We investigate the accuracy of stress intensity factors computed along planar, curved cracks in homogeneous materials using a simplified interaction-integral that omits terms to reflect specifically the effects of local crack-front curvature. We examine the significance of the crack-face-traction term in the interaction integral, and demonstrate the benefit of a simple, exact numerical integration procedure to evaluate the integral for one class of 3-D elements. The work also discusses two approaches to compute auxiliary, interaction-integral quantities along cracks discretized by linear and curved elements. Comparisons of numerical results with analytical solutions for stress-intensity factors verify the accuracy of the proposed interaction-integral procedures.

Chapter 4 applies a two-state interaction integral to obtain stress intensity factors along cracks in three-dimensional functionally-graded materials. The procedures are applicable to planar cracks with curved fronts under mechanical loading, including crack-face tractions. Interaction-integral terms necessary to capture the effects of material nonhomogeneity are identical in form to terms that arise due to crack-front curvature. A discussion reviews the origin and effects of these terms, and a simplified, approximate interaction-integral expression is used in this work to compute stress intensity factors. The selection of terms is driven by requirements imposed by material nonhomogeneity (and not crack-front curvature) in conjunction with appropriate mesh discretization along the crack front. Aspects of the numerical implementation with (iso-parametric) graded finite elements are addressed, and examples demonstrate the accuracy of the proposed method.

Chapter 5 develops two-state interaction-integral procedures for the computation of T -stresses for three-dimensional cracks in FGMs under mixed-mode, remote mechanical loading. Previous techniques address mixed-mode loading of cracks in two-dimensional functionally-graded materials, and mode-I loading of three-dimensional cracks in homogeneous solids. This study extends these procedures to the computation of T -stress along three-dimensional crack fronts in functionally-graded material under mixed-mode loading conditions. In addition, the approach widely used in the literature to compute T -stresses for cracks under remote mechanical loading is investigated for computing T -stresses in the presence of crack-face tractions, and is found unsuitable.

The present chapter provides some final comments on domain-integral techniques for computation of fracture parameters, and discusses future directions where research is needed to extend their capabilities for some important problems.

6.1 Some comments on crack-analysis techniques

Domain integral techniques remain one of the most powerful and robust methods to compute fracture parameters for static cracks. Their strength arises from their basis on the energy stored in a cracked body. Many methods based on stress analysis, rely upon the accuracy of computed displacements, strains and stresses at specific locations with a finite-element mesh. These computed field quantities can then be correlated to analytical expressions involving fracture parameters such as stress intensity factors or T -stresses [10]. The displacement correlation technique employs Williams' [221] expressions involving the mixed-mode stress intensity factors, with computed displacements at a specific location described by r and θ from a crack front. This process is open to the question of what location should be selected from which to deduce K ? Any node within the K -dominant region should, theoretically, yield an identical value of K . But

in most finite-element meshes, this is clearly not the case. The displacement correlation technique normally produces a fairly large variation in K at nodes near to the crack and far from the crack. A consistent approach might deduce K from nodes at locations described by fixed values of either r or θ or both. Another option is to compute values at a fixed θ but at multiple r -values, and then fit a line through computed values of K . Extrapolation of this line to $r = 0$ should produce an accurate value for K . But the question then still involves selecting a proper set of r - K points through which to fit the line. Some region should exhibit a somewhat linear variation, but this region may change significantly between various locations along a curved 3-D crack. Between a semi-elliptical surface crack, a penny-shaped embedded crack, or an SE(T) specimen with a straight crack front, it requires subjective judgement to deduce fracture parameters using these stress-based methods.

The use of hybrid or enriched elements enables computation of mixed-mode stress intensity factors by embedding into elements surrounding the crack front, analytical expressions for stress, strain and displacement, such as Williams' [221] solution [22, 12, 163]. These techniques are similar to domain-integral techniques in that they employ a group of elements surrounding the crack, and have much in common with interaction-integral methods because both normally use closed-form expressions to incorporate fracture parameters such as stress intensity factors. Hybrid and enriched elements are normally integrated into the boundary-value-problem solution, whereas domain-integral techniques rely entirely upon post-processing routines. Both techniques require comparable effort to implement, especially to achieve user-friendly, automatic definitions of the integration domains. A major strength of domain and interaction-integral procedures is the ability to compute the fracture parameters using elements remote from the crack front. The path-independent nature of the domain-based approaches allows many different volumes within a single structure to be employed, each of which should yield a fairly similar value when a converged solution is achieved. Elements remote from the crack can yield very precise values for field variables, whereas elements incident on the crack front will always require special treatment in order to capture accurately the singular behavior induced by the discontinuity. For analysis of stationary cracks, computations with elements remote from the crack, and redundancy obtained from the use of multiple domains, give domain and interaction-integral methods a significant advantage over enriched-element procedures that extract fracture parameters from elements incident on the crack. Enriched elements can be used over larger areas surrounding the crack, however [163], and they can also be used in conjunction with domain-integral techniques, thus providing both improved accuracy near the crack, and the benefit of using remote field variables (see, e.g. [52]). The previous descriptions do not represent a thorough review of numerical techniques to compute fracture paramete-

ters for cracks in 3-D bodies, but they do represent some of the more common, and by implication, more useful, approaches.

6.2 Limitations of crack analysis with finite elements

Traditional finite-element methods require a crack to lie along element boundaries. This requirement usually makes it very time consuming to construct a mesh with a crack, especially in 3-D, because the mesh must include refined elements situated according to the crack geometry. If the engineer prefers hexagonal elements because of their well-known superior accuracy to tetrahedral elements, it will most likely be impossible to generate automatically a mesh for a geometry with an arbitrary crack. Software companies, such as the makers of FEACrack software [66], find success with powerful, user-friendly mesh assembly programs that generate ready-to-use meshes, composed of hexagonal elements, for a library of complicated cracked geometries.

A significant challenge in computational fracture mechanics is the simulation of crack propagation. The challenge lies in two areas: mesh generation and crack-propagation criteria. For finite-element methods, remeshing a cracked body after each increment of crack propagation becomes extremely costly. In three dimensions, automatic crack propagation is much more difficult than in two dimensions, and because of remeshing requirements, the traditional finite-element method, in this endeavor, is not the most streamlined numerical procedure. Boundary-element methods (BEMs), because of a reduced dimensionality of the boundary-value problem, become much more attractive for 3-D crack propagation, because only the surface of the body, including crack faces, must be meshed. The addition of 2-D elements to an extending crack surface is much simpler than the remeshing of an entire 3-D region surrounding an advancing crack front [30]. Domain-integral procedures, similar to those employed in this study, have been developed as post-processing tools in conjunction with boundary element methods [207]. Crack propagation is a much simpler task for the many problems for which BEMs may be used.

Recently, a large variety of mesh-free methods have been developed that are powerful for modeling arbitrary and propagating cracks (e.g. [17, 58, 18, 158, 19, 57, 58, 125]). For ease of modeling, mesh-free methods have an advantage over traditional finite-elements, in that they employ groups of nodes, rather than a regular assembly of elements, over which to estimate the solution to the boundary-value problem. These methods largely eliminate the requirement for tedious mesh construction in the vicinity of irregular geometrical features such as cracks. Because of their significant differences with traditional finite-element approaches, mesh-free methods cannot straightforwardly employ the large variety of powerful solvers and pre and post-processing software that

has been developed for finite-element methods. This potential drawback has driven the development of new crack analysis and crack-modeling techniques that employ a traditional finite-element framework [158, 159, 160, 52, 125, 204, 55, 56, 205, 85]. These methods enable crack growth simulations to be performed using a single finite-element mesh. Without the requirement for remeshing, these techniques offer a promising alternative to crack-propagation simulations using the traditional finite-element method. These new methods allow for computation of fracture parameters such as the energy release rate and stress intensity factors through domain-based J -integral and interaction-integral procedures [52, 170]. The domain and interaction integrals studied in the present work should also be useful for the analysis of 3-D cracks using these new techniques.

6.3 Future directions

Various possible extensions of the domain and interaction integrals studied in this work remain unexplored. The robustness and accuracy of the integrals examined in the previous chapters, warrants their further development. Some promising areas include:

- An examination of the general form of the domain integral employed here to compute energy release rates for FGMs, indicates that two terms numerically cancel each other. This cancellation may be due to the principle of reciprocal work, or perhaps the symmetry of the q -function. For problems involving linear-elasticity and small-deformations, the form of the integral that omits the cancelled terms, leads to a simplified domain-integral expression. All numerical values reported for domain-integral computations in Chapter 2 would remain essential unchanged without the additional terms. The simpler domain integral might also be explored for the possibility of leading to a simplified interaction integral for FGMs.
- Krysl and Belytschko [125] have employed the interaction integral to compute stress intensity factors for dynamically-propagating cracks in 3-D homogeneous bodies. Song and Paulino [202] compute dynamic stress intensity factors for cracks in 2-D FGMs. Sladek and Sladek [196, 199] have developed the interaction integral to compute T -stress T_{11} for dynamic loading. Computation of stress intensity factors and T -stresses for dynamic loading of cracks in 3-D FGMs remains unexplored.
- An interaction integral for thermal loading has been developed by Sladek and Sladek [195]. Because FGMs have significant potential as thermal barrier coatings, the interaction integral for 3-D FGMs invites extension to the thermal loading case for computation of stress intensity factors and T -stresses.

- Chapter 5 explores the computation of T -stresses for mechanical loading, and discusses a proof that current formulations employing auxiliary fields derived from a point (line) load acting at the crack tip (front), lead to a zero contribution from the crack-face traction integral in Eq. (160) (see also Eq. (183)). To compute an accurate value of T for cracks that carry surface tractions, it will likely be necessary to employ different auxiliary fields. One possibility for auxiliary fields in this situation might be the analytical solution for traction loading on the surface(s) of an infinite wedge (e.g. [25, 101]).
- With the verification of the 3-D numerical techniques in this study, and with their availability in the WARP3D [78] software, it is now possible to easily employ them to study behaviors of cracked 3-D FGM bodies. For example, Jin and Dodds [96] employ the numerical procedure described in Chapter 2 with WARP3D to study R -curve behavior in FGMs. Shim et al. [193] employ the numerical procedures in Chapter 5 to develop a small-scale-yielding boundary-layer model that enables the prediction of the plastic zone size in FGM specimens. In addition to these studies, there is a wide variety of crack behaviors in 3-D FGM configurations that the numerical procedures in this work permit investigating. In addition, the sets of stress intensity factors listed in Chapter 2 are available for analysts to either estimate stress intensity factors in experimental specimens, or to verify numerical computations.

Appendix A

Asymptotic Crack-Tip Fields

Auxiliary fields employed here follow the 2-D analytical solutions obtained by Williams [221] for asymptotic stresses and displacements near a crack tip [NO TAG]:

$$\sigma_{11}^{aux} = \frac{1}{\sqrt{2\pi r}} \left[K_I^{aux} \cos \frac{\theta}{2} \left(1 - \sin \frac{\theta}{2} \sin \frac{3\theta}{2} \right) - K_{II}^{aux} \sin \frac{\theta}{2} \left(2 + \cos \frac{\theta}{2} \cos \frac{3\theta}{2} \right) \right], \quad (A1)$$

$$\sigma_{22}^{aux} = \frac{1}{\sqrt{2\pi r}} \left[K_I^{aux} \cos \frac{\theta}{2} \left(1 + \sin \frac{\theta}{2} \sin \frac{3\theta}{2} \right) + K_{II}^{aux} \sin \frac{\theta}{2} \cos \frac{\theta}{2} \cos \frac{3\theta}{2} \right], \quad (A2)$$

$$\sigma_{12}^{aux} = \frac{1}{\sqrt{2\pi r}} \left[K_I^{aux} \cos \frac{\theta}{2} \sin \frac{\theta}{2} \cos \frac{3\theta}{2} + K_{II}^{aux} \cos \frac{\theta}{2} \left(1 - \sin \frac{\theta}{2} \sin \frac{3\theta}{2} \right) \right], \quad (A3)$$

$$\sigma_{13}^{aux} = - \frac{K_{III}^{aux}}{\sqrt{2\pi r}} \sin \frac{\theta}{2}, \quad (A4)$$

$$\sigma_{23}^{aux} = \frac{K_{III}^{aux}}{\sqrt{2\pi r}} \cos \frac{\theta}{2}, \quad (A5)$$

$$\sigma_{33}^{aux} = \begin{cases} \nu(\sigma_{11}^{aux} + \sigma_{22}^{aux}) & \text{plane strain} \\ 0 & \text{plane stress,} \end{cases} \quad (A6)$$

$$u_1^{aux} = \frac{1}{2\mu} \sqrt{\frac{r}{2\pi}} \left[K_I^{aux} \cos \frac{\theta}{2} \left(\kappa - 1 + 2 \sin^2 \frac{\theta}{2} \right) + K_{II}^{aux} \sin \frac{\theta}{2} \left(\kappa + 1 + 2 \cos^2 \frac{\theta}{2} \right) \right], \quad (A7)$$

$$u_2^{aux} = \frac{1}{2\mu} \sqrt{\frac{r}{2\pi}} \left[K_I^{aux} \sin \frac{\theta}{2} \left(\kappa + 1 - 2 \cos^2 \frac{\theta}{2} \right) - K_{II}^{aux} \cos \frac{\theta}{2} \left(\kappa - 1 - 2 \sin^2 \frac{\theta}{2} \right) \right], \quad (A8)$$

$$u_3^{aux} = \frac{K_{III}^{aux}}{\mu} \sqrt{\frac{2r}{\pi}} \sin \frac{\theta}{2}, \quad (A9)$$

where ν and μ are respectively Poisson's ratio and the shear modulus, and

$$\kappa = \begin{cases} 3 - 4\nu & \text{plane strain} \\ \frac{3 - \nu}{1 + \nu} & \text{plane stress .} \end{cases} \quad (A10)$$

Appendix B

Exact Integration of Crack-Face-Traction Integral

A change of variables permits the exact integration of Eq. (68). For a 1-D function $f(r)$ with an inverse square-root singularity at one boundary of the domain of integration, the substitution of $r = t^2 + a$, removes the singularity [172]:

$$\int_a^b f(r) dr = \int_0^{\sqrt{b-a}} 2t f(t^2 + a) dt \quad (b > a). \quad (\text{C1})$$

For example, define $f(r) = 1/\sqrt{r}$, and assign integration limits a and b as $r = 0$ and $r = L_e$, the length of an element adjacent to the crack front, illustrated in Fig. 3.3(d). The relationship $t^2 = r$ leads to $f(t^2 + a) = 1/t$, giving

$$\int_0^{L_e} \frac{1}{\sqrt{r}} dr = \int_0^{\sqrt{L_e}} 2t \frac{1}{t} dt = \int_0^{\sqrt{L_e}} 2 dt = 2\sqrt{L_e}, \quad (\text{C2})$$

which is the exact result. To evaluate Eq. (68) over a flat 2-D surface where coordinate z is tangent to the crack front, $f(z, r)$ includes traction values, t_j , auxiliary-displacement derivatives, $u_{j,1}^{aux}$, and q -function values. Standard Gauss quadrature is adequate to integrate exactly in the z -direction.

To implement the above procedure numerically, a change of variables in parent (natural, intrinsic) coordinates is performed. From (C1), we have

$$\int_{-1}^1 \int_{-1}^1 f(\xi, \eta) d\eta d\xi = \int_{-1}^1 \int_0^{\sqrt{2}} 2t f(\xi, t^2 - 1) dt d\xi, \quad (\text{C3})$$

where the inverse square-root singularity of $f(\xi, \eta)$ in parent coordinates corresponds to the lower integration boundary $\eta = -1$. In Eq. (C3) and in the steps that follow, we assume that parent coordinate ξ is tangent to the crack front, and that η corresponds to distance r from the crack front. Integrands in Eq. (C3) include traction values, t_j , auxiliary-displacement derivatives, $u_{j,1}^{aux}$, q -function values, and the determinant of the coordinate Jacobian, $\det \mathbf{J}$.

In order to apply a Gauss quadrature rule formulated for the interval $[-1, 1]$, to the inner integral of Eq. (C3) over interval $[0, \sqrt{2}]$, it is necessary to employ the standard transformation [65]:

$$t = \frac{b-a}{2}\eta + \frac{b+a}{2}, \quad (\text{C4})$$

where a and b are the new limits of integration, 0 and $\sqrt{2}$, respectively. Equation (C4) gives

$$t = \frac{1}{\sqrt{2}}(\eta + 1), \text{ and } \frac{dt}{d\eta} = \frac{1}{\sqrt{2}}, \quad (\text{C5})$$

and the quadrature for Eq. (C3) over one element face becomes

$$\frac{1}{\sqrt{2}} \sum_p^{\text{gpts}} 2t f(\xi, t^2 - 1) w_p, \quad (\text{C6})$$

where the summation includes all Gauss integration points at parent coordinates (ξ, t) , where Eq. (C5) defines t . Weights w_p in Eq. (C6) correspond to the standard Gauss-quadrature rule formulated over interval $\xi = \eta = [-1, 1]$, and $1/\sqrt{2}$ is the Jacobian of the interval transformation, or $dt/d\eta$ in (C5).

The following steps describe the procedure for evaluating Eq. (68) through the quadrature described by Eq. (C6).

- 1) Collect data for element faces and nodes (coordinates, q -values, tractions etc.).
- 2) Loop over integration points. A 2×2 quadrature rule yields exact results for the constant face tractions employed in this study.
- 3) For the current integration point, obtain weight w_p , and parent coordinates (ξ, η) based on a standard rule for the interval $\xi = \eta = [-1, 1]$.
- 4) Shift the value of η according to Eq. (C5): $\eta_{\text{new}} = t = 1/\sqrt{2}(\eta + 1)$.
- 5) Redefine η as in Eq. (C3): $\eta = (\eta_{\text{new}})^2 - 1$.
- 6) Evaluate standard element shape functions, shape-function derivatives, the coordinate Jacobian matrix, and the determinant of the coordinate Jacobian matrix, $\det \mathbf{J}$, using the standard value for ξ , and the value of η obtained from step 5.
- 7) Use element shape functions to determine the local coordinates, (X_1^p, X_2^p, X_3^p) , of the current integration point, and the q -value and traction value at the integration point.
- 8) Compute distance r and angle $\theta = \pm \pi$ from the crack front to the integration point based on the coordinates determined in step 7.
- 9) Evaluate the auxiliary-displacement derivative $u_{j,1}^{\text{aux}}$ using μ , r and θ from the previous step, and 1.0 for the stress intensity factor.
- 10) Evaluate the integrand in Eq. (C6) as: $w_p \times q(\xi, \eta) \times t_j(\xi, \eta) \times u_{j,1}^{\text{aux}}(\xi, \eta) \times \det \mathbf{J}$, where summation is implied by the repeated index, and η follows from step 5.

- 11) Complete the quadrature in Eq. (C6) by multiplying the result of step 10 by $1/\sqrt{2} \times 2\eta_{\text{new}}$.
- 12) Sum contribution from integration point, and cycle to next point.

In steps 1-12, only steps 4, 5 and 11 differ from standard quadrature procedures. Examples in Sections 3.5 and 3.6 demonstrate that including these three simple steps to integrate Eq. (68) exactly, may markedly improve the accuracy of stress intensity factors. Steps 4, 5 and 11 are required for the exact integration of Eq. (68) for 8-noded elements with four nodes on each face, and for 20-noded elements with 8 nodes on each face. When quarter-point elements border the crack front, steps 4, 5 and 11 should not be employed because the quarter-point nodes cause standard quadrature to integrate Eq. (68) exactly. Standard Gauss quadrature provides good accuracy for elements not incident on the crack front.

Appendix C

Computation of r and θ for Elements With Straight Edges

The following steps describe one procedure to compute r and θ for curved, planar crack fronts defined by elements with straight edges. Definitions use coordinates in the local crack-front coordinate system shown in Fig. 2.5, and the notation described in Figs. 3.1(a)-(b):

- 1) Determine the crack-front segment nearest the integration point, and obtain coordinates of the nodes at each end of the segment. Call these points A and B , where B has the larger value of X_3 .
- 2) Use element shape functions to determine the coordinates of the integration point P in the local crack-front system, (X_1^p, X_2^p, X_3^p) :

$$X_i^p = \sum_{I=1}^n N_I(X_i)_I. \quad (\text{B1})$$

- 3) The area of the parallelogram defined by AB and AP equals the magnitude of the cross product of AB and AP , or $\|AB \times AP\|$. Compute height r of the parallelogram as the area divided by the length of the base AB :

$$r = \frac{\|AB \times AP\|}{\|AB\|}. \quad (\text{B2})$$

Point C is the projection of integration point P onto the crack plane, which is the X_1 - X_3 plane. In local coordinates, $C = (X_1^p, 0, X_3^p)$. Point D is the point on segment AB closest to point C . Angle PDC defines θ . The plane PDC on which r is defined, coincides with the local X_1 - X_2 plane only for straight crack fronts. Figure 3.1(b) illustrates quadrants of a coordinate system in the plane defined by points PDC , with point D at the origin, and segment DC orthogonal to the local X_2 -axis. Computation of θ involves two additional steps:

- 4) Use X_2^p to determine if P lies above or below the crack plane, and use the sign of cross product $AB \times AC$ to determine whether the integration point is ahead of or behind segment AB .
- 5) For quadrants I - IV illustrated in Fig. 3.1(b), compute θ as

$$\text{I: } \theta = \sin^{-1}\left(\frac{X_2^p}{r}\right); \quad \text{II: } \theta = 180^\circ - \sin^{-1}\left(\frac{X_2^p}{r}\right), \quad (\text{B3})$$

$$\text{III: } \theta = -180^\circ - \sin^{-1}\left(\frac{X_2^P}{r}\right); \quad \text{IV: } \theta = \sin^{-1}\left(\frac{X_2^P}{r}\right). \quad (\text{B4})$$

For the crack-face-traction integral where $\theta = \pm\pi$, the sign of the X_2 -coordinate of the centroid of the loaded element conveniently indicates the sign of θ .

Appendix D

Stress Intensity Factor Solutions

D.1 Circular crack in an infinite body loaded by point forces

Kassir and Sih [103] provide analytical solutions for the stress intensity factors around a penny-shaped crack in an infinite homogeneous medium loaded by point forces above the crack plane. Figure 3.6 illustrates the geometry and nomenclature used in the following expressions. For point-load P , which acts parallel to the x -axis at distance b from the crack plane, the stress intensity factors are

$$K_I = \frac{P \cos \theta}{4\pi^{3/2}(1-\nu)a^{3/2}} \left[(1-2\nu) \left(\cot^{-1} z_0 - \frac{z_0}{1+z_0^2} \right) - \frac{2z_0}{(1+z_0^2)^2} \right], \quad (D1)$$

$$K_{II} = \frac{P \cos \theta}{4\pi^{3/2}(1-\nu)(2-\nu)a^{3/2}} \left\{ 3(1-\nu)(1-2\nu)z_0 \left[\cot^{-1} z_0 - \frac{z_0}{1+z_0^2} \right] + \frac{2}{1+z_0^2} \left[2(1-\nu^2) - \frac{(2-\nu)z_0^2}{1+z_0^2} \right] \right\}, \quad (D2)$$

$$K_{III} = \frac{(1-2\nu)P \sin \theta}{4\pi^{3/2}(2-\nu)a^{3/2}} \left[3 - 3z_0 \cot^{-1} z_0 + \frac{1}{1+z_0^2} \right], \quad (D3)$$

where constant $z_0 = b/a$. Here, the sign of Eq. (D3) agrees with the definition of auxiliary displacement u_3 (Eq. (A9)), as defined in the crack-front coordinate system shown in Fig. 2.5. For point force R , which acts parallel to the z -axis at distance b from the crack plane, the stress intensity factors are

$$K_I = \frac{R}{2\pi^{3/2}(1-\nu)a^{3/2}} \left(\frac{1}{1+z_0^2} \right) \left[1 - \nu + \frac{z_0^2}{1+z_0^2} \right], \quad (D4)$$

$$K_{II} = \frac{R}{4\pi^{3/2}(1-\nu)a^{3/2}} \left\{ (1-2\nu) \left[\frac{z_0}{1+z_0^2} - \cot^{-1} z_0 \right] - \frac{2z_0}{(1+z_0^2)^2} \right\}, \quad (D5)$$

$$K_{III} = 0. \quad (D6)$$

D.2 Elliptical crack in an infinite body under shear

Kassir and Sih [102] obtain expressions for mode-II and mode-III stress intensity factors along the front of a shear-loaded, flat elliptical crack in a homogeneous solid. Figure

2.9 illustrates the measurement of crack-front location ϕ , and the orientation ω of shear loading with respect to the axes of the ellipse. Expressions for the mode-II and mode-III stress intensity factors at location ϕ , are [102]:

$$K_{\text{II}} = -\frac{4\mu}{(ca)^{3/2}}(a^2 \sin^2 \phi + b^2 \cos^2 \phi)^{-1/4}(cB \sin \phi + aA \cos \phi), \quad (\text{D7})$$

$$K_{\text{III}} = \frac{4\mu(1-\nu)}{(ca)^{3/2}}(a^2 \sin^2 \phi + b^2 \cos^2 \phi)^{-1/4}(cA \sin \phi - aB \cos \phi), \quad (\text{D8})$$

where μ is the shear modulus, and quantities A and B equal

$$A = \frac{ca^2 k^2 T \cos \omega}{4\mu[(k^2 - \nu)E(k) + \nu k'^2 K(k)]}, \quad (\text{D9})$$

$$B = \frac{ca^2 k^2 T \sin \omega}{4\mu[(k^2 + \nu k'^2)E(k) - \nu k'^2 K(k)]}, \quad (\text{D10})$$

where

$$k^2 = 1 - \left(\frac{a}{c}\right)^2, \text{ and } k^2 + k'^2 = 1. \quad (\text{D11})$$

Solutions to complete elliptical integrals of the first and second kinds, represented respectively by $E(k)$ and $K(k)$, are available through many commercial mathematical software packages, and are tabularized in standard references such as Abramowitz and Stegun [2].

Appendix E

Constitutive Relations for FGM Interaction-Integral Terms

E.1 Constitutive and compliance tensors

Constitutive relations for an isotropic elastic material under isothermal mechanical loading relate stress components, σ_{ij} , to strain components, ε_{ij} , according to $\sigma_{ij} = \lambda \varepsilon_{kk} \delta_{ij} + 2\mu \varepsilon_{ij}$ (e.g. Fung, 1965). Here, $ijk = 1, 2$ or 3 , and the repeated index implies summation. The symbol δ_{ij} is the Kronecker delta, and $E = E(\mathbf{x})$ and $\nu = \nu(\mathbf{x})$ are Young's modulus and Poisson's ratio for the FGM. The Lamé parameters λ and μ are

$$\lambda = \frac{\nu(\mathbf{x})E(\mathbf{x})}{(1 + \nu(\mathbf{x}))(1 - 2\nu(\mathbf{x}))} \text{ and } \mu = \frac{E(\mathbf{x})}{2(1 + \nu(\mathbf{x}))}. \quad (\text{B5})$$

Current formulations of the interaction integral for functionally-graded solids include the term $C_{ijkl,1}(\mathbf{x})\varepsilon_{kl}^{(1)}\varepsilon_{ij}^{(2)}$, where in this study, $\varepsilon_{kl}^{(1)}$ denotes mechanical strain components for the actual 3-D field, and $\varepsilon_{ij}^{(2)}$ denotes 2-D plane-stress or plane-strain auxiliary fields corresponding to Williams' solution (Williams, 1957). This term and the relations expressed in Eq. (64) require the constitutive tensor $C_{ijkl}(\mathbf{x})$ to be identical for actual (3-D) and auxiliary (2-D) fields. The constitutive relation in matrix form for actual fields is

$$\begin{bmatrix} \sigma_{11} \\ \sigma_{22} \\ \sigma_{33} \\ \sigma_{12} \\ \sigma_{23} \\ \sigma_{13} \end{bmatrix} = \begin{bmatrix} \lambda(\mathbf{x}) + 2\mu(\mathbf{x}) & \lambda(\mathbf{x}) & \lambda(\mathbf{x}) & 0 & 0 & 0 \\ \lambda(\mathbf{x}) & \lambda(\mathbf{x}) + 2\mu(\mathbf{x}) & \lambda(\mathbf{x}) & 0 & 0 & 0 \\ \lambda(\mathbf{x}) & \lambda(\mathbf{x}) & \lambda(\mathbf{x}) + 2\mu(\mathbf{x}) & 0 & 0 & 0 \\ 0 & 0 & 0 & 2\mu(\mathbf{x}) & 0 & 0 \\ 0 & 0 & 0 & 0 & 2\mu(\mathbf{x}) & 0 \\ 0 & 0 & 0 & 0 & 0 & 2\mu(\mathbf{x}) \end{bmatrix} \begin{bmatrix} \varepsilon_{11} \\ \varepsilon_{22} \\ \varepsilon_{33} \\ \varepsilon_{12} \\ \varepsilon_{23} \\ \varepsilon_{13} \end{bmatrix}, \quad (\text{B6})$$

where ε_{ij} are (symmetric) tensor-strain components. With appropriate definitions of strain components, Eq. (B6) is valid for 3-D actual fields, and 2-D plane-stress and plane-strain auxiliary fields. Equation (B6) corresponds to plane stress when $\varepsilon_{33} \equiv \nu(\varepsilon_{11} + \varepsilon_{22})/(\nu - 1)$, and $\varepsilon_{23} \equiv \varepsilon_{13} \equiv 0$, and corresponds to plane strain when $\varepsilon_{33} \equiv \varepsilon_{23} \equiv \varepsilon_{13} \equiv 0$. Therefore, for isotropic elastic functionally-graded material, the generalized Hooke's law for 3-D actual and 2-D auxiliary fields is

$$\sigma_{ij} = C_{ijkl}(\mathbf{x})\varepsilon_{kl}, \text{ and } \sigma_{ij}^{\text{aux}} = C_{ijkl}(\mathbf{x})\varepsilon_{kl}^{\text{aux}}, \quad (\text{B7})$$

where the constitutive tensor $C_{ijkl}(\mathbf{x})$ is identical in both expressions. This permits the straightforward computation of $C_{ijkl,1}(\mathbf{x})\varepsilon_{kl}\varepsilon_{ij}^{aux}$ in Eq. (64).

The interaction-integral formulation used in this work defines strain components as the product of the compliance and auxiliary-stress tensors, $\varepsilon_{ij}^{aux} = S_{ijkl}(\mathbf{x})\sigma_{kl}^{aux}$. The compliance relations are $\varepsilon_{ij} = -\lambda\sigma_{kk}\delta_{ij}/(2\mu(3\lambda + 2\mu)) + 1/2\mu\sigma_{ij}$ (Fung 1965). Thus for auxiliary fields, the compliance relationships may be expressed as

$$\begin{bmatrix} \varepsilon_{11}^{aux} \\ \varepsilon_{22}^{aux} \\ \varepsilon_{33}^{aux} \\ \varepsilon_{12}^{aux} \\ \varepsilon_{23}^{aux} \\ \varepsilon_{13}^{aux} \end{bmatrix} = \frac{1}{E(\mathbf{x})} \begin{bmatrix} 1 & -\nu(\mathbf{x}) & -\nu(\mathbf{x}) & 0 & 0 & 0 \\ -\nu(\mathbf{x}) & 1 & -\nu(\mathbf{x}) & 0 & 0 & 0 \\ -\nu(\mathbf{x}) & -\nu(\mathbf{x}) & 1 & 0 & 0 & 0 \\ 0 & 0 & 0 & 1 + \nu(\mathbf{x}) & 0 & 0 \\ 0 & 0 & 0 & 0 & 1 + \nu(\mathbf{x}) & 0 \\ 0 & 0 & 0 & 0 & 0 & 1 + \nu(\mathbf{x}) \end{bmatrix} \begin{bmatrix} \sigma_{11}^{aux} \\ \sigma_{22}^{aux} \\ \sigma_{33}^{aux} \\ \sigma_{12}^{aux} \\ \sigma_{23}^{aux} \\ \sigma_{13}^{aux} \end{bmatrix}. \quad (\text{B8})$$

where ε_{ij}^{aux} are (symmetric) tensor-strain components. Appropriate stress definitions make Eq. (B8) valid for 3-D actual fields, and 2-D plane-stress and plane-strain auxiliary fields. Equation (B8) corresponds to plane stress when $\sigma_{33}^{aux} \equiv \sigma_{23}^{aux} \equiv \sigma_{13}^{aux} \equiv 0$, and corresponds to plane strain when $\sigma_{33}^{aux} \equiv \nu(\sigma_{11}^{aux} + \sigma_{22}^{aux})$, and $\sigma_{23}^{aux} \equiv \sigma_{13}^{aux} \equiv 0$. Therefore, for isotropic elastic functionally-graded materials, the compliance relation for 3-D actual and 2-D auxiliary fields is

$$\varepsilon_{ij} = S_{ijkl}(\mathbf{x})\sigma_{kl}, \text{ and } \varepsilon_{ij}^{aux} = S_{ijkl}(\mathbf{x})\sigma_{kl}^{aux}. \quad (\text{B9})$$

E.2 Derivatives of constitutive- and compliance-tensor components

For the incompatibility formulation, derivatives of constitutive and compliance tensor components are necessary for the evaluation of $C_{ijkl,1}(\mathbf{x})\varepsilon_{kl}^{(1)}\varepsilon_{ij}^{(2)}$ and auxiliary strain derivatives $\varepsilon_{ij,1}^{(2)} = S_{ijkl,1}(\mathbf{x})\sigma_{kl}^{(2)} + S_{ijkl}(\mathbf{x})\sigma_{kl,1}^{(2)}$. According to the method described in Section 4.4.2, this procedure requires explicit derivatives of the constitutive and compliance tensor components with respect to material properties $E(\mathbf{x})$ and $\nu(\mathbf{x})$. The matrix representations in the Appendix E Section E.1 have six non-zero components. Derivatives of the constitutive matrix components are

$$\frac{\partial(\lambda + 2\mu)}{\partial E(\mathbf{x})} = \frac{(1 - \nu(\mathbf{x}))}{(1 + \nu(\mathbf{x}))(1 - 2\nu(\mathbf{x}))}, \quad \frac{\partial(\lambda + 2\mu)}{\partial \nu(\mathbf{x})} = \frac{2E(\mathbf{x})\nu(\mathbf{x})(2 - \nu(\mathbf{x}))}{(1 + \nu(\mathbf{x}))^2(1 - 2\nu(\mathbf{x}))^2}$$

$$\frac{\partial\lambda}{\partial E(\mathbf{x})} = \frac{\nu(\mathbf{x})}{(1 + \nu(\mathbf{x}))(1 - 2\nu(\mathbf{x}))}, \quad \frac{\partial\lambda}{\partial \nu(\mathbf{x})} = \frac{E(\mathbf{x})(1 + 2\nu(\mathbf{x})^2)}{(1 + \nu(\mathbf{x}))^2(1 - 2\nu(\mathbf{x}))^2},$$

$$\frac{\partial 2\mu}{\partial E(\mathbf{x})} = \frac{1}{(1 + \nu(\mathbf{x}))}, \quad \frac{\partial 2\mu}{\partial \nu(\mathbf{x})} = \frac{-E(\mathbf{x})}{(1 + \nu(\mathbf{x}))^2}.$$

Derivatives of the compliance matrix components are

$$\begin{aligned}\frac{\partial}{\partial E(\mathbf{x})} \left(\frac{1}{E(\mathbf{x})} \right) &= \frac{-1}{E(\mathbf{x})^2}, & \frac{\partial}{\partial \nu(\mathbf{x})} \left(\frac{1}{E(\mathbf{x})} \right) &= 0, \\ \frac{\partial}{\partial E(\mathbf{x})} \left(\frac{-\nu(\mathbf{x})}{E(\mathbf{x})} \right) &= \frac{\nu(\mathbf{x})}{E(\mathbf{x})^2}, & \frac{\partial}{\partial \nu(\mathbf{x})} \left(\frac{-\nu(\mathbf{x})}{E(\mathbf{x})} \right) &= \frac{-1}{E(\mathbf{x})}, \\ \frac{\partial}{\partial E(\mathbf{x})} \left(\frac{1+\nu(\mathbf{x})}{E(\mathbf{x})} \right) &= \frac{-(1+\nu(\mathbf{x}))}{E(\mathbf{x})^2}, & \frac{\partial}{\partial \nu(\mathbf{x})} \left(\frac{1+\nu(\mathbf{x})}{E(\mathbf{x})} \right) &= \frac{1}{E(\mathbf{x})}.\end{aligned}$$

References

- [1] ABAQUS/Standard User's Manual, version 6.4-3, Hibbitt, Karlsson and Sorenson, Inc., 1080 Main Street, Pawtucket, RI, 62860-4847, USA, 2004.
- [2] Abramowitz, M., Stegun, I.A., Handbook of Mathematical Functions. Dover Publications, Inc., New York, 1972.
- [3] Al-Ani, A.M., Hancock, J.W., J-dominance of short cracks in tension and bending. *Journal of the Mechanics and Physics of Solids* 1991;39:23-43.
- [4] Al-Falou, A.A., Larralde, H., Ball, R.C., Effect of T-stresses on the path of a three-dimensional crack propagating quasistatically under type-I loading. *International Journal of Solids and Structures* 1997;34:569-580.
- [5] Anifantis, N.K., Crack surface interference: a finite element analysis. *Engineering Fracture Mechanics* 2001;68:1403-1415.
- [6] Anderson, T.L., *Fracture Mechanics, Fundamentals and Applications*, 2nd ed. CRC Press, New York 1995.
- [7] Anlas, G., Santare, M.H., Lambros, J., Numerical calculation of stress intensity factors in functionally graded materials. *International Journal of Fracture* 2000;104:131-143.
- [8] Anlas, G., Santare, M.H., Lambros, J., Dominance of asymptotic crack tip fields in elastic functionally graded materials. *International Journal of Fracture* 2002;115: 193-204.
- [9] Aoki, S., Kishimoto, K., Sakata, M., Elastic-plastic analysis of crack in thermally-loaded structures. *Engineering Fracture Mechanics* 1982;16:405-413.
- [10] Atluri, S.N., Nishioka, T., Computational methods for three-dimensional problems of fracture. In: *Computational Methods in Mechanics*, vol. 2, ed. Atluri, S.N., Elsevier Science Publishers, Amsterdam, 1986:229-287.
- [11] Ayatollahi, M.R., Pavier, M.J., Smith, D.J., Determination of T-stress from finite-element analysis for mode I and mixed mode I/II loading. *International Journal of Fracture* 1998;91:283-298.
- [12] Ayhan, A.O., Nied, H.F., Stress intensity factors for three-dimensional surface cracks using enriched finite elements. *International Journal for Numerical Methods in Engineering* 2002;54:899-921.
- [13] Bahr, H.-A., Fischer, G., Weiss, H.-J., Thermal shock crack patterns explained by single and multiple crack propagation. *Journal of Materials Science* 1986;21:2716-2720.
- [14] Bao, G., Cai, H., Delamination cracking in functionally graded coating/metal substrate systems. *Acta Materialia* 1997;45:1055-1066.
- [15] Bazant, Z.P., Estenssoro, L.F., Surface singularity and crack propagation. *International Journal of Solids and Structures* 1979;15:405-426.

- [16] Becker, T.L. Jr., Cannon, R.M., Ritchie, R.O., Finite crack kinking and T-stress in functionally graded materials. *International Journal of Solids and Structures* 2001;38:5545-5563.
- [17] Belytschko, T., Gu, L., Lu, Y.Y., Fracture and crack growth by element-free Galerkin methods. *Modelling and Simulation in Materials Science and Engineering* 1994;2:519-534.
- [18] Belytschko, T., Krongauz, Y., Organ, D., Fleming, M., Krysl, P., Meshless methods: an overview and recent developments. *Computer Methods in Applied Mechanics and Engineering* 1996;139:3-47.
- [19] Belytschko, T., Organ, D., Gerlach C., Element-free Galerkin methods for dynamic fracture in concrete. *Computer Methods in Applied Mechanics and Engineering* 2000;187:385-399.
- [20] Benthem, J.P., State of stress at the vertex of a quarter-infinite crack in a half-space. *International Journal of Solids and Structures* 1977;13:479-492.
- [21] Benthem, J.P., Koiter, W.T., Asymptotic approximations to crack problems. In: G.C. Sih (Ed.), *Mechanics of Fracture 1, Methods of Analysis and Solutions of Crack Problems*. Noordhoff International Publishing, Leyden, 1973.
- [22] Benzley, S.E., Representation of singularities with isoparametric finite elements. *International Journal for Numerical Methods in Engineering* 1974;8:537-545.
- [23] Beom, H.G., Earmme, Y.Y., Evaluation of elastic T-stress using a conservation integral. In: *Computational Engineering*, eds. Kwak, B.M., Tanaka, M., *Proceedings of the First Pan-Pacific Conference on Computational Engineering* 1993;43-48.
- [24] Bicanic, N., Hinton, E., Spurious modes in two-dimensional isoparametric elements. *International Journal for Numerical Methods in Engineering* 1979;14:1545-1557.
- [25] Blinova, V.T., Linkov, A.M., A method of finding asymptotic forms at the common apex of elastic wedges. *Journal of Applied Mathematics and Mechanics* 1995;59:187-195.
- [26] Bruck, H.A., Gershon, A.L., Three-dimensional effects near the interface in a functionally graded Ni-Al₂O₃ plate specimen. *International Journal of Solids and Structures* 2002;39:547-557.
- [27] Budiansky, B., Rice, J.R., Conservation Laws and Energy Release Rates. *ASME Journal of Applied Mechanics* 1973;40:201-203.
- [28] Cai, H., Bao, G., Crack bridging in functionally graded coatings. *International Journal of Solids and Structures* 1998;35:701-717.
- [29] Cardew, G.E., Goldthorpe, M.R., Howard, I.C., Kfoury, A.P., On the elastic T-term, in: *Fundamentals of Deformation and Fracture*, eds. Bilby, B.A., Miller, K.J., Willis, J.R., Cambridge University Press, Sheffield, 1985.

- [30] Carter, B.J., Wawrzynek, P.A., Ingraffea, A.R., Automated 3-D crack growth simulation. *International Journal for Numerical Methods in Engineering* 2000;47:229-253.
- [31] Chan, Y.-S., Paulino, G.H., Fannjiang, A.C., The crack problem for nonhomogeneous materials under antiplane shear loading—a displacement based formulation. *International Journal of Solids and Structures* 2001;38:2989-3005.
- [32] Chan, Y.-S., Fannjiang, A.C., Paulino, G.H., Integral equations with hypersingular kernels—theory and applications to fracture mechanics. *International Journal of Engineering Science* 2003;41:683-720.
- [33] Chen, C.-S., Krause, R., Pettit, R.G., Banks-Sills, L., Ingraffea, A.R., Numerical assessment of T -stress computation using a p-version finite element method. *International Journal of Fracture* 2001;107:177-199.
- [34] Chen, F.H.K., Shield, R.T., Conservation laws in elasticity of the J-integral type. *Journal of Applied Mathematics and Physics (ZAMP)* 1977;28:1-22.
- [35] Chen, J., Wu, L., Du, S., A modified J integral for functionally graded materials. *Mechanics Research Communications* 2000;27:301-306.
- [36] Cherepanov, G.P., The propagation of cracks in a continuous medium. *Journal of Applied Mathematics and Mechanics* 1967;31:503-512.
- [37] Cho, Y.J., Beom, H.G., Earmme Y.Y. Application of a conservation integral to an interface crack interacting with singularities. *International Journal of Fracture* 1994;65:63-73.
- [38] Choi, N.Y., Earmme, Y.Y., Evaluation of stress intensity factors in a circular arc-shaped interfacial crack using L -integral. *Mechanics of Materials* 1992;14:141-153.
- [39] Choules, B.D., Kokini, K., Taylor, T.A., Thermal fracture of ceramic thermal barrier coatings under high heat flux with time-dependent behavior—part 1—experimental results. *Materials Science and Engineering* 2001;A299:296-304.
- [40] Chuntu, L., Yingzhi, L., Study on cracked plates, shells and three dimensional bodies. *Engineering Fracture Mechanics* 1987;28:741-760.
- [41] Cook, R.D., Malkus, D.S., Plesha, M.E., Witt, R.J., *Concepts and Applications of Finite Element Analysis*, 4th ed. John Wiley and Sons, New York 2002.
- [42] Curry, D.A., Knott, J.F., The Relationship Between Fracture Toughness and Microstructure in the Cleavage Fracture of Mild Steel. *Metal Science* 1976;10: 1-10.
- [43] Dag, S., Erdogan, F., A surface crack in a graded medium under general loading conditions. *ASME Journal of Applied Mechanics* 2002;69:580-588.
- [44] Dag, S., Kadioglu, S., Yahsi, O.S., Circumferential crack problem for an FGM cylinder under thermal stresses. *Journal of Thermal Stresses* 1999;22:659-687.
- [45] Delale, F., Erdogan, F., The crack problem for a nonhomogeneous plane. *ASME Journal of Applied Mechanics* 1983;50:609-614.

- [46] DeLorenzi, H.G., On the energy release rate and the J-integral for 3-D crack configurations. *International Journal of Fracture* 1982;19:183-193.
- [47] DeLorenzi, H.G., Shih, C.F., 3-D elastic-plastic investigation of fracture parameters in side-grooved compact specimen. *International Journal of Fracture* 1983;21:195-220.
- [48] Dhondt, G., On corner point singularities along a quarter circular crack subject to shear loading. *International Journal of Fracture* 1998;89: L33-L38.
- [49] Dhondt, G., 3-D mixed-mode K -calculations with the interaction integral method and the quarter point element stress method. *Communications in Numerical Methods for Engineering* 2001;17:303-307.
- [50] Dhondt, G., Mixed-mode K -calculations in anisotropic materials. *Engineering Fracture Mechanics* 2002;69:909-922.
- [51] Dodds, R.H. Jr., Vargas, P.M., Numerical evaluation of domain and contour integrals for nonlinear fracture mechanics: formulation and implementation aspects. Report No. UILU-ENG-88-2006, Civil Engineering, University of Illinois, Urbana, IL 61801, USA, 1988.
- [52] Dolbow, J.E., An Extended Finite Element Method with Discontinuous Enrichment for Applied Mechanics. PhD Thesis, Northwestern University, Evanston, Illinois, USA, 1999.
- [53] Dolbow, J.E., Gosz, M., On the computation of mixed-mode stress intensity factors in functionally graded materials. *International Journal of Solids and Structures* 2002;39:2557-2574.
- [54] Dong, Z., Paulino, G.H., The mixed mode crack problem in a finite nonhomogeneous elastic medium under various boundary conditions. 2004 submitted.
- [55] Duarte, C.A., Babuska, I., Oden, J.T., Generalized finite element methods for three-dimensional structural mechanics problems. *Computers and Structures* 2000;77:215-232.
- [56] Duarte, C.A., Hamzeh, O.N., Liszka, T.J., Tworzydlo, W.W., A generalized finite element method for the simulation of three-dimensional dynamic crack propagation. *Computer Methods in Applied Mechanics and Engineering* 2001;190:2227-2262.
- [57] Duarte, C.A., Oden, J.T., H - p clouds—an h - p meshless method. *Computer Methods in Applied Mechanics and Engineering* 1996;139:237-262.
- [58] Duarte, C.A., Oden, J.T., An h - p adaptive method using clouds. *Computer Methods in Applied Mechanics and Engineering* 1996;139:237-262.
- [59] Eischen, J.W., Fracture of nonhomogeneous materials. *International Journal of Fracture* 1987;34:3-22.
- [60] Erdogan, F., Wu, B.H., Crack problems in FGM layers under thermal stresses. *Journal of Thermal Stresses* 1996;19:237-265.

- [61] Erdogan, F., Wu, B.H., The surface crack problem for a plate with functionally graded properties. *ASME Journal of Applied Mechanics* 1997;64:449-456.
- [62] Eriksson, K., A domain independent integral expression for the crack extension force of a curved crack in three dimensions. *Journal of the Mechanics and Physics of Solids* 2002;50:381-403.
- [63] Eshelby, J.D., The continuum theory of lattice defects. *Solid State Physics*, vol. 3, Academic Press, New York, 1956.
- [64] Eshelby, J.D., Energy relations and the energy-momentum tensor in continuum mechanics. *Inelastic Behavior of Solids*, McGraw-Hill, New York 1970.
- [65] Evans, G., *Practical Numerical Integration*. John Wiley and Sons, Chichester, 1993.
- [66] FEACrack, version 2.6.000, Structural Reliability Technology, 1898 South Flat-iron Court, #235, Boulder, CO, 80301, USA.
- [67] Fernlund, G., McCammond, D., Spelt, J.K. Curvilinear formulation of the 3-D J integral: application to delamination cracking of curved laminates. *Composite Structures* 1994;28: 123-130.
- [68] Forth, S.C., Favrow, L.H., Keat, W.D., Newman, J.A., Three-dimensional mixed-mode fatigue crack growth in a functionally graded titanium alloy. *Engineering Fracture Mechanics* 2003;70:2175-2185.
- [69] Frangi, A., Fracture propagation in 3D by the symmetric Galerkin boundary element method. *International Journal of Fracture* 2002;116:313-330.
- [70] Fujimoto, T., Noda, N., Crack propagation in a functionally graded plate under thermal shock. *Archive of Applied Mechanics* 2000;70:377-386.
- [71] Fujimoto, T., Noda, N., Influence of the compositional profile of functionally graded material on the crack path under thermal shock. *Journal of the American Ceramic Society* 2001;84:1480-86.
- [72] Fung, Y.C., *Foundations of Solid Mechanics*. Prentice-Hall, Englewood Cliffs, New Jersey, 1965.
- [73] Gaudette, F.G., Giannakopoulos, A.E., Suresh, S., Interface cracks in layered materials subjected to a uniform temperature change. *International Journal of Fracture* 2001;110:325-349.
- [74] Gosz, M., Dolbow, J., Moran, B., Domain integral formulation for stress intensity factor computation along curved three-dimensional interface cracks. *International Journal of Solids and Structures* 1998;35:1763-1783.
- [75] Gosz, M., Moran, B., An interaction energy integral method for computation of mixed-mode stress intensity factors along non-planar crack fronts in three dimensions. *Engineering Fracture Mechanics* 2002;69:299-319.
- [76] Gu, P., Asaro, R.J., Cracks in functionally graded materials. *International Journal of Solids and Structures* 1997;34:1-17.

- [77] Gu, P., Dao, M., Asaro, R.J., A simplified method for calculating the crack tip field of functionally graded materials using the domain integral. *ASME Journal of Applied Mechanics* 1999;66:101-108.
- [78] Gullerud, A.S., Bichon, B., Cochran, K., Koppenhoefer, K.C., Roy, A., RoyChowdhury, S., Walters, M.C., Dodds, Jr. R.H. WARP3D—release 15 manual. Report No. UILU-ENG-95-2012, Civil Engineering, University of Illinois, Urbana, IL 61801, USA, 2004.
- [79] Hartranft, R.J., Sih, G.C., The use of eigenfunction expansions in the general solution of three-dimensional crack problems. *Journal of Mathematics and Mechanics* 1969;19:123-138.
- [80] Hartranft, R.J., Sih, G.C., An approximate three-dimensional theory of plates with applications to crack problems. *International Journal of Engineering Science* 1970;8:711-729.
- [81] Hasselman, D.P.H., Youngblood, G.E., Enhanced thermal resistance of structural ceramics with thermal conductivity gradients. *Journal of the American Ceramic Society* 1978;61:49-52.
- [82] Hellen, T.K., On the method of virtual crack extensions. *International Journal for Numerical Methods in Engineering* 1975;9:187-207.
- [83] Henry, B.S., Luxmoore, A.R., Three-dimensional evaluation of the T-stress in centre cracked plates. *International Journal of Fracture* 1995;70:35-50.
- [84] Huang, G.-Y., Wang, Y.-S., A new model for fracture analysis of a functionally graded interfacial zone under harmonic anti-plane loading. *Engineering Fracture Mechanics* 2004;71:1841-1851.
- [85] Huang, R., Sukumar, N., Prevost, J.-H., Modeling quasi-static crack growth with the extended finite element method, part II: numerical applications. *International Journal of Solids and Structures* 2003;40:7539-7552.
- [86] Huber, O., Nickel, J., Kuhn, G., On the decomposition of the J -integral for 3D crack problems. *International Journal of Fracture* 1993;64:339-348.
- [87] Hutchinson, J.W., Singular behavior at the end of a tensile crack tip in a hardening material. *Journal of the Mechanics and Physics of Solids* 1968;16:13-31.
- [88] Im, S., Kim, K.-S., An application of two-state M -integral for computing the intensity of the singular near-tip field for a generic wedge. *Journal of the Mechanics and Physics of Solids* 2000;48:129-151.
- [89] Irwin, G.R., Onset of fast crack propagation in high strength steel and aluminum alloys. *Sagamore Research Conference Proceedings* 1956;2:289-305.
- [90] Irwin, G.R., Analysis of stresses and strains near the end of a crack traversing a plate. *ASME Journal of Applied Mechanics* 1957;24:361-364.
- [91] Irwin, G.R., The crack extension force for a part through crack in a plate. *ASME Journal of Applied Mechanics* 1962;29:651-654.

- [92] Jayadevan, K.R., Narasimhan, R., Ramamurthy, T.S., Dattaguru, B., A numerical study of T-stress in dynamically loaded fracture specimens. *International Journal of Solids and Structures* 2001;38:4987-5005.
- [93] Jeon, I., Im, S., The role of higher order eigenfields in elastic-plastic cracks. *Journal of the Mechanics and Physics of Solids* 2001;49:2789-2818.
- [94] Jin, Z.-H., Batra, R.C., Some basic fracture mechanics concepts in functionally graded materials. *Journal of the Mechanics and Physics of Solids* 1996;44:1221-1235.
- [95] Jin, Z.-H., Batra, R.C., R-curve and strength behavior of a functionally graded material. *Materials Science and Engineering A242* 1998;70-76.
- [96] Jin, Z.-H., Dodds, R. H. Jr., Crack growth resistance behavior of a functionally graded material: computational studies. *Engineering Fracture Mechanics* 2004;71:1651-1672.
- [97] Jin, Z.H., Noda, N., Crack tip singular fields in nonhomogeneous materials. *ASME Journal of Applied Mechanics* 1994;61:738-740.
- [98] Jin, Z.-H., Paulino, G.H., Dodds, R.H. Jr., Finite element investigation of quasi-static crack growth in functionally graded materials using a novel cohesive zone fracture model. *ASME Journal of Applied Mechanics* 2002;69:370-379.
- [99] Jin, Z.-H., Paulino, G.H., Dodds, R.H. Jr., Cohesive fracture modeling of elastic-plastic crack growth in functionally graded materials. *Engineering Fracture Mechanics* 2003;70:1885-1912.
- [100] Jin, Z.-H., Sun, C.T., On J-Integral and Potential Energy Variation. *International Journal of Fracture* 2004;126:L19-L24.
- [101] Kargarnovin, M.H., Fariborz, S.J., Analysis of a dissimilar finite wedge under antiplane deformation. *Mechanics Research Communications* 2000;27:109-116.
- [102] Kassir, M.K., Sih, G.C., Three-dimensional stress distribution around an elliptical crack under arbitrary loadings. *ASME Journal of Applied Mechanics* 1966;33:601-611.
- [103] Kassir, M.K., Sih, G.C., *Mechanics of Fracture 2, Three-Dimensional Crack Problems*. Noordhoff International Publishing, Leyden, 1975.
- [104] Kawasaki, A., Watanabe, R., Fabrication of disk-shaped functionally graded materials by hot pressing and their thermomechanical performance. In: J.B. Holt, M. Koizumi, T. Hirai and Z.A. Munir (Eds.), *Proceedings of the Second International Symposium on Functionally Gradient Materials*. American Ceramic Society, Westerville, Ohio 1993, pp. 157-164.
- [105] Kfourir, A.P., Some evaluations of the elastic T -term using Eshelby's method. *International Journal of Fracture* 1986;30:301-315.

- [106] Kim, Y.J., Kim, H.-G., Im, S., Mode decomposition of three-dimensional mixed-mode cracks via two-state integrals. *International Journal of Solids and Structures* 2001;38; 6405-6426.
- [107] Kim, J.H., Moon, H.J., Earmme, Y.Y., Inplane and antiplane T-stresses for an interface crack in anisotropic bimaterial. *Mechanics of Materials* 2001;33; 21-32.
- [108] Kim, J.-H., Mixed-Mode Crack Propagation in Functionally Graded Materials. PhD thesis, University of Illinois at Urbana-Champaign, Urbana, USA, 2003.
- [109] Kim, J.H., Paulino, G.H., Finite element evaluation of mixed mode stress intensity factors in functionally graded materials. *International Journal for Numerical Methods in Engineering* 2002;53:1903-1935.
- [110] Kim, J.H., Paulino, G.H., Mixed-mode fracture of orthotropic functionally graded materials using finite elements and the modified crack closure method. *Engineering Fracture Mechanics* 2002;69:1557-1586.
- [111] Kim, J.H., Paulino, G.H., Isoparametric graded finite elements for nonhomogeneous isotropic and orthotropic materials. *ASME Journal of Applied Mechanics* 2002;69:502-514.
- [112] Kim, J.-H., Paulino, G.H., Mixed-mode J-integral formulation and implementation using graded finite elements for fracture analysis of nonhomogeneous orthotropic materials. *Mechanics of Materials* 2003;35:107-128.
- [113] Kim, J.-H., Paulino, G.H., T-stress, mixed-mode stress intensity factors, and crack initiation angles in functionally graded materials: a unified approach using the interaction integral method. *Computer Methods in Applied Mechanics and Engineering* 2003;192:1463-1494.
- [114] Kim, J.-H., Paulino, G.H. The interaction integral for fracture of orthotropic functionally graded materials: evaluation of stress intensity factors. *International Journal of Solids and Structures* 2003;40:3967-4001.
- [115] Kim, J.-H., Paulino, G.H., An accurate scheme for mixed-mode fracture analysis of functionally graded materials using the interaction integral and micromechanics models. *International Journal for Numerical Methods in Engineering* 2003;58:1457-1497.
- [116] Kim, J.-H., Paulino, G.H., T-stress in orthotropic functionally graded materials: Lekhnitskii and Stroh formalisms. *International Journal of Fracture* 2004;126:345-389.
- [117] Kim, J.-H., Paulino, G.H., A new approach to compute T-stress in functionally graded materials by means of the interaction integral method. *Engineering Fracture Mechanics* 2004;71:1907-1950.
- [118] Kim, J.H., Paulino, G.H., On the Poisson's ratio effect on mixed-mode stress intensity factors and T-stress in functionally graded materials. *International Journal of Computational Engineering Science* (in press).

- [119] Kim, J.H., Moon, H.J., Earmme, Y.Y., Inplane and antiplane T-stresses for an interface crack in anisotropic bimaterial. *Mechanics of Materials* 2001;33: 21-32.
- [120] Kim, Y.H., Jones, R.F., Lee, S.W., Study of 20-node solid element. *Communications in Applied Numerical Methods* 1990;6:197-205.
- [121] Kim, Y.J., Kim, H.-G., Im, S., Mode decomposition of three-dimensional mixed-mode cracks via two-state integrals. *International Journal of Solids and Structures* 2001;38:6405-6426.
- [122] Knowles, J.K., Sternberg, E., On a class of conservation laws in linearized and finite elastostatics. *Archive of Rational Mechanics Analysis* 1972;7:55-129.
- [123] Kokini, K., Takeuchi, Y.R., Choules, B.D., Thermal crack initiation mechanisms on the surface of functionally graded ceramic thermal barrier coatings. *Ceramics International* 1996;22:397-401.
- [124] Konda, N., Erdogan, F., The mixed-mode crack problem in a nonhomogeneous elastic medium. *Engineering Fracture Mechanics* 1994;47:533-545.
- [125] Krysl, P., Belytschko, T., The element free Galerkin method for dynamic propagation of arbitrary 3-D cracks. *International Journal for Numerical Methods in Engineering* 1999;44:767-800.
- [126] Larsson, S.G., Carlsson, A.J., Influence of non-singular stress terms and specimen geometry on small-scale yielding at crack tips in elastic-plastic materials. *Journal of the Mechanics and Physics of Solids* 1973;21:263-277.
- [127] Lee, Y.-D., Erdogan, F., Residual/thermal stresses in FGM and laminated thermal barrier coatings. *International Journal of Fracture* 1995;69:145-165.
- [128] Lee, Y.-D., Erdogan, F., Interface cracking of FGM coatings under steady-state heat flow. *Engineering Fracture Mechanics* 1998;59:361-380.
- [129] Li, C., Zou, Z., Internally circumferentially cracked cylinders with functionally graded material properties. *International Journal of Pressure Vessels and Piping* 1998a;75: 499-507.
- [130] Li, C., Zou, Z., Stress intensity factors for a functionally graded material cylinder with an external circumferential crack. *Fatigue and Fracture of Engineering Materials and Structures* 1998b;21:1447-1457.
- [131] Li, C., Zou, Z., Duan, Z., Stress intensity factors for functionally graded solid cylinders. *Engineering Fracture Mechanics* 1999;63:735-749.
- [132] Li, C., Zou, Z., Duan Z., Multiple isoparametric finite element method for nonhomogeneous media. *Mechanics Research Communications* 2000;27:137-142.
- [133] Li, F.Z., Shih, C.F., Needleman, A., A comparison of methods for calculating energy release rates. *Engineering Fracture Mechanics* 1985;21:405-421.
- [134] Li, S., Mear, M.E., Xiao, L., Symmetric weak-form integral equation method for three-dimensional fracture analysis. *Computer Methods in Applied Mechanics and Engineering* 1998;151:435-459.

- [135] Marur, P.R., Tippur, H.V., Numerical analysis of crack-tip fields in functionally graded materials with a crack normal to the elastic gradient. *International Journal of Solids and Structures* 2000;37:5353-5370.
- [136] Merkle, J.G., A review of some of the existing stress intensity factor solutions for part-through surface cracks. ORNL-TM-3983, U.S. Atomic Energy Commission 1973.
- [137] Michell, J.H., Elementary distributions of plane stress. *Proceedings of the London Mathematical Society* 1900;32:35-61.
- [138] Miyamoto, Y., Kaysser, W.A., Rabin, B.H., Kawasaki, A., Ford, A.G., *Functionally Graded Materials: Design, Processing and Applications*, Kluwer Academic Publishers, Boston 1999.
- [139] Moon, H.J., Earmme, Y.Y., Calculation of elastic T -stresses near interface crack tip under in-plane and anti-plane loading. *International Journal of Fracture* 1998;91:179-195.
- [140] Moran, B., Shih, C.F., Crack tip and associated domain integrals from momentum and energy balance. *Engineering Fracture Mechanics* 1987;27:615-642.
- [141] Moran, B., Shih, C.F., A general treatment of crack tip contour integrals. *International Journal of Fracture* 1987;35:295-310.
- [142] Nahta, R., Moran, B., Domain integrals for axisymmetric interface problems. *International Journal of Solids and Structures* 1993;30:2027-2040.
- [143] Nakamura, T., Three-dimensional stress fields of elastic interface cracks *ASME Journal of Applied Mechanics* 1991;58:939-946.
- [144] Nakamura, T., Parks, D.M., Three-dimensional stress field near the crack front of a thin elastic plate. *ASME Journal of Applied Mechanics* 1988;55: 805-813.
- [145] Nakamura, T., Parks, D.M., Antisymmetrical 3-D stress field near the crack front of a thin elastic plate. *International Journal of Solids and Structures* 1989;25:1411-1426.
- [146] Nakamura, T., Parks, D.M., Determination of elastic T -stress along three-dimensional crack fronts using an interaction integral. *International Journal of Solids and Structures* 1992;29:1597-1611.
- [147] Nakamura, T., Shih, C.F., Freund, L.B., Computational methods based on an energy integral in dynamic fracture. *International Journal of Fracture* 1985;27:229-243.
- [148] Narayana, K.B., George, S., Dattaguru, B., Ramamurthy, T.S., Vijayakumar, K., Modified crack closure integral (MCCI) for 3-d problems using 20-noded brick elements. *Fatigue and Fracture of Engineering Materials and Structures* 1994;17:145-157.
- [149] Nemat-Nasser, S., Hori, M., *Micromechanics: Overall Properties of Heterogeneous Materials*. Elsevier, North-Holland 1993.

- [150] Newman, J.C., Raju, I.S., Analyses of surface cracks in finite plates under tension or bending loads. NASA Technical Paper 1578 1979.
- [151] Nikishkov, G.P., Atluri, S.N., Calculation of fracture mechanics parameters for an arbitrary three-dimensional crack, by the 'equivalent domain integral' method. International Journal for Numerical Methods in Engineering 1987;24:1801-1821.
- [152] Nikishkov, G.P., Atluri, S.N., An equivalent domain integral method for computing crack-tip integral parameters in non-elastic, thermomechanical fracture. Engineering Fracture Mechanics 1987;26:851-867.
- [153] Noda, N., Jin, Z.-H., Thermal stress intensity factors for a crack in a strip of a functionally gradient material. International Journal of Solids and Structures 1993;30:1039-1056.
- [154] Noda, N., Thermal stresses intensity factor for functionally gradient plate with an edge crack. Journal of Thermal Stresses 1997;20:373-387.
- [155] Noda, N., Thermal stresses in functionally graded materials. Journal of Thermal Stresses 1999;22:477-512.
- [156] Noda, N., Stress intensity formulas for three-dimensional cracks in homogeneous and bonded dissimilar materials. Engineering Fracture Mechanics 2004;71:1-15.
- [157] Nomura, N., Gasik, M., Kawasaki, A., Watanabe, R., Thermomechanical modeling of functionally graded thermal barrier coatings. In: Proceedings of the 6th International Symposium on Functionally Graded Materials 2001; 114:223-229.
- [158] Oden, J.T., Duarte, C.A., Solution of singular problems using h - p clouds. In: Whiteman, J.R., The Mathematics of Finite Elements and Applications 96, Wiley, New York 1997;35-54.
- [159] Oden, J.T., Duarte, C.A., Clouds, cracks and FEM's. In: Reddy, B.D., ed., Recent Developments in Computational and Applied Mechanics. International Center for Numerical Methods in Engineering, CIMNE, Barcelona, Spain, 1997;302-321.
- [160] Oden, J.T., Duarte, C.A., Zienkiewicz, O.C., A new cloud-based hp finite element method. Computer Methods in Applied Mechanics and Engineering 1998;153:117-126.
- [161] Ozturk, M., Erdogan, F., An axisymmetric crack in bonded materials with a non-homogeneous interfacial zone under torsion. ASME Journal of Applied Mechanics 1995;62:116-125.
- [162] Ozturk, M., Erdogan, F., Axisymmetric crack problem in bonded materials with a graded interfacial region. International Journal of Solids and Structures 1996;33:193-219.
- [163] Pageau, S.S., Biggers, S.B. Jr., Enrichment of finite elements with numerical solutions for singular stress fields. International Journal for Numerical Methods in Engineering 1997;40:2693-2713.

- [164] Parameswaran, V., Shukla, A., Asymptotic stress fields for stationary cracks along the gradient in functionally graded materials. *ASME Journal of Applied Mechanics* 2002;69:240-243.
- [165] Parks, D.M., A stiffness derivative finite element technique for determination of crack tip stress intensity factors. *International Journal of Fracture* 1974;10:487-502.
- [166] Parks, D.M., The virtual crack extension method for nonlinear material behavior. *Computer Methods in Applied Mechanics and Engineering* 1977;12:353-364.
- [167] Parks, D.M., Three-dimensional aspects of HRR-dominance. In: *Defect Assessment in Components-Fundamentals and Applications*, ed. Blauel, J.G., Schwalbe, K.-H., Mechanical Engineering Publications, London 1991;205-231.
- [168] Paulino, G.H., Jin, Z.-H., Dodds, R.H. Jr., Failure of Functionally Graded Materials. *Comprehensive Structural Integrity*, Vol. 2, B. Karahaloo and W.G. Knauss, eds., Elsevier, New York, Chapter 13, 2002.
- [169] Paulino, G.H., Kim, J.-H., A new approach to compute T-stress in functionally graded materials using the interaction integral method. *Engineering Fracture Mechanics* 2004;71:1907-1950.
- [170] Pereira, J.P., Duarte, C.A., Extraction of stress intensity factors from generalized finite element solutions. *Engineering Analysis with Boundary Elements* 2005;(in press).
- [171] Pook, L.P., Some implications of corner point singularities. *Engineering Fracture Mechanics* 1994;48:367-378.
- [172] Press, W.H., Teukolsky, S.A., Vetterling, W.T., Flannery, B.P., *Numerical Recipes in Fortran 77*. Press Syndicate of the University of Cambridge, Cambridge, 2001.
- [173] Quian, G., Nakamura, T., Berndt, C.C., Effects of thermal gradient and residual stresses on thermal barrier coating fracture. *Mechanics of Materials* 1998;27:91-110.
- [174] Rajaram, H., Socrate, S., Parks, D.M., Application of domain integral methods using tetrahedral elements to the determination of stress intensity factors. *Engineering Fracture Mechanics* 2000;66:455-482.
- [175] Raju, I.S., Newman, J.C., Stress-intensity factors for a wide range of semi-elliptical surface cracks in finite-thickness plates. *Engineering Fracture Mechanics* 1979;11:817-829.
- [176] Raju, I.S., Calculation of strain-energy release rates with high order and singular finite elements. *Engineering Fracture Mechanics* 1987;28:251-274.
- [177] Ramamurthy, T.S., Krishnamurthy, T., Narayana, K.B., Vijayakumar, K., Dataguru, B., Modified crack closure integral method with quarter point elements. *Mechanics Research Communications* 1986;13:179-186.

- [178] Rangaraj, S., Kokini, K., Interface thermal fracture in functionally graded zirconia-mullite-bond coat alloy thermal barrier coatings. *Acta Materialia* 2003;51:251-267.
- [179] Rao, B.N., Rahman, S., Mesh-free analysis of cracks in isotropic functionally graded materials. *Engineering Fracture Mechanics* 2003;70:1-27.
- [180] Ravichandran, K.S., Thermal residual stresses in a functionally graded material system. *Materials Science and Engineering A201* 1995;269-276.
- [181] Rice, J.R., A path-independent integral and the approximate analysis of strain concentration by notches and cracks. *ASME Journal of Applied Mechanics* 1968;35:379-386.
- [182] Rice, J.R., Limitations to the small scale yielding approximation for crack tip plasticity. *Journal of Mechanics and Physics of Solids* 1974;22:17-26.
- [183] Rice, J.R., Levy, N., The part-through surface crack in an elastic plate. *ASME Journal of Applied Mechanics* 1972;39:185-194.
- [184] Rice, J.R., Paris, P.C., Merkle, J.G., Some further results on J -integral analysis and estimates. In: *Progress in Flaw Growth and Fracture Toughness Testing*. ASTM STP 536, American Society for Testing and Materials, Philadelphia, 1973. p. 231-245.
- [185] Rice, J.R., Rosengren, G.F., Plane strain deformation near a crack tip in a power-law hardening material. *Journal of the Mechanics and Physics of Solids* 1968;16:1-12.
- [186] Rousseau, C.-E., Tippur, H.V., Influence of elastic gradient profiles on dynamically loaded functionally graded materials: cracks along the gradient. *International Journal of Solids and Structures* 2001;38:7839-7856.
- [187] Rybicki, E.F., Kanninen, M.F., A finite element calculation of stress intensity factors by a modified crack closure integral. *Engineering Fracture Mechanics* 1977;9:931-938.
- [188] Santare, M.H., Lambros, J., Use of graded finite elements to model the behavior of nonhomogeneous materials. *ASME Journal of Applied Mechanics* 2000;67:819-822.
- [189] Selvadurai, A.P.S., The penny-shaped crack at a bonded plane with localized elastic non-homogeneity. *European Journal of Mechanics and Solids* 2000;19: 525-534.
- [190] Shih, C.F., Asaro, R.J., Elastic-plastic analysis of cracks on bimaterial interfaces: part I—small scale yielding. *ASME Journal of Applied Mechanics* 1988;55:299-316.
- [191] Shih, C.F., deLorenzi, H.G., German, M.D., Crack extension modeling with singular quadratic isoparametric elements. *International Journal of Fracture* 1976;12:647-651.

- [192] Shih, C.F., Moran, B., Nakamura, T., Energy release rate along a three-dimensional crack front in a thermally stressed body. *International Journal of Fracture* 1986;30:79-102.
- [193] Shim, D.-J., Dodds, R.H. Jr., Paulino, G.H., A boundary-layer framework considering material gradation effects (submitted) 2005.
- [194] Shivakumar, K.N., Raju, I.S., An equivalent domain integral method for three-dimensional mixed-mode fracture problems. *Engineering Fracture Mechanics* 1992;42:935-959.
- [195] Sladek, J., Sladek, V., Evaluation of T-stresses and stress intensity factors in stationary thermoelasticity by the conservation integral method. *International Journal of Fracture* 1997;86:199-219.
- [196] Sladek, J., Sladek, V., Fedelinski, P., Integral formulation for elastodynamic T-stresses. *International Journal of Fracture* 1997;84:103-116.
- [197] Sladek, J., Sladek, V., Fedelinski, P., Contour integrals for mixed-mode crack analysis: effect of nonsingular terms. *Theoretical and Applied Fracture Mechanics* 1997;27:115-127.
- [198] Sladek, J., Sladek, V., Evaluations of the T-stress for interface cracks by the boundary element method. *Engineering Fracture Mechanics* 1997;56: 813-825.
- [199] Sladek, J., Sladek, V., Fedelinski, P., Computation of the second fracture parameter in elastodynamics by the boundary element method. *Advances in Engineering Software* 1999;30:725-734.
- [200] Sladek, J., Sladek, V., Evaluation of the elastic T-stress in three-dimensional crack problems using an integral formula. *International Journal of Fracture* 2000;101:L47-L52.
- [201] Smith, D.J., Ayatollahi, M.R., Pavier, M.J., The role of T-stress in brittle fracture for linear elastic materials under mixed-mode loading. *Fatigue and Fracture of Engineering Materials and Structures* 2001;24:137-150.
- [202] Song, S.-H., Paulino, G.H., Computation of dynamic stress intensity factors in FGMs using the interaction integral (to be submitted) 2005.
- [203] Stern, M., Becker, E.B., Dunham, R.S., A contour integral computation of mixed-mode stress intensity factors. *International Journal of Fracture* 1976;12:359-368.
- [204] Sukumar, N., Moes, N., Moran, B., Belytschko, T., Extended finite element method for three-dimensional crack modelling. *International Journal for Numerical Methods in Engineering* 2000;48:1549-1570.
- [205] Sukumar, N., Prevost, J.-H., Modeling quasi-static crack growth with the extended finite element method, part I: computer implementation. *International Journal of Solids and Structures* 2003;40:7513-7537.
- [206] Suresh, S., Mortensen, A., *Fundamentals of Functionally Graded Materials*, Institute of Materials, London, 1998.

- [207] Sutradhar, S., Paulino, G.H., Symmetric Galerkin boundary element computation of T -stress and stress intensity factors for mixed-mode cracks by the interaction integral method. *Engineering Analysis with Boundary Elements* 2004;28:1335-1350.
- [208] Szabó, B.A., Babuska, I., Computation of the amplitude of stress singular terms for cracks and reentrant corners. *Fracture Mechanics: Nineteenth Symposium*, ASTM STP 969, T.A. Cruse ed., American Society for Testing and Materials, Philadelphia, 1988:101-124.
- [209] Takahashi, H., Ishikawa, T., Okugawa, D., Hashida, T., Laser and plasma-ARC thermal shock/fatigue fracture evaluation procedure for functionally gradient materials. In: *Thermal Shock and Thermal Fatigue Behavior of Advanced Ceramics*. Kluwer Academic Publishers, Dordrecht 1993.
- [210] Timoshenko, S.P., Goodier, J.N., *Theory of Elasticity*. McGraw-Hill, New York 1987.
- [211] Tohgo, K., Sakaguchi, M., Ishii, H., Applicability of fracture mechanics in strength evaluation of functionally graded materials. *JSME International Journal Series A* 1996;39:479-488.
- [212] Walters, M.C., Paulino, G.H., Dodds, R.H. Jr., Stress intensity factors for surface cracks in functionally graded materials under mode-I thermomechanical loading. *International Journal of Solids and Structures*, 2004;41:1081-1118.
- [213] Walters, M.C., Paulino, G.H., Dodds, R.H. Jr., Interaction integral procedures for 3-D curved cracks including surface tractions. *Engineering Fracture Mechanics*, 2005;72:1635-1663.
- [214] Walters, M.C., Paulino, G.H., Dodds, R.H. Jr., Computation of mixed-mode stress intensity factors for cracks in three-dimensional functionally graded materials, 2005 (accepted).
- [215] Walters, M.C., Paulino, G.H., Dodds, R.H. Jr., Computation of T -stresses for three-dimensional functionally graded solids (in preparation).
- [216] Wang, S.S., Yau, J.F., Corten, H.T., A mixed-mode crack analysis of rectilinear anisotropic solids using conservation laws of elasticity. *International Journal of Fracture* 1980;16:247-259.
- [217] Wang, X., Elastic T -stress solutions for penny-shaped cracks under tension and bending. *Engineering Fracture Mechanics*, 2004;71:2283-2298.
- [218] Wang, Y.-Y., On the two-parameter characterization of elastic-plastic crack-front fields in surface-cracked plates. In: *Constraint Effects in Fracture*, ASTM STP 1171, American Society for Testing and Materials, Philadelphia, USA, 1993;120-138.

- [219] Wang, Y.-Y., Parks, D.M., Evaluation of the elastic T-stress in surface-cracked plates using the line-spring method. *International Journal of Fracture* 1992;56:25-40.
- [220] Wei, L.W., Edwards, L., Fitzpatrick, M.E., FE analysis of stresses and stress intensity factors of interfacial cracks in a CTS specimen. *Engineering Fracture Mechanics* 2002;69:85-90.
- [221] Williams, M.L., On the stress distribution at the base of a stationary crack. *ASME Journal of Applied Mechanics* 1957;24:109-114.
- [222] Williamson, R.L., Rabin, B.H., Numerical modeling of residual stresses in Ni-Al₂O₃ gradient materials. In: *Ceramic Transactions, Proceedings of the 2nd International Symposium on Functionally Gradient Materials*. The American Ceramic Society, Westerville, Ohio, 1992.
- [223] Wilson, W.K., Yu, I.W., The use of the *J*-integral in thermal stress crack problems. *International Journal of Fracture* 1979;15:377-387.
- [224] Xu, G., Bower, A.F., Ortiz, M., An analysis of non-planar crack growth under mixed-mode loading. *International Journal of Solids and Structures* 1994;31:2167-2193.
- [225] Yang, B., Ravi-Chandar, K., Evaluation of elastic T-stress by the stress difference method. *Engineering Fracture Mechanics* 1999;64:589-605.
- [226] Yau, J.F., Wang, S.S., Corten, H.T., A mixed-mode crack analysis of isotropic solids using conservation laws of elasticity. *ASME Journal of Applied Mechanics* 1980;47:335-341.
- [227] Yang, S., Yuan, F.G., Determination and representation of the stress coefficient terms by path-independent integrals in anisotropic cracked solids. *International Journal of Fracture* 2000;101:291-319.

Author's Biography

Matthew C. Walters was born to Sandra and Kenneth Walters in Pasadena, California on October 1, 1971. After graduating in 1989 from High School in San Marino, California, he attended one year of school at Brigham Young University in Utah. He then served for two years among the Spanish-speaking immigrants in Montreal, Canada as a representative of the Church of Jesus Christ of Latter-Day Saints, commonly known as the "Mormon" Church. Matt returned to Brigham Young University in the Spring of 1993, and graduated from the Department of Civil Engineering in 1997.

Graduate studies commenced that same year at the University of Illinois at Urbana-Champaign. In the summer of 1998, Matt began part-time work at the U.S. Army Construction Engineering Research Laboratory in Champaign, Illinois. He worked for Jim Wilcoski and performed analyses of air-traffic control towers using SAP2000. During the next 1.5 years, he also assisted with laboratory experiments, including wood and cold-formed-steel shear wall tests, and shaking-table tests. Next came eight months performing finite-element analysis at Caterpillar's Champaign Simulation Center, where thoughts of a career in computational mechanics were born. He looked for research in finite-element analysis, and joined Professor Paulino's group in the fall of 2000. He completed requirements for a master's degree in 2002, and many a group meeting later, finished the work necessary for a Ph.D., graduating in May, 2005.

After school, Matt will work for ATK Thiokol in Promontory, Utah, where he will participate in fracture control for NASA-space-shuttle solid-rocket motors.